

ÉCOLE DOCTORALE Sciences de la Terre et Environnement (ED 413)

Laboratoire d'Hydrologie et de Géochimie de Strasbourg (UMR 7517)

THÈSE

présentée par :

Behshad KOOHBOR

Soutenance prévue : le **17 septembre 2020**

pour obtenir le grade de : **Docteur de l'Université de Strasbourg**

Discipline/ Spécialité : Sciences de l'environnement

Modeling water flow and mass transport in fractured porous media application to seawater intrusion and unsaturated zone

THÈSE dirigée par :

Monsieur FAHS Marwan
Monsieur BELFORT Benjamin

Maître de conférences – HDR, ENGEES
Maître de conférences, Université de Strasbourg

RAPPORTEURS :

Monsieur GRAF Thomas
Monsieur NOETINGER Benoît

Professeur, Université de Hanovre – Allemagne
Directeur de Recherche, IFPEN

AUTRES MEMBRES DU JURY :

Madame BERRE Inga
Monsieur OUDE ESSINK Gualbert
Madame ROSIER Carole
Monsieur TOUSSAINT Renaud

Professeur, Université de Bergen – Norvège
Directeur de Recherche, Université de Utrecht – Pays-Bas
Professeur, Université du Littoral Côte d'Opale
Directeur de Recherche, CNRS – EOST

Table of contents

| | |
|--|------------|
| List of figures..... | IV |
| Acknowledgements..... | VII |
| Chapter I: Introduction | 1 |
| 1.1. Overview | 1 |
| 1.2. Seawater Intrusion in coastal aquifers | 3 |
| 1.2.1 An overview of Chapter II: A Generalized Semi-Analytical Solution for the Dispersive Henry Problem | 4 |
| 1.2.2. An overview of Chapter III: Semi-analytical solution of contaminant transport in coastal aquifers | 6 |
| 1.2.3. An overview of Chapter IV: Uncertainty analysis for seawater intrusion in fractured coastal aquifers: application to Clashnessie Bay, UK..... | 6 |
| 1.3. Variably saturated flow in fractured domains: Application to El Assal aquifer in Lebanon | 8 |
| Chapitre I : Introduction | 10 |
| 1.1. Prolégomènes | 10 |
| 1.2. Intrusion d'eau de mer dans les aquifères côtiers | 12 |
| 1.2.1 Aperçu du chapitre II : solution semi-analytique généralisée au problème de dispersion de Henry | 14 |
| 1.2.2. Aperçu du chapitre III : solution semi-analytique du transport de contaminants dans les aquifères côtiers..... | 16 |
| 1.2.3. Aperçu du chapitre IV : analyse d'incertitudes pour l'intrusion d'eau de mer dans les aquifères côtiers fracturés : application à la baie de Clashnessie, Royaume-Uni | 16 |
| 1.3. Ecoulements variablement saturés dans les domaines fracturés : application à l'aquifère d'El Assal au Liban..... | 18 |
| Chapter II: Dispersive Henry problem: a generalization of the semianalytical solution to anisotropic and layered coastal aquifers | 21 |
| 2.1. Introduction | 21 |
| 2.2. The mathematical model and boundary conditions..... | 25 |
| 2.3. Semianalytical solution..... | 26 |
| 2.4. New technique for solving the equations in the spectral space..... | 29 |
| 2.5. Results and discussions..... | 31 |
| 2.5.1. Verification: Stability of the Fourier series solution and comparison against numerical solution..... | 31 |
| 2.5.2. Effect of anisotropy on seawater intrusion in homogenous aquifer..... | 37 |
| 2.5.3. Coupled effect of anisotropy and stratified heterogeneity on seawater intrusion.. | 41 |
| 2.6. Conclusion..... | 44 |

| | |
|--|------------|
| Chapter III: Semi-analytical solutions for contaminant transport under variable velocity field in a coastal aquifer | 47 |
| 3.1. Introduction | 47 |
| 3.2. Problem description and methodology | 49 |
| 3.3. Governing Equations | 52 |
| 3.4. The semi-analytical solution | 54 |
| 3.4.1. Adaptation of the FG method | 54 |
| 3.4.2. Implementation | 57 |
| 3.5. Evaluation of the contaminant transport characteristics | 58 |
| 3.6. Results: test examples, verification and comparison against numerical solution | 60 |
| 3.6.1. Stability of the semi-analytical solution and effect of Péclet number..... | 61 |
| 3.6.2. Comparison against numerical solution: verification, efficiency of the FG implementation and benchmarking issues..... | 67 |
| 3.7. Effect of seawater intrusion on contaminant transport | 70 |
| 3.8. Conclusion..... | 78 |
| Chapter IV: Uncertainty analysis for seawater intrusion in fractured coastal aquifers: Effects of fracture location, aperture, density and hydrodynamic parameters..... | 81 |
| 4.1. Introduction | 81 |
| 4.2. Material and methods..... | 85 |
| 4.2.1. Conceptual model: Fractured Henry Problem | 85 |
| 4.2.2. DFMM-VDF mathematical model:..... | 86 |
| 4.2.3. DFMM-VDF finite element model: COMSOL Multiphysics®: | 87 |
| 4.2.4. Metrics Design: | 88 |
| 4.3. Global sensitivity analysis..... | 89 |
| 4.3.1. Sobol' indices..... | 90 |
| 4.3.2. Polynomials Chaos Expansion (PCE) | 91 |
| 4.3.3. Sparse polynomial chaos expansion..... | 92 |
| 4.4. Validations: COMSOL model and Boussinesq approximation | 93 |
| 4.5. Global sensitivity Analysis: results and discussion | 97 |
| 4.5.1. The single horizontal fracture configuration (SHF)..... | 99 |
| 4.5.2. The network of orthogonal fractures configuration (NOF) | 108 |
| 4.6. Conclusion..... | 116 |
| 4.7. Field case study: Application to Clashnessie Bay, UK..... | 118 |
| Chapter V: An advanced discrete fracture model for variably saturated flow in fractured porous media | 125 |
| 5.1. Introduction | 125 |

| | |
|---|------------|
| 5.2. Governing Equations of VSF in fractured domains | 130 |
| 5.3. Numerical solution: MHFE method, ML technique, and MOL..... | 132 |
| 5.3.1. Trial functions of the MHFE method for the matrix and fractures | 132 |
| 5.3.2. Flux discretization in the matrix elements (MHFE method and ML technique) .. | 133 |
| 5.3.3. Flux discretization for a fracture element..... | 134 |
| 5.3.4. Hybridization: mass conservation on edges..... | 135 |
| 5.3.5. The new ML technique for fractures..... | 135 |
| 5.3.6. High-order adaptive time integration | 138 |
| 5.4. Results: Verification and advantages of the new developed numerical scheme | 138 |
| 5.4.1. Verifications: Fractured Vauclin test case | 138 |
| 5.4.2. Advantages of the ML technique for fractures | 143 |
| 5.5. Results: Field Scale Applications | 147 |
| 5.5.1. Objectives and overall presentation of the site | 147 |
| 5.5.2. Methodology for simulation and analysis..... | 150 |
| 5.5.3. Simulations with real data from 2013 to 2019..... | 150 |
| 5.5.4. Predictions under climate change from 2019 to 2099 | 155 |
| 5.6. Conclusion..... | 160 |
| Chapter VI: Conclusion and perspectives..... | 163 |
| 6.1. General conclusion | 163 |
| 6.2. Perspective | 166 |
| Chapitre VI : Conclusion et perspectives..... | 168 |
| 6.1. Conclusion générale..... | 168 |
| 6.2. Perspectives | 173 |
| References..... | 175 |
| Appendices | 199 |
| Appendix A. | 199 |
| Appendix B. | 201 |
| Appendix C. | 203 |

List of figures

| | |
|--|-----|
| Fig. 2.1. The HP assumptions (a) real configuration and (b) conceptual model..... | 21 |
| Fig. 2.2. Variation of the horizontal and vertical hydraulic conductivities..... | 33 |
| Fig. 2.3. Nonphysical oscillations related to the Gibbs phenomenon..... | 34 |
| Fig. 2.4. Semianalytical and numerical isochlors for the pure diffusive cases | 35 |
| Fig. 2.5. Semianalytical and numerical isochlors for the dispersive cases | 37 |
| Fig. 2.6. Effect of anisotropy on the isochlors' positions. | 40 |
| Fig. 2.7. Effect of anisotropy ratio on the 50% isochlor's position..... | 40 |
| Fig. 2.8. Variation of the SWI metrics versus r_k | 41 |
| Fig. 2.9. Coupled influence of anisotropy and heterogeneity on the main isochlors | 43 |
| Fig. 2.10. Effect of the heterogeneity for varying average gravity number..... | 44 |
| Fig. 3.1. Domain of the studied problem and contamination scenarios..... | 50 |
| Fig. 3.2. Simultaneous depiction of contaminant plume, velocity field of and saltwater..... | 63 |
| Fig. 3.3. Simultaneous depiction of contaminant plume, velocity field of and saltwater..... | 66 |
| Fig. 3.4. Comparison between semi-analytical and numerical solutions..... | 69 |
| Fig. 3.5. Effect of α on the main contamination contours (Scenario 1)..... | 72 |
| Fig. 3.6. Variation of the metrics characterizing the contaminant transport (Scenario 1)..... | 73 |
| Fig. 3.7. Effect of N_g on the main contamination contours (Scenario 2) | 76 |
| Fig. 3.8. Variation of the metrics characterizing the contaminant transport (Scenario 2)..... | 77 |
| Fig. 4.1. Conceptual model of the fractured Henry Problem. | 86 |
| Fig. 4.2. Schematic representation of the SWI metrics..... | 89 |
| Fig. 4.3. Isochlors obtained using the semi-analytical solution (SA) and COMSOL model.. | 95 |
| Fig. 4.4. Isochlors obtained using TRACES (in-house code) and COMSOL model | 97 |
| Fig. 4.5. A flowchart describing the methodology and approaches used to perform the global sensitivity analysis | 98 |
| Fig. 4.6. Comparison between the PCE surrogate model and physical (COMSOL) model for the SHF configuration | 102 |
| Fig. 4.7. GSA results for the spatial distribution of the salt (SHF configuration)..... | 104 |
| Fig. 4.8. Total (blue) and first order (red) SIs for the SHF configuration. | 106 |
| Fig. 4.9. The marginal effects of uncertain parameters on SWI metrics (SHF)..... | 107 |
| Fig. 4.10. Comparison between the PCE surrogate and physical (COMSOL) models for the NOF configuration | 110 |

| | |
|---|-----|
| Fig. 4.11. GSA results for the spatial distribution of the salt concentration (NOF configuration): | 111 |
| Fig. 4.12. Isochlors distribution for the NOF configuration | 112 |
| Fig. 4.13. Total (blue) and first order (red) SIs for the NOF configuration | 113 |
| Fig. 4.14. The marginal effects of uncertain parameters on SWI metrics (NOF) | 115 |
| Fig. 4.15. The location of Clashnessie coastal aquifer | 119 |
| Fig. 4.16. Representation of the (a) domain boundaries in plan-view and (b) the schematic 3D representation of the problem domain | 120 |
| Fig. 4.17. ERT maps for: (a) A-A' line, (b) for B-B' line and (c) for C-C' line | 120 |
| Fig. 4.18. Representation of the: (a) domain and the fracture network orientation and (b) the meshing grid (i.e. approximately 50K hexahedral elements) | 122 |
| Fig. 4.19. Distribution of salt in an arbitrary case in the domain | 123 |
| Fig. 5.1. Fluxes across the interfaces of a computational cell | 133 |
| Fig. 5.2. Decomposition of the global matrix into nine sub-matrices | 136 |
| Fig. 5.3. Schematic of the numerical integration of the integrals of the matrix M_k | 137 |
| Fig. 5.4. Mesh used in (a) the code MH-2D/2D and COMSOL-2D/2D and (b) in the new code MH-Lump-1D/2D | 141 |
| Fig. 5.5. Water content maps at $t=1h$ for the 4 fractured examples of the Vauclin test case | 143 |
| Fig. 5.6. The test case of infiltration in fractured dry soil | 146 |
| Fig. 5.7. CPU time vs. the number of elements of the computational mesh for both MH-Lump-1D/2D and MH-Cons-1D/2D codes | 147 |
| Fig. 5.8. Representation of: (a) the location of the El Assal karst aquifer, (b) schematic domain used to simulate the aquifer and (c) the monthly average recharge projection | 149 |
| Fig. 5.9. Maps of aquifer water content at the end of the simulation 2013-2019 | 152 |
| Fig. 5.10. Flow streamlines maps for: (a) The far-field flow direction in the aquifer, (b) Flow direction around fractures and (c) Flow around stagnation points | 152 |
| Fig. 5.11. Temporal distribution of (a) Vm (average amount of available water), (b) $H0$ (maximum level of the water table), and (c) q_{out} (spring outlet discharge) | 154 |
| Fig. 5.12. Spatial distribution of aquifer water content in 2009 | 156 |
| Fig. 5.13. Temporal distribution of (a) Vm , (b) $H0$, and (c) q_{out} for 2012-2009 period with the three models: F/CC (blue curves), NF/CC (orange curves) and F/NCC (red curves) | 157 |
| Fig. 5.14. Exploring the effect of fractures on the predicted spring outlet discharge | 159 |

Acknowledgements

I wish to offer my deepest gratitude to my research advisers, Dr. Marwan Fahs and Dr. Benjamin Belfort, for their continued support and guidance over the entire course of my Ph.D. studies.

Dr. Anis Younes and Dr. Hussein Hoteit are highly acknowledged for their generous support and guidance through various projects in the past three years. Dr. Behzad Ataie-Ashtiani and Dr. Craig T. Simmons are acknowledged for their valuable comments and advice during my Ph.D. studies. I am also grateful to Dr. Joanna Doummar for her great contributions to provide us with field data. Dr. Jean-Christophe Comte and Dr. Andrés González Quirós are highly acknowledged for their continued support and advice in the past few months. My appreciation extends to Dr. Philippe Ackerer and Dr. François Lehmann for their support and guidance. I would also like to thank the members of the defense committee, Dr. Thomas Graf, Dr. Renaud Toussaint, Dr. Carole Rosier, Dr. Benoît Noetinger, Dr. Inga Berre and Dr. Gualbert Oude Essink, for their time and effort.

I would like to take the opportunity to thank my parents, Bijan and Maryam, for their love and encouragement throughout my entire life. I would like to thank my wonderful brother, Behrad, who receives the most credit in supporting me through my academic studies. Finally, and most importantly, I would like to thank my partner, Coralie Ranchoux, for her kindness, love and unconditional support in the past three years.

Chapter I: Introduction

1.1. Overview

The applications of flow and mass transport in natural porous media are encountered in various fields of environmental sciences and industries. Examples of such applications include, and are not limited to, groundwater resources management (*Singh, 2014*), geothermal energy (*Al-Khoury, 2012; Nield and Bejan, 2013*) oil and gas production (*Chen, 2007*), carbon sequestration (*Class et al., 2009; Firoozabadi and Myint, 2010; Juanes and Class, 2013; Vilarrasa and Carrera, 2015*), mine operation (*Khalili et al., 2014*), waste disposal and radioactive waste management (*Zhang and Schwartz, 1995*), sea-aquifers interaction (*Werner et al., 2013*). Most of these applications affect directly or indirectly the lives of vast population and compel the geoscientists to consider relatively large scales of space and time in the process of their study. However, when large time and space scales are involved, the study of flow and transport in porous media becomes an over-complex and hard task where traditional experimental methods may be inefficient, expensive and even impractical (*Zhao et al., 2009*).

Numerical modeling provides rapid and economical tools for studying flow and mass transport in porous media (*Diaz Viera, 2012; May, 2014; Miller et al., 2013; Zhao et al., 2009*). When combined with experimental data and/or site observations, numerical models are helpful and useful for multiple purposes. They are extensively used for multiple purposes such as gaining insights into the physical processes, helping to understand the complex problem behind these processes and improving the design of hydrogeological systems and decision making. The emergence of capable computing systems and more advanced numerical methods in the past five decades has facilitated the efforts for modeling flow and mass transport in natural porous media. These modern numerical methods and techniques have improved the resolving procedure of numerical models and render them more practical for investigating real configurations. Nowadays, numerical modeling has become an irreplaceable tool in hydrogeology and geosciences.

Generally speaking, the methodology of numerical modeling consists of translating the studied problem into mathematical models and then solving the governing equations (in most cases a system of partial differential equations) numerically or in some cases analytically. However, the process is not as straightforward and simple as it may sound. Numerical modeling of flow and mass transport in natural porous media reveals specific challenges that are not common in

all engineering applications (*Miller et al., 2013; Zhao, 2016*). These challenges are related to the nature of porous media and the governing equations. A wide range of spatial (i.e. from few micrometers to hundreds of kilometers) and temporal (i.e. a fraction of a second to millions of years) scales combined with nonlinear nature of the associated physics underline this challenging task. Furthermore, real field simulations require a procedure for parameter estimation based on confronting simulations to measured data from the field and/or laboratory experiments. In addition, more reliable modeling studies require sensitivity analysis that can improve the parameter estimation procedure by identifying the most relevant ones. Usually, the parameter estimation procedure leads to uncertainties in the input parameters. These uncertainties propagate through the model and affect its outputs. So, in the modeling procedure, an uncertainty analysis should be performed to investigate the reliability of the model outputs. Parameter estimation procedure, sensitivity analysis and uncertainty analysis require repetitive simulations. But we know that one simulation, at real-time and space scales, is already highly expensive in computational requirements. Thus, there is a need for efficient and accurate numerical methods to improve model applicability in real field studies.

Remarkable advancement in the development of sophisticated numerical models for flow and transport in porous media has been achieved in the last 10 years. However, due to the broad nature of related problems applications, this topic is still at a developing stage (*Zhao et al., 2009*). The demand for faster, more accurate and inclusive simulating tools is still growing and the development of newer and more robust modeling schemes in this field is still on the focus. The main goal behind new models and numerical schemes development is to improve the capacity of models in simulating real cases at large time and space scales. In addition, as both parameter estimation procedure and sensitivity/uncertainty analysis require repetitive simulations, practical applications of models require, on one hand, efficient and robust forward models and, on the other hand, efficient algorithms for parameter estimation and sensitivity analysis. Thus, there is a growing need for new numerical methods, techniques and algorithms to take advantage of the new computer designs and continued improvements in computing technology. This brought us to the main objective of our work; to consider some ongoing topics of interest and contribute our effort to improve the existing models and numerical techniques as well as understanding flow and mass transport in porous media.

In the context of modeling flow and mass transport in porous media, the main focus of this work is on two applications: (i) seawater intrusion in coastal aquifers and (ii) variably saturated flow in fractured aquifers.

1.2. Seawater Intrusion in coastal aquifers

The population density of coastal regions around the world is nearly three times the average global population density (*Small and Nicholls, 2003*). The inhabitants of coastal regions rely greatly on groundwater resources as freshwater supplies around the world. This reliance is increased in dry countries and regions where the supply of surface water does not suffice the demand of a growing population (esp. close to the urban areas). Anthropogenic activity (e.g. over-pumping) (*Pokhrel et al., 2015*) and climate-change (*Oude Essink et al., 2010; Ranjan et al., 2006*) can cause the depletion of groundwater resources. The depletion of groundwater in coastal regions can result in, or further aggravate, hazards such as seawater intrusion. Seawater intrusion is reported to be the most significant threat to the groundwater resort quality in coastal regions (*Werner et al., 2013*).

Seawater intrusion is the subterranean movement of saltwater into the freshwater resorts due to the effect of density and dispersion (*Jiao and Post, 2019; Werner et al., 2013*). It has been declared a major threat by environmental protection agencies for decades (e.g. EEA, EPA, USGS, BRGM). This phenomenon can lead to the long-term salinization of freshwater resorts and soil in coastal regions which can endanger agricultural activity and impose great economic losses in these regions. Over-exploitation of groundwater resorts due to anthropogenic activities (e.g. over-pumping) or the local heterogeneity (e.g. stratification and existence of fractures) are of the most influential contributors to the extension of the saltwater wedge (i.e. the intruding saltwater front).

Seawater intrusion is usually tackled by numerical simulation. There are two types of models to simulate seawater intrusion: sharp interface approximation and variable-density flow. In sharp interface approximation, freshwater and saltwater are assumed as two immiscible fluids, having a common interface along which the pressures of the two fluids are continuous. In variable-density flow, there is a transition zone with finite thickness, in which the density of the fluid and the concentration of the salt varies continuously from saltwater to the freshwater (*Werner et al., 2013*). Variable density flow is usually considered more realistic than sharp interface approximation because it has the privilege of considering the transition zone between the freshwater and saltwater, known as the mixing zone. Only the variable-density flow model provides salinity distribution that can be compared and applied on field measurements (*Werner et al., 2013*).

To properly model seawater intrusion using variable-density flow model, a coupled system of variable-density flow and solute transport equations need to be discretized and solved. The system of equations is fundamentally nonlinear. Loosely speaking, the salt concentration results in a density difference between saltwater and freshwater. The density difference causes a convective flow which is highly sensitive to the density difference (e.g. on average there is only around 2.5% difference in density between the seawater and freshwater). The flow causes dispersion (i.e. velocity-dependent dispersion) and dispersion changes the concentration gradient and results in a new state of density distribution. These aforementioned interactions subjected to the presence of heterogeneity can result in a complex and in most cases a complicated, mathematical problem.

Numerical modeling of seawater intrusion with realistic assumptions is a challenging task. Common numerical techniques such as Finite Difference and Finite Element methods perform well while solving the flow equation, however, they result in large numerical dispersion when applied to solve the solute transport equation. One solution for such a problem is to refine the grid meshing, but the trade-off between the accuracy of the solution and the computational time consumption limits the refinement process (*Werner et al., 2013*). Therefore, there is a need for accurate numerical methods with proper performance to model seawater intrusion in a realistic configuration. In this part of the work, we contribute to the development of new semi-analytical solutions that can be used in the assessment of newly developed numerical techniques. We were also interested in seawater intrusion in fractured coastal aquifers. For such a case, it is well known that uncertainties related to fractures characteristics and topology have a significant impact on the model outputs. Thus, we contribute an efficient technique of uncertainty analysis based on surrogate modeling. These contributions are discussed in the next sub-sections.

1.2.1 An overview of Chapter II: A Generalized Semi-Analytical Solution for the Dispersive Henry Problem

Analytical solutions are of great interest due to their ability to benchmark new numerical solutions and the insights they provide for understanding the physics of problems and the inter-relation of coexisting parameters. Due to their high performance and accuracy, they are ideally suited for the interpretation of physical processes and performing sensitivity analysis and parameter estimation. Analytical solutions of seawater intrusion are predominantly based on sharp interface approximation in the literature (*Bear et al., 1999; Bruggeman, 1999; Kacimov, 2001; Kacimov et al., 2006; Reilly and Goodman, 1985; Werner et al., 2013*). For variable-density flow model there is no analytical solution due to the complexities associated with the

mathematical model and complex boundary conditions. Semi-analytical solutions are alternatives to analytical solutions. They provide high accuracy and performance as analytical solutions and they are more suitable to deal with nonlinearity and complex boundary conditions, as numerical methods. This Henry problem (Henry, 1964), is the only existing semi-analytical solution for seawater intrusion, with the variable density flow model. After more than five decades of its first introduction, the Henry problem and its variants are still widely used as simplified abstractions of seawater intrusion. The popularity of the Henry problem is due to its simplicity and existence of a closed-form unique semi-analytical solution. The first semi-analytical solution was proposed by H. Henry (1964) and was developed for a high uniform diffusion coefficient with oversimplifying density effects assumptions (*Ségol, 1994; Simpson and Clement, 2004, 2003; Voss et al., 2010*). Several further studies have contributed more realistic solutions with lower diffusion coefficients or velocity-dependent dispersion. However, the previous extensions of the Henry problem did not deliver a robust analytical solution with the inclusion of hydrodynamic dispersion, anisotropy and heterogeneity. This restricts the applicability of the solution to more realistic configurations.

Our contribution in this context is the development of a new semi-analytical solution, based on the Fourier series solutions, for an anisotropic and stratified (i.e. layered heterogeneity) configuration of the dispersive Henry problem. In addition to velocity-dependent dispersion, which was previously included in the solution by *Fahs et al. (2016)*, the effects of anisotropy and stratification are also added to the solution. The solution is obtained using the Fourier series method. A special model is used to describe hydraulic conductivity–depth in stratified heterogeneity. An efficient technique is developed to solve the flow and transport equations in the spectral space. The results provide a better understanding of the combined effect of anisotropy and stratification on seawater intrusion and quantifying metrics such as saltwater toe and flux. The results also helped to explain about some contradictory results stated in previous works in the literature. The proposed solution can be used for benchmarking purposes or explaining the inter-relation of the parameters associated with the physics of the problem.

This topic is developed in chapter II. It has been the subject of a paper published in the journal *Water (Fahs et al, 2018)*.

1.2.2. An overview of Chapter III: Semi-analytical solution of contaminant transport in coastal aquifers

In addition to seawater intrusion, coastal aquifers are susceptible to contamination coming from industrial and anthropogenic activities that are situated near the coastal regions. We were interested in contaminant transport in coastal aquifers. Accurate closed-form solutions of this problem are scarce (*Bolster et al., 2007*). Part of the reason because contaminant transport in coastal aquifers is inherently complex. This complexity mainly comes from the highly variable velocity field near the sea boundary due to the effect of seawater intrusion. Some analytical solutions have been developed for non-uniform velocity with simplifying assumptions or theoretical velocity fields (*Bolster et al., 2007; Craig and Heidlauf, 2009; Tartakovsky and Di Federico, 1997*). In Chapter III, a robust implementation of the Fourier series method is developed to deliver a semi-analytical solution for contaminant transport in coastal aquifers under variable-velocity field.

This work is inspired by the implementation of Fourier series method on density-driven flow (*Fahs et al., 2014; van Reeuwijk et al., 2009*). Two scenarios of contaminant sources are considered in this problem. The first scenario is defined by considering a contaminant source at the aquifer top surface. In the second scenario, the contaminant source is located upstream of the freshwater influx boundary. The considered configuration, the domain and the seawater intrusion boundary conditions are inspired by the Henry problem.

The work on this topic has been published as a journal article in the Journal of Hydrology (*Koohbor et al., 2018*).

1.2.3. An overview of Chapter IV: Uncertainty analysis for seawater intrusion in fractured coastal aquifers: application to Clashnessie Bay, UK

Fractured Coastal Aquifers are found globally. Several examples can be found France, USA, UK and all around the Mediterranean region (*Arfib and Charlier, 2016; Bakalowicz et al., 2008; Chen et al., 2017; Comte et al., 2018; Doukou and Karatzas, 2012; Perriquet et al., 2014; Xu et al., 2018*). Fractures play an important role in controlling seawater intrusion as they represent preferential pathways for water flow and can enhance seawater intrusion (*Bear et al., 1999*). However, fractures properties and topology are usually uncertain. These uncertainties lead to uncertainty in the model output and question the reliability of its predictive results. Global sensitivity analysis can be applied as an effective step towards understating

uncertainty propagation through models. In seawater intrusion, global sensitivity analysis has been applied to study the effects of hydrodynamic parameters in homogeneous coastal aquifers (*Herckenrath et al., 2011; Rajabi et al., 2015a; Rajabi et al., 2015b; Rajabi and Ataie-Ashtiani, 2014; Riva et al., 2015; Dell'Oca et al., 2017*). However, to the best of our knowledge, global sensitivity analysis has never been applied to seawater intrusion in fractured coastal aquifers. In this study, we present an efficient approach to evaluate uncertainty related to fractures on model outputs. This approach is based on the use of the Polynomial Chaos Expansion as a surrogate model of seawater intrusion. We analyze the uncertainties imposed by some key parameters associated with fractured coastal aquifers (e.g. fracture location, density, hydraulic conductivity, aperture and dispersivity) on the seawater intrusion and relevant metrics (e.g. saltwater toe, salinized area and intruding saltwater flux).

A coupled approach based on a Discrete Fracture Network model and variable-density flow is implemented with COMSOL Multiphysics® to act as model input for generating the metamodel used for the uncertainty quantification. The metamodel is generated by Polynomial Chaos Expansion. In addition to the conventional full order polynomial chaos expansion, we used a sparse polynomial chaos expansion algorithm that allows for reducing the number of simulations required to generate the metamodel. The uncertainty measures used to quantify and discuss the sensitivity of the model output to the model inputs are Sobol' indices. Sobol' Indices are used to identify the key variable imposing uncertainty on the various seawater intrusion metrics. Spatial analysis of the Sobol' indices also helps in locating the most sensitive parts of domain salinity distribution in regards to the input parameters. Additionally, marginal effects are calculated to further understand the contribution of each parameter to the model output. The findings in this chapter can contribute to various environmental applications such as preliminary assessment for field data collection and monitoring purposes associated with seawater intrusion in fractured coastal aquifers. They also show the potential for quality control and management of fresh groundwater resorts in coastal aquifers. The results related to this work have been published as a journal article in the Journal of Hydrology (*Koohbor et al., 2019*).

The developed strategy for uncertainty analysis has been applied for a hypothetical case. Further investigation of this strategy is its applicability to field studies. The field chosen for the application is in Clashnessie Bay (Scotland, UK) which is a fractured basement-rock coastal aquifer (Lewisian gneiss complex aged Precambrian) intersected by a densely fractured regional fault zone. In the context of this Ph.D., we started this application by developing a 3D

seawater intrusion model for the aquifer. Geophysical data (i.e. electrical resistivity tomography) have been used to estimate variations in fracture density and certain equivalent hydrodynamic properties. The model is developed with a discrete fracture approach. This work is a preliminary step to global sensitivity application. It has been developed during my research visit to the School of Geosciences at the University of Aberdeen.

1.3. Variably saturated flow in fractured domains: Application to El Assal aquifer in Lebanon

Accurate modeling of variably saturated flow in fractured porous media with relatively low computational time remains a challenge. This challenge is partly due to the nonlinear nature of Richards' Equation (RE), used to describe the flow in unsaturated porous media, and partly due to the complexity in heterogeneity imposed by fractures as conduits. The numerical solution of RE, even in unfractured domains, is among the most challenging problems in hydrogeology (*Miller et al., 2013*). Mathematical characteristics and strong nonlinearity induced by the constitutive relationships (*Suk and Park, 2019*) impose numerical difficulties in the process of discretization/resolving RE using conventional methods. The existence of fracture networks can add-up to this challenge. Therefore, numerical solutions of RE in explicitly fractured domains are not well-developed in the literature.

In Chapter V, we present an efficient numerical scheme based on advanced numerical techniques, for both space discretization and time integration, to model variably saturated flow in fractured porous media. A hybrid dimension Discrete Fracture/Matrix model is used to study the flow in the fracture (i.e. 1D elements) and porous matrix (i.e. 2D elements) explicitly and with high resolution. The Richards' equation is discretized using a mass-lumped mixed hybrid finite element method and integrated over time using the Method of Lines. A newly mass lumping scheme is developed for the fracture in order to improve the robustness of the mixed hybrid finite element method. The newly developed numerical scheme is shown to outstanding performance and accuracy when comparing with conventional simulation software packages (e.g. COMSOL Multiphysics®). The results are validated thoroughly for spatial and temporal discretization and the applicability of the scheme in field-scale studies by applying on the response of a fractured aquifer in Lebanon (El Assal) to the predicted recharge distribution of 2020-2100 considering the effect of climate change. The proposed numerical schemes show

great promises and perspective in applying the Discrete Fracture/Matrix model to field-scale studies.

This work has been published as a journal article in the journal of Advances in Water Resources (*Koohbor et al., 2020*).

Chapitre I : Introduction

1.1. Prolégomènes

Les applications dédiées à l'écoulement et au transport de masse en milieux poreux naturels se rencontrent dans divers domaines des sciences environnementales et de l'industrie. Ces applications comprennent, entre autres, la gestion des ressources en eaux souterraines (*Singh, 2014*), l'énergie géothermique (*Al-Khoury, 2012 ; Nield et Bejan, 2013*), la production de pétrole et de gaz (*Chen, 2007*), la séquestration du carbone (*Class et al, 200 ; Firoozabadi et Myint, 2010 ; Juanes et Class, 2013 ; Vilarrasa et Carrera, 2015*), l'exploitation minière (*Khalili et al., 2014*), l'élimination des déchets et la gestion des déchets radioactifs (*Zhang et Schwartz, 1995*), les interactions mer-aquifères (*Werner et al., 2013*). La plupart de ces applications affectent directement ou indirectement la vie de vastes populations et obligent les spécialistes des géosciences à considérer, dans leurs études, les processus à des échelles spatiale et temporelle relativement grandes. Cependant, l'étude de l'écoulements et du transport en milieux poreux, sur des domaines importants et de longues durées, devient une tâche très complexe et délicate car les méthodes expérimentales traditionnelles peuvent devenir inefficaces, s'avérer coûteuses et peu pratiques (*Zhao et al., 2009*).

La modélisation numérique fournit des outils rapides et économiques pour étudier les flux et le transport de masse dans les milieux poreux (*Diaz Viera, 2012 ; May, 2014 ; Miller et al., 2013 ; Zhao et al., 2009*). Lorsqu'ils sont combinés avec des données expérimentales et/ou des observations in-situ, les modèles numériques sont bénéfiques à des fins multiples. Ils sont largement utilisés, par exemple, pour mieux comprendre les processus physiques, pour aider à appréhender les problèmes complexes qui se cachent derrière ces processus, ou pour améliorer la caractérisation des systèmes hydrogéologiques et éclairer la prise de décision. L'émergence de systèmes informatiques performants et de méthodes numériques continuellement plus avancées au cours des cinq dernières décennies a facilité les efforts de modélisation des écoulements et du transport de masse dans les milieux poreux naturels. Ces méthodes et outils numériques modernes ont amélioré la résolution des modèles mathématiques, rendant ainsi la modélisation numérique davantage adaptée pour l'étude de configurations réelles. Aujourd'hui, celle-ci est devenue un outil irremplaçable en hydrogéologie et en géosciences.

D'une manière générale, la méthodologie de la modélisation numérique consiste à traduire le problème étudié en modèles mathématiques, puis à résoudre les équations associées (il s'agit,

dans la plupart des cas, d'un système d'équations aux dérivées partielles) numériquement ou, dans certains cas, analytiquement. Toutefois, la réalisation des différentes étapes de cette démarche méthodologique n'est pas toujours aussi simple et directe qu'il n'y paraît. La modélisation numérique de l'écoulement et du transport de masse dans les milieux poreux naturels révèle des défis spécifiques qui ne sont pas communs à toutes les applications d'ingénierie (*Miller et al., 2013 ; Zhao, 2016*). Ces défis sont liés à la nature même des milieux poreux et aux équations qui régissent les processus considérés. Un large éventail d'échelles spatiales (de quelques micromètres à des centaines de kilomètres) et temporelles (d'une fraction de seconde à des millions d'années), combiné à la nature non linéaire de la physique associée, laisse entrevoir toute la difficulté de la tâche confiée au modélisateur. Egalement, les simulations concernant des domaines réels et intégrant des conditions réalistes nécessitent souvent une procédure d'estimation de paramètres basée sur la confrontation des simulations aux données mesurées lors d'expériences sur le terrain et/ou en laboratoire. Dans ce contexte, le recours à l'analyse de sensibilité peut améliorer la procédure d'estimation en sélectionnant les paramètres les plus pertinents, ce qui peut ensuite renforcer la fiabilité des études de modélisation. Habituellement, la procédure d'estimation de paramètres entraîne des incertitudes sur les paramètres d'entrée. Ces incertitudes se propagent dans le modèle et affectent ses résultats. Dans la procédure de modélisation, une analyse d'incertitudes gagne donc à être effectuée pour renseigner sur la fiabilité des sorties du modèle. La procédure d'estimation de paramètres, l'analyse de sensibilité et l'analyse d'incertitudes nécessitent des simulations répétitives. Or, une seule simulation, pour un domaine réel et une durée hydrogéologique standard, s'avère déjà souvent très coûteuse en termes de ressources de calcul. Il est donc nécessaire de disposer de méthodes numériques efficaces et précises pour améliorer l'applicabilité des modèles dans les études réelles de terrain.

Des progrès remarquables ont été réalisés au cours des dix dernières années dans le développement de modèles numériques sophistiqués traitant des écoulements et du transport en milieux poreux. Cependant, en raison de la nature diversifiée des problèmes et applications abordés, ce sujet reste encore à un stade de développement (*Zhao et al., 2009*). La demande d'outils de simulation plus rapides, plus précis et plus complets continue de croître et le développement de nouveaux schémas de modélisation plus robustes dans ce domaine est toujours d'actualité. Un des objectifs principaux du développement de nouveaux modèles et schémas numériques est d'améliorer leur capacité à simuler des cas réels, sur de grandes échelles de temps et d'espace. En outre, comme la procédure d'estimation des paramètres et

l'analyse de sensibilité/incertitudes nécessitent des simulations répétitives, sa mise en œuvre pratique exige, d'une part, des modèles prévisionnels directs qui soient efficaces et robustes, et, d'autre part, des algorithmes pour l'estimation des paramètres et l'analyse de sensibilité qui soient également performants et optimisés. Il existe donc un besoin croissant de nouvelles méthodes, techniques et algorithmes numériques pour tirer parti des nouvelles configurations machines et des améliorations constantes de la technologie informatique. Ce panorama succinct nous conduit naturellement à exposer les principaux enjeux de ce travail de thèse : examiner/approfondir certains sujets d'intérêt qui mobilisent actuellement la communauté scientifique, apporter une contribution pour l'amélioration des modèles et des techniques numériques existants, mieux comprendre les écoulements et le transport de masse dans les milieux poreux.

Dans ce contexte de modélisation des écoulements et du transport de masse en milieux poreux, les travaux entreprise durant cette thèse apportent une contribution importante, principalement sur deux applications : (i) l'intrusion d'eau de mer dans les aquifères côtiers et (ii) l'écoulement variablement saturé dans les aquifères fracturés.

1.2. Intrusion d'eau de mer dans les aquifères côtiers

A l'échelle de la planète, la densité de population des régions côtières est presque trois fois supérieure à la densité moyenne de la population mondiale (*Small et Nicholls, 2003*). Dans le monde entier, les habitants des régions côtières dépendent largement des ressources en eau souterraine comme source d'approvisionnement en eau douce. Cette dépendance est accrue dans les pays et régions arides où l'approvisionnement en eau de surface ne suffit pas à couvrir la demande d'une population croissante (surtout à proximité des zones urbaines). Les activités anthropiques (par exemple le pompage excessif) (*Pokhrel et al., 2015*) et le changement climatique (*Oude Essink et al., 2010 ; Ranjan et al., 2006*) peuvent provoquer l'épuisement des ressources en eau souterraine. La raréfaction des eaux souterraines dans les régions côtières peut entraîner ou aggraver encore des risques tels que l'intrusion d'eau de mer. Ce phénomène est d'ailleurs considéré comme la menace la plus importante pour la qualité des eaux souterraines dans les régions côtières (*Werner et al., 2013*).

L'intrusion saline correspond au mouvement souterrain de pénétration de l'eau salée dans les ressources d'eau douce dû à l'effet de la densité et de la dispersion (*Jiao et Post, 2019 ; Werner et al., 2013*). Elle a été déclarée comme une menace majeure par les agences de protection de l'environnement depuis des décennies (par exemple l'AEE, l'EPA, l'USGS, le BRGM). Ce

phénomène peut conduire à la salinisation, à long terme, des nappes d'eau douce et des sols dans les régions côtières, mettant ainsi en danger les activités agricoles et provoquant alors de grandes pertes économiques dans ces régions. La surexploitation des ressources d'eau souterraine due à des activités anthropiques (par exemple, le pompage excessif) ou l'hétérogénéité locale (par exemple, la stratification et l'existence de fractures) sont les facteurs qui contribuent le plus à l'extension du biseau salée (i.e. l'intrusion d'un front d'eau salée).

L'intrusion d'eau de mer est généralement traitée par simulation numérique. Il existe deux types de modèles pour simuler l'intrusion saline : une approche basée sur l'approximation d'interface nette (ou abrupte) et une approche basée sur les écoulements à densité variable (ou écoulements densitaires). Dans l'approximation d'interface nette, l'eau douce et l'eau de mer sont supposées être deux fluides non miscibles, ayant une interface commune le long de laquelle les pressions des deux fluides sont continues. Pour les écoulements intégrant la variation de densité, il existe une zone de transition d'épaisseur finie, dans laquelle la densité du fluide et la concentration en sel varient continument de l'eau salée à l'eau douce (*Werner et al., 2013*). L'écoulement à contraste de densité est généralement considéré comme une approche plus réaliste que l'approximation d'interface nette, car, physiquement, elle tient compte de l'existence d'une zone de transition entre l'eau douce et l'eau salée, connue sous le nom de zone de mélange. Seul le modèle d'écoulements densitaires fournit une distribution de la salinité qui peut être appliquée à des études de terrain et comparée à des mesures (*Werner et al., 2013*).

Pour modéliser correctement l'intrusion saline à l'aide d'un modèle à écoulements densitaires, il faut discrétiser et résoudre un système d'équations d'écoulement et de transport de solutés, couplées à l'aide d'une équation d'état qui relie la densité du soluté à la concentration du soluté dans la solution. Le système d'équations est alors fondamentalement non linéaire. Succinctement, la concentration en sel entraîne une différence de densité entre l'eau salée et l'eau douce. La différence de densité provoque un flux convectif qui est très sensible à la variation de densité (en moyenne, il n'y a qu'une différence de densité d'environ 2,5 % entre l'eau de mer et l'eau douce). L'écoulement provoque une dispersion (dépendante de la vitesse), qui modifie le gradient de concentration et entraîne ainsi un nouvel état de distribution de la densité. Les interactions susmentionnées, s'ajoutant à la présence d'hétérogénéités au sein du milieu poreux, peuvent donner lieu à un problème mathématique complexe et, dans la plupart des cas, délicat à résoudre.

La modélisation numérique de l'intrusion saline avec des hypothèses réalistes est une tâche ardue. Les techniques numériques courantes telles que la méthode des différences finies et la méthode des éléments finis fonctionnent relativement bien pour résoudre l'équation d'écoulement, mais elles entraînent une grande dispersion numérique lorsqu'elles sont appliquées pour résoudre l'équation de transport du soluté. Une solution à ce problème consiste à affiner le maillage du domaine considéré, mais le compromis entre la précision de la solution et la consommation en temps de calcul limite cette stratégie de raffinement (*Werner et al., 2013*). Il est donc nécessaire de disposer de méthodes numériques précises et performantes pour modéliser l'intrusion saline dans une configuration réaliste. Dans cette partie du travail, notre contribution porte sur le développement de nouvelles solutions semi-analytiques qui peuvent notamment être utilisées dans l'évaluation des performances des techniques numériques nouvellement élaborées. Nous nous sommes également intéressés à l'intrusion saline dans les aquifères côtiers fracturés. Dans ce contexte, il est bien connu que les incertitudes liées aux caractéristiques et à la topologie des fractures ont un impact significatif sur les sorties des modèles. Aussi, nous proposons une technique efficace d'analyse d'incertitudes basée sur une modélisation de substitution. Ces différentes contributions sont examinées dans les 3 sous-sections suivantes.

1.2.1 Aperçu du chapitre II : solution semi-analytique généralisée au problème de dispersion de Henry

Les solutions analytiques présentent un grand intérêt car elles offrent la possibilité de tester / valider de nouvelles solutions numériques et apportent des connaissances pour comprendre la physique des problèmes et les relations entre les différents paramètres. En raison de leurs grandes performances et de leur précision élevée, elles conviennent parfaitement à l'interprétation des processus physiques et à la réalisation d'analyses de sensibilité et d'estimations de paramètres. Dans la littérature, les solutions analytiques pour le problème d'intrusion saline sont principalement basées sur l'approximation d'interfaces nettes (*Bear et al., 1999 ; Bruggeman, 1999 ; Kacimov, 2001 ; Kacimov et al., 2006 ; Reilly et Goodman, 1985 ; Werner et al., 2013*). Pour le modèle d'écoulement densitaire, il n'y a pas de solution analytique en raison des difficultés associées au modèle mathématique et aux conditions aux limites complexes. Les solutions semi-analytiques sont des alternatives aux solutions analytiques. Elles offrent une grande précision et des performances élevées comme les solutions analytiques et sont mieux adaptées pour traiter la non-linéarité du modèle et les

conditions limites complexes, comme les méthodes numériques. Seul le problème de Henry (*Henry, 1964*) dispose d'une solution semi-analytique pour représenter l'intrusion d'eau de mer avec le modèle d'écoulement densitaire. Après plus de cinq décennies depuis sa première introduction, le problème de Henry, et ses variantes, sont encore largement utilisés comme des abstractions simplifiées de l'intrusion saline. La popularité du problème de Henry est due à sa simplicité et à l'existence d'une solution semi-analytique unique exacte. La première solution semi-analytique a été proposée par H. Henry (1964) et a été développée pour un coefficient de diffusion uniforme élevé avec des hypothèses très simplificatrices sur les effets densitaires (*Ségol, 1994 ; Simpson et Clement, 2004, 2003 ; Voss et al., 2010*). Par la suite, plusieurs études ont apporté des solutions plus réalistes, notamment avec des coefficients de diffusion plus faibles ou une dispersion dépendant de la vitesse. Cependant, les extensions précédentes du problème de Henry n'ont pas fourni de solution analytique robuste prenant en compte la dispersion hydrodynamique, l'anisotropie et l'hétérogénéité. L'applicabilité de ces solutions à des configurations plus réalistes reste donc limitée.

Dans ce contexte, la contribution de ce travail de thèse porte sur le développement d'une nouvelle solution semi-analytique, basée sur la décomposition en séries de Fourier et incluant à la fois de l'anisotropie et une stratification (i.e. une hétérogénéité par couches) du problème dispersif de Henry. Dans la continuité de l'étude de Fahs et al. (2016), dont la solution prend en compte la dispersion en fonction de la vitesse, la solution proposée ici intègre, en sus, les effets de l'anisotropie et de la stratification. La solution est obtenue en utilisant la méthode des séries de Fourier. Un modèle spécial est utilisé pour introduire de l'hétérogénéité, décrite sous forme de stratification par une relation liant la conductivité hydraulique à la profondeur dans le domaine. Une technique efficace est ensuite développée pour résoudre les équations d'écoulement et de transport dans l'espace spectral. Les résultats permettent de mieux comprendre l'effet combiné de l'anisotropie et de la stratification sur l'intrusion saline et de quantifier des indicateurs tels que la longueur du biseau salé et le flux d'eau salée. En outre, l'étude a également permis d'expliquer certains résultats contradictoires énoncés dans des travaux antérieurs publiés dans la littérature. La solution proposée peut être utilisée à des fins de benchmarking ou pour expliquer l'interrelation des paramètres associés à la physique du problème.

Ce sujet est traité en détail dans le chapitre II de ce mémoire de thèse. Il a fait l'objet d'un article publié dans la revue *Water* (*Fahs et al, 2018*).

1.2.2. Aperçu du chapitre III : solution semi-analytique du transport de contaminants dans les aquifères côtiers

En plus de l'intrusion d'eau de mer, les aquifères côtiers sont susceptibles d'être contaminés par des pollutions anthropiques liées par exemple aux activités industrielles opérées dans les régions côtières. Nous nous sommes ainsi intéressés au transport de contaminants dans les aquifères côtiers. Les solutions précises exactes à ce problème sont rares (*Bolster et al., 2007*). Cela s'explique en partie par la complexité inhérente au transport de contaminants dans les aquifères côtiers. Et la difficulté provient principalement du champ de vitesse très variable au niveau de l'interface avec la mer en raison de l'effet de l'intrusion saline. Certaines solutions analytiques ont été développées pour des vitesses non uniformes avec des hypothèses simplificatrices ou des champs de vitesse théoriques (*Bolster et al., 2007 ; Craig et Heidlauf, 2009 ; Tartakovsky et Di Federico, 1997*). Le chapitre III de ce mémoire de thèse décrit une approche semi-analytique robuste, basée sur les séries de Fourier, et qui permet de résoudre le problème du transport de contaminants dans les aquifères côtiers sous un champ de vitesse variable.

Ce travail s'inspire de la méthode des séries de Fourier mise en œuvre pour traiter sur les écoulements densitaires (*Fahs et al., 2014 ; van Reeuwijk et al., 2009*). Deux scénarios de contamination sont considérés pour aborder cette problématique. Le premier scénario examine une source de contaminant situé en surface de l'aquifère. Dans le second scénario, la source de contamination est localisée en amont, sur la limite verticale d'entrée de l'eau douce. La configuration adoptée, le domaine et les conditions aux limites de l'intrusion saline sont inspirés du problème de Henry.

Le cadre méthodologique, les outils et les résultats obtenus sur cette problématique ont été présentés dans un article publié dans le Journal of Hydrology (*Koohbor et al., 2018*).

1.2.3. Aperçu du chapitre IV : analyse d'incertitudes pour l'intrusion d'eau de mer dans les aquifères côtiers fracturés : application à la baie de Clashnessie, Royaume-Uni

Les aquifères côtiers fracturés sont présents dans le monde entier. Plusieurs sites ont par exemple été identifiés en France, aux États-Unis, au Royaume-Uni et tout autour de la région méditerranéenne (*Arfib et Charlier, 2016 ; Bakalowicz et al., 2008 ; Chen et al., 2017 ; Comte et al., 2018 ; Doukou et Karatzas, 2012 ; Perriquet et al., 2014 ; Xu et al., 2018*). Les fractures

jouent un rôle important dans le contrôle de l'intrusion saline car elles représentent des voies préférentielles d'écoulement qui peuvent renforcer la pénétration de l'eau de mer (*Bear et al., 1999*). Cependant, la topologie et les propriétés des fractures sont généralement incertaines. Ces incertitudes, en entrée du problème, entraînent une variabilité des sorties du modèle qui peut remettre en question la fiabilité de leurs résultats et des prédictions associées. L'analyse de sensibilité globale peut constituer une étape efficace pour réduire la propagation de l'incertitude à travers les modèles. Dans le cas de l'intrusion saline, l'analyse de sensibilité globale a été appliquée pour étudier les effets des paramètres hydrodynamiques caractérisant des aquifères côtiers homogènes (*Herckenrath et al., 2011 ; Rajabi et al., 2015a ; Rajabi et al., 2015b ; Rajabi et Ataie-Ashtiani, 2014 ; Riva et al., 2015 ; Dell'Oca et al., 2017*). Cependant, à notre connaissance, l'analyse de sensibilité globale n'a jamais été appliquée à l'intrusion saline dans les aquifères côtiers fracturés. Dans cette étude, une approche efficace est présentée pour évaluer l'incertitude liée aux fractures sur les sorties de modèles. Cette approche est basée sur l'utilisation d'un modèle de substitution décrivant l'intrusion saline et construit avec un développement en polynômes du chaos. Les incertitudes associées à certains paramètres clés décrivant les aquifères côtiers fracturés (par exemple, l'emplacement des fractures, la densité et l'ouverture des fractures, la conductivité hydraulique et la dispersivité) engendrent une variabilité de l'intrusion saline qui est analysée dans ce travail par le biais d'indicateurs pertinents (par exemple, l'extension biseau salé, l'extension de la zone de mélange ou le flux d'eau salée entrant).

Une approche couplée, basée sur un modèle de réseau de fractures discrètes et d'écoulement dense, est mise en œuvre avec COMSOL Multiphysics® et constitue le modèle source pour générer le métamodèle destiné à la quantification des incertitudes. Le métamodèle est généré par une décomposition en polynômes du chaos. En plus de la technique d'expansion classique avec les polynômes du chaos d'ordre complet, un algorithme d'expansion à un ordre limité a été utilisé dans cette étude afin de réduire le nombre de simulations nécessaires à la génération du métamodèle. Les mesures d'incertitude utilisées pour quantifier et discuter de la sensibilité des sorties du modèle relativement à ses entrées sont les indices de Sobol'. Les indices de Sobol' sont utilisés pour identifier / discriminer les variables clés qui induisent une incertitude sur les différents indicateurs quantifiant l'intrusion saline. L'analyse spatiale des indices de Sobol' permet également de localiser les parties les plus sensibles de la distribution de salinité du domaine eu égard aux paramètres d'entrée. En outre, les effets marginaux sont calculés pour mieux comprendre la contribution de chaque paramètre sur la sortie du modèle. Les résultats

de ce chapitre peuvent contribuer à diverses applications environnementales telles que l'évaluation préliminaire pour orienter/optimiser la collecte de données sur le terrain et la surveillance associée à l'intrusion d'eau de mer dans les aquifères côtiers fracturés. Ils montrent également l'intérêt des outils développés pour gérer et contrôler la qualité des ressources d'eau douce dans les aquifères côtiers. Les résultats liés à ces travaux ont fait l'objet d'un article paru dans le *Journal of Hydrology* (Koohbor et al., 2019).

La stratégie développée pour l'analyse d'incertitude, introduite dans le paragraphe précédent, a été appliquée sur un cas synthétique. Dans un second temps, la démarche a fait l'objet d'un examen plus approfondi pour éprouver son applicabilité aux études de terrain. Le champ d'application choisi se trouve dans la baie de Clashnessie (Écosse, Royaume-Uni), qui est un aquifère côtier rocheux de socle fracturé (gneiss du complexe lewisien datant du Précambrien) recoupé par une zone de faille régionale fortement fracturée. Dans le cadre de ce doctorat, nous avons entamé cette application en développant un modèle 3D d'intrusion saline dans l'aquifère. Des données géophysiques (notamment de la tomographie par résistivité électrique) ont été utilisées pour estimer les variations de densité de fractures et certaines propriétés hydrodynamiques équivalentes. Le modèle est développé avec une approche de fractures discrètes. Ce travail constitue une étape préliminaire à l'application de la méthode d'analyse de sensibilité globale. Il a été engagé au cours d'un séjour de recherche à l'école des géosciences de l'Université d'Aberdeen.

1.3. Ecoulements variablement saturés dans les domaines fracturés :

application à l'aquifère d'El Assal au Liban

La modélisation précise de l'écoulement en milieux poreux fracturés et variablement saturés, avec un temps de calcul relativement faible, reste un défi. Ce challenge s'explique d'une part par la nature non linéaire de la physique du problème, par exemple l'équation de Richards (ER) utilisée pour décrire l'écoulement en milieux poreux non saturés, et d'autre part, en raison de la complexité des hétérogénéités introduites par les fractures en tant que conduits. La résolution numérique de l'ER, a fortiori dans les domaines non fracturés, est l'un des problèmes les plus difficiles à résoudre en hydrogéologie (Miller et al., 2013). Les caractéristiques mathématiques et la forte non-linéarité induite par les relations hydrodynamiques constitutives (Suk et Park, 2019) entraînent des difficultés numériques pour la discrétisation et la résolution de l'ER avec

des méthodes conventionnelles. L'existence de réseaux de fractures vient encore relever le niveau du défi. Cela explique certainement que les solutions numériques de l'ER dans les domaines explicitement fracturés ne sont pas très développées dans la littérature.

Dans le chapitre V de ce mémoire de thèse, un schéma numérique efficace est présenté pour modéliser l'écoulement variablement saturé en milieux poreux fracturés ; il s'appuie sur des techniques numériques avancées, à la fois pour la discrétisation spatiale et l'intégration temporelle. Un modèle à dimension hybride, incorporant les fractures discrètes et la matrice, est utilisé pour étudier l'écoulement dans les fractures (représentée par des éléments 1D) et la matrice poreuse (constituée d'éléments 2D), définies de manière explicite et avec une haute résolution. L'équation de Richards est discrétisée avec la méthode des éléments finis mixtes hybrides avec un schéma de condensation de la masse, et intégrée en temps à l'aide de la méthode des lignes. Un nouveau schéma de condensation de la masse a été développé pour les fractures afin d'améliorer la robustesse de la méthode des éléments finis mixtes hybrides. Ce nouveau schéma numérique mis au point se révèle très performant et d'une précision exceptionnelle par rapport aux logiciels de simulation classiques (par exemple COMSOL Multiphysics®). Une étude approfondie des résultats a permis de valider les stratégies de discrétisations spatiale et temporelle et d'aborder l'applicabilité du schéma pour des études de terrain. Dans cette optique, notre étude s'est intéressée à la réponse d'un aquifère fracturé au Liban (El Assal) soumis à une distribution prévisionnelle de sa recharge superficielle pour la période 2020-2100 qui intègre les effets du changement climatique. Les schémas numériques proposés sont très prometteurs et offrent de belles perspectives en ce qui concerne l'application aux études de terrain du modèle incorporant fractures discrètes et matrice.

Un article publié dans le journal *Advances in Water Resources* restitue les principaux développements théoriques et les résultats obtenus (*Koohbor et al., 2020*).

Chapter II: Dispersive Henry problem: a generalization of the semianalytical solution to anisotropic and layered coastal aquifers

2.1. Introduction

The Henry problem (HP) (Henry, 1964) is widely used as a surrogate for the understanding of seawater intrusion (SWI) processes in coastal aquifers (Werner *et al.*, 2013). This is an abstraction of SWI in a vertical cross-section of a confined coastal aquifer perpendicular to the shoreline. In this aquifer, an inland freshwater flow is in equilibrium with the seawater intruded due to its higher density from the seaside (Fig. 2.1). The aquifer is assumed to be homogenous and isotropic.

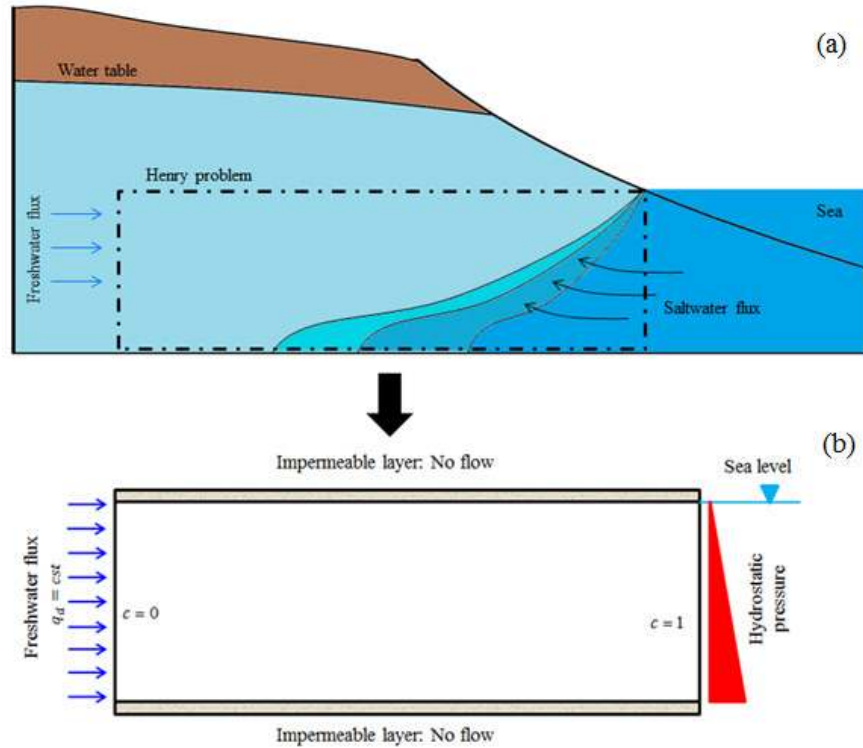


Fig. 2.1. The HP assumptions (a) real configuration and (b) conceptual model (Yang *et al.*, 2013).

Recently, a variation of the HP has been used to understand SWI in fractured coastal aquifers (Grillo *et al.*, 2010; Sebben *et al.*, 2015). A reactive HP has been presented to investigate the

interplay between dispersion and reactive processes in coastal aquifers (*Nick et al., 2013*) and to study the effect of calcite dissolution on SWI (*Laabidi and Bouhlila, 2015*). HP has been considered in the several works investigating the effect of heterogeneity (*Alhama Manteca et al., 2014; Held et al., 2005; Kerrou and Renard, 2010*), anisotropy (*Abarca et al., 2007; Qu et al., 2014*), mass dispersion (*Abarca et al., 2007*), salinity dependent permeability (*Mehnert and Jennings, 1985*), seafloor slope (*Walther et al., 2017*) and inland boundary conditions (*Sun et al., 2017*) on the SWI extent. Three variants of this problem have been used in *Post et al. (2013)* to interpret the groundwater ages in coastal aquifers. *Javadi et al. (2015)* developed a multi-objective optimization algorithm and applied it to the HP in order to assess different management method for controlling SWI. *Hardyanto and Merkel (2007)*, *Herckenrath et al. (2011)*, *Rajabi et al. (2015a; 2015b)*, *Rajabi and Ataie-Ashtiani (2014)*, *Burrows and Doherty (2015)* and *Riva et al. (2015)* investigated the HP and conducted uncertainty analysis to evaluate the effect of incomplete knowledge of the aquifer parameters on the predictions of SWI models. (*Sanz and Voss, 2006*) developed a posteriori parameter covariance matrix analysis of the HP and provided insight about parameter sensitivities that can help in improving the inverse modeling procedure. Parameters sensitivity analysis based on the HP is also reported in (*Carrera et al., 2010*) who presented a general analysis of the inverse problem for SWI.

This brief review points out the importance of the HP for theoretical and practical investigations of conceptual and modeling aspects of SWI. Nonetheless, the popularity of this problem stems precisely from the existence of a semianalytical (SA) solution (*Henry, 1964*). The formulation of the HP is based on the density-driven flow (DDF) model that incorporates a system of variable density-flow equation, advection-dispersion equation and state relation expressing the mixture density in terms of the saltwater concentration. The SA solution of HP is the only existing exact solution for the DDF model. Due to this SA solution, HP has been accepted as one of the primarily used benchmarks for the assessment of DDF numerical codes (*e.g. Hany F. Abd-Elhamid and Javadi, 2011; H.F. Abd-Elhamid and Javadi, 2011; Boufadel et al., 1999; Chen and Hsu, 2004; Emami-Meybodi and Hassanzadeh, 2015; Gotovac et al., 2007; Jamshidzadeh et al., 2013; Javadi et al., 2012; Langevin et al., 2010; Langevin and Guo, 2006; Li et al., 2013; Mugunthan et al., 2017; Nick et al., 2013; Pool et al., 2011; Servan-Camas and Tsai, 2010; Soto Meca et al., 2007; Yoon et al., 2017; Younes et al., 2009*).

The first SA solution of the HP has been developed by (*Henry, 1964*) using the Fourier series method. This solution has undergone a revision by (*Ségol, 1994*) who pointed out some errors in the Henry's solution and proposed appropriate corrections. With this revision, (*Ségol, 1994*)

was able to recreate the SA solution numerically. The worthiness of this SA solution for benchmarking DDF models codes have been widely discussed in the literature (*Diersch and Kolditz, 2002; Goswami and Clement, 2007; Prasad and Simmons, 2005; Simpson and Clement, 2004, 2003; Weatherill et al., 2004; Werner et al., 2013; Voss et al., 2007*). These studies concluded that this solution is not sufficient to test DDF numerical models because the buoyancy effects are dominated by the influence of boundary forcing exerted by the freshwater inland flow and by the diffusion effects as the solution is limited to exaggerated diffusion coefficients. Consequently, *Simpson and Clement (2004)* suggested an improved version of the SA solution by decreasing the freshwater recharge by half. *Younes and Fahs (2014) and Zidane et al. (2012)* developed new implementations of the SA method and obtained solutions with reduced diffusion coefficients. A further limitation of the Henry's SA solution is its unrepresentativeness of the real-world SWI as only uniform diffusion and no velocity-dependent dispersion are considered. Dispersion processes are important factors that effectively influence the mixing between fresh and salt waters (*Abarca et al., 2007; Chang et al., 2011; Qu et al., 2014*). A dispersive HP has been suggested by *Abarca et al. (2007)* based on numerical simulations. As claimed by *Abarca et al. (2007)*, the major drawback of this problem is that there is no reference solution with which the results can be compared. Recently *Fahs et al. (2016)* addressed this issue and developed a new SA solution for the dispersive HP. While all the existing SA solutions are based on the positions of the main concentration isochlors, *Fahs et al. (2016)* derived analytically several metrics characterizing the SWI as the toe length, thickness of the mixing zone, saltwater flux to the aquifer, depth of the groundwater discharge zone at the sea boundary.

This study attempts to generalize the SA solution of the dispersive HP to more realistic configurations. Indeed, anisotropy and heterogeneity are primary characteristics of real aquifers that the SA solutions of the HP do not account for. Several former studies indicated that anisotropy can affect the saltwater penetration, the saltwater flux and submarine groundwater discharge (*Abarca et al., 2007; Michael et al., 2013; Qu et al., 2014*). Heterogeneity has been also found to play an important role in SWI processes (*Chang and Yeh, 2010; Held et al., 2005; Kerrou and Renard, 2010; Lu et al., 2013; Simmons et al., 2001*). Thus, the aim of this work is to extend the SA solution of the dispersive HP, developed by *Fahs et al. (2016)*, to anisotropic and heterogeneous coastal aquifer.

The developed SA solution is based on the Fourier series method applied to the stream function form of the governing equations. This method combines the exactness of the analytical methods with an important extent of generality in describing the geometry and boundary conditions of

the numerical methods (*BniLam and Al-Khoury, 2017*). It proceeds by expending the unknowns (stream function and salt concentration) into infinite Fourier series and applying a Galerkin treatment using the Fourier modes as trial functions. We derived the stream function formulation in the case of a heterogeneous and anisotropic domain. Heterogeneity introduces terms involving the space derivative of the permeability that require specific permeability–depth relationships to be addressed analytically. This was achieved by considering stratified domain characterized via the Gardner exponential permeability function Gardner et al. (1958) widely used in layered aquifers (*e.g. Fajraoui et al., 2017; Ghezzehei et al., 2007; Jiang et al., 2009; Kuang and Jiao, 2014; Wang et al., 2011; Younes and Fahs, 2015; Zlotnik et al., 2011*). Solving the flow and transport equations in the spectral space is a challenging task, especially when large numbers of Fourier modes should be used to obtain oscillation-free solutions. Heterogeneity compounds these challenges as it involves high local gravity numbers that require a large number of Fourier modes to be represented adequately (*Fahs et al., 2014*). A new technique is developed here for solving the spectral flow and transport equations with reduced number of unknowns. With this technique, we show that the HP can be solved in the spectral space with only the concentration as primary unknowns.

Various illustrative test cases are generated and the SA solutions are compared against an in-house finite element code. The SWI metrics are evaluated analytically based on the Fourier series. This metrics represents quantitative indicators more suitable for code validation and benchmarking than the isochlors' positions. They are also used to investigate the effect of anisotropy and stratified heterogeneity on SWI. Indeed, few studies have reported the effect of anisotropy on the isochlors' positions (*Abarca et al., 2007; Michael et al., 2013; Qu et al., 2014*). The contradictory results of these studies call for further investigations (*Qu et al., 2014*). Besides, effect of heterogeneity on SWI has been considered experimentally and numerically in *Dose et al.(2014)*, *Houben et al. (2018)*, *Kerrou and Renard (2010)*, *Lu et al.(2013)* and *Pool et al.(2015)*. To the best of our knowledge, coupled effects of anisotropy and stratified heterogeneity has never been investigated. Here we take advantage of the developed SA solution to address this gap. While previous numerical or experimental studies investigated visually the uncoupled effects of anisotropy and stratification on the isochlors, this work aims to analytically provide deeper understanding of their coupled effects on several relevant metrics characterizing SWI.

2.2. The mathematical model and boundary conditions

The DDF mathematical model for SWI is based upon the coupled variable-density flow and mass transport equation. Under Oberbeck-Boussinesq approximation (*Guevara Morel et al., 2015*) and steady-state conditions, the flow system is given by the following continuity equation and Darcy's law (*Huyakorn et al., 1987*):

$$\nabla \cdot \mathbf{q} = 0 \quad (2.1)$$

$$\mathbf{q} = -\mathbf{K} \left(\nabla h + \frac{\rho - \rho_0}{\rho_0} \nabla z \right) \quad (2.2)$$

where \mathbf{q} is the Darcy's velocity $[LT^{-1}]$; ρ_0 the freshwater density $[ML^{-3}]$; g the gravitational acceleration $[LT^{-2}]$; μ the dynamic viscosity of the fluid $[ML^{-1}T^{-1}]$, \mathbf{K} freshwater hydraulic conductivity tensor $[LT^{-1}]$ (diagonal with components K_x and K_z); h the equivalent freshwater head $[L]$; ρ the density of mixture fluid $[ML^{-3}]$ and z is the elevation $[L]$.

The salt transport processes can be described by the advection-dispersion equation:

$$\varepsilon \frac{\partial c}{\partial t} + \mathbf{q} \cdot \nabla c - \nabla \cdot (\varepsilon D_m \mathbf{I} + \mathbf{D}) \nabla c = 0 \quad (2.3)$$

where c is the dimensionless solute concentration $[-]$; D_m the molecular diffusion coefficient $[L^2T^{-1}]$; ε the porosity $[-]$, \mathbf{I} the identity matrix and \mathbf{D} is the dispersion tensor defined by:

$$\mathbf{D} = (\alpha_L - \alpha_T) \frac{\mathbf{q} \otimes \mathbf{q}}{|\mathbf{q}|} + \alpha_T |\mathbf{q}| \mathbf{I} \quad (2.4)$$

Where α_L and α_T are the longitudinal and transverse dispersion coefficient respectively $[L]$.

Flow and transport equations are coupled via the linear mixture density equation:

$$\rho = \rho_0 + \Delta \rho \cdot c \quad (2.5)$$

Where $\Delta \rho = \rho_1 - \rho_0$ is the density difference between seawater (ρ_1) and freshwater (ρ_0).

The geometry of the aquifer is simplified to a rectangle of length (ℓ) and depth (d). The freshwater recharge flux per unit of width imposed on the inland side is noted $q_d [L^2T^{-1}]$. At

the seaside, seawater's equivalent freshwater head is specified and constant salt concentration ($c=I$) is imposed.

2.3. Semianalytical solution

In isotropic domains, the freshwater head (h) can be eliminated from the flow equation by applying the curl operator to Darcy's law (Eq. (2.2)). For anisotropic domain, equivalent procedure is to differentiate the x-component (resp. z-component) of Darcy's law with respect to z (resp. x) and divide it by K_x (resp. K_z), while accounting for spatial hydraulic conductivity variation as the domain is heterogeneous. Subtracting the resulting equations, one from the other, gives:

$$r_k \frac{\partial q_x}{\partial z} - \frac{\partial q_z}{\partial x} = \frac{K_z}{\rho_0} \frac{\partial \rho}{\partial x} + r_k q_x \frac{1}{K_x} \frac{\partial K_x}{\partial z} - q_z \frac{1}{K_z} \frac{\partial K_z}{\partial x} \quad (2.6)$$

where q_x and q_z are the velocity components and $r_k = K_z/K_x$ is the hydraulic conductivity anisotropy ratio as defined in *Abarca et al. (2007)*.

The Stream function can satisfy the continuity equation. Using Eq. (2.5) and the stream function, equation (2.6) writes:

$$r_k \frac{\partial^2 \psi}{\partial z^2} + \frac{\partial^2 \psi}{\partial x^2} - r_k \frac{\partial \psi}{\partial z} \frac{1}{K_x} \frac{\partial K_x}{\partial z} - \frac{\partial \psi}{\partial x} \frac{1}{K_z} \frac{\partial K_z}{\partial x} - \frac{K_z \Delta \rho}{\rho_0} \frac{\partial c}{\partial x} = 0 \quad (2.7)$$

As in the Standard HP, the following changes of variables are considered to obtain periodic boundary conditions (essential for the Fourier series method) and to derive the non-dimensional form of the flow equation:

$$X = \frac{x}{d}, \quad Z = \frac{z}{d}, \quad \Psi = \frac{\psi}{q_d} - Z, \quad C = c - \frac{X}{\xi} \quad (2.8)$$

where $\xi = \ell/d$ is the aspect ratio.

$$r_k \frac{\partial^2 \Psi}{\partial Z^2} + \frac{\partial^2 \Psi}{\partial X^2} - r_k \frac{1}{K_x} \frac{\partial K_x}{\partial Z} \left(\frac{\partial \Psi}{\partial Z} + 1 \right) + \frac{1}{K_z} \frac{\partial K_z}{\partial X} \frac{\partial \Psi}{\partial X} - NG \left(\frac{\partial C}{\partial X} + \frac{1}{\xi} \right) = 0 \quad (2.9)$$

$NG = \frac{K_z d \Delta \rho}{\rho_0 q_d}$ is the local gravity number which compares the buoyancy flux to the inland freshwater flux.

Due to heterogeneity, the stream function formulation of the flow equation incorporates the spatial derivatives of the hydraulic conductivity. Consequently, the SA solution cannot be obtained under discontinuous depth-hydraulic conductivity relationship. To overcome this

limitation, we considered heterogeneities corresponding to vertical stratification. We assume that heterogeneity is perfectly layering with an exponential trend of hydraulic conductivity with depth. This picture is widespread and agrees with most coastal sedimentary aquifers (*Alberti et al., 2017; Lu et al., 2013; Mehdizadeh et al., 2014*). The exponential trend of hydraulic conductivity has been suggested as a simplified model to describe stratified heterogeneity by *Gardner (1958)*. It appears to have considerable generality and field evidence (*Fajraoui et al., 2017; Ghezzehei et al., 2007; Jiang et al., 2009; Kuang and Jiao, 2014; Wang et al., 2011; Younes and Fahs, 2015; Zlotnik et al., 2011*). In anisotropic aquifers, the exponential depth-hydraulic conductivity model is given by (Zlotnik et al., 2011):

$$K_x(Z) = K_{x,0}e^{\Upsilon Z}; \quad K_z(Z) = K_{z,0}e^{\Upsilon Z} \quad (2.10)$$

Where $K_{x,0}$ and $K_{z,0}$ are the local horizontal and vertical hydraulic conductivity at the aquifer bottom surface, respectively. Υ is the rate of hydraulic conductivity change with depth.

Usually, the hydraulic conductivity is decreasing with depth. Thus, Υ is mostly positive. In certain cases, hydraulic conductivity can increase with depth (Υ negative) due to hydro-fracturing. The developed SA can be applied to both negative and positive values of Υ , but results are presented only for the common case of decreasing hydraulic conductivity with depth. The considered model (Eq. (2.10)) assumes constant local (or small) scale anisotropy as the anisotropy ratio is the same for all layers ($r_K = K_z/K_x = K_{z,0}/K_{x,0}$). Based on the adopted depth-hydraulic conductivity model, Eq. (2.9) becomes:

$$r_K \frac{\partial^2 \Psi}{\partial Z^2} + \frac{\partial^2 \Psi}{\partial X^2} - \Upsilon r_K \left(\frac{\partial \Psi}{\partial Z} + 1 \right) - NG_0 e^{\Upsilon Z} \left(\frac{\partial C}{\partial X} + \frac{1}{\xi} \right) = 0 \quad (2.11)$$

where $NG_0 = K_{z,0}d\Delta\rho/\rho_0q_d$ is the local gravity number at the aquifer bottom surface.

The unknowns are expanded into infinite Fourier series that satisfy the boundary conditions:

$$\Psi = \sum_{m=1}^{Nm} \sum_{n=0}^{Nn} A_{m,n} \sin(m\pi Z) \cos(n\pi X/\xi) \quad (2.12)$$

$$C = \sum_{r=0}^{Nr} \sum_{s=1}^{Ns} B_{r,s} \cos(r\pi Z) \sin(s\pi X/\xi) \quad (2.13)$$

where $A_{m,n}$ (resp. $B_{r,s}$) are the Fourier series coefficients for the stream function (resp. concentration). Nm and Nn are the truncation orders for the stream function in the X and Z directions, respectively. Nr and Ns are the ones for salt concentration.

The Fourier series expansions are appropriately substituted in Eq. (2.11). Then a Galerkin treatment is applied with the Fourier modes as trial function. This leads to the following system of equations:

$$R_{g,h}^F = \varpi_h^1 \pi^2 \xi A_{g,h} \left(r_k g^2 + \frac{h^2}{\xi^2} \right) + \varpi_h^1 r_K \Upsilon \xi \sum_{m=1}^{Nm} m A_{m,h} \Pi_{g,m} + \pi^2 N G_0 h \sum_{r=0}^{Nr} \tilde{B}_{r,h} \Gamma_{g,r} + 2\pi N G_0 \delta_{h,0} \Gamma_{g,0} + \frac{2r_K \Upsilon \xi}{\pi} \Pi_{g,0} \delta_{h,0} = 0 \quad (g = 1..Nm, h = 0..Nn) \quad (2.14)$$

where R^F is the residual vector of the flow equation and $\delta_{i,j}$ is the Kronecker symbol.

The above procedure is similarly applied to the transport equation. This gives:

$$b_m \left(\frac{\partial^2 C}{\partial X^2} + \frac{\partial^2 C}{\partial Z^2} \right) - \frac{\partial \Psi}{\partial Z} \frac{\partial C}{\partial X} + \frac{\partial \Psi}{\partial X} \frac{\partial C}{\partial Z} - \frac{1}{\xi} \frac{\partial \Psi}{\partial Z} - \frac{\partial C}{\partial X} - \frac{1}{\xi} + \Delta_{1,1} \frac{\partial^2 C}{\partial X^2} + 2\Delta_{1,2} \frac{\partial^2 C}{\partial X \partial Z} + \Delta_{2,2} \frac{\partial^2 C}{\partial Z^2} + \left(\frac{\partial C}{\partial X} + \frac{1}{\xi} \right) \left(\frac{\partial \Delta_{1,1}}{\partial X} + \frac{\partial \Delta_{1,2}}{\partial Z} \right) + \frac{\partial C}{\partial Z} \left(\frac{\partial \Delta_{1,2}}{\partial X} + \frac{\partial \Delta_{2,2}}{\partial Z} \right) = 0 \quad (2.15)$$

where $b_m = \varepsilon D_m / q_d$ and $\Delta_{i,j} = D_{i,j} / q_d$.

The Fourier series method applied to Eq. (2.15) gives the following system of equations (see *Fahs et al. (2016)*):

$$R_{g,h}^T = \varpi_g^2 b_m \pi^2 B_{g,h} \left(\frac{h^2}{\xi^2} + g^2 \right) \xi - \frac{\pi}{4} \sum_{m=1}^{Nm} \sum_{n=0}^{Nn} \sum_{r=0}^{Nr} \sum_{s=1}^{Ns} B_{r,s} A_{m,n} (s.m.\eta_{g,m,r} \theta_{h,n,s} - r.n.\kappa_{g,m,r} \lambda_{h,n,s}) - g \sum_{n=0}^{Nn} \tilde{A}_{g,n} \Lambda_{h,n} - \varpi_g^2 \sum_{s=1}^{Ns} s B_{g,s} \Lambda_{h,s} - \frac{2}{\pi} \Lambda_{h,0} \delta_{g,0} - 4 \sum_{i=1}^{Np} W p_i F^{Disp} (X p_i, Z p_i) \cos(g \pi Z p_i) \sin \left(h \pi \frac{X p_i}{\xi} \right) = 0 \quad (g = 0..Nr; h = 1..Ns) \quad (2.16)$$

where R^T is the residual vector corresponding to the transport equation. The coefficients and matrices of Eqs. (2.14) and (2.16) are defined in appendix A. Np is the number of integration points used to evaluate the dispersion terms. Wp , Xp and Zp are the integration weight and the coordinates of the integration points, respectively.

We should mention that, as in *Fahs et al. (2016)*, the Fourier series are used to evaluate analytically the four dimensionless metrics characterizing the SWI:

- The length of the toe (L_{toe}): which is the dimensionless distance between the seaside boundary and the point where the 50% isochlor intersect the aquifer bottom.

- The average vertical width of the mixing zone (W_{MZ}): defined as the average of the vertical dimensionless distances between the 10% and 90% isochlors. The mixing zone is defined on the interval $0.3 \times L_{toe}$ to $0.7 \times L_{toe}$
- The total dimensionless salt flux (Q_s): which represents the advective, diffusive and dispersive salt flux that enters the domain from the seaside boundary normalized by the freshwater inland flux.
- The depth of the zone of groundwater discharge to the sea (d_{disch}): which is equal to the distance of the aquifer top surface to the point separating the discharge zone and seawater inland flow zone at the sea boundary.

2.4. New technique for solving the equations in the spectral space

Solving the coupled system of flow and salt transport of the HP in the spectral space (Eqs. (2.14) and (2.16)) is not an easy task, particularly for the cases involving large numbers of Fourier modes. *Henry (1964)*, *Ségol (1994)* and *Simpson and Clement (2004)* employed the Picard method and solved the system by a sequential procedure between the flow and Eqs. (2.14) and (2.16). This approach is computationally efficient because it splits the system into two smaller systems. But it cannot converge for the high nonlinear cases. This is why first solutions were limited to high diffusion coefficient with relatively small number of Fourier modes. *Zidane et al. (2012)* solved the system simultaneously using the Newton method with a numerical approximation of the Jacobian matrix. This method provides better convergence properties but it is limited in computational efficiency as both flow and transport equations are solved simultaneously in one large system. *Younes and Fahs (2014)* tried to circumvent this drawback by using the Powell algorithm (a variation of Newton's method) with analytical Jacobian matrix. In the present work, we develop a new technique that preserves the same convergence property as the one developed by *Younes and Fahs (2014)* but without scarifying computational efficiency of the sequential resolution. We show that the flow (stream function) can be analytically calculated in terms of the salt concentration and the spectral transport equation can be solved via the Newton's method, with only the Fourier series coefficients of the salt concentration as primary unknowns.

The proof is firstly developed for homogenous aquifer. In this case, the second and third terms of Eq. (2.14) drops out. This allows calculating explicitly the Fourier series coefficients of the stream function in terms of the ones for salt concentration. This gives:

$$A_{i,j} = -\frac{1}{\pi\xi} \frac{NG_0}{\omega_j^1} \frac{\pi j \sum_{r=0}^{Nr} \tilde{B}_{r,j} \Gamma_{i,r} + 2\delta_{j,0} \Gamma_{i,0}}{r_k i^2 + j^2 / \xi^2} \quad (2.17)$$

Eq. (2.17) is then substituted into Equation (2.16). This eliminates the coefficient $A_{g,h}$:

$$\begin{aligned} R_{g,h}^T &= \omega_g^2 b_m \pi^2 B_{g,h} \left(\frac{h^2}{\xi^2} + g^2 \right) \xi \\ &+ \frac{NG_0}{4\xi} \sum_{m=1}^{Nm} \sum_{n=0}^{Nn} \sum_{r=0}^{Nr} \sum_{s=1}^{Ns} B_{r,s} \frac{1}{\omega_n^1} \frac{\pi n \sum_{r=0}^{Nr} \tilde{B}_{r,n} \Gamma_{m,r} + 2\delta_{n,0} \Gamma_{m,0}}{r_k m^2 + n^2 / \xi^2} (s.m.\eta_{g,m,r} \theta_{h,n,s} - r.n.\kappa_{g,m,r} \lambda_{h,n,s}) \\ &+ \frac{gNG_0}{\pi\xi} \sum_{n=0}^{Nn} \frac{1}{\omega_n^1} \frac{\pi n \sum_{r=0}^{Nr} \tilde{B}_{r,n} \Gamma_{g,r} + 2\delta_{n,0} \Gamma_{g,0}}{r_k g^2 + n^2 / \xi^2} \Lambda_{h,n} - \omega_g^2 \sum_{s=1}^{Ns} s B_{g,s} \Lambda_{h,s} - \frac{2}{\pi} \Lambda_{h,0} \delta_{g,0} \\ &- 4 \sum_{i=1}^{Np} W p_i F^{Disp} (X p_i, Z p_i) \cos(g\pi Z p_i) \sin\left(h\pi \frac{X p_i}{\xi}\right) = 0 \end{aligned} \quad (2.18)$$

In the case of heterogeneous domain, expression of $A_{i,j}$ in Eq. (2.17) can be obtained explicitly by considering the matrix form of Eq. (2.17):

$$[\mathbf{M}].\mathbf{A} = [\mathbf{N}].\mathbf{B} + \mathbf{V} \quad (2.19)$$

where \mathbf{M} is the matrix coefficients of $A_{g,h}$ (first two terms in Eq. (2.17)), \mathbf{N} is the matrix coefficients of $B_{g,h}$ (third term in Eq. (2.17)), \mathbf{A} and \mathbf{B} are two vectors representing respectively the Fourier series coefficients $A_{g,h}$ and $B_{g,h}$ and \mathbf{V} is a constant vector (last two terms in Eq. (2.17)).

Eq. (2.18) represents a closed system of $(Nr+1) \times Ns$ equations with the coefficients $B_{g,h}$ as unknowns. This system can be solved alone without any coupling with the flow equation. In this work, we solved it using the nonlinear solver of the IMSL library. Jacobian matrix is provided analytically and the term with 4 nested summations is simplified to 3 summations as in *Fahs et al. (2016)*. Similarly, the three resolving steps, i.e. residual vector, Jacobian matrix and linear system are implemented in parallel on shared memory architecture.

2.5. Results and discussions

2.5.1. Verification: Stability of the Fourier series solution and comparison against numerical solution

A FORTRAN code has been developed to solve the final system of nonlinear equations resulting from the Fourier series method. To examine the correctness of this code, we compared it against a full numerical solution obtained using an advanced in-house model (*Younes et al., 2009*). The numerical model is based on the combination of the method of lines for higher order time integration and advanced methods for spatial discretization. The mixed hybrid finite element method, which is appropriate for anisotropic and heterogeneous domains, is used to solve the flow equation. The transport equation is discretized based on the discontinuous Galerkin finite element method that can accurately handle sharp solution with relatively coarse meshes (*Younes et al., 2009*). The numerical simulations are performed with a fine mesh involving 10,000 triangular elements obtained by subdividing 2,500 squares in four equal triangles. This regular mesh is used to avoid numerical artifacts related to irregular meshes. All the simulations are developed under transient regime for a long duration to reach the steady-state solution.

Besides validation, this section aims also to investigate the effect of heterogeneity and anisotropy on the stability of the Fourier series solution. For this propose, four test cases based on the standard pure diffusive (*Henry, 1964*) and dispersive HP (*Abarca et al., 2007*) are generated. The results are compared in terms of isochlors' positions and SWI metrics (L_{toe} , W_{MZ} , Q_s and d_{disch}). For an adequate comparison, we assume same effective large-scale gravity number for all the cases. The large-scale gravity number is calculated based on the average hydraulic conductivity ($\overline{K_z}$):

$$\overline{NG} = \frac{\overline{K_z} d \Delta \rho}{\rho_0 q_d}, \quad (2.20)$$

The average hydraulic conductivity (in the vertical direction) for layered aquifers with depth-dependent hydraulic conductivity is given by *Zlotnik et al. (2011)* :

$$\overline{K_z} = \frac{1}{\int_0^1 \frac{dZ}{K_z(Z)}} = \frac{K_{z,0} \Upsilon}{1 - e^{-\Upsilon}}, \quad (2.21)$$

Thus, the large scale gravity number is calculated as follows:

$$\overline{NG} = \frac{\Upsilon}{1 - e^{-\Upsilon}} NG_0, \quad (2.22)$$

For all cases, the domain aspect ratio (ξ) is increased to be 4. This is to ensure perfect horizontal streamlines at the land boundary, essential to satisfy the freshwater recharge boundary conditions with the Fourier series solution (*Zidane et al., 2012*).

- *The pure diffusive Henry problem*

Two pure diffusive cases are considered using the same parameters as in standard Henry problem. The first case deals with homogenous domain ($\Upsilon = 0$) while in the second one, the aquifer is assumed to be stratified ($\Upsilon = 1.5$). Anisotropy is acknowledged with $r_k = 0.66$, as in *Abarca et al. (2007)*. The variations of K_x and K_z with depth are given in Fig. 2.2. The non-dimensional parameters used for these cases are given in Table 2.1. Corresponding physical parameters used in the numerical code are summarized in Table 2.2.

For the homogenous case, the SA solution for anisotropic domain is sought using 1,868 Fourier modes ($Nm = 8$, $Nn = 40$, $Nr = 10$ and $Ns = 140$), similar to the isotropic domain in *Fahs et al. (2016)*. This indicates that anisotropy does not affect the stability of the Fourier series solution. For the heterogeneous case, the same number of Fourier modes leads to unstable SA solution with some unphysical oscillations at the top of the aquifer (Fig. 2.3). In fact, in this upper zone, the local permeability is 5 times more important than the aquifer bottom. This high permeability leads to stronger buoyancy effects than in the homogenous case. The buoyancy forces act at smaller space scale than convection-dispersion processes and require, consequently, a higher number of Fourier modes to be accurately simulated (*Fahs et al., 2014*). Oscillation-free solution has been obtained with 2,968 coefficients ($Nm = 8$, $Nn = 40$, $Nr = 10$ and $Ns = 240$). Several runs confirm that heterogeneity affects only the truncation order of the concentration Fourier series in the x-direction. The SA and numerical isochlors are plotted in Fig. 2.4. The corresponding SWI metrics are given in Table 2.3. Results show an excellent agreement between the SA and numerical solutions. This gives more confidence in the correctness of both numerical and SA codes. The agreement between the numerical and SA values of Q_s is less than other metrics. This can be explained by the fact that Q_s involves the x-derivative of the concentration that is very sensitive to the Fourier modes (in the SA solution) and the mesh size (in the numerical solution).

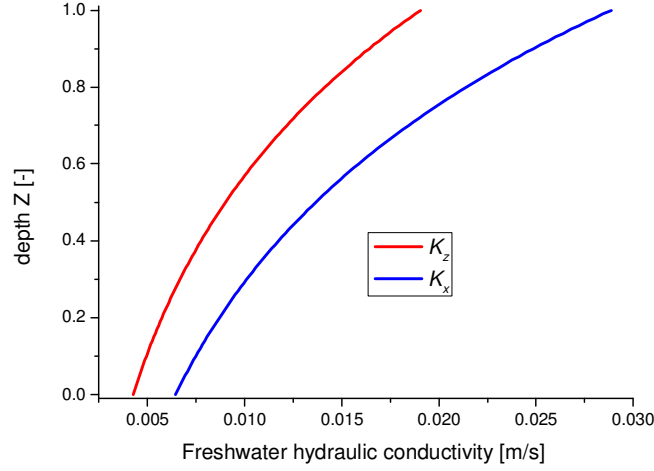


Fig. 2.2. Variation of the horizontal and vertical hydraulic conductivities with respect to depth for $\Upsilon = 1.5$ and $\overline{K_z} = 8.213 \times 10^{-3} \text{ m/s}$.

Table 2.1. Non-dimensional parameters used in the semianalytical solution for the verification test cases

| <i>Parameters</i> | <i>Value</i> | <i>Cases</i> |
|----------------------------------|--------------------|---------------------|
| \overline{NG} | 3.11 | All cases |
| b_m | 0.1 | Diffusive cases |
| | 5×10^{-4} | Dispersive cases |
| $b_L = \alpha_L / d$ | 0 | Diffusive cases |
| | 0.1 | Dispersive cases |
| $r_\alpha = \alpha_T / \alpha_L$ | 0 | Diffusive cases |
| | 0.1 | Dispersive cases |
| r_k | 0.66 | All cases |
| Υ | 0 | Homogenous cases |
| | 1.5 | Heterogeneous cases |

Table 2.2. Physical parameters used in the numerical model for the verification test cases.

| <i>Parameters</i> | <i>Value</i> | <i>Cases</i> |
|-----------------------------------|-----------------------|---------------------|
| $\Delta\rho$ [kg/m ³] | 25 | All cases |
| ρ_0 [kg/m ³] | 1000 | All cases |
| q_d [m ² /s] | 6.6×10^{-5} | All cases |
| d [m] | 1 | All cases |
| ℓ [m] | 4 | All cases |
| $\overline{K_z}$ [m/s] | 8.213×10^{-3} | All cases |
| r_k [-] | 0.66 | All cases |
| ε [-] | 0.35 | All cases |
| D_m [m ² /s] | 53.88×10^{-6} | Diffusive cases |
| | 3.300×10^{-8} | Dispersive cases |
| α_L [m] | 0 | Diffusive cases |
| | 0.1 | Dispersive cases |
| α_T [m] | 0 | Diffusive cases |
| | 0.01 | Dispersive cases |
| Υ [-] | 0 | Homogenous cases |
| | 1.5 | Heterogeneous cases |

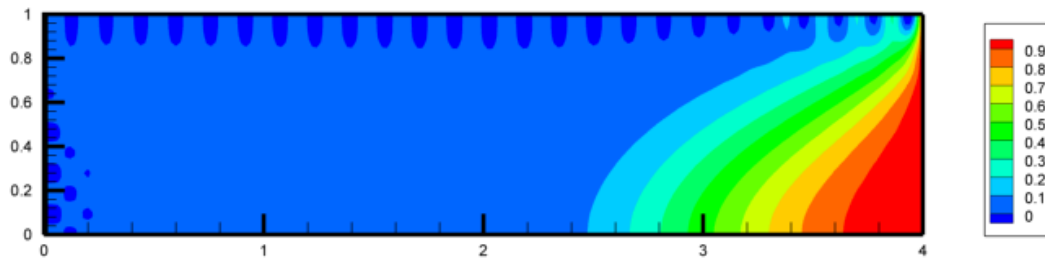


Fig. 2.3. Nonphysical oscillations related to the Gibbs phenomenon: the heterogeneous pure diffusive case evaluated with insufficient number of Fourier modes.

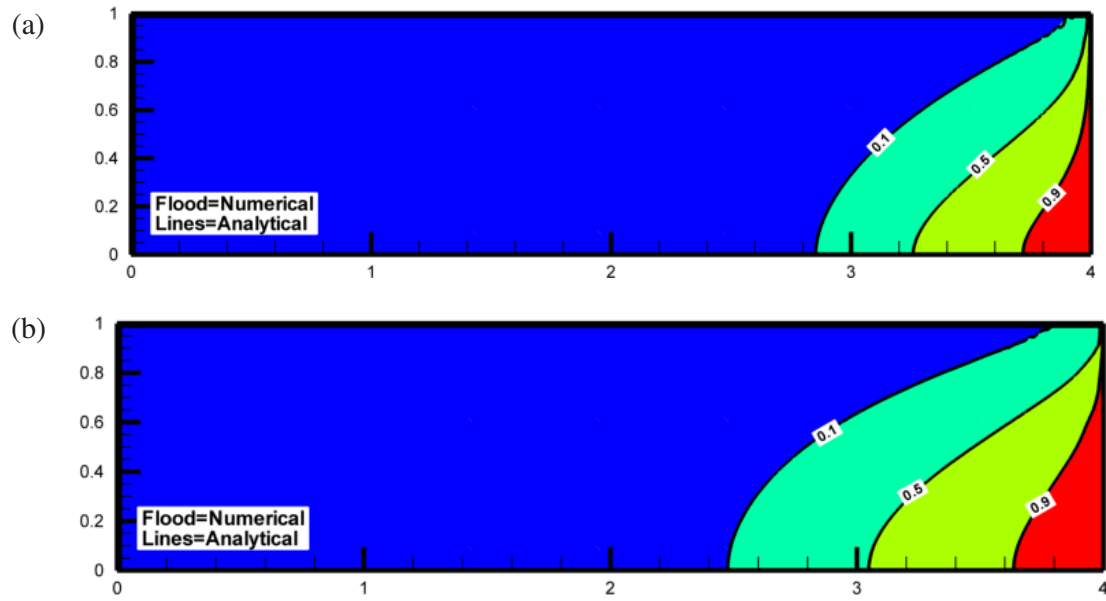


Fig. 2.4. Semianalytical and numerical isochlors (10%, 50% and 90%) for the pure diffusive cases: (a) homogenous and (b) heterogonous aquifer.

Table 2.3. Seawater intrusion metrics obtained with the semianalytical and numerical solutions

| Metrics | <i>Semi-Analytical solution</i> | | | | <i>Numerical solution</i> | | | |
|--------------------------|---------------------------------|----------|-------|-------------|---------------------------|----------|-------|-------------|
| | L_{toe} | W_{MZ} | Q_s | d_{disch} | L_{toe} | W_{MZ} | Q_s | d_{disch} |
| Diffusive homogenous | 0.74 | 0.78 | 1.06 | 0.57 | 0.74 | 0.79 | 1.09 | 0.56 |
| Diffusive heterogeneous | 0.95 | 0.83 | 1.09 | 0.35 | 0.95 | 0.84 | 1.01 | 0.36 |
| Dispersive homogenous | 1.54 | 0.29 | 1.07 | 0.46 | 1.53 | 0.29 | 1.09 | 0.47 |
| Dispersive heterogeneous | 2.30 | 0.59 | 1.09 | 0.31 | 2.29 | 0.59 | 1.12 | 0.31 |

- *The dispersive Henry problem*

For the dispersive HP, all parameters are set as in *Abarca et al. (2007)* except the molecular diffusion coefficient (b_m) which is, for convenience, assumed to be very small (5×10^{-4}) (*Fahs et al., 2016*). The anisotropy ratio (r_k) and the rate of stratification (Υ) are kept the same as for the pure diffusive cases. Non-dimensional and corresponding physical parameters are given in Tables 1 and 2. For homogenous and heterogeneous cases, oscillation-free solutions have been obtained using 4,725 ($Nm = 15$, $Nn = 90$, $Nr = 20$ and $Ns = 160$) and 6,405 ($Nm = 15$, $Nn = 90$, $Nr = 20$ and $Ns = 240$) Fourier modes, respectively. This confirms that only the concentration Fourier modes in the x-direction are mainly affected by heterogeneity. The SA and numerical isochlors are depicted in Fig. 2.5. SWI metrics are given in Table 3. As for the homogenous case, Fig. 2.5 and Table 2.3 highlight the excellent agreement between the analytical and numerical solutions. The same remark, as in the homogenous case, can be made regarding the agreement between SA and numerical values of Q_s . Table 2.3 provides quantitative indicators that can be useful for benchmarking DDF codes in realistic configuration of anisotropy and heterogeneity. First observation from the comparison between the Figs. 2.4 and 2.5 indicates that the effect of heterogeneity on SWI is more important in the dispersive case. Fig. 2.5 shows that the solution of the dispersive HP is sharper and more realistic than for the diffusive case. This sharpness explains why the dispersive test case requires more Fourier modes than the diffusive one.

It should be noted that, with the new technique developed here for solving the HP in the spectral space, the solution can be obtained with a reduced number of unknowns. For instance, in the pure diffusive homogenous case, the final system to be solved involves about 1,400 coefficients instead of 1,868. For more complex cases, such the heterogeneous dispersive case, the final system is solved with 4,800 unknowns instead of 6,405.

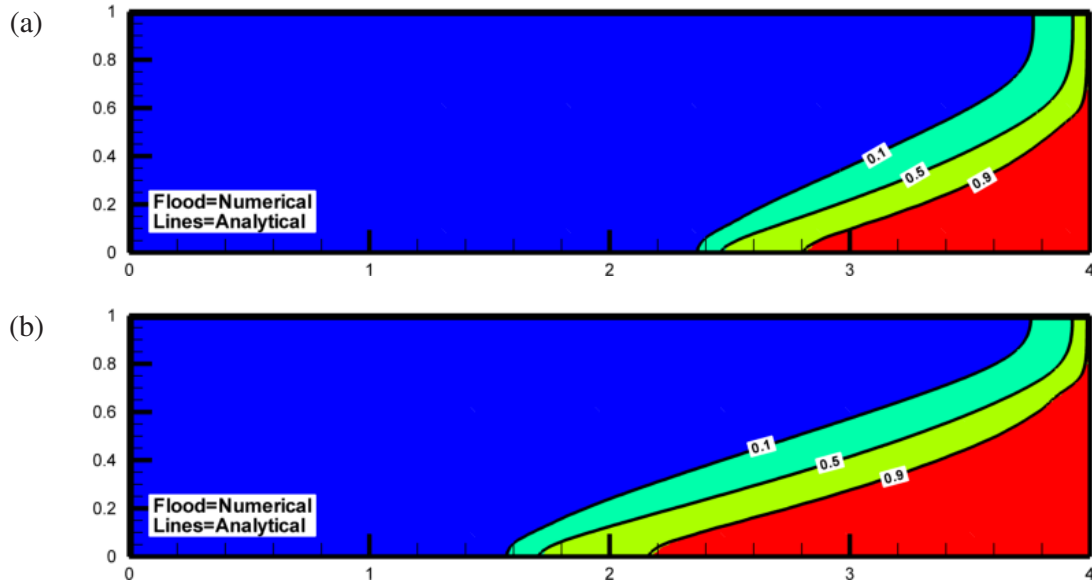


Fig. 2.5. Semianalytical and numerical isochlors (10%, 50%, 90%) for the dispersive cases: (a) homogenous and (b) heterogonous aquifer.

2.5.2. Effect of anisotropy on seawater intrusion in homogenous aquifer

Effect of anisotropy on SWI has been often investigated using the sharp interface model (Mehdizadeh *et al.*, 2014) which assumes that freshwater and saltwater are immiscible (Felisa *et al.*, 2013; Marion *et al.*, 2014; Masciopinto *et al.*, 2017; Najib and Rosier, 2011). Abarca *et al.* (2007) were the first to investigate the influence of anisotropy on the saltwater wedge using the DDF model. They demonstrated that a decrease of the anisotropy ratio ($r_K = K_z/K_x$, vertical to horizontal permeability) pushes the saltwater wedge landward. Michael *et al.* (2013) studied numerically (based on the DDF model) the effect of anisotropy on the position of the salinity transition zone. They showed that for the lower value of the vertical hydraulic conductivity relative to a constant horizontal conductivity (i.e. lower value of $r_K = K_z/K_x$), the salinity transition zone moves seaward and can occur farther offshore. Qu *et al.* (2014) investigated the effect of anisotropy on salinity distribution in an unconfined aquifer. Their results show that the toe recedes when the ratio of horizontal to vertical hydraulic conductivity increases (i.e. $r_K = K_z/K_x$ decreases). The results obtained by Qu *et al.* (2014) and Michael *et al.* (2013) are coherent but they are in contradiction with Abarca *et al.* (2007). This contradiction has been reported in Qu *et al.* (2014). The authors tried to explain it by simulating

their SWI problem with vertical sea–land boundaries (similar to *Abarca et al. (2007)*) and showed that freshwater–seawater interface also moves seaward as r_K decreases. In this section, we aim to take advantage of the developed SA solution to provide a better understanding on the effect of anisotropy on SWI. Our goal is i) to explain the contradictory results in the previously mentioned studies and ii) to investigate the effect of anisotropy, not only on isochlors' position but also on several relevant metrics characterizing the SWI.

Thus, we consider again the dispersive homogenous configuration described above in Table 2.2. We derive the SA solution for different cases dealing with increasing anisotropy ratio from 0.1 to 1. Specific Fourier modes are used to obtain a stable solution for each case. Fig. 2.6 represents the salinity distribution for three selected values of r_K (0.2, 0.5 and 0.8). This figure shows that the saltwater wedge moves landward with the decrease of r_K . It confirms analytically the results of *Abarca et al. (2007)*. The contradiction with the results of *Michael et al. (2013)* and *Qu et al. (2014)* can be explained based on the non-dimensional analysis presented in section 2.2. In fact, Michael et al. (2013) and *Qu et al. (2014)* changed the anisotropy ratio by changing the vertical hydraulic conductivity (K_z) while keeping the horizontal conductivity (K_x) constant. This means that the isochlors' positions are investigated at different gravity numbers as this later is based on the vertical hydraulic conductivity ($NG = K_z d \Delta \rho / \rho_0 q_d$). In this work as well as in *Abarca et al. (2007)*, K_z is kept constant and r_K is varied based on K_x . This means that isochlors' positions are compared at constant NG . In Michael et al. (2013) and *Qu et al. (2014)* the decrease of K_z will decrease both r_K and NG . The latter can be alternatively seen as an increase of q_d and expresses the intensification of the advection effects related to the inland freshwater recharge against the buoyancy effects (responsible for SWI). This explains why the seawater–freshwater interface is pushed back seaward when r_K is decreased in Michael et al. (2013) and *Qu et al. (2014)*. In *Abarca et al. (2007)* as well as in this work, increasing K_x is equivalent to decreasing r_K at constant gravity number. At a fixed balance between the advection and buoyancy effects, the increase of horizontal permeability (K_x) intensifies the horizontal flow of seawater. Consequently the saltwater wedge moves landward. To verify this conclusion, we re-evaluated the SA solution of the homogenous dispersive case by decreasing vertical hydraulic conductivity. The results

are illustrated in Fig. 2.7 which confirms that when the decrease of r_K is obtained by decreasing the vertical hydraulic conductivity, the saltwater wedge moves seaward.

Fig. 2.8 presents the variations of L_{toe} , W_{MZ} , Q_s and d_{disch} with respect to r_K . Results for the homogenous case are plotted in black solid lines. Fig. 2.8a shows that L_{toe} decreases with the increase of r_K , which is coherent with the results in Fig. 2.6. Fig. 2.8b indicates that the average width of the mixing zone decreases also with r_K . This means that anisotropy reduces the mixing between freshwater and intruded saltwater.

Fig. 2.8c shows that the saltwater flux to the aquifer is also controlled by the anisotropy. It decreases with the increase of r_K . *Qu et al. (2014)* studied the influence of anisotropy on the submarine groundwater discharge flow. They demonstrated that the freshwater discharge is independent of anisotropy, while seawater recirculation rate decreases as K_x/K_z increases. This is in contradiction with our results which is understandable as in *Qu et al. (2014)* r_K is changed based on K_z which means that the gravity number is not constant. To explain the variation of Q_s against r_K , let us interpret the increase of r_K at constant gravity number as a decrease of the horizontal hydraulic conductivity (K_x). The horizontal flow near the sea-aquifer interface, which mainly depends on K_x , is attenuated and consequently reduces the advective saltwater flux. A closer look at the saltwater flux confirms that the advective saltwater flux is mostly influence by r_K . It decreases when r_K is increased. From Fig. 2.8d we can observe that the depth of the zone of groundwater discharge to the sea increases with r_K . This is also related to the drop of horizontal velocity near the sea boundary which pushes the inflection point of the velocity downward.

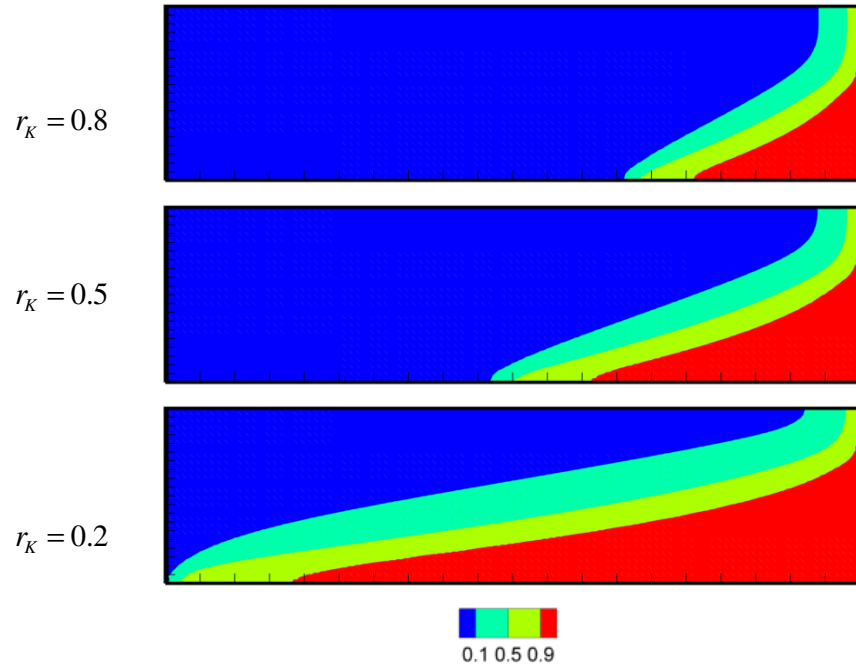


Fig. 2.6. Effect of anisotropy on the isochlors' positions (90%, 50%, 10%): Results obtained for the dispersive homogenous case (see Table 2.1 for all parameters except r_K which is given in the figure).

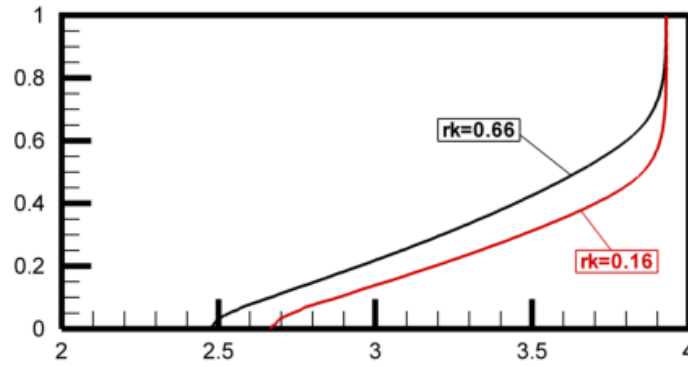


Fig. 2.7. Effect of anisotropy ratio on the 50% isochlor's position when r_K is changed based on the vertical hydraulic conductivity. The case $r_K = 0.66$ corresponds to the homogenous dispersive case (Table 2.2). The case $r_K = 0.16$ is obtained with reduced K_z (divided by 4.125).

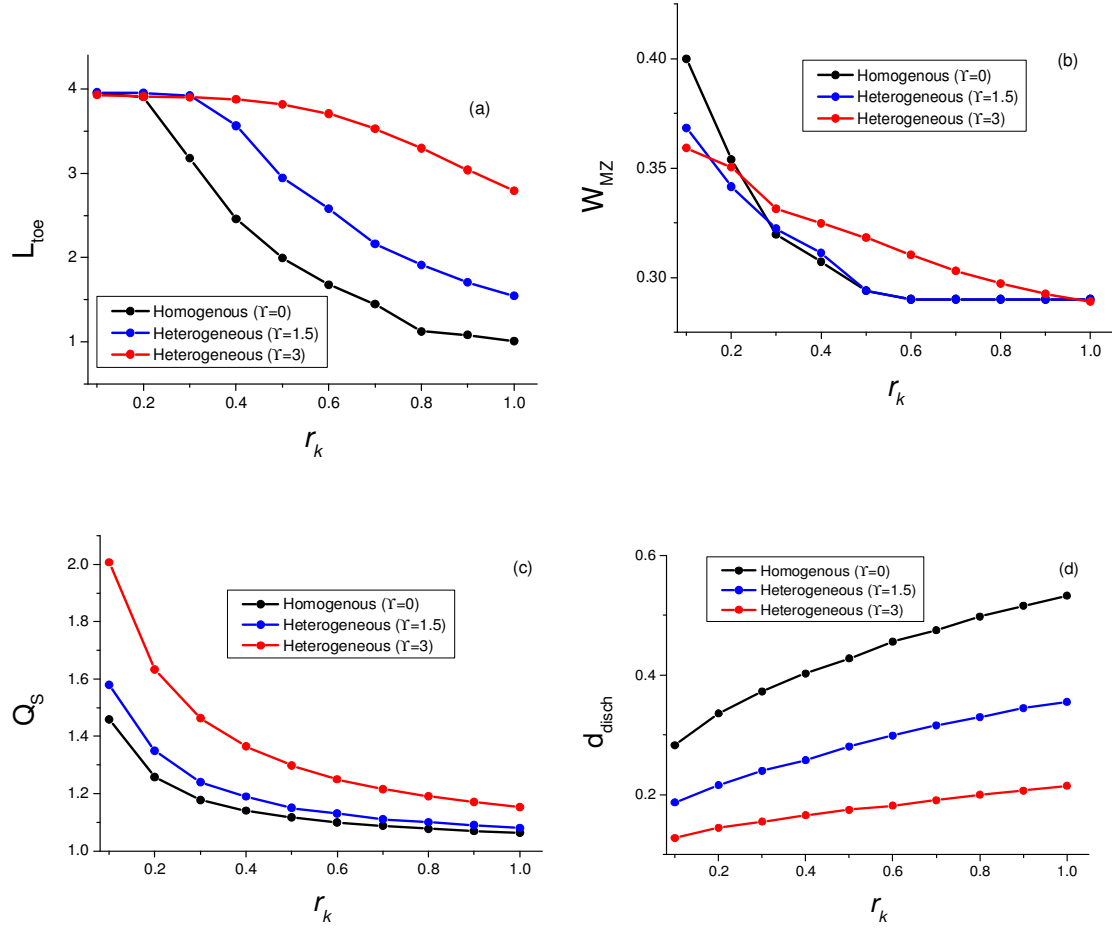


Fig. 2.8. Variation of the SWI metrics (L_{toe} , W_{MZ} , Q_s and d_{disch}) versus r_k . Results obtained for the dispersive case (see Table 2.1 for all parameters except r_k and Υ which are given in the figure).

2.5.3. Coupled effect of anisotropy and stratified heterogeneity on seawater intrusion

Significant research has been devoted to the evaluation of the influence of heterogeneity on SWI (Chang and Yeh, 2010; Held et al., 2005; Kerrou and Renard, 2010; Pool et al., 2015). Particular attention has been paid to the stratified heterogeneity using the sharp interface model (Dagan and Zeitoun, 1998; Essaid, 1990; Mehdizadeh et al., 2014; Pistiner and Shapiro, 1993). Influence of stratification on SWI has been also investigated experimentally and numerically (using the DDF model) (BniLam and Al-Khoury, 2017; Liu et al., 2014; Mehdizadeh et al., 2014). All these studies focused on the effect of stratified heterogeneity on the isochlors' positions. Very limited works investigated the influence of stratification on the

thickness of mixing zone and saltwater flux to the aquifer (*Lu et al., 2013*). On the other hand, combined effects of anisotropy and heterogeneity on solute transport mechanisms have been demonstrated in *Qin et al. (2013)* and *Woumeni and Vauclin (2006)*. Few studies considered this combined effect on SWI (*Pool et al., 2015*). To the best of our knowledge, combined effect of stratification and anisotropy on SWI has been never discussed in previous studies. Here, we used the SA solution to address these gaps. To do so, we evaluated the SA solutions for two cases dealing with increased rate of heterogeneity ($\Upsilon = 1.5$ and 3) and constant large-scale gravity number ($\overline{NG} = 3.11$). We should mention that exponent Υ is assumed to be positive. This corresponds to decreasing hydraulic conductivity with depth which is naturally prevalent in coastal aquifers.

For each case of heterogeneity, the SA is evaluated for increasing anisotropy ratio from 0.1 to 1. The main isochlors (10%, 50 and 90%) for three selected values of r_k (0.2, 0.5 and 0.8) in the case of homogenous and heterogeneous (both $\Upsilon = 1.5$ and 3) aquifers are depicted in Fig. 2.9. This figure shows that anisotropy and rate of stratification (Υ) have complementary effects on the position of the isochlors. As for the homogenous case, increasing anisotropy pushes the saltwater wedge landward. At constant large-scale gravity number, the increase of the heterogeneity rate leads also to a landward migration of the transition zone. This is not in agreement with the results by *Lu et al. (2013)* (see Fig. 8 in their paper). This disagreement is related to the gravity number. The results presented by *Lu et al. (2013)* are obtained with two different large scale gravity numbers. In *Lu et al. (2013)*, the average vertical hydraulic conductivity is 10^{-4} and 2.7×10^{-5} m/s for the homogenous and increasing stratified permeability, respectively. This means that the average gravity number in the homogenous case is greater than the stratified case. This will lead to more intruded saltwater wedge in the homogenous case, as higher gravity number corresponds to stronger buoyancy effect against freshwater recharge. To confirm this conclusion, we have compared the homogenous case of the dispersive HP (Fig. 2.5a) to a heterogeneous case dealing with smaller average gravity number. This latter is obtained by using the same parameters of the heterogeneous dispersive case (as in Table 2.1) except the large scale gravity number which is fixed at 0.84 (to get the same ratio as in *Lu et al. (2013)*). Fig. 2.10 illustrates the 50% isochlor for the homogenous case with $\overline{NG} = 3.11$, heterogeneous case ($\Upsilon = 1.5$) with the same gravity number $\overline{NG} = 3.11$ and heterogeneous case ($\Upsilon = 1.5$) with reduced gravity number ($\overline{NG} = 0.84$). This figure shows a significant recede of the saltwater wedge in the case of a heterogeneous aquifer with

a large scale gravity number less than the one in homogenous aquifer, which is in agreement with the results of *Lu et al. (2013)*.

Fig. 2.8a shows that L_{Toe} increase with Υ whatever the level of anisotropy. This agrees well with the results in Fig. 2.9. However, for highly anisotropic cases (smallest value of r_k), L_{Toe} becomes slightly sensitive to Υ . This is related to domain length as in this case, the saltwater wedge reaches the inland boundary. Fig. 2.8b shows that in general, heterogeneity intensifies the mixing between fresh and saltwater. Except for the highest anisotropic case, heterogeneity increases the average width of the mixing zone. However, it can be observed that for moderate hydraulic conductivity increasing ($\Upsilon = 1.5$), the influence of heterogeneity is negligible except in the high anisotropic cases. Fig. 2.8c shows that the heterogeneity intensifies the saltwater flux into the aquifer. The increase in saltwater flux becomes more pronounced in highly anisotropic domains. From Fig. 2.8d, it can be observed that the depth of the zone of groundwater discharge increases with heterogeneity, whatever the degree of anisotropy.

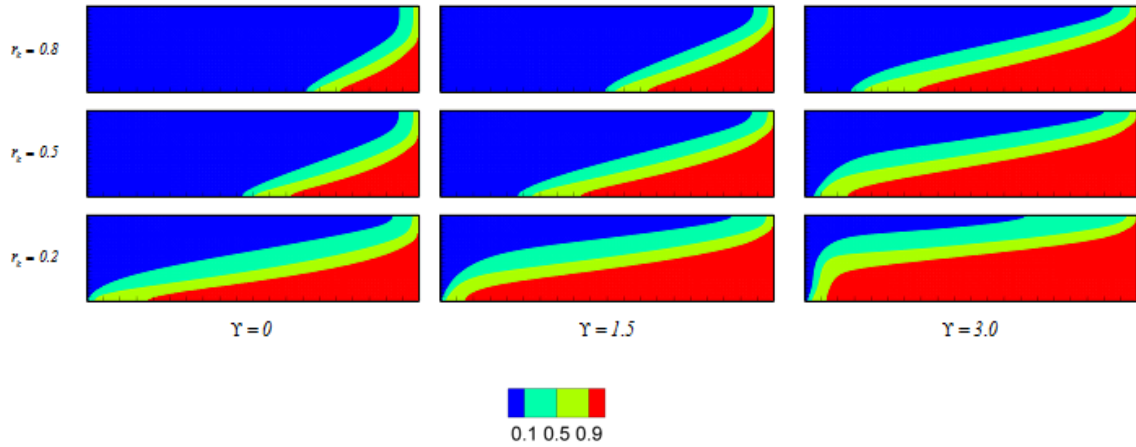


Fig. 2.9. Coupled influence of anisotropy and heterogeneity on the main isochlors (10%, 50%, 90%). Results obtained for a fixed large scale gravity number $\overline{NG} = 3.11$. All other parameters are similar to the dispersive case in Table 2.1.

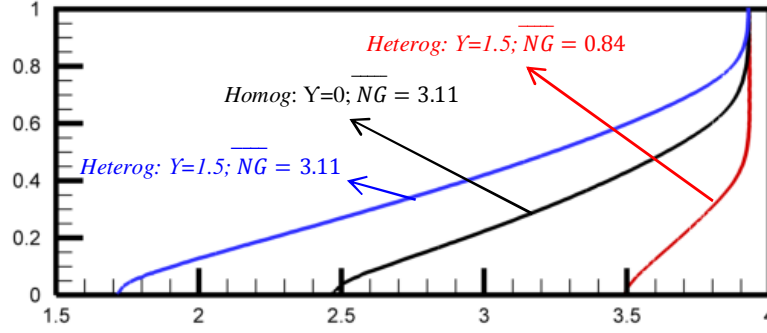


Fig. 2.10. Effect of the heterogeneity for varying average gravity number. The 50% isochlor in the case of homogenous aquifer with $\overline{NG} = 3.11$ (black line), heterogeneous aquifer with $\overline{NG} = 3.11$ (blue line) and heterogeneous aquifer with $\overline{NG} = 0.84$ (red line). Heterogeneous cases are obtained with $\Upsilon = 1.5$.

2.6. Conclusion

In this study, the SA solution of the dispersive Henry problem is generalized to anisotropic and heterogeneous porous media. Stratified heterogeneity described with the Gardner's model is considered to derive the SA solution. Our work leads to the following major contributions:

- i) We derived the first SA solution of the SWI with DDF model in an anisotropic and heterogeneous domain with velocity dependent dispersion. The SA solution is useful for testing and validating DDF numerical models in realistic configuration of anisotropy and stratification. In this context, we derived analytically (using the Fourier series) quantitative indicators (i.e. seawater intrusion metrics L_{toe} , W_{MZ} , d_{disch} and Q_s) that can be effectively used for code verification.
- ii) From numerical point of view; we presented an efficient technique for solving the HP in the spectral space. With this technique, we showed that the governing equations in the spectral space can be solved with only the concentration as primary unknowns. The spectral velocity field can be analytically expressed in terms of concentration. This technique improves the practicality of the Henry problem's SA solution and renders it more suitable for further studies requiring repetitive evaluations as in inverse modeling or sensitivity analysis.
- iii) We used the developed SA solution to investigate the effects of anisotropy and stratification on SWI. This is the first time that these effects have been investigated analytically with the DDF model. In previous works, analytical studies on this issue are limited to the sharp interface

model. While in the most existing studies, the effect of anisotropy and heterogeneity is mainly discussed on the position of the saltwater wedge, we provide here a deeper understanding of these effects on several metrics characterizing SWI.

iv) Taking advantage of the SA solution we explained contradictory results about the effect of anisotropy on the position of the saltwater wedge. We showed that at constant gravity number, the decrease of the anisotropic ratio leads to landward migration of the saltwater wedge. Contradiction in the previous studies is related to the way in which the anisotropy ratio is changed (whether based on horizontal or vertical hydraulic conductivity). The SA solution shows also that anisotropy leads to a wider mixing zone and intensifies the saltwater flux to the aquifer. It leads to a shallower zone of groundwater discharge zone to the sea.

v) We investigate analytically the combined effect of anisotropy and stratification on SWI. We showed that the width of the mixing zone is slightly sensitive to the rate of stratification. This sensitivity is more important in highly anisotropic aquifers. Complementary effects of anisotropy and heterogeneity are observed on the saltwater wedge and toe position as well as on the saltwater flux, while opposite effects are observed on the depth of the groundwater discharge zone.

The present study is limited to vertical seafloor. The comparisons against previous numerical studies dealing with inclined seafloor showed that the conclusions drawn here are not impacted by seafloor inclination. Future extensions of this work could include how the SA solution can be used to deal with inclined seafloor and variable saltwater concentration at the sea boundary.

The work has been published in the journal *Water* on February 2018 (*Fahs et al., 2018*).
<https://doi.org/10.3390/w10020230>

Chapter III: Semi-analytical solutions for contaminant transport under variable velocity field in a coastal aquifer

3.1. Introduction

Coastal zones are the most populated regions in the world. In Europe, for example, according to Eurostat, 40.8% of the population lives in coastal regions which cover 40% of the European Union territory (*Collet and Engelbert, 2013*). In many coastal ecosystems, groundwater is considered as the major source of freshwater. However, due to the higher population density and anthropogenic perturbations, coastal aquifers are vulnerable to serious contamination risks and groundwater is increasingly under threat from pollution. The protection of the groundwater reserves demands accurate predictions and assessments of the pollution impact on the aquifers. Therefore, the study of contaminant transport in coastal aquifers (CTCA) is essential for the management of freshwater resources and planning in coastal areas.

Contaminant transport processes in coastal aquifers are inherently complex. Groundwater flow in these aquifers is significantly influenced by various processes at the seaward boundary such as variable density flow, sea-level rise and tidal fluctuations (*e.g. Ataie-Ashtiani et al., 2013; Abd-Elhamid and Javadi, 2011; Bakhtyar et al. 2013; Anwar et al., 2014; Ketabchi et al., 2016, Lu et al., 2015*). Coastal aquifers are primarily characterized by variations of groundwater salinity in space and time as they are often subject to seawater intrusion (*Werner et al. 2013*). Due to variable density effects, this salinity may affect the flow patterns and consequently the mass transport processes (*Volker et al., 2002*). CTCA has been investigated using laboratory experiments (*Zhang et al., 2002; Chang and Clement, 2013; Liu et al., 2014; Oz et al., 2015*). Comprehensive numerical models have been developed to account for the aforementioned complexities (*e.g. Ataie-Ashtiani, 2007; Miller et al., 2013*). Despite the advances in numerical modeling, the development of analytical solutions is still necessary to verify the computer models and to perform scoping calculations (*e.g. Bolster et al., 2007; Chen et al., 2012; Hayek et al., 2012; Shahkarami et al., 2015; Parker and Kim, 2015*). Analytical solutions are ideally suited for the interpretation of the physical processes. They are suitable for conducting sensitivity and uncertainty analysis as well as for parameter estimation because they can be computed more efficiently than numerical solutions. However, due to the complexity of the

mathematical model, analytical solutions of contaminant transport can be only obtained under simplified configurations.

For CTCA, and in general for 2D contaminant transport in variable velocity fields, there is a scarcity of analytical solutions (*Bolster et al., 2007*). Some analytical solutions have been developed for non-uniform velocity by transforming the variable coefficients of the advection-dispersion equation to constant coefficients (*Tartakovsky and Federico, 1997; Tartakovsky, 2000; Craig and Heidlauf, 2009*). These solutions have been obtained for cases dealing with theoretical variable velocity fields. *Bolster et al. (2007)* developed analytical solutions for contaminant transport in coastal aquifer on the basis of a perturbation expansion in the parameters that describes the coupling between the flow and salt transport processes. The perturbation method may result in poor accuracy when the perturbation parameter is not sufficiently small (*Yeh et al., 2010*). Semi-analytical methods, by taking advantage of both analytical methods and numerical techniques, circumvent many limitations of the analytical methods and can be applied in more complex problems (*Suk, 2016; Ameli and Craig, 2014*). Recently *Suk (2017)*, based on the classical integral transformation technique, has developed a semi-analytical solution for solute transport in coastal aquifer under tidal fluctuation but the saltwater wedge and density difference were not considered.

The Fourier Galerkin (FG) method has been widely used to derive high accurate solutions for problems involving fluid flow, mass and/or heat transfer. This method combines the exactness of the analytical methods with an important extent of generality in describing the geometry and boundary conditions of the numerical methods (*BniLam and Al-Khoury, 2017*). In the frame of flow and transfer in porous media, FG method has been used for density driven flow (*Fahs et al., 2014; van Reeuwijk et al., 2009*), thermal natural convection (*Fahs et al., 2015; Nield and Kuznetsov 2012*), double diffusive convection (*Shao et al., 2016*) and heat flow in geothermal systems (*BniLam and Al-Khoury, 2017*). In the context of coastal aquifers, the FG method has been used to obtain the semi-analytical solutions of the popular Henry seawater intrusion problem (*Henry, 1964; Ségol, 1994; Simpson and Clement, 2004; Zidane et al., 2012*). Recently *Fahs et al. (2016)* and *Younes and Fahs (2014)* have developed efficient implementations of the FG method to solve the Henry problem with increasing levels of complexity and realism.

In view of the scarcity of the analytical solutions for CTCA, the objective of this work is to derive semi-analytical solutions for problems dealing with contaminant transport in coastal aquifer using the FG method, and to take advantage of these solutions to investigate the effect of seawater intrusion on contaminant transport. An adaptation of the FG method is introduced

to solve coupled flow, salt transport and contaminant transport equations. Efficient implementation is presented to deal with discontinuous contaminant boundary condition. To the best of our knowledge, such a kind of boundary condition has been never handled with the FG method. Necessary assumptions (i.e. vertical sea floor, constant salt concentration at the sea boundary and constant dispersion tensor) were made to obtain these semi-analytical solutions. Despite these simplifications, the results of this study highlight the worthiness of the developed semi-analytical solutions for validating and benchmarking numerical models and provide clear understanding on the processes of CTCA.

3.2. Problem description and methodology

The configuration under consideration is inspired from the Henry problem which has a long history in the investigation of seawater intrusion in coastal aquifers (*Henry, 1964*). The problem considers a rectangular aquifer of length (ℓ) and depth (d). It is subject to a constant flux of freshwater on its left vertical edge. The right vertical edge is assumed to be in contact with the sea. The top and bottom horizontal surfaces are impermeable (Fig. 3.1). This is an idealization of coastal aquifers that made the assumption of vertical sea floor and neglect the effect of freshwater discharge on the seawater salinity. These assumptions are necessary to obtain the semi-analytical solution. *Yang et al., 2013* have shown how the idealized vertical sea floor can be used to model real coastal aquifers. Despite these idealized assumptions, Henry problem continue to be used as surrogate for the understanding of seawater intrusion mechanisms (*Abarca et al., 2007; Lu et al., 2009; Kerrou and Renard 2010; Yang et al., 2013; Nick et al., 2013; Rajabi and Ataie-Ashtiani, 2014; Riva et al., 2014; Sebben et al., 2015; Fahs et al., 2016*).

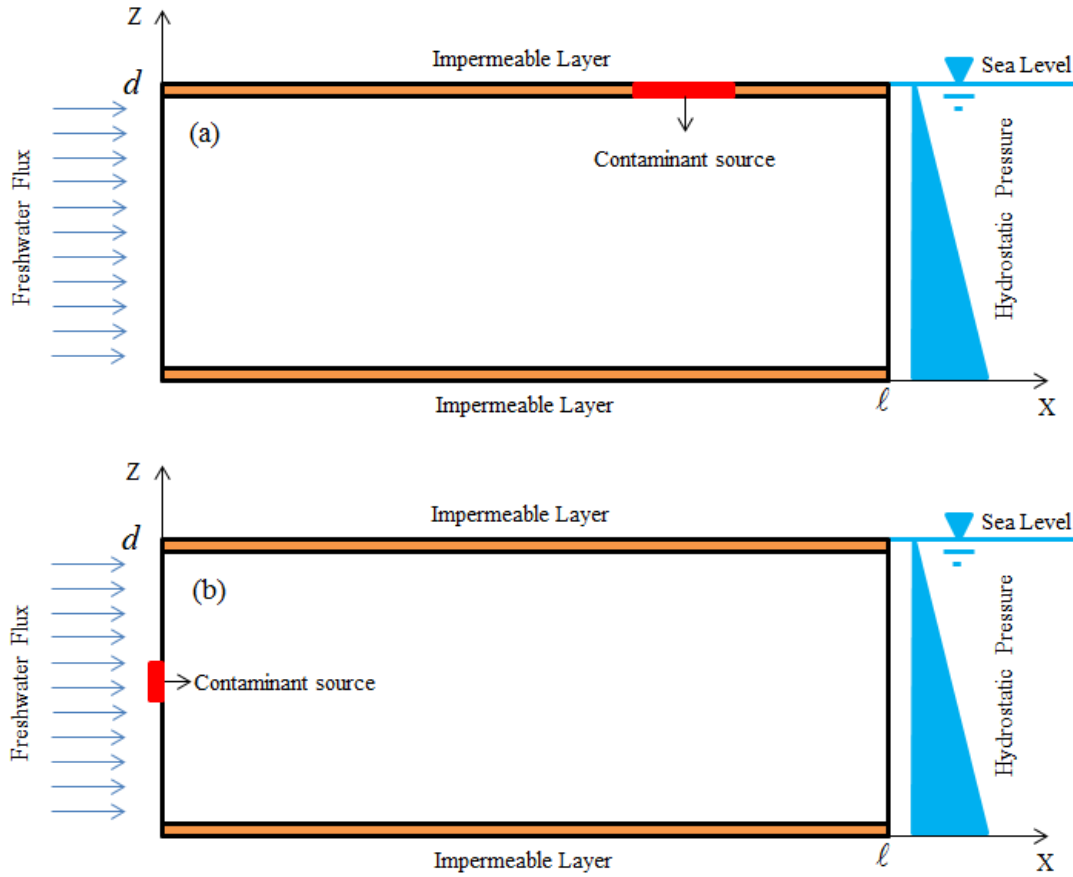


Fig. 3.1. Domain of the studied problem and contamination scenarios: contamination source at aquifer top surface (a) and landward boundary (b).

Two contamination scenarios are studied in this work. The first scenario is defined by considering a contaminant source at the aquifer top surface (Fig. 3.1a). This scenario corresponds to practical applications where the contaminant reaches the aquifer surface by diffusive leakage through the upper confined unit. Typical examples of this scenario could be the contaminants leaking through the confined unit from waste disposal and landfill sites, septic tanks, fuel storage tanks and pesticide spills (Woumeni and Vauclin, 2006; Kopp et al., 2010; Bakhtyar et al., 2013; Geng et al., 2016). An analytical solution pertaining to a similar scenario in an inland confined aquifer under uniform velocity field has been developed by Emami-Meybodi et al. (2015). In the second scenario, the contaminant source is located in the upstream of the freshwater flow (Fig. 3.1b). This source may represent leaching from relatively deep

waste disposal facility (*J.-S. Chen et al., 2016a*). This scenario is widely used for testing numerical algorithms of transport in inland aquifers (*Younes and Ackerer, 2008; Burdakov et al., 2012; Finkel et al., 2016*) and for understanding transport processes (*J.-S. Chen et al., 2016b; K. Chen et al., 2016*). Analytical solutions for this scenario in inland aquifer have been presented by *Leij and Dane (1990)* and *J.-S. Chen et al. (2016b)*.

The semi-analytical solutions of these contamination scenarios are derived using the FG method applied to the stream function form of the fluid flow salt transport and contaminant transport equations. Specific changes of variables are applied for each contamination scenarios in order to obtain periodic boundary conditions that are essential for the FG method. The stream function, saltwater concentration and contaminant concentration are expanded into infinite Fourier series that satisfy the boundary conditions. The final system of equations is obtained by an appropriate substitution of the Fourier series expansion and by using a Galerkin treatment with the Fourier modes as trial functions. The source discontinuity in boundary conditions can lead to inaccurate results as the Fourier series solutions may suffer from the Gibbs phenomenon if the solution is not smooth enough (*Ameli et al., 2013*). To avoid this problem and to have control over the sharpness of the transition, discontinuous boundary conditions are approximated by smoother functions. As a result of this approximation, the corresponding integrals cannot be evaluated analytically and we resort to an accurate numerical integration technique based on adaptive order processing. However, numerical integration can affect the efficiency of the semi-analytical method and render it impractical. This undermines the first advantage of the analytical (or semi-analytical) solutions regarding their practicality when compared to the numerical solutions. This issue is alleviated by evaluating the integrals preliminary for a wide range of Fourier modes before using them directly in the semi-analytical solution. Furthermore, the performance of the semi-analytical solution is improved taking advantage of parallel computing on shared memory architecture.

The stability of the FG solution is assessed in terms of the Fourier modes. The developed semi-analytical solutions are compared against the results of an advanced numerical model (*Younes and Ackerer, 2008; Younes et al., 2009*). The Fourier series are used to evaluate several metrics assessing the contaminant transport such as the discharge flux to the sea, the amount of contaminant persisting in the groundwater, the area of the contaminated zone and the solute flux as measured by the Sherwood number. These metrics represent quantitative data useful for code validation and benchmarking. They are also used to investigate the effect of seawater intrusion in contaminant plume migration.

3.3. Governing Equations

For both scenarios, the contaminant is considered as tracer. Such a configuration was investigated experimentally by *Chang and Clement (2013)* and analytically by *Bolster et al. (2007)*. This assumption is made in this work to decouple saltwater intrusion and contaminant transport systems which alleviates computationally the Fourier series solution procedure.

Water flow in the domain can be modeled using the continuity equation and Darcy's law. Under steady-state conditions, the governing equations can be written as follows (*Guevara Morel et al., 2015*):

$$\nabla \cdot \mathbf{q} = 0 \quad (3.1)$$

$$\mathbf{q} = -\frac{\rho_0 g}{\mu} k \left(\nabla h + \frac{\rho - \rho_0}{\rho_0} \nabla z \right) \quad (3.2)$$

where \mathbf{q} is the Darcy's velocity [LT^{-1}], h is the equivalent freshwater head [L], g is the gravitational acceleration [LT^{-2}], ρ is the density of the fluid [ML^{-3}], μ is the dynamic viscosity of the fluid [$ML^{-1}T^{-1}$], k is the permeability [L^2], ρ_0 is the freshwater density [ML^{-3}] and z is depth [L].

Steady state condition is assumed for both saltwater and passive contaminant mass transport. Such a condition is common for the investigation of seawater intrusion as salt transport in coastal aquifers is a long-term natural process. The leakage of contaminants is usually accidental and transient. Steady state condition can be reached if the contaminant source is permanent. Practical examples corresponding to this configuration could be the permanent landfills located near shorelines (*Cox et al., 1996; Njue et al., 2012*). In this work, contaminant transport steady state conditions are assumed because, at this stage of research, FG method cannot be applied for transient systems. Furthermore steady state solutions are relevant to understand the asymptotic behavior of transient problems. The steady state salt and contaminant transport equations write:

$$\mathbf{q} \cdot \nabla s - \nabla \cdot D^s \nabla s = 0 \quad (3.3)$$

$$\mathbf{q} \cdot \nabla c - \nabla \cdot D^c \nabla c = 0 \quad (3.4)$$

where c (resp. s) is the relative solute concentration of contaminant (resp. saltwater) $[-]$ which corresponds to the solute concentration normalized by the concentration of the source contamination (resp. seawater). D^c (resp. D^s) is the diffusion-dispersion coefficient for contaminant (resp. salt) [L^2T^{-1}].

The saltwater transport equation is coupled with the flow system via the linear mixture density equation as follows:

$$\rho = \rho_0 + (\rho_1 - \rho_0)s \quad (3.5)$$

where ρ_1 is the seawater density [ML^{-3}].

In this work a constant isotropic dispersion tensor is considered. For the sake of ultimate accuracy, this assumption is necessary to obtain the semi-analytical solution without numerical integration required to include velocity dependent dispersion terms. It is also necessary to render this solution affordable without excessive computational requirement (*Fahs et al., 2016*). The assumption of constant dispersion tensor was firstly suggested by *Henry (1964)* and widely considered in subsequent studies related to the Henry problem. *Kalejaiye and Cardoso (2005)* have shown that, in the case where gravity is the main driving force (natural convection); this assumption is a legitimate for flows where the Rayleigh number is less than 1000. *Bolster et al. (2007)* have generalized this assumption to contaminant transport in coastal aquifers. In such a case the Rayleigh number quantifies the relative importance of the buoyancy and dispersive forces within the saltwater wedge. As defined by *Kalejaiye and Cardoso (2005)* and *Bolster et al. (2007)*, the Rayleigh number is given by:

$$Ra = \frac{(\rho_1 - \rho_0).k.d.g}{\mu D^s} \quad (3.6)$$

where ε is the porosity of the porous medium.

The boundary conditions for flow and salt transport are similar to the standard Henry problem. The contaminant transport is subject to the boundary conditions as in Eqs (3.7) and (3.8) for the top surface and landward contamination scenarios, respectively.

$$\begin{aligned} \frac{\partial c}{\partial x} &= 0, \quad x = 0, \quad x = \ell \\ c &= 0, \quad z = 0 \end{aligned} \quad (3.7)$$

$$\begin{aligned} c &= f_{Top}(x), \quad z = d \\ \frac{\partial c}{\partial z} &= 0, \quad z = 0, \quad z = d \\ c &= f_{Land}(z), \quad x = 0 \\ c &= 0, \quad x = \ell \end{aligned} \quad (3.8)$$

where $f_{Top}(x)$ and $f_{Land}(z)$ are functions simulating the distribution of the contaminant source. They will be introduced and discussed further in the text.

3.4. The semi-analytical solution

3.4.1. Adaptation of the FG method

The stream function non-dimensional form of the flow and saltwater transport equations are used to obtain given as follows (*Fahs et al., 2016*):

$$\frac{1}{N_g} \left(\frac{\partial^2 \Psi}{\partial X^2} + \frac{\partial^2 \Psi}{\partial Z^2} \right) - \frac{\partial S}{\partial X} - \frac{1}{\xi} = 0 \quad (3.9)$$

$$\frac{1}{Pe^s} \left(\frac{\partial^2 S}{\partial X^2} + \frac{\partial^2 S}{\partial Z^2} \right) - \frac{\partial \Psi}{\partial Z} \frac{\partial S}{\partial X} + \frac{\partial \Psi}{\partial X} \frac{\partial S}{\partial Z} - \frac{1}{\xi} \frac{\partial \Psi}{\partial Z} - \frac{\partial S}{\partial X} - \frac{1}{\xi} = 0 \quad (3.10)$$

where $N_g = \frac{kg(\rho_1 - \rho_0)d}{\mu q_d}$ is the gravity number representing the ratio between the free

convection (or buoyancy) and advection effects (*Riva et al., 2015*), $Pe^s = \frac{q_d}{D^s}$ is the saltwater

Péclet number quantifying the relative importance of the advection and dispersion mechanisms

(*Bolster et al., 2007*), $q_d [L^2T^{-1}]$ is the recharge of freshwater from the landward boundary

into the domain, $\xi = \ell / d$ is the aspect ratio, $X = \frac{x}{d}$ and $Z = \frac{z}{d}$, $\Psi = \frac{\psi}{q_d} - Z$ and $S = s - \frac{X}{\xi}$

are the new non-dimensional forms of the stream function and salt concentration after the change of variables required to yield periodic boundary conditions.

Fourier series used to solve Eqs. (3.9) and (3.10) are given by:

$$\Psi = \sum_{m=1}^{Nm} \sum_{n=0}^{Nn} A_{m,n} \sin(m\pi Z) \cos\left(n\pi \frac{X}{\xi}\right) \quad (3.11)$$

$$S = \sum_{r=0}^{Nr} \sum_{s=1}^{Ns} B_{r,s} \cos(r\pi Z) \sin\left(s\pi \frac{X}{\xi}\right) \quad (3.12)$$

where Nn , Nm , Ns and Nr are the number of Fourier series modes (or the truncation orders) for the stream function and saltwater concentration in the x and z direction, pairwise and respectively. $A_{m,n}$ and $B_{r,s}$ are the Fourier series coefficients for the expansions of the mentioned variables.

Next, the Fourier series expansions are substituted into Eqs. (3.9) and (3.10) and the resulting equations are multiplied by trial functions (the Fourier modes) and integrated over the domain. This yields a final system of nonlinear equations with the Fourier coefficients as unknowns.

$$R_{g=1..Nm, h=0..Nn}^F = \frac{1}{N_g} \varpi_h \pi^2 \xi \left(\frac{h^2}{\xi^2} + g^2 \right) A_{g,h} - \sum_{r=0}^{Nr} h \Lambda_{g,r} \tilde{B}_{r,h} - \frac{2}{\pi} \Lambda_{g,0} \delta_{h,0} = 0 \quad (3.13)$$

$$R_{g=0..Nr, h=1..Ns}^{Ts} = \frac{1}{Pe^s} \varpi_g \pi^2 \xi \left(\frac{h^2}{\xi^2} + g^2 \right) B_{g,h} - g \sum_{n=0}^{Nn} \Lambda_{h,n} \tilde{A}_{g,n} - \varpi_g \sum_{s=1}^{Ns} s \Lambda_{h,s} B_{g,s} - \frac{\pi}{4} \sum_{m=1}^{Nm} \sum_{n=0}^{Nn} \sum_{r=0}^{Nr} \sum_{s=1}^{Ns} (s.m.\eta_{g,m,r} \theta_{h,n,s} - r.n.\kappa_{g,m,r} \lambda_{h,n,s}) B_{r,s} A_{m,n} - \frac{2}{\pi} \Lambda_{h,0} \delta_{g,0} = 0 \quad (3.14)$$

where R^F and R^{Ts} are the residual vectors for the flow and salt transport equations, respectively. The coefficients of this system are given in appendix B.

- Contaminant transport for scenario 1 (surface contamination):

The contaminant transport equation is reformulated by applying specific change of variables to get periodic boundary conditions and by deriving its non-dimensional form:

$$\frac{1}{Pe^c} \left(\frac{\partial^2 C}{\partial X^2} + \frac{\partial^2 C}{\partial Z^2} + Z.f_{Top}'' \right) - \left(\frac{\partial \Psi}{\partial Z} + 1 \right) \left(\frac{\partial C}{\partial X} + Z.f_{Top}' \right) + \frac{\partial \Psi}{\partial X} \left(\frac{\partial C}{\partial Z} + f_{Top} \right) = 0 \quad (3.15)$$

where $Pe^c = \frac{q_d}{D^c}$ is the Péclet number for contaminant transport, C is the new contaminant concentration after the change of variable, defined by:

$$C = c - Z.f_{Top}(X) \quad (3.16)$$

The Fourier series used in the formulation of the FG method to solve Eq. (3.15) is:

$$C = \sum_{k=1}^{Nk} \sum_{l=0}^{Nl} E_{k,l} \sin(k\pi Z) \cos\left(l\pi \frac{X}{\xi}\right) \quad (3.17)$$

where Nl and Nk are the number of Fourier series modes(truncation orders) in the x and z direction, respectively. $E_{k,l}$ represents the Fourier series coefficients.

The FG method can give high accurate solutions with relatively few Fourier modes as it converges exponentially to the exact solution. However, the number of Fourier modes should be considerably increased in order to prevent the occurrence of nonphysical oscillations in the case of sharp solutions. For the surface contamination scenario, there is a discontinuity in the boundary condition as the source of contamination is imposed at a given interval of the top surface. In order to control the sharpness of the transition, we approximated the source by a smoother function based on hyperbolic tangent as in *van Reeuwijk et al. (2009)*. The source function used in the semi-analytical solution is therefore:

$$f_{Top}(X) = 1 - \tanh\left(\left(\frac{X - X_c}{L_c}\right)^2\right) \quad (3.18)$$

Where X_c is the dimensionless abscissa of the contaminant source and L_c is the dimensionless source diameter, both of them normalized by the aquifer depth (d).

The justification behind defining this source function is that, depending on X_c and L_c , the values of the first derivative can be zero on left and right boundary ($f'_{Top}(0) = f'_{Top}(\xi) = 0$).

Thus, the boundary conditions on the top and bottom surfaces remain periodic. Similar to the flow and saltwater system, the Fourier expansions of the stream function (Ψ) and contaminant concentration (S) are substituted into Eq. (3.15). The arising equations are then multiplied by the trial function $\Theta = 4 \sin(g \pi Z) \cos\left(\frac{h \pi X}{\xi}\right)$ (for $g=1, \dots, Nk$ and $h=0, \dots, Nl$) and integrated over the 2D space domain. All the resulting integrals can be evaluated analytically except the integrals corresponding to the contamination source function ($f_{Top}(X)$) which are integrated numerically.

Hence the final system writes:

$$\begin{aligned} R_{g=1 \dots Nk, h=0 \dots Nl}^{Tc} &= \frac{1}{Pe^c} \varpi_h \pi^2 \xi \left(\frac{h^2}{\xi^2} + g^2 \right) E_{g,h} \\ &- \frac{\pi}{4} \sum_{m=1}^{Nm} \sum_{n=0}^{Nn} \sum_{k=1}^{Nk} \sum_{l=0}^{Nl} \left(k.n.\hat{\kappa}_{g,m,k} \hat{\lambda}_{h,n,l} - m.l.\hat{\eta}_{g,m,k} \hat{\theta}_{h,n,l} \right) E_{k,l} A_{m,n} + \sum_{l=0}^{Nl} l.E_{g,l} \Lambda_{l,h} \\ &+ \frac{2\pi}{\xi} \sum_{n=0}^{Nn} n \tilde{A}_{g,n} I_1^{BC} - \sum_{m=1}^{Nm} \sum_{n=0}^{Nn} m A_{m,n} \Upsilon_{g,m} I_2^{BC} + \frac{4}{\pi} \frac{(-1)^g}{g} I_3^{BC} = 0 \end{aligned} \quad (3.19)$$

where I_1^{BC} , I_2^{BC} , I_3^{BC} are the integrals on the x-direction. These integrals and the coefficients of Eq. (3.19) are given in the Appendix B.

- *Contaminant transport for scenario 2 (landward contamination):*

The governing non-dimensional differential equation for contaminant transport is given by:

$$\begin{aligned} &\frac{1}{Pe^c} \left[\frac{\partial^2 C}{\partial X^2} + \frac{\partial^2 C}{\partial Z^2} + f'_{Land} \left(1 - \frac{X}{\xi} \right) \right] - \left(\frac{\partial \Psi}{\partial Z} + 1 \right) \left(\frac{\partial C}{\partial X} - \frac{f_{Land}}{\xi} \right) \\ &+ \frac{\partial \Psi}{\partial X} \left(\frac{\partial C}{\partial Z} + f'_{Land} \left[1 - \frac{X}{\xi} \right] \right) = 0 \end{aligned} \quad (3.20)$$

The change of variable applied on C to insure periodic boundary conditions is:

$$C = c - f_{Land}(Z) \cdot \left[1 - \frac{X}{\xi} \right] \quad (3.21)$$

The Fourier series expansion used to satisfy the boundary conditions is given by:

$$C = \sum_{k=0}^{Nk} \sum_{l=1}^{Nl} E_{k,l} \cos(k\pi Z) \sin\left(\frac{l\pi X}{\xi}\right) \quad (3.22)$$

As for the first scenario, the contaminant source $g(Z)$ is approximated using a smooth function in order to control the discontinuity. The contaminant source function is defined as follows (van Reeuwijk et al., 2009):

$$f_{Land}(Z) = 1 - \tanh\left(\left(\frac{Z - Z_c}{L_c}\right)^2\right) \quad (3.23)$$

where L_c is the diameter and Z_c is the location of the source center.

This function can (depending on Z_c and L_c) satisfies the periodic boundary conditions given by $f'_{Land}(0) = f'_{Land}(1) = 0$.

Eq. (3.21) is treated as for the first scenario using the trial function $\Theta = 4 \cos(g\pi Z) \sin\left(\frac{h\pi X}{\xi}\right)$

(for $g=0, \dots, Nk$ and $h=1, \dots, Nl$). The final system of equations for scenario 2 is:

$$\begin{aligned} R_{g=0..Nk, h=1..Nl}^{Tc} &= \frac{1}{Pe^c} \omega_g \pi^2 \xi \left(\frac{h^2}{\xi^2} + g^2 \right) E_{g,h} - \omega_g \sum_{l=1}^{Nl} l \Lambda_{h,l} E_{g,l} \\ &- \frac{\pi}{4} \sum_{m=1}^{Nm} \sum_{n=0}^{Nn} \sum_{k=0}^{Nk} \sum_{l=1}^{Nl} \left(k.n.\bar{\kappa}_{g,m,k} \bar{\lambda}_{h,n,l} - m.l.\bar{\eta}_{g,m,k} \bar{\theta}_{h,n,l} \right) E_{g,h} A_{m,n} \\ &+ 2 \sum_{m=1}^{Nm} \sum_{n=0}^{Nn} \left(m J_1^{BC} \Lambda_{h,n} + n J_2^{BC} \Sigma_{n,h} \right) A_{m,n} + \frac{2}{\pi} J_3^{BC} \Lambda_{h,0} - \frac{4}{\pi} \frac{\xi}{h} b^c J_4^{BC} = 0 \end{aligned} \quad (3.24)$$

Integrals and coefficients of Eq. (3.24) are listed in the Appendix B.

3.4.2. Implementation

For the surface contamination scenario, the semi-analytical solution is obtained by solving system of Eqs. (3.13), (3.14) and (3.19). This system is solved sequentially. Thus, Eqs. (3.13) and (3.14) are firstly solved as nonlinear system to obtain the coefficients $A_{m,n}$ and $B_{r,s}$. This step is performed using the FORTRAN computer code developed by Fahs et al. (2016). Next, the coefficients $A_{m,n}$ are substituted in Eq. (3.19). This yields a linear system with the coefficients $E_{g,h}$ as unknowns. The same procedure is applied for the landward contamination scenario by replacing Eq. (3.19) by Eq. (3.24). Two computer codes are developed in

FORTTRAN language to obtain the Fourier series solution for both considered scenarios. In these codes we implemented the unifrontal/multifrontal parallel linear solver UMFPACK (Davis, 2004) which has shown several advantages in the numerical simulation of water resources problems (Miller *et al.*, 2013). Preliminary runs of these codes have shown that despite the advantage of the linear solver, the solution is CPU consuming and impractical. Close scrutiny reveals that the most time-consuming part of the resolving procedure is the numerical evaluation of the integrals I_1^{BC}, I_2^{BC} and I_3^{BC} (for the first scenario) and $J_1^{BC}, J_2^{BC}, J_3^{BC}$ and J_4^{BC} (for the second scenario). These integrals are independent of the parameters describing the flow and the transport processes. Hence, we evaluated them separately and used them directly in the codes. For the evaluation of the numerical integrals, we used a specific integration routine from the IMSL libraries (QDAWO) [<http://www.roguewave.com/products-services/imsl-numerical-libraries/fortran-libraries>]. This procedure allows for considerable reduction in the number of operations required for the numerical integration. For instance, if we consider a hypothetical case where $Nm = Nn = Nk = Nl = 100$ and use 1000 points for the numerical integration, the evaluation of the term involving I_2^{BC} in the final system requires $O(10^{12})$ operations. By applying the procedure described here, the number of operations can be reduced to be $O(10^9)$. In addition, the computational efficiency of the semi-analytical method is enhanced by an OPENMP parallel implementation for the evaluation of the matrix and the right hand side of the system. More details about the efficiency of our implementation are provided in the results section.

3.5. Evaluation of the contaminant transport characteristics

In our analysis we address several practical and logical concerns related to the migration of contaminants in the coastal aquifer as for example the mass rate of contaminant released in the domain, the location and the area of the contaminated zone and the contaminant discharge to the sea. Thus, we used the Fourier series to evaluate analytically i) the concentration contours, ii) the contaminant plume area (A_c), iii) the amount of contaminant remaining in the aquifer (M_c), iv) the average Sherwood number (\overline{Sh}) and v) the mass flux of contaminant discharge to the sea (F_c). A_c is defined by the area of the domain where the contaminant concentration is greater than 0.1. It is calculated by numerical integration. The mass of the contaminant that persists in the aquifer at the steady state regime is defined by $M_c = \int_0^1 \int_0^\xi c.dXdZ$.

It can be expressed in terms of the Fourier coefficients as follows:

$$M_c = \begin{cases} \frac{\xi}{\pi} \sum_{k=1}^{Nk} \frac{1-(-1)^k}{k} E_{k,0} + \frac{1}{2} \int_0^\xi f_{Top}(X) dX & \text{for scenario 1} \\ \frac{\xi}{\pi} \sum_{l=1}^{Nl} \frac{1-(-1)^l}{l} E_{0,l} + \frac{\xi}{2} \int_0^1 f_{Land}(Z) dZ & \text{for scenario 2} \end{cases} \quad (3.25)$$

The Sherwood number is analogous to the Nusselt number in heat transfer. It represents the ratio of the mass rate transferred due to forced convection to the one transferred by dispersion at the boundary (Xie *et al.*, 2012):

$$Sh = \frac{h_m}{D^c / d} \quad (3.26)$$

where h_m is the forced convection mass transfer coefficient.

For the first scenario, the mass transfer between the impermeable layer and the groundwater in the aquifer occurs by forced convection within the solute boundary layer along the aquifer top surface. In this case, the total mass flow rate can be calculated using the mass analogous Newton's cooling law. Conservation between the forced convection and dispersive fluxes at the top surface can be written as follows:

$$\left| \frac{D^c}{d} \frac{\partial c}{\partial Z} \right|_{Z=1} = \left| h_m (c_{surf} - c_0) \right| \quad (3.27)$$

where c_{surf} and c_0 are the contaminant concentration at the surface and within the entering freshwater.

In our case, we have $c_{surf} = f_{Top}(X)$ and $c_0 = 0$. Hence, using Eq. (3.27), the local Sherwood number can be expressed in terms of the concentration gradient at the aquifer top surface by:

$$Sh = \frac{h_m}{D^c / d} = \frac{1}{f_{Top}(X)} \left| \frac{\partial c}{\partial Z} \right|_{Z=1} \quad (3.28)$$

Sh can be calculated using the Fourier series expansion of the concentration as follows:

$$Sh = \frac{\pi}{f_{Top}(X)} \sum_{k=1}^{Nk} \sum_{l=0}^{Nl} k (-1)^k E_{k,l} \cos \left(l \pi \frac{X}{\xi} \right) + 1 \quad (3.29)$$

The average Sherwood number (\overline{Sh}) is given by:

$$\overline{Sh} = \frac{1}{L_c} \int_{x_c - L_c/2}^{x_c + L_c/2} Sh.dX \quad (3.30)$$

For the second scenario, the contaminant enters the aquifer by advection-dispersion. The mass conservation at the landward boundary doesn't allow expressing Sh in terms of the concentration. Thus, the Sherwood number is not evaluated.

For the surface contamination scenario, the contaminant discharge flux to the sea can be calculated as follows:

$$F_c = \int_{Z_l}^1 Q_x c|_{X=\xi} dZ = \frac{1}{\pi} \sum_{k=1}^{Nk} \sum_{l=0}^{Nl} (-1)^l \frac{\cos(k\pi Z_l) - (-1)^k}{k} E_{k,l} + \frac{1}{2} \sum_{m=1}^{Nm} \sum_{n=0}^{Nn} \sum_{k=1}^{Nk} \sum_{l=0}^{Nl} m(-1)^{n+l} A_{m,n} E_{k,l} \left[\frac{\cos(\pi(k+m)Z_l) - (-1)^{k+m}}{k+m} + \frac{\cos(\pi(k-m)Z_l) - (-1)^{k-m}}{k-m} \right] \quad (3.31)$$

where $Q_x = q_x d / q_d$ is the dimensionless horizontal velocity and Z_l is the coordinate of the point at the seaside boundary separating the freshwater discharge zone and the seawater inland flow zone. Z_l is evaluated analytically using the Fourier series.

In the landward contamination scenario, the contaminant discharge to the sea is given by:

$$F_c = \frac{1}{Pe^c} \int_0^1 \frac{\partial c}{\partial X} \Big|_{X=\xi} dZ = \frac{\pi}{Pe^c \xi} \sum_{l=1}^{Nl} l(-1)^l E_{0,l} - \frac{1}{Pe^c \xi} \int_0^1 f_{Land}(Z) dZ \quad (3.32)$$

The integrals in Eqs. (3.30) and (3.32) are evaluated numerically using the IMSL library.

3.6. Results: test examples, verification and comparison against numerical solution

In this section, three test examples dealing with different dispersion coefficients are examined for each scenario. We based the discussion on test cases with different dispersion coefficient because the sharpness of the solution (and in consequence the accuracy) is chiefly controlled by this parameter. In addition, these cases can be relevant to assess the effect of the Péclet number on the contaminant transport. The physical parameters used for the three test cases are $d = 1m$, $\ell = 2.5m$, $\rho_0 = 1000 \text{ kg.m}^{-3}$, $\rho_1 = 1025 \text{ kg.m}^{-3}$, $q_d = 6.6 \times 10^{-5} m^2 s^{-1}$, $k = 1.0204 \times 10^{-9} m^2$, $\mu = 10^{-3} \text{ kg.m}^{-1}.s^{-1}$, $\varepsilon = 0.35$ and $g = 9.81 m.s^{-2}$. These parameters are

identical to the ones used in the Henry problem except the domain length. As in *Zidane et al. (2012)*, ℓ is increased to be 2.5m (instead of 2m in the standard Henry problem). This is to reduce the inland boundary effects on the semi-analytical solution. We assume equal values for D^e and D^s (*Bolster et al. 2007*). Three values extracted from the literature are considered: $6.601 \times 10^{-6} m^2 s^{-1}$, $1.3202 \times 10^{-6} m^2 s^{-1}$ and $3.3005 \times 10^{-7} m^2 s^{-1}$ (*Henry 1964, Zidane et al., 2012; Younes and Fahs, 2014*), respectively. The corresponding Péclet numbers are 10, 50 and 200. For the surface contamination scenario, we assume $X_c = 1.5$ and $L_c = 0.4$. This is to satisfy the conditions on the function $f_{Top}(X)$ ($f'_{Top}(0) = 4 \times 10^{-11}$ and $f'_{Top}(\xi) = -10^{-4}$) and for the source to be as close as possible to the sea. For the landward contamination scenario, we assume $Z_c = 0.5$ and $L_c = 0.2$, as it is customary in the literature. In such a case the conditions on the function $f_{Land}(Z)$ are satisfied because $f'_{Land}(0) = -f'_{Land}(1) = 0.0003$. For all cases, the coupled flow and saltwater transport system is solved as in *Fahs et al. (2016)* with 19,120 Fourier coefficients ($Nm = 40, Nn = 90, Nr = 42$ and $Ns = 360$).

3.6.1. Stability of the semi-analytical solution and effect of Péclet number

As mention previously, the Fourier series solution may suffer from unphysical oscillations related to the Gibbs phenomenon (*Durran, 1999; Ameli et al., 2013; Fahs et al., 2014*). Large number of Fourier modes should be used to obtain stable concentration contours when the solution is relatively sharp. The evaluation of the Sherwood number (\overline{Sh}) for the first scenario and the discharge flux (F_c) for the second scenario involves the first order derivative of the contaminant concentration Fourier series expansion. Hence, accurate values of (\overline{Sh}) and (F_c) requires stable first order derivative of the Fourier series and by consequence more Fourier modes than that required to obtain stable concentration contours. In this study, the use of large number of Fourier modes is made possible thanks to the newly efficient FG implementation.

- *Results for the surface contamination scenario:*

For the first test case, we obtained stable concentrations contours with 210 Fourier coefficients ($Nk = 10; Nl = 20$). The stable value of the Sherwood number requires 1,550 Fourier coefficients ($Nk = 50; Nl = 30$). In the second and third test cases, the solution is sharper than the first one. Stable solutions are respectively obtained using 4,550 ($Nk = 50; Nl = 90$) and 7,770 ($Nk = 70; Nl = 110$) Fourier coefficients. The semi-analytical results (contaminant plume, velocity field and saltwater isochlors) are given in Fig. 3.2. This figure displays the different behavior observed for the plume migration, saltwater wedge intrusion and contaminant discharge to the sea, depending on the Péclet number ($Pe = Pe^c = Pe^s$). For the first test case (low Péclet number), Fig. 3.2a shows that the saltwater wedge is relatively close to the contaminant source. Due to the high dispersivity, the contaminant transport occurs within the saltwater wedge. The contaminant mainly reaches the sea through the saltwater wedge. Fig. 3.2b and 3.2c show that the increase of Pe (equivalent to the decrease of the dispersion coefficient at constant recharge flux) leads to greater penetration of the seawater tongue at the bottom of the aquifer and retreating of the intrusion at the top surface. The increase of Pe is equivalent to the increase of the Rayleigh number ($Ra = N_g \cdot Pe^s$). This can be interpreted as an intensification of the buoyancy effects against dispersion mechanisms and results in more accelerated downward vertical flow near the sea boundary. Fluid mass conservation and boundary conditions convert the acceleration of the vertical velocity into an acceleration of the horizontal flow near the bottom surface and causes greater penetration of the seawater tongue. At the top surface, the advection dominates the dispersion processes. The freshwater discharge washes out the saltwater and prohibits the saltwater penetration in this zone. Contrary to the first test case, for intermediate and high Péclet number regimes, the contaminant transport doesn't occur in the saltwater wedge. Indeed, when the plume approaches the saltwater interface it is uplifted by the flow and exits to the sea through the freshwater discharge zone near the top surface of the aquifer.

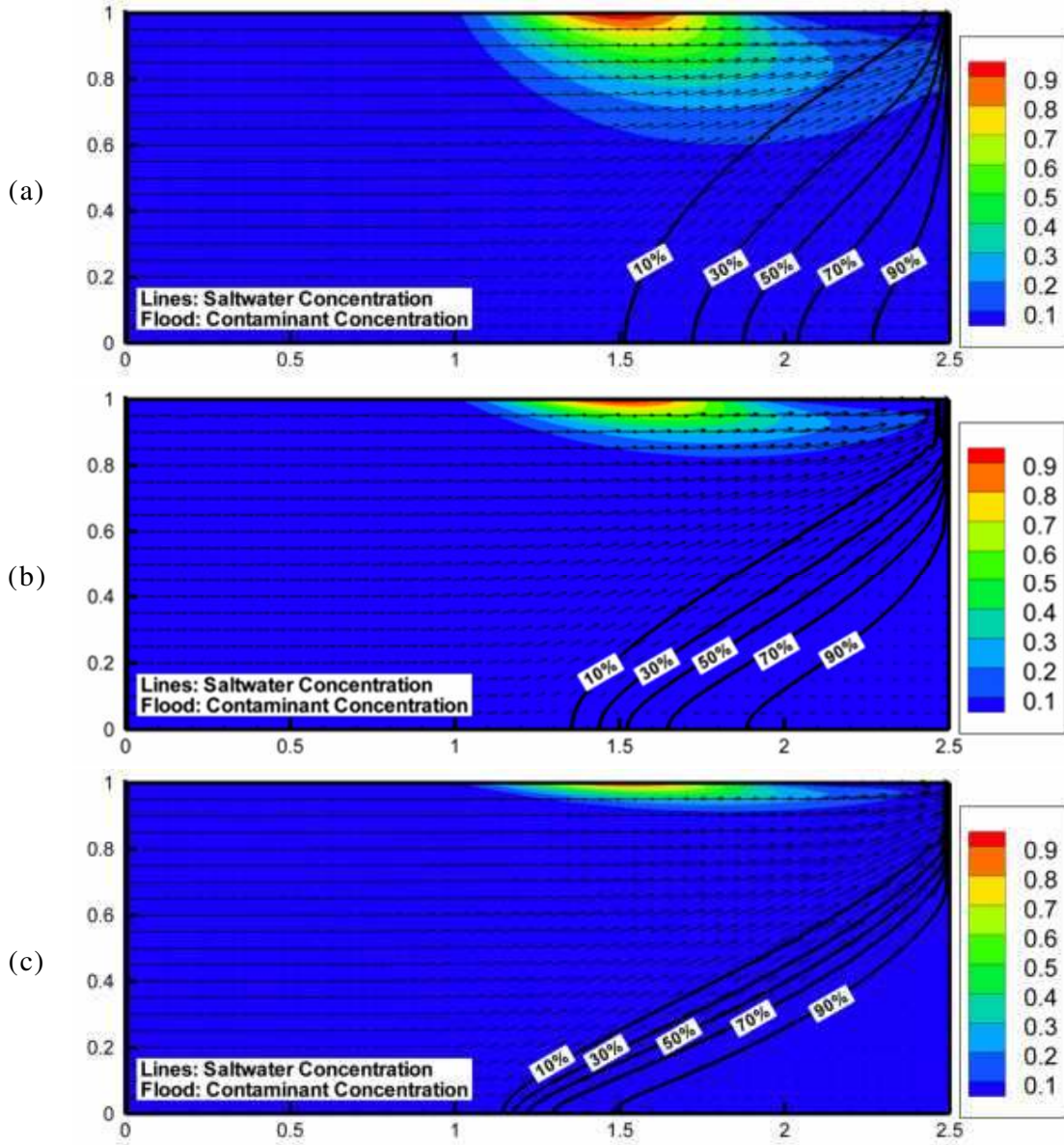


Fig. 3.2. Simultaneous depiction of contaminant plume, velocity field of and saltwater isochlors for surface contamination scenario: (a) test case1 (low Péclet number), (b) test case 2 (intermediate Péclet number) and (c) test case 3 (high Péclet number).

Fig. 3.2 shows also that the contaminated zone contracts and the plume migration becomes nearly horizontal above the saltwater wedge when Pe is increased. This is firstly related to the reduction in the dispersion processes. And secondly to the flow intensification in front the contaminant source. This latter can be explained as follows. The increase in Pe pushes the saltwater wedge towards the landward boundary. The saltwater wedge forms a barrier (near the bottom surface) narrowing the area through it the freshwater is discharged to the sea. This

causes the acceleration of the freshwater flow above the saltwater wedge. As a consequence, the solute boundary shrinks and the contaminated zone contracts.

Table 3.1 summarizes the ultimate values of the metrics characterizing the contaminant transport (A_c , M_c , F_c and \overline{Sh}) for the three test cases. As expected, this table shows a reduction of A_c with the increase of Pe , which is consistent with the results shown in Fig. 3.2. Table 3.1 also indicates that M_c is a declining function of Pe . This is due to the attenuation of the contaminant release (as will be explained at the end of this paragraph) and to the diminution of the time duration required to reach the steady state condition. This duration depends mainly on the advection processes. It diminishes with increasing Pe as this leads to the acceleration of the water flow in front of the contaminant source.

Table 3.1. Values of A_c , M_c , F_c and \overline{Sh} calculated analytically for both contamination scenarios

| Test Case | Nk | Nl | Number of Coefficients | Contaminated Zone Area (A_c) | Mass of contaminant (M_c) | Discharge Flux (F_c) | Sherwood Number (\overline{Sh}) |
|---------------------------------|------|------|------------------------|----------------------------------|-------------------------------|--------------------------|-------------------------------------|
| Surface contamination scenario | | | | | | | |
| 1 | 50 | 30 | 1,550 | 0.43 | 0.14 | 0.09 | 4.95 |
| 2 | 50 | 90 | 4,550 | 0.17 | 0.06 | 0.04 | 10.15 |
| 3 | 70 | 110 | 7,770 | 0.09 | 0.04 | 0.02 | 20.12 |
| Landward contamination scenario | | | | | | | |
| 1 | 30 | 90 | 2,790 | 2.22 | 0.65 | 0.30 | NC* |
| 2 | 40 | 150 | 6,150 | 1.79 | 0.62 | 0.30 | NC* |
| 3 | 50 | 300 | 15,300 | 1.20 | 0.59 | 0.30 | NC* |

*NC: Not calculated

Table 3.1 shows that \overline{Sh} increases with Pe . In fact, \overline{Sh} is proportional to the concentration gradient. With the increase of Pe , the solute boundary layer shrinks and the concentration gradient increases. In general, \overline{Sh} provides a measure of the forced convection mass transfer occurring at the surface. Its augmentation is often seen as an increase of the average forced convection mass transfer coefficient ($\overline{h_m} = D^c \overline{Sh}/d$) and indicates the amplification of the mass transfer from the contaminated surface to the aquifer. However, this assumption is not valid in our case because the dispersion coefficient is variable. To further elaborate the effect of Pe on the amount of contaminant entering the domain, we calculated the rate of mass transfer between the contaminated surface and the aquifer. The values for the three test cases are calculated to be 0.09, 0.04 and 0.02, respectively. They indicate that despite the concentration gradient increasing with increasing Pe (due to seawater intrusion), the mass rate of contaminant entering the domain decreases. Finally, Table 3.1 shows that F_c decreases with increasing Pe . This is related to the attenuation of contaminant release because in steady state the contaminant discharge flux to the sea is equal to the mass flux entering the domain.

- *Results for the landward contamination scenario:*

For the three test cases, stable solutions have been obtained with 2,790 ($Nk = 30; Nl = 90$), 6,150 ($Nk = 40; Nl = 150$) and 15,300 ($Nk = 50; Nl = 300$) Fourier coefficients, respectively. The semi-analytical results are plotted in Fig. 3.3. The first observation is that, second scenario leads to more widespread contamination in the aquifer than the first one. For the three regimes of Pe , the contaminant plume travels within the domain toward the freshwater discharge zone at the upper part of the seaside boundary. Fig. 3.3a shows that the contaminant transport in the saltwater wedge is compelling but it is limited to the zone of low isochlors. Unlike the first test case of the surface contamination scenario, the contaminant does not reach the sea through the saltwater wedge. It is transported by the upward velocity and discharged mainly near the top of the seaside boundary. For the intermediate value of Pe , the contaminant concentration contours closely follow the flow structure (Fig. 3.3b). The contaminant transport is still occurring in the saltwater wedge (in contrast to the first scenario) but its occurrence is relatively attenuated. For the highest value of Pe (test case 3), the contaminant travels from the source to the sea through the freshwater discharge zone. The contaminant transport doesn't occur in the saltwater wedge (Fig. 3.3c).

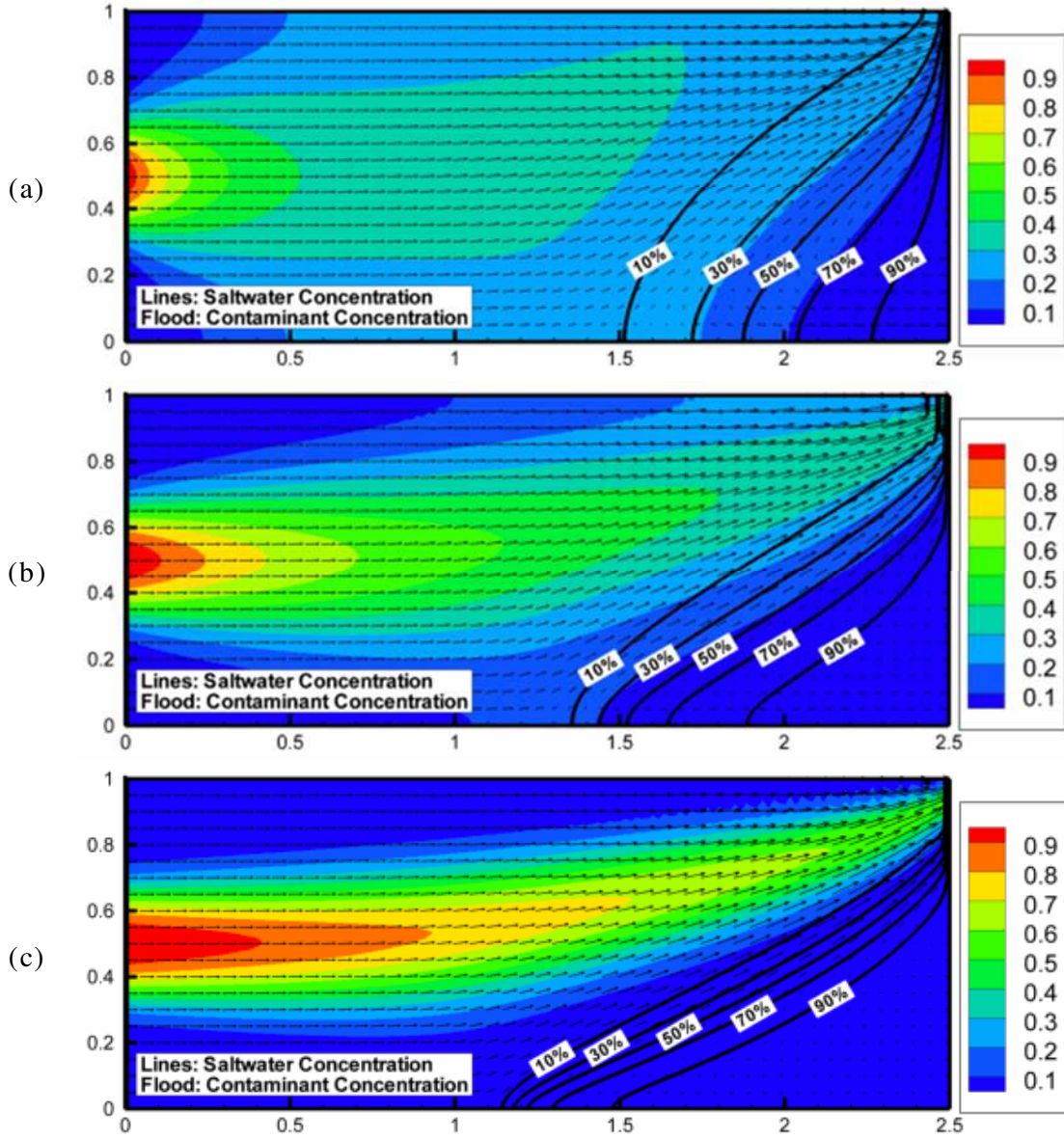


Fig. 3.3. Simultaneous depiction of contaminant plume, velocity field of and saltwater isochlors for landward contamination scenario: (a) test case1 (low Péclet number), (b) test case 2 (intermediate Péclet number) and (c) test Case 3 (high Péclet number).

The ultimate values of A_c , M_c and F_c are listed in Table 3.1. The first observation is that, the conclusions drawn for the first scenario concerning the variation of A_c , M_c are still applicable. F_c appears to be insensitive to Pe . Behavior of A_c is evident and only the variations of M_c and F_c will be discussed here. The behavior of F_c can be explained as follows. At steady state, the rate of contaminant discharge to the sea is equal to the rate of mass entering through the

landward boundary. This latter is mainly due to advection as the concentration gradient is negligible. Hence it is slightly sensitive to Pe at constant gravity number. The value of F_c is equal to the dimensionless mass rate of contaminant entering the domain $\left(= \int_0^1 f_{Land}(Z) dZ = 0.303 \right)$ which confirms the good mass balance of the semi-analytical method. Despite that the input and output fluxes are insensitive to Pe , M_c is slightly decreasing. The reason for this variation is related to the time duration required to reach the steady state condition which (as for the first scenario) decreases with increasing Pe .

3.6.2. Comparison against numerical solution: verification, efficiency of the FG implementation and benchmarking issues

As mentioned previously, two computer codes have been developed to obtain the semi-analytical solutions for both considered scenarios. To examine the correctness of these codes we compare their results with those obtained using an advanced in-house numerical model (Younes and Ackerer, 2008; Younes et al., 2009). This model is based on specific techniques for both space and time discretization. The efficiency and the accuracy of this model have been investigated for several applications related to density driven flow and transport in porous media (Konz et al., 2009, Fahs et al., 2014, 2015, 2016; Shao et al., 2016). To compare transient numerical solutions against steady state semi-analytical solutions, we performed transient simulations until a long duration to reach the steady state conditions. For ultimate accuracy, numerical simulations are performed using a fine mesh with 36,000 regular triangles. The results of the numerical model have been compared against the semi-analytical solutions for seawater intrusion in Younes and Fahs (2014) and Fahs et al. (2016). For the sake of brevity, we present here the comparison only for the contaminant transport. Fig. 3.4 illustrates the numerical and semi-analytical main concentration contours (10%, 30%, 50%, 70% and 90%) for both scenarios. Close agreement between the semi-analytical and numerical solutions can be seen. Table 3.2 lists the metrics characterizing the contaminant transport obtained using the numerical model. It confirms also the excellent agreement between the numerical and semi-analytical solutions. This comparison provides compelling evidence on the correctness of the codes developed for the semi-analytical solutions and provides also more confidence on the robustness of the numerical model.

Table 3.2. Values of Ac , M_c , F_c and \overline{Sh} calculated numerically for both contamination scenarios

| Test Case | Contaminated Zone Area (A_c) | Mass of contaminant (M_c) | Discharge Flux (F_c) | Sherwood Number (\overline{Sh}) |
|---------------------------------|----------------------------------|-------------------------------|--------------------------|-------------------------------------|
| Surface contamination scenario | | | | |
| 1 | 0.43 | 0.14 | 0.09 | 4.94 |
| 2 | 0.17 | 0.06 | 0.04 | 10.19 |
| 3 | 0.08 | 0.03 | 0.02 | 20.51 |
| Landward contamination scenario | | | | |
| 1 | 2.22 | 0.65 | 0.30 | NC* |
| 2 | 1.80 | 0.62 | 0.30 | NC* |
| 3 | 1.21 | 0.59 | 0.30 | NC* |

*NC: Not calculated

Further numerical simulations are performed to highlight the relevance of the semi-analytical solution in avoiding time and space discretization artefacts. These artefacts may affect seriously the accuracy of the predictive results, the parameter estimation procedure and the sensitivity analysis outcomes (*Nassar and Ginn, 2014; Esfandiar et al., 2015*). The results (not presented for sake of brevity) show that in the case of high Péclet number, the numerical solution is sensitive to the level of mesh refinement. Coarse mesh introduces important numerical dispersion that can lead to significant anomalies when comparing numerical and semi-analytical solutions. Numerical simulations show also that careful attention must be paid to the time step size in order to avoid possible unphysical oscillations. In some cases, the oscillations are related to seawater intrusion because they appear at the interface between the freshwater and saltwater wedge.

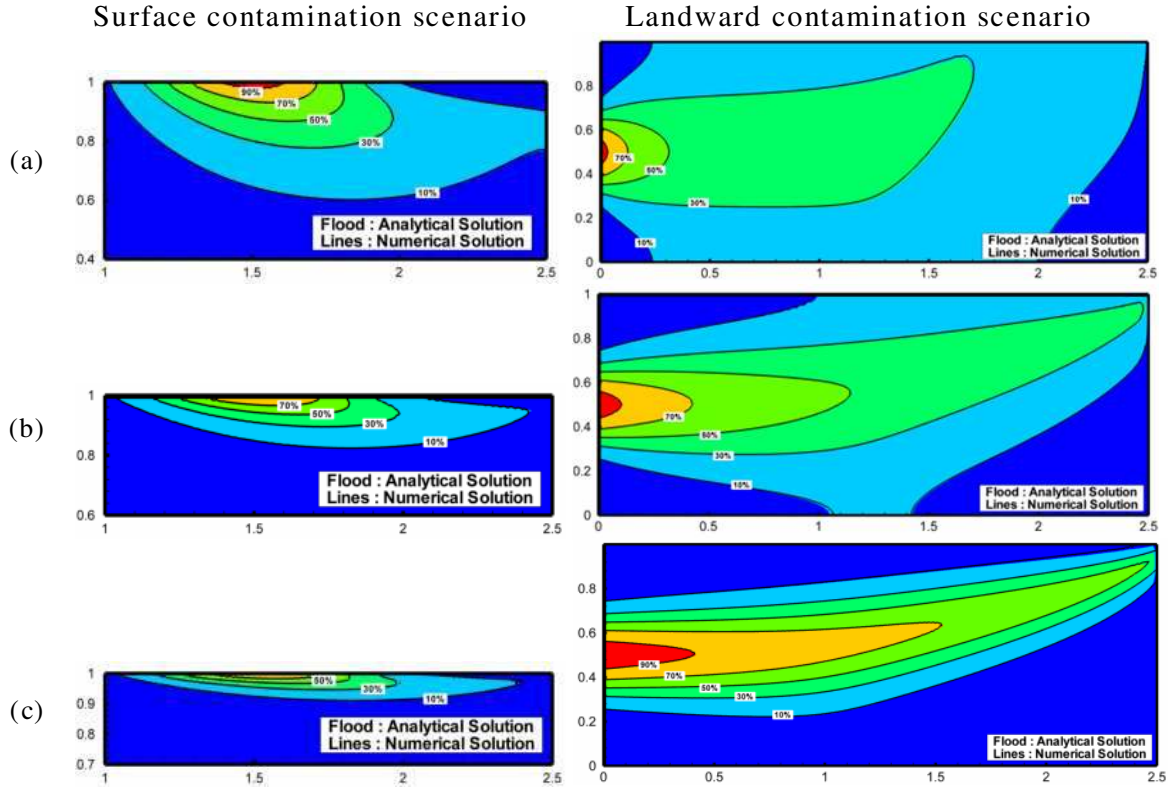


Fig. 3.4. Comparison between semi-analytical and numerical solutions for both scenarios: (a) test case1, (b) test case 2 and (c) test case 3.

Numerical simulations are also relevant to highlight the efficiency of the semi-analytical solution from a computational point of view. The comparison between the number of Fourier modes required to obtain the stable semi-analytical solution and the number of unknowns of the numerical model required to obtain equivalent accuracy shows that the semi-analytical method requires many less unknowns than the numerical model, irrespective of Pe and for both contamination scenarios. The superiority of the semi-analytical method become more pronounced as Pe is increased. For instance, in the high Peclet number case (surface contamination scenario), the semi-analytical solution requires about 7000 Fourier coefficients. Equivalent accuracy can be obtained with a numerical solution involving a mesh of about 20,000 elements corresponding to about 90,000 degrees of freedom.

To further highlight the computational efficiency of the semi-analytical method we evaluated the amount of improvement obtained by applying the specific technique implemented in the codes for the evaluation of the numerical integrals (see section 3.4). We considered, as an

example, a case of the first scenario in which about 4,500 Fourier coefficients should be used to obtain the semi-analytical solution. We performed the calculations on a single computer with two Intel Xeon E5-2690 series (2×12 cores) sharing 64GB of memory. The results show that, with the standard procedure, the CPU time is measured to be more than 1 hour. For the same case, the CPU time with the new technique for the evaluation of numerical integrals reduces to be only 12min. This represents a gain of performance of about 450%. With the parallel implementation, the evaluation of this solution takes only 78sec. This result highlights, on the one hand, the high efficiency of our implementation and on the other hand the flexibility of the semi-analytical method to enable parallel programming.

The developed semi-analytical solutions can be used for validating and testing numerical codes in the case of coupled flow and transport processes or only transport under known flow field conditions. In this context, the results presented in this study (mainly Fig. 3.4) can be directly used in further comparative studies. Tables 3.1 and 3.2 provide also a high accurate quantitative data that can be used for benchmarking purposes. Furthermore, to facilitate the validation and benchmarking tasks for other configurations we provide the full semi-analytical codes on the website <https://lhyges.unistra.fr/FAHS-Marwan>.

3.7. Effect of seawater intrusion on contaminant transport

In this section we take advantage of the semi-analytical solution to investigate of the effect of N_g on the contaminant transport. We aim to provide a better understanding on the influence of seawater intrusion on the contaminant plume migration and discharge to the sea. 16 runs were carried out for each test case of the contamination scenarios by varying the value of N_g . Similar to *Abarca et al. (2007)*, N_g was varied between 0.625 and 20. In this discussion, for sake of clarity, the variation of N_g (at constant Pe) will be interpreted as a variation of the aquifer permeability. Thus, the increase of N_g will be seen as an increase of the aquifer permeability. This leads to an intensification of the flow within the saltwater wedge and results in greater intrusion of the saltwater tongue. The intensification of seawater intrusion, in turn, accelerates the freshwater main flow as it narrows the pathway through which the freshwater is discharged to the sea. In the following we will discuss the influence of this velocity variation on the contaminant plume characteristics.

- *Results for surface contamination scenario*

Fig. 3.5 reports the main contaminant concentration contours (20%, 50% and 80%) for three selected values of N_g . It shows that, whatever the Péclet number, the contaminant plume moves up toward the aquifer top surface when N_g is increased. This is related to the shrinking of the solute boundary layer caused by the acceleration of the freshwater flow in front of the contaminant source. The effects of N_g on A_c, M_c, F_c and \overline{Sh} are reported in Fig. 3.6. A decreasing variation of A_c is reported which is consistent with Fig. 3.5. M_c is also decreasing (Fig. 3.6b) due to the reduction in the time required to reach steady state conditions. The results reveal strong correlation between A_c and M_c . Both A_c and M_c fit very well with the bi-exponential regression model given by: $y_0 + A_1 e^{-N_g/t_1} + A_2 e^{-N_g/t_2}$. The coefficients y_0, A_1, t_1, A_2 and t_2 are given in Appendix II. This model explains that A_c and M_c are exponentially decaying when N_g is increased but with different rates at small and large values of N_g . Indeed, as we can see in Appendix II, t_1 is significantly less than t_2 . This means that for small values of N_g , we have $N_g/t_2 \approx 0$. Hence the term corresponding to the rate of decay t_1 is dominant. The reverse is true for the largest values of N_g .

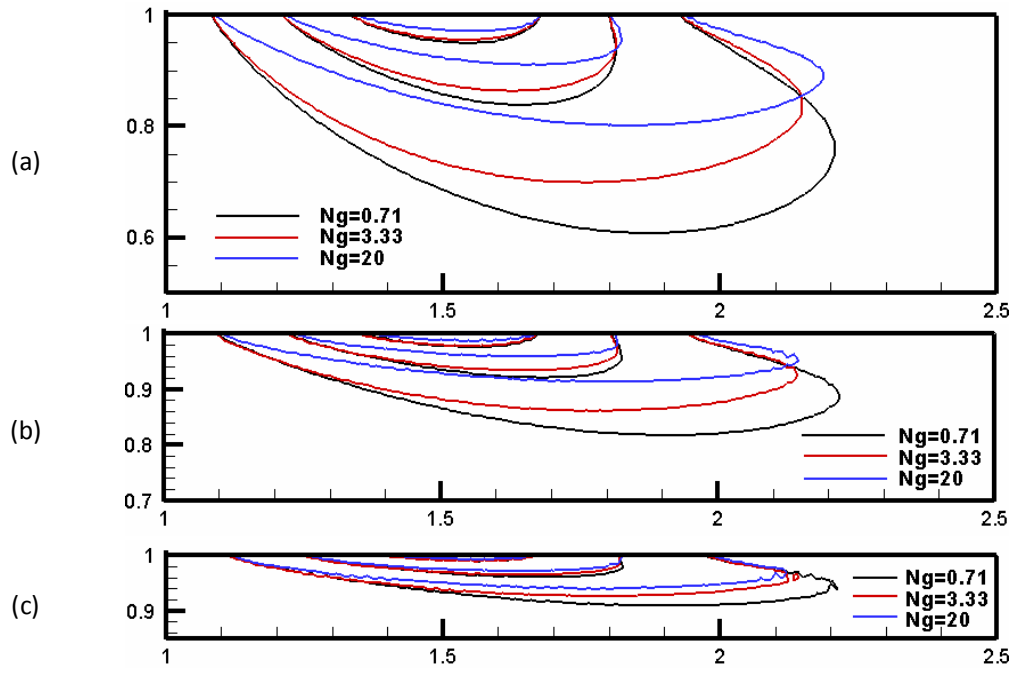


Fig. 3.5. Effect of N_g on the main contamination contours (20%, 50% and 80%) for surface contamination scenario: (a) test case 1, (b) test case 2 and (c) test case 3.

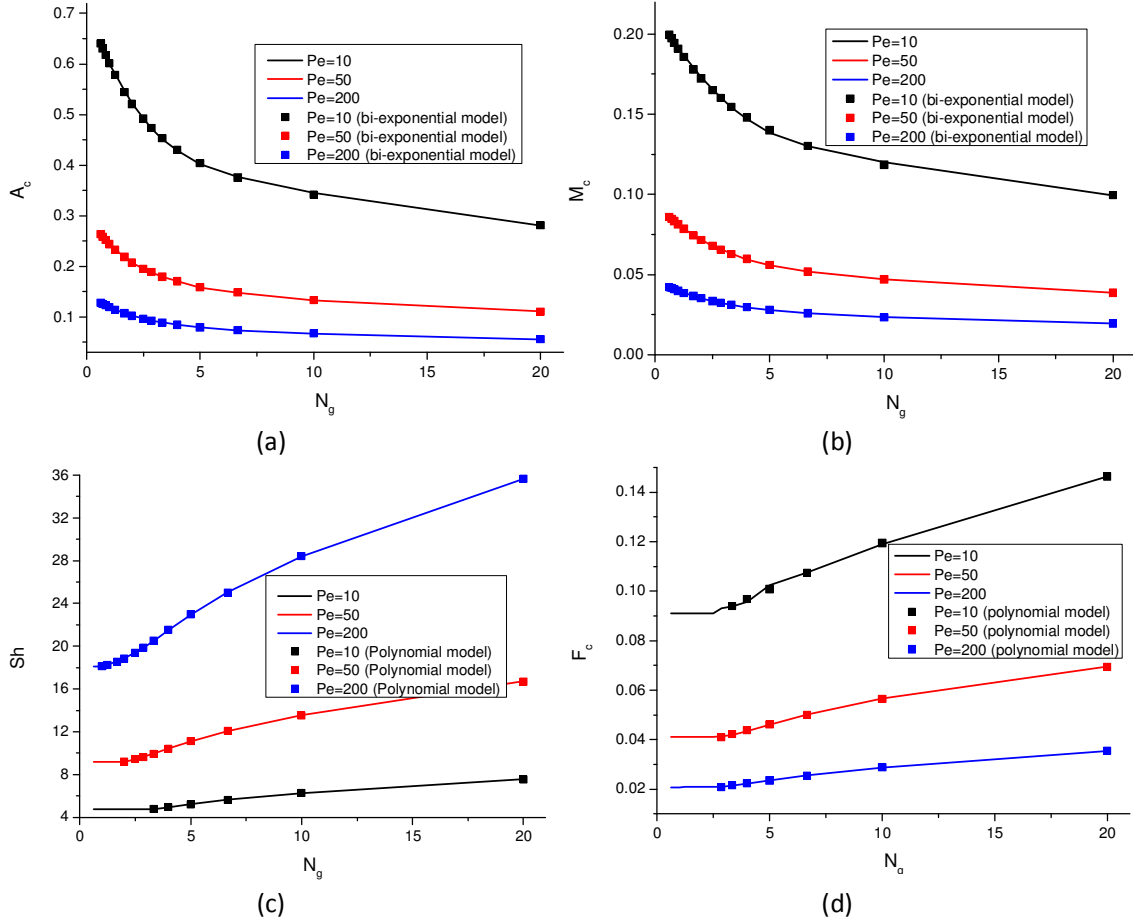


Fig. 3.6. Variation of the metrics characterizing the contaminant transport versus the gravity number (N_g) and corresponding regression models (surface contamination scenario).

Fig. 3.6c and 6d show that \overline{Sh} and F_c are perfectly correlated. In fact \overline{Sh} is related to the mass rate of contaminant at the inlet which is equal, at steady state condition, to the rate of contaminant discharge to the sea. This good correlation highlights the accuracy of the simulations and gives more confidence in the robustness of the analysis. Only variation of \overline{Sh} will be discussed here. Fig. 3.6c indicates the existence of two regimes for the evolution of \overline{Sh} . Thus, we have almost constant value for low gravity number and increasing variation otherwise. For low gravity number, the seawater wedge is very far from the contamination source. Hence, there is no influence of the seawater intrusion on the contaminant concentration distribution. When N_g is increased the intense seawater intrusion produces a thinner solute

boundary layer around the contaminant source, leading to the increase of the concentration gradient. This result indicates that seawater intrusion can increase the contaminant leakage to the aquifer and as a consequence the risk of contaminant discharge to the sea. The regression analysis reveals a good fitting of \overline{Sh} with a second degree polynomial model, for the regime where N_g is influential. The polynomial model is given by: $B_0 + B_1 N_g + B_2 (N_g)^2$. The coefficients are given in appendix II.

- *Results for the landward contamination scenario*

Fig. 3.7 displays the main contaminant concentration contours (20%, 50% and 80%) for three selected values of N_g (same values as for scenario 1). It shows that the plume migration is more sensitive to the seawater intrusion than the first scenario. With the increase of N_g , the plume moves up toward the top surface of the aquifer. For the smallest values of N_g , seawater intrusion affects mainly the low concentration contours near the sea. For the largest values of N_g , all the concentration contours are impacted by the variation of N_g and everywhere in the aquifer.

Fig. 3.8 displays the variations of A_c , M_c and F_c as a function of N_g . Fig. 3.8a indicates a decreasing variation of A_c at constant Péclet number. This behavior is related to the intensification of the groundwater flow (relative to the increase of N_g) that reduces the effect of the dispersion mechanisms. The same behavior is recorded for M_c (Fig. 3.8b) which is also related to the flow acceleration leading to the shortness of the duration required to reach the steady state condition. Fig. 3.8b also shows that, at low gravity number ($N_g < 1$) M_c is almost insensitive to Pe . This is logical because, for $N_g < 1$, the seawater intrusion is very weak. Hence, the increase of Pe has a slight impact on the flow velocity and by consequence has limited impact on the duration required to reach the steady state condition.

The variation of F_c exhibits two regimes depending on N_g (Fig. 3.8c). Better understanding of this behavior can be gained by investigating the effect of N_g on the mass rate of contaminant entering the aquifer which is possible due to the mass balance under steady state conditions. At low gravity numbers, F_c is almost constant. In this case the contaminant mainly enters the domain by advection due to the freshwater recharge flux. Hence F_c is independent of N_g . For

the extreme cases of seawater intrusion (largest values of N_g), the saltwater wedge can reach the landward boundary and generates an uplifting flow along the landward vertical boundary. The vertical component of the velocity can generate a concentration gradient and amplify the contaminant penetration in the aquifer because the diffusive flux becomes a significant component of the contaminant flux. Behind the critical N_g (corresponding to the transition between the two regimes of evolution) a further increase of N_g leads to intense seawater intrusion and causes the increase of contaminant mass entering the domain and consequently the increase of F_c . Good regression for all metrics can be obtained using the second degree polynomial model ($B_0 + B_1 N_g + B_1 (N_g)^2$). The coefficients are given in Appendix II. The good regression gives additional confidence on the physical plausibility of the results.

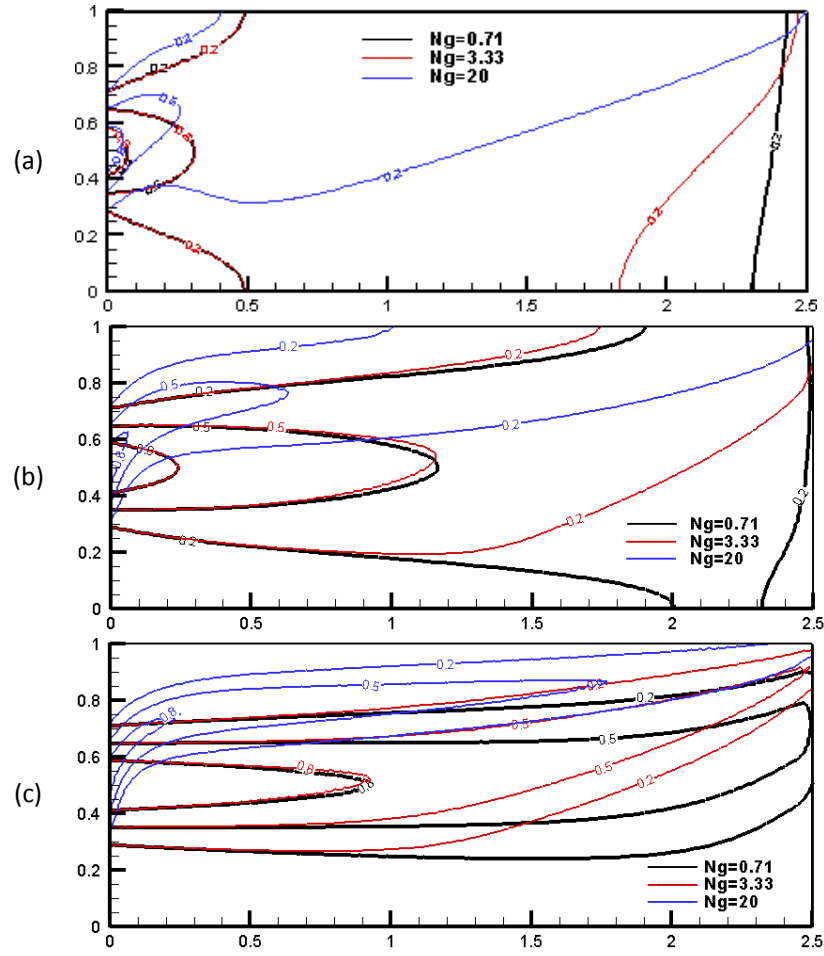


Fig. 3.7. Effect of N_g on the main contamination contours (20%, 50% and 80%) for landward contamination scenario: (a) test case 1, (b) test case 2 and (c) test case 3.

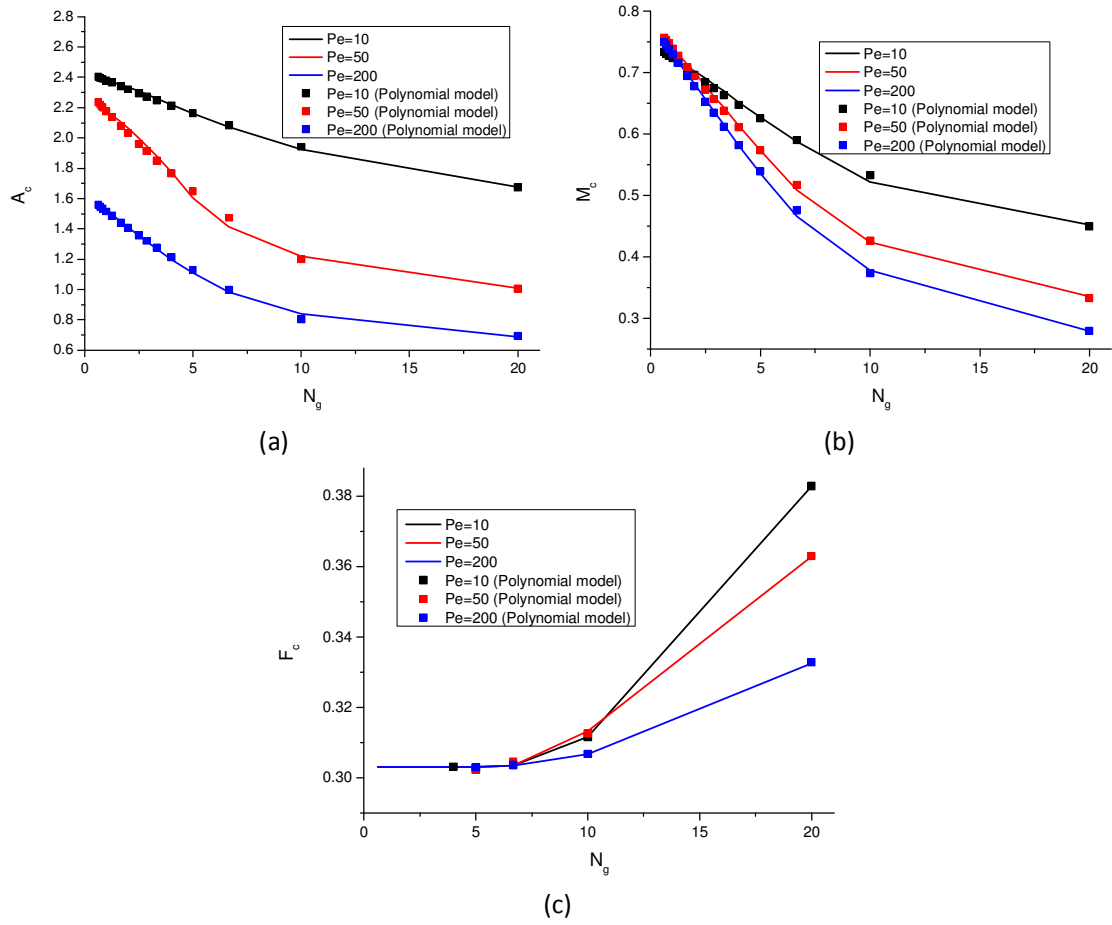


Fig. 3.8. Variation of the metrics characterizing the contaminant transport versus the gravity number (N_g) and corresponding regression models (landward contamination scenario).

3.8. Conclusion

A semi-analytical solution is derived for the simulation of contaminant transport in a coastal aquifer subject to seawater intrusion. The problem geometry and configuration are inspired from the Henry problem. Two contamination scenarios, dealing with contaminant leakage from a source at the aquifer top surface and aquifer contamination from the landward boundary, are considered. The semi-analytical solution is developed based on the FG method. An adaptation of this method is developed to deal with discontinuous contaminant boundary conditions. Specific changes of variables have been applied in order to include the contamination source according to the prescribed contamination scenarios. The Fourier series have been used to evaluate several metric characterizing the contaminant transport. A sound implementation of the FG based on OpenMP parallel programming and an appropriate evaluation of the Fourier series has been developed to optimize the computational requirement of the semi-analytical method for the cases where relatively large number of Fourier modes should be used to obtain stable solution. Thanks to this implementation, the semi-analytical solutions have been obtained for example cases dealing with high Peclet number. The main inconvenience of the FG solution is related to its rather implementation complexity. For practical usage in further studies, the full open source semi-analytical code is made available at the website <https://lhyges.unistra.fr/FAHS-Marwan>.

The developed semi-analytical solution is compared against the numerical solution of an in house code. Perfect agreement has been observed which gives confidence on the correctness of both semi-analytical and numerical solutions. This comparison shows that the semi-analytical solutions avoid several numerical artifacts related to space discretization and time integration. This highlights their benefits as useful mathematical tools for validating numerical models of CTCA and in general for contaminant transport under variable velocity field. In this context, we should mention that the analytical values of the metrics characterizing the contaminant transport (A_c , M_c , F_c and \overline{Sh}) provide high quality quantitative well suitable for code benchmarking.

The high robustness and computational efficiency of the developed semi-analytical method render it suitable for forward analysis where a large number of solutions must be evaluated such as in parameter estimation methods and global sensitivity analysis.

Furthermore, results show that the semi-analytical solutions developed in this work help to improve our understanding of the contaminant transport mechanisms in coastal aquifers subjected to seawater intrusion. The findings and conclusions drawn are relevant for the

management of groundwater pollution in coastal aquifer as the developed test cases can be found in several real applications related to aquifers contamination. Results indicate that, in the case of surface contamination, seawater intrusion leads to contracted contaminant plume but increases the contaminant discharge to the sea. In the case of landward contamination, moderate seawater intrusion only affects the spatial distribution of the contaminant plume and has no effect on the contaminant discharge to the sea. However, extreme seawater intrusion can increase the contaminant discharge to the sea. Analytical expressions of the contaminant transport metrics in terms of the gravity number (characterizing seawater intrusion) are derived. The introduced semi-analytical method is not limited to the scenarios discussed in this work. It can be applied to other interesting scenarios of contaminant transport in coastal aquifers and a wide range of applications involving coupled flow and transport processes. We should recall that the presented semi-analytical solution can be extended to dense plume contamination and heterogeneous coastal aquifer. Questions about how FG method can be effectively used to solve velocity dependent dispersion transport and/or transient problems is worthy of future inquiry.

The work has been published in the Journal of Hydrology on March 2018 (*Koohbor et al., 2018*). <https://doi.org/10.1016/j.jhydrol.2018.03.048>

Chapter IV: Uncertainty analysis for seawater intrusion in fractured coastal aquifers: Effects of fracture location, aperture, density and hydrodynamic parameters

4.1. Introduction

Coastal aquifers (CAs) are currently in a critical situation throughout the world. These aquifers are essential sources of freshwater for more than 40% of the world's population living in coastal areas (*IOC/UNESCO, IMO, FAO, UNDP, 2011; Barragán and de Andrés, 2015*). The phenomenon of seawater intrusion (SWI), which encompasses the advancement of saline water into fresh groundwater mainly caused by excessive groundwater extraction, is the first source of contamination in CAs (*Werner et al., 2013*). The European Environment Agency (www.eea.europa.eu) declared SWI as a major threat for many CAs worldwide. This phenomenon is exacerbated by the increasing demand for groundwater as a result of the increase in population and anthropogenic activity. It is also amplified due to natural causes such as climate change, Tsunami events and sea-level rise expected in the next century (*e.g., Ataie-Ashtiani et al., 2013; Ketabchi et al., 2016*).

The impacts of local heterogeneities of CAs on the extent of SWI at the scale relevant for management scenarios is well documented in the literature (*e.g. Simmons et al., 2001; Kerrou and Renard, 2010; Lu et al., 2013; Mehdizadeh et al., 2014; Pool et al., 2015; Stoeckl et al., 2015; Shi et al., 2018*). Fractured geology is the most challenging form of natural heterogeneity. Fractures represent the preferential pathways that may enable faster SWI or intensify freshwater discharge to the sea (*Bear et al. 1999*). Fractured coastal aquifers (FCAs) are found globally. Several examples can be found in France (*Arfib and Charlier, 2016*), USA (*Xu et al., 2018*), Greece (*Dokou and Karatzas, 2012*), Italy (*Fidelibus et al., 2011*), Ireland (*Perriquet et al., 2014; Comte et al., 2018*), UK (*MacAllister et al., 2018*) and in the Mediterranean zone where more than 25% of CAs are typically karstic (*Bakalowicz et al., 2008; Chen et al., 2017*). Despite the fact that FCAs are distributed throughout the world and they often contain significant groundwater resources due to their high porosity, SWI in these aquifers is rarely investigated and related processes are still largely unexplored and poorly understood (*Dokou and Karatzas, 2012; Sebben et al., 2015*). In the review paper of *Werner et*

al. (2013), the authors suggested SWI in FCAs as one of the potential remaining challenging problems.

SWI can be tackled using either the sharp interface approximation or variable-density flow (VDF) model (*Werner et al., 2013; Llopis-Albert et al., 2016; Szymkiewicz et al., 2018*). VDF model involves flow and mass transfer equations coupled by a mixture state equation expressing the density in terms of salt concentration. This model is usually used in field applications as it is more realistic than the sharp interface approximation and has the privilege of considering the transition zone between the freshwater and saltwater, known as the mixing zone. Flow in fractured porous media can be described using three alternative approaches: i) equivalent porous medium in which averaged estimations of the hydrogeological properties over a representative elementary volume are used to represent the domain (*Dietrich et al., 2005*), ii) dual-porosity models where the domain is considered as the superposition of two continuums representing, respectively, rocks and fractures (*Fahs et al., 2014; Jerbi et al., 2017*) and iii) discrete fracture model in which the fractures and matrix are handled explicitly (*Berre et al., 2018*). Discrete fracture model is the most accurate model because fractures are considered without any simplification. It is usually used for domains with a relatively small number of fractures (*Hirthe and Graf, 2015; Ramasomanana et al., 2018*) and has come into practical use in recent years. However, discrete fracture models require enormous computational time and memory due to the dense meshes resulting from the explicit discretization of the fractures. Discrete Fracture Matrix Model (DFMM), in which the fractures are embedded in $(d-1)$ dimensional elements in (d) dimensional physical domain, is an alternative approximation that reduces the overhead computations of the discrete fracture model.

DFMM model has been successfully coupled with VDF model to simulate SWI in FCAs. For instance, *Grillo et al. (2010)*, based on a single fracture configuration of Henry Problem, showed that DFMM-VDF model is a valid alternative to the discrete fracture model for simulating SWI. *Dokou and Karatzas (2012)* developed a hybrid model based on the combination of the DFMM model (for main fractures and faults) and the equivalent porous media model (for lower-order fractures) to investigate SWI in a FCA in Greece. By confronting numerical simulations to chloride concentration observations, they showed that the DFMM model is necessary to accurately simulate SWI. *Sebben et al. (2015)* used the DFMM-VDF model to present a preliminary deterministic study on the effect of fractured heterogeneity on SWI, using different fractured configurations of Henry Problem. *Mozafari et al. (2018)*

developed a DFMM-VDF model in the finite element frame-work of COMSOL Multiphysics®. Nevertheless, the DFMM-VDF model requires the basic characteristics of fractures as location, aperture, permeability, porosity, etc. These characteristics are subject to a large amount of uncertainties as they are often determined using model calibration procedure based on relatively insufficient historical data provided by several measurement techniques as surface electrical resistivity tomography (*Beaujean et al., 2014*), borehole concentrations and head measurements, multiperiod oscillatory hydraulic tests (*Sayler et al., 2018*), self-potential measurements (*MacAllister et al., 2018*), among others. These uncertainties would reduce the predictive capability of the DFMM-VDF model and impair the reliability of SWI management based on these predictions. Thus, it is important to understand how these uncertainties could propagate in the model and lead to uncertainty in outputs.

This work goes a step further in the understanding of SWI processes in FCAs. It aims to provide a preliminary investigation on the impacts of uncertainty associated to fractures characteristics on the extent of the steady-state saltwater wedge simulated using the DFMM-VDF model. In particular, we investigate the effects of uncertainties on fracture network characteristics (location, aperture, density, permeability and dispersivity) on several SWI metrics, as the length of the saltwater toe, thickness of the mixing zone, area of the salted zone and salinity flux penetrating to the aquifer. As the underpinning conceptual model, we consider the fractured Henry Problem suggested in *Sebben et al. (2015)*. A finite element DFMM-VDF numerical model is implemented using COMSOL Multiphysics® software. We include the Boussinesq approximation in the COMSOL model to reduce nonlinearity and improve computational efficiency.

In order to quantify the variability in model outputs resulting from the uncertain parameters, we use the global sensitivity analysis (GSA). GSA is more appropriate than local sensitivity analysis as it provides a robust and practical framework to explore the entire inputs space and to assess the key variables driving the model outputs uncertainty (*Saltelli, 2002; Sudret, 2008; De Rocquigny, 2012*). GSA is a powerful approach to fully understand the complex physical processes and assess the applicability of models. It is also important for risk assessment and decision-making. In hydrogeological applications, GSA has been used to investigate saturated/unsaturated flow (*Younes et al., 2013, 2018; Dai et al., 2017; Meng and Li, 2017; Maina and Guadagnini, 2018; Miller et al., 2018*), solute transport (*Fajraoui et al., 2011, 2012; Ciriello et al., 2013; Younes et al., 2016*), geological CO₂ sequestration (*Jia et al., 2016*), natural convection (*Fajraoui et al., 2017*) and double-diffusive convection (*Shao et al., 2017*).

In SWI, GSA has been applied to study the effects of hydrodynamics parameters in homogeneous CAs (*Herckenrath et al., 2011; Rajabi and Ataie-Ashtiani, 2014; Rajabi et al., 2015; Riva et al., 2015; Dell'Oca et al., 2017*). *Rajabi et al. (2015)* have shown that GSA is the best-suited method for uncertainty analysis of SWI. Recently, *Xu et al. (2018)* used GSA to investigate SWI in a karstic CA with conduit networks. To the best of our knowledge, GSA has never been applied to SWI in heterogeneous and/or FCAs. Different alternatives can be used to perform GSA (*Iooss and Lemaître, 2015*). Among these alternatives, in this work, we use the variance-based technique with the Sobol' indices (SIs) as sensitivity metrics (*Sobol', 2001*). These indices are widely used because they do not assume any simplification regarding the physical model and provide the sensitivity of individual contribution from each parameter uncertainty as well as the mixed contributions (*Sarkar and Witteveen, 2016*). SIs are usually evaluated through Monte Carlo methods which require a large number of simulations to cover the parameters space and, as a consequence, might be impractical in high CPU consuming problems (as is the case for SWI in FCAs) (*Sudret, 2008; Herckenrath et al., 2011*). To meet the numerical challenges of Monte Carlo methods, we use the polynomial chaos expansions (PCE) which proceeds by expressing each model output as a linear combination of orthogonal multivariate polynomials, for a specified probability measure (*Crestaux et al., 2009; Konakli and Sudret, 2016; Fajraoui et al., 2017*). In particular, we implement the sparse PCE technique developed by *Shao et al. (2017)* to allow high polynomial orders (i.e. high accuracy) with an optimized number of deterministic samples. With this technique, the number of terms in the PCE decomposition is reduced by excluding insignificant terms. The polynomial order is updated progressively until reaching a prescribed accuracy. During the procedure, Kashyap information criterion is used to measure the relevance of PCE terms (*Shao et al., 2017*). The sparsity of the PCE allows accurate surrogate model even if the optimal number of samples necessary for a total order expansion is not achieved. Once the PCE is constructed for each model output, the SIs can be directly calculated, with no extra computational cost, by a post-processing treatment of the PCE coefficients.

The study is organized as follows: Section 4.2 is for material and methods in which we present two fractured scenarios of the Henry Problem investigated in this study, the DFMM-VDF model developed with COMSOL and the SWI metrics used as model outputs. Section 4.3 is devoted to the GSA method. In section 4.4, we validate the developed COMSOL model and the Boussinesq approximation by comparison against exact solutions and an in-house research

code. Section 4.5 discusses the GSA results; it includes PCE construction, validation of PCE and uncertainties propagation. A conclusion is given in section 4.6.

4.2. Material and methods

4.2.1. Conceptual model: Fractured Henry Problem

The conceptual model is based on the fractured Henry Problem, suggested by *Sebben et al. (2015)*. A detailed review of the Henry Problem and its applications can be found in *Fahs et al. (2018)*. This problem deals with SWI in a confined CA of depth H and length ℓ . Sea boundary condition (constant concentration and depth-dependent pressure head) is imposed at the left side and constant freshwater flux ($q_d [L^2T^{-1}]$) with zero concentration is assumed at the right side. Two fracture configurations are investigated in our analysis. The first configuration deals with a single horizontal fracture (SHF) extending on the whole domain and located at a distance (d^F) from the aquifer top surface (Fig. 4.1a). This configuration is specifically considered to investigate the effect of uncertainty related to fracture location on the extent of saltwater wedge. In the second configuration, we assume a network of orthogonal fractures (NOF) (Fig. 4.1b), as in *Sebben et al. (2015)*. Square sugar-cube model with elementary size δ^F (distance between 2 consecutive fractures) is considered as fracture network. This configuration is considered since it allows for performing uncertainty analysis of the SWI metrics with respect to the fracture density. Furthermore, vertical fractures are important to investigate buoyancy effects.

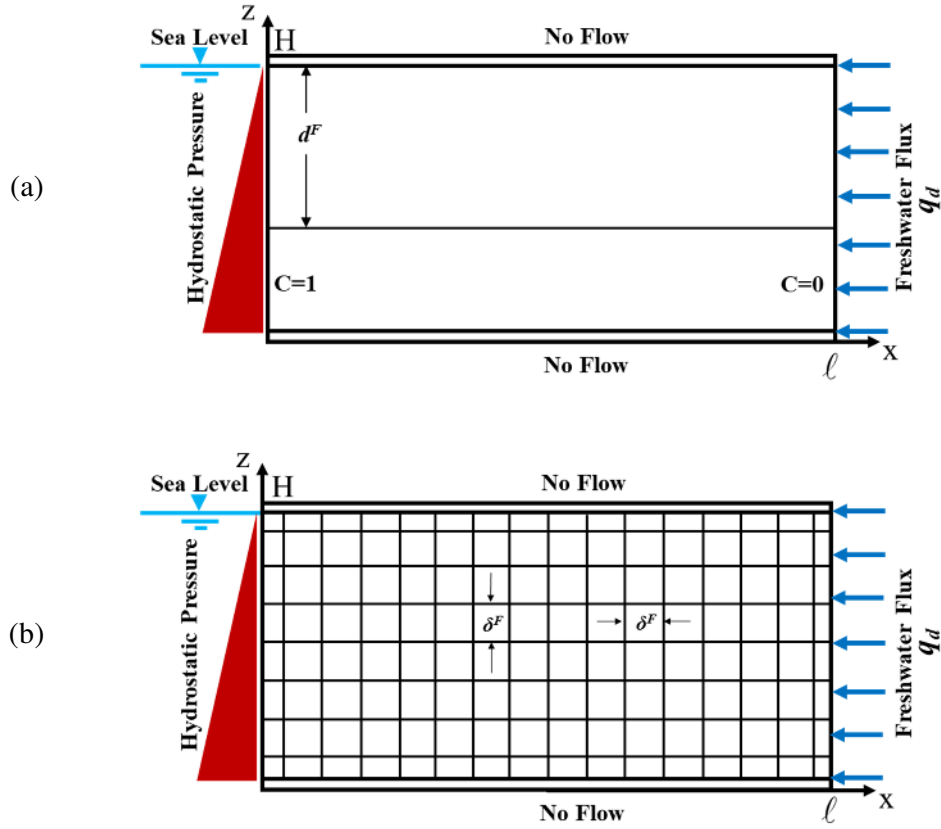


Fig. 4.1. Conceptual model of the fractured Henry Problem: (a) Single horizontal fracture configuration (SHF) and (b) Network of orthogonal fractures configuration (NOF).

4.2.2. DFMM-VDF mathematical model:

Under steady-state conditions and based on Boussinesq approximation, the VDF model in the porous matrix is given by (Guevara Morel et al., 2015):

$$\nabla \cdot \mathbf{q} = 0 \quad (4.1)$$

$$\mathbf{q} = -K^M \left(\nabla h + \frac{\rho - \rho_0}{\rho_0} \nabla z \right) \quad (4.2)$$

$$\mathbf{q} \nabla c - \nabla \cdot (\varepsilon^M D_m \mathbf{I} + \mathbf{D}) \nabla c = 0 \quad (4.3)$$

$$\mathbf{D} = (\alpha_L^M - \alpha_T^M) \frac{\mathbf{q} \times \mathbf{q}}{|\mathbf{q}|} + \alpha_T^M |\mathbf{q}| \mathbf{I} \quad (4.4)$$

$$\rho = \rho_0 + \Delta \rho \cdot c \quad (4.5)$$

where q is the Darcy's velocity $[LT^{-1}]$; ρ_0 the freshwater density $[ML^{-3}]$; g the gravitational acceleration $[LT^{-2}]$; K^M is the freshwater hydraulic conductivity of the porous matrix $[LT^{-1}]$; h the equivalent freshwater head $[L]$; ρ $[ML^{-3}]$ the density of mixture fluid and z is the elevation $[L]$; c is the relative solute concentration $[-]$; D_m the molecular diffusion coefficient $[L^2T^{-1}]$; ϵ^M is the porosity $[-]$ of the porous matrix; \mathbf{I} the identity matrix and \mathbf{D} is the dispersion tensor; $\alpha_L^M [L]$ and $\alpha_T^M [L]$ are the longitudinal and transverse dispersion coefficient of the porous matrix, respectively.

With the DFMM approach, the mathematical model for fractures can be obtained by assuming 1D flow and mass transport equations along the fractures direction. The resulting equations are similar to the ones in the porous matrix, but with ϵ^F , K^F and α_L^F as porosity, hydraulic conductivity and longitudinal dispersivity in the fractures, respectively. Transverse dispersivity in the fracture (α_T^F) is neglected, as in *Sebben et al. (2015)*. The 1D flow and mass transport equations in fracture involve the thickness of the fracture (e^F) as parameter.

4.2.3. DFMM-VDF finite element model: COMSOL Multiphysics®:

The DFMM-VDF simulations are performed using a finite element model developed with COMSOL Multiphysics® software package. COMSOL is a comprehensive simulation software environment for various applications. The use of COMSOL in applications related to hydrogeology is increasingly frequent as this software is a user-friendly tool that facilitates all the modeling steps (preprocessing, meshing, solving and post-processing) and allows an easy coupling of different physical processes (*Ren et al., 2017; Fischer et al., 2018*). Our COMSOL model is created by coupling the “Subsurface Flow” and “Transport of Diluted Species” modules and by assuming concentration-dependent fluid density. The Subsurface Flow module is an extension of COMSOL modeling environment to applications related to fluid flow in saturated and variably saturated porous media. In this module, we use the “Darcy's Flow” interface. The fractures are included via the DFMM model by adding the “Fracture Flow” feature to the “Darcy's law” interface. The “Transport of Diluted Species” module is used to solve the advection-dispersion equation. The Boussinesq approximation is implemented by considering constant density in the fluid properties and setting a buoyancy volume force depending on the salt concentration. The numerical scheme suggested by default in COMSOL is used to solve the system of equations. The flow and transport models are solved sequentially

via the segregated solver. Accurate solutions of the flow model can be obtained using finite volume or finite difference methods (*Deng and Wang, 2017*). However, in COMSOL, quadratic basis finite element functions are used for the discretization of the pressure in the flow model while the concentration in the transport model is discretized using the linear basis functions. The consistent stabilization technique is used to avoid unphysical oscillations related to the discretization of the advection term. This technique is often called upwinding. It adds diffusion in the streamline direction. Triangular meshes suggested by the COMSOL meshing tool are used in the simulations. With the DFMM model, the COMSOL meshing tool generates 2D triangular cells to represent the matrix and 1D cells to represent the fractures. The fracture cells are positioned along the sides of the matrix triangular cells. With the finite-element modeling framework, the common degrees of freedom at the triangle nodes in the matrix and at the 1D segments in the fractures are used to model the volumetric and mass fluxes between the matrix and the fractures. First runs have shown that, with the steady-state mode, COMSOL is bound to run into convergence difficulties. To avoid this problem, we used the transient mode. This problem is related to the initial guesses, required for the nonlinear solver, that are often hard to obtain. Hence, the steady-state solutions are obtained by letting the system evolve under transient conditions until steady-state.

4.2.4. Metrics Design:

The main purpose of this study is to perform GSA in regards to certain metrics characterizing the steady state salt-wedge and saltwater flux associated with SWI. The model inputs will be discussed later in the results section since they are dependent on the fracture configuration. As model outputs, we consider the following SWI metrics:

- The spatial distribution of the salt concentration: It is obtained in a pattern of a 100×50 regular 2D square grid (5,000 nodes).
- Length of the saltwater toe (L_{toe}): The distance from sea boundary to the 0.5 isochlor on the bottom surface of the aquifer (Fig. 4.2).
- Thickness of the saltwater wedge (L_s): The distance between the 0.1 and 0.9 isochlors on the aquifer bottom surface (Fig. 4.2).
- Average horizontal width of the mixing zone (\overline{W}_{mz}): The average horizontal distance between the 0.1 and 0.9 isochlors from the bottom to the top of the aquifer (Fig. 2).

- The height of the inflection point (Z_I): The freshwater-seawater inflection point located on the seaward boundary (Fig. 4.2). Below this point, the seawater flows toward the land, and above it the freshwater is discharged to the sea.
- The dimensionless mass of salt persisting in the aquifer $\left(M_s = \frac{1}{\ell \cdot H} \int_0^\ell \int_0^H c \cdot dx dz \right)$: The double integral is calculated with the grid used for the spatial distribution of salt concentration. Only nodes with concentration above 0.01 are considered.
- Total dimensionless flux of saltwater entering the aquifer (Q_s^{total}): defined as the flux of saltwater entering the domain by advection, diffusion and dispersion normalized by the freshwater flux imposed at the inland boundary (q_d).

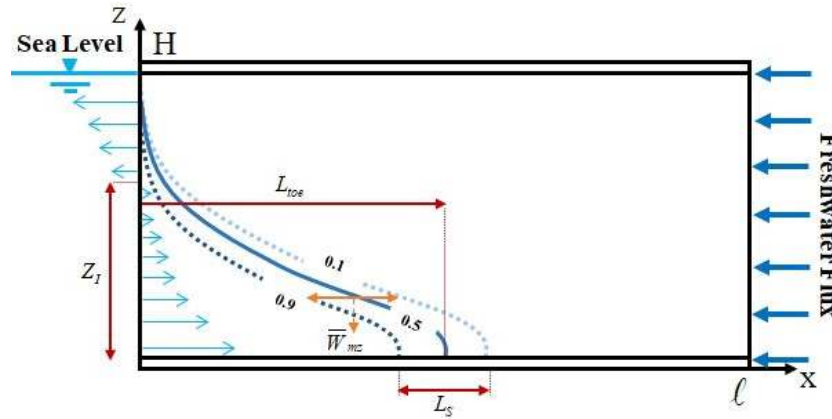


Fig. 4.2. Schematic representation of the SWI metrics.

4.3. Global sensitivity analysis

GSA is a useful and a widespread tool that aims to quantify and evaluate the output uncertainties resulting from the uncertainties in the model inputs, which could be considered singly (for one parameter) or coupled together (several parameters). In this study, the variability of the model responses is quantified throughout a variance based technique using SIs as sensitivity metrics. On the one hand, variance-based sensitivity measures are of interest as they typically specify the relationship between model outputs and input parameters. And on the other hand, the major advantage of using SIs is that they do not require any assumptions of monotonicity or linearity in the physical model. The main stages of this technique are

developed here. More details can be found in *Sudret (2008)*, *Fajraoui et al. (2017)* and *Le Gratiot et al. (2017)*

Let us consider a mathematical model, $Y = M(\mathbf{X})$, delivering the outputs of a physical system that presumably depends on M -uncertain input parameters $\mathbf{X} = \{X_1, X_2, \dots, X_M\}$. For further developments, $f_{X_i}(x_i)$ and $f_x = \prod_{i=1}^M f_{X_i}(x_i)$ refer to their marginal probability density function (PDF) and the corresponding joint PDF of a given set.

4.3.1. Sobol' indices

The Sobol' decomposition of $M(\mathbf{X})$ reads (*Sudret, 2008; Fajraoui et al., 2017*):

$$M(\mathbf{X}) = M_0 + \sum_{i=1}^M M_i(X_i) + \sum_{1 \leq i < j \leq M} M_{ij}(X_i, X_j) + \dots + M_{1,2,\dots,M}(X_1, \dots, X_M), \quad (4.6)$$

where M_0 is the expected value of $M(\mathbf{X})$ and the integral of each summand $M_{i_1, i_2, \dots, i_s}(X_{i_1}, X_{i_2}, \dots, X_{i_s})$ over any of its independent variables is zero, that is:

$$\int_{\Gamma_{X_{i_k}}} M_{i_1, i_2, \dots, i_s}(X_{i_1}, X_{i_2}, \dots, X_{i_s}) f_{X_{i_k}}(x_{i_k}) dx_{i_k} = 0 \text{ for } 1 \leq k \leq s, \quad (4.7)$$

where $f_{X_{i_k}}(x_{i_k})$ and $\Gamma_{X_{i_k}}$ represent the marginal PDF and support of X_{i_k} , respectively.

The orthogonality M_i leads a unique Sobol' decomposition:

$$E[M_u(X_u)M_v(X_v)] = 0, \quad (4.8)$$

Where, $E[\cdot]$ is the mathematical expectation operator, $u = \{i_1, i_2, \dots, i_M\} \subseteq \{1, 2, \dots, M\}$ represents the index sets and X_u are the subvectors involving the components for which the indices belong to u . As a result of uniqueness and orthogonality of Y , its total variance D is decomposed as below:

$$D = \text{Var}[M(X)] = \sum_{u \neq 0} D_u = \sum_{u \neq 0} \text{Var}[M_u(X_u)], \quad (4.9)$$

where D_u is the partial variance expressed as below:

$$D_u = \text{Var}[M_u(X_u)] = E[M_u^2(X_u)] \quad (4.10)$$

Consequently, the SIs are naturally defined as:

$$S_u = \frac{D_u}{D} \quad (4.11)$$

The influence on Y , of each parameter (considered singly), is given by the first order Sobol' indices (S_i) defined by:

$$S_i = \frac{D_i}{D} \quad (4.12)$$

The total SI that includes the effect of an input parameter with the contribution from other parameters, is defined as follows (*Homma and Saltelli, 1996*):

$$S_i^T = \sum_{v_i} \frac{D_v}{D}, \quad v_i = \{u \supset i\} \quad (4.13)$$

The SIs can be calculated by performing Monte-Carlo simulations. This can be done using the estimates of the mean value, total and partial variance of a large number of samples, as explained in Sudret (2008). The drawback of Monte-Carlo simulations lies in the computational cost especially when time-consuming models are investigated. To circumvent this problem, *Sudret (2008)* introduced the PCE for the computation of SIs.

4.3.2. Polynomials Chaos Expansion (PCE)

Each model output is expanded into a set of orthonormal multivariate polynomials of maximum degree M :

$$Y = M(X) \approx \sum_{\alpha \in A} y_{\alpha} \Phi_{\alpha}(X), \quad (4.14)$$

where A is a multi-index $\alpha = \{\alpha_1, \alpha_2, \dots, \alpha_M\}$ and $\{y_{\alpha}, \alpha \in A\}$ are the polynomial coefficients. $\Phi_{\alpha}(X)$ are the base functions of vector space of polynomial functions. These functions should be orthogonal in the vector space with the joint PDF f_X of X as a dot product.

The polynomial coefficients $\{y_{\alpha}\}$ are evaluated using the regression method (least-square technique) that proceeds by minimizing an objective function representing the difference between the meta-model and physical model (see *Fajraoui et al. (2017)*). Based on the PCE, the mean value (μ) and total variance (D) of any model output can be calculated as follows:

$$\mu = y_0 \quad (4.15)$$

$$D = \sum_{\alpha \in A \setminus 0} y_{\alpha}^2 \quad (4.16)$$

Then the SIs of any order can be computed using the coefficients, D and μ in a straightforward manner as followed:

$$S_i = \sum_{\alpha \in A_i \setminus 0} y_\alpha^2 / D, \quad A_i = \{\alpha \in A : \alpha_i > 0, \alpha_{j \neq i} = 0\}, \quad (4.17)$$

and

$$S_i^T = \sum_{\alpha \in A_i^T \setminus 0} y_\alpha^2 / D, \quad A_i^T = \{\alpha \in A : \alpha_i > 0\} \quad (4.18)$$

As suggested by *Deman et al. (2016)*, we also evaluate the marginal effect (ME) to understand the relation between the important variables and the model outputs. ME is given by:

$$E[M(X) | X_i = x_i] = M_0 + \sum_{\alpha \in A_i} y_\alpha \Phi_\alpha(x_i) \quad (4.19)$$

4.3.3. Sparse polynomial chaos expansion

To minimize the number of physical model evaluations and therefore reduce the computational cost, the estimation of the Sobol' indices could be done with a sparse PCE instead of a full PCE approach. In other words, instead of using the expression Eq. (4.14), we can only use some relevant coefficients of the PCE. The key idea consists in discarding the irrelevant terms in the estimated truncated PCE and for this purpose, several approaches have been developed. *Blatman and Sudret (2010)* utilized an iterative forward-backward approach based on nonintrusive regression or a truncation strategy based on hyperbolic index sets coupled with an adaptive algorithm involving a least angle regression (LAR). *Meng and Li (2017)* modified the LAR algorithm with a least absolute shrinkage and selection operator (LASSO-LAR). An adaptive procedure using projections on a minimized number of bivariate basis functions has been provided by *Hu and Youn (2011)*, whereas *Fajraoui et al. (2012)* worked with a fixed experimental design and retained only significant coefficients that could contribute to the model variance. The approach developed in *Shao et al. (2017)*, which has been implemented in this work, consists in progressively increasing the degree of an initial PCE until a satisfactory representation of the model responses is obtained. The computation of the Kashyap information criterion (KIC) based on a Bayesian model averaging is used to determine the best sparse PCE for a input/output sample. Evaluating KIC is an efficient (from a computational point of view) and feasible alternative to directly computing the Bayesian model evidence, being known that this later evaluates the likelihood of the observed data integrated over each model's parameter space. Hence, it is a key term to obtain the posterior probability in the Bayesian framework.

For more details on the Bayesian sparse PCE, for constructing the algorithm and computing the KIC, readers can refer to *Shao et al. (2017)*.

4.4. Validations: COMSOL model and Boussinesq approximation

Although COMSOL has great potential for modelling density-driven flow problems, it has rarely been used for SWI. Thus, the main purpose of this section is to validate our developed COMSOL model. In addition, as explained previously, Boussinesq approximation was implemented in our COMSOL model to improve its computational efficiency. This is a popular approximation for the VDF model as it allows for reducing the computational costs and renders convergence more likely to be achieved. It assumes that variations in density only give rise to buoyancy forces and have no impact on the flow field. Boussinesq approximation ignores density-concentration dependence except in the buoyancy term. This approximation is common for SWI in non-fractured CAs (*Guevara Morel et al., 2015*). Its validity for SWI in FCAs is not discussed in the literature. Thus, another goal of this section is to investigate the validity of this approximation for such a case.

For this purpose, we first use the new semi-analytical solutions of the Henry Problem (homogeneous aquifer) developed by *Fahs et al. (2016)*. We compare these solutions against two COMSOL models: i) SWI-COMSOL model based on the standard COMSOL approach and ii) SWI-COMSOL-Bq based on the Boussinesq approximation. We investigate two test cases presented in *Fahs et al. (2016)* which deal with constant and velocity-dependent dispersion tensor, respectively. The corresponding physical parameters are summarized in Table 4.1. It is noteworthy that, for the validation cases, similar to the semi-analytical solution, the sea boundary is assumed at the right side of the domain. The main isochlors (0.1, 0.5 and 0.9) obtained with COMSOL models as well as the semi-analytical ones are plotted in Fig. 4.3. The corresponding SWI metrics are given in Table 4.2. The COMSOL simulations have been performed using a mesh consisting of about 18,000 elements. As is obvious from Fig. 4.3, excellent agreement is obtained between the COMSOL and the semi-analytical results. This highlights the accuracy of the developed COMSOL models and the related post-treatment procedure applied to obtain the SWI metrics. It also confirms the validity of the Boussinesq approximation for SWI in homogenous CAs.

Table 4.1. Physical parameters used for the validation of homogeneous and fractured cases

| Parameters | Homogenous cases | | Fractured cases |
|-------------------------------|------------------------|-----------------|--|
| ρ_1 [kg/m ³] | 1,025 | | 1,025 |
| ρ_0 [kg/m ³] | 1,000 | | 1,000 |
| q_d [m ² /s] | 6.6×10^{-5} | | 6.6×10^{-6} |
| H [m] | 1 | | 1 |
| ℓ [m] | 3 | | 2 |
| K^M [m/s] | 1.001×10^{-2} | | 2.5×10^{-4} Horizontal Fracture 1.0×10^{-3} Vertical Fracture |
| K^F [m/s] | - | | 7.72×10^{-1} |
| ε^M [-] | 0.35 | | 0.2 |
| ε^F [-] | - | | 1.0 |
| e^F [m] | - | | 0.001 |
| d^F [m] | - | | 0.5 |
| D_m [m ² /s] | 18.86×10^{-6} | Diffusive case | 18.86×10^{-7} Horizontal Fracture |
| | 9.43×10^{-8} | Dispersive case | 1.0×10^{-6} Vertical Fracture |
| α_L^M [m] | 0 | Diffusive case | 0 |
| | 0.1 | Dispersive case | |
| α_T^M [m] | 0 | Diffusive case | 0 |
| | 0.01 | Dispersive case | |
| α_L^F [m] | - | | 0 |
| α_T^F [m] | - | | 0 |

Table 4.2. SWI metrics for the validation cases: Semi-analytical solution (S-Anl), SWI-COMSOL (Co-St) and SWI-COMSOL-Bq (CO-Bq). The width of the mixing zone for the homogenous case is calculated vertically as in *Fahs et al. (2016)*.

| Metrics | Homogenous Diffusive | | | Homogenous Dispersive | | | Fractured (Horizontal) | | |
|---------------------|----------------------|-------|-------|-----------------------|-------|-------|------------------------|-------|-------|
| | S-Anl | CO-St | CO-Bq | S-Anl | CO-St | CO-Bq | TRACES | CO-St | CO-Bq |
| L_{toe} | 0.624 | 0.626 | 0.625 | 1.256 | 1.253 | 1.251 | 0.460 | 0.461 | 0.460 |
| L_S | 0.751 | 0.754 | 0.752 | 0.368 | 0.392 | 0.391 | 0.768 | 0.777 | 0.776 |
| \overline{W}_{mz} | 0.757 | 0.763 | 0.760 | 0.295 | 0.295 | 0.294 | 0.451 | 0.455 | 0.455 |
| Z_I | 0.419 | 0.430 | 0.429 | 0.527 | 0.521 | 0.519 | 0.492 | 0.478 | 0.478 |
| M_S | 0.109 | 0.109 | 0.109 | 0.150 | 0.151 | 0.150 | 0.113 | 0.114 | 0.114 |
| Q_S^{total} | 1.068 | 0.970 | 0.976 | 1.061 | 1.037 | 1.049 | 0.625 | 0.618 | 0.622 |

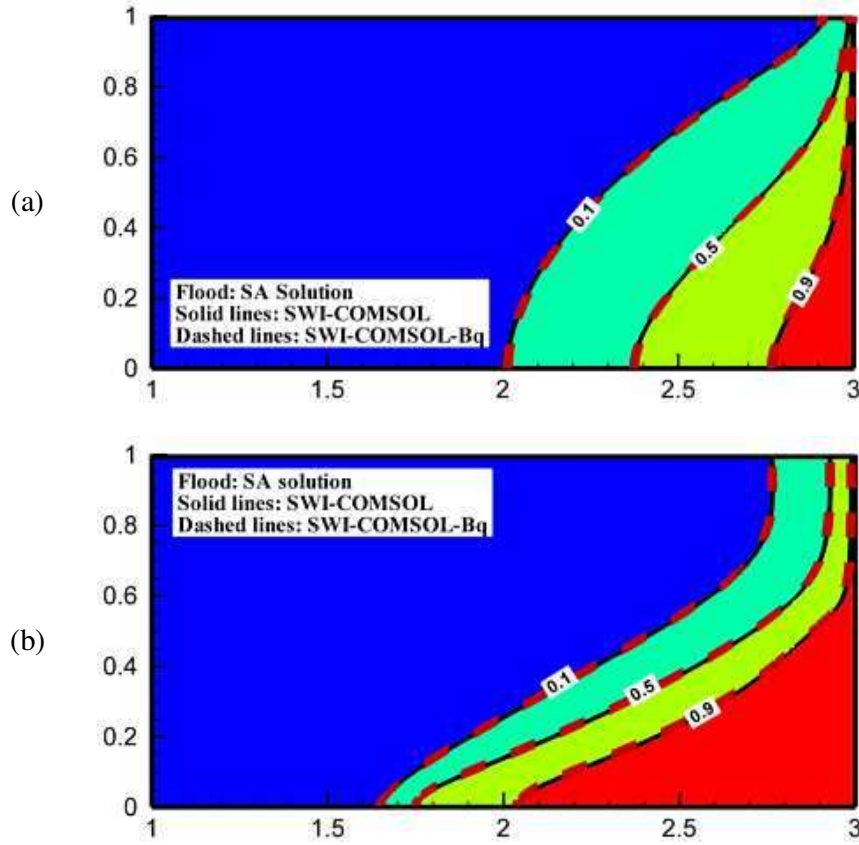


Fig. 4.3. Isochlors obtained using the semi-analytical solution (SA) and COMSOL model (with and without Boussinesq approximation) for the homogenous test cases: (a) diffusive case and (b) dispersive case.

For FCAs, analytical or semi-analytical solutions do not exist. We compare the developed COMSOL models (SWI-COMSOL and SWI-COMSOL-Bq) against an in-house research code (TRACES) based on advanced space and time discretization techniques (Younes *et al.*, 2009). This code has been validated by comparison against several configurations of semi-analytical solutions in Fahs *et al.* (2018). It has proven to be a robust tool for the simulation of SWI in both homogeneous and heterogeneous domains. DFMM approach, which is based on average properties over the fracture width, is not available in TRACES. Thus, the fractures are modeled by considering heterogeneity of material without reduction of the dimensionality; i.e. fracture is a specific layer of the 2D domain with different assigned properties. We considered two validation cases which are based on a single horizontal and vertical fractures, respectively. The horizontal fracture is located at the aquifer middle-depth ($d^F = 0.5m$) while the vertical fracture is located near the seaside at $x=1.8m$. The physical parameters are given in Table 4.1.

The mesh used in the COMSOL simulations involves about 50,000 elements. In the in-house code we use a mesh with about 70,000 elements. The obtained main isochlors are given in Fig. 4.4 and the corresponding SWI metrics are summarized in Table 4.2. Fig. 4.4a shows that, in the case of single horizontal fracture, the high conductivity in the fracture increases the freshwater discharge to the sea and pushes the saltwater wedge toward the sea, especially around the fracture. In the case of vertical fracture (Fig. 4.4b), the high permeability in the fracture enhances the upward flow and push up the saltwater around the fracture Fig. 4.4 and Table 4.2 show excellent agreement between COMSOL and TRACES. They confirm the validity of the Boussinesq approximation in the presence of fractures and highlight the accuracy of the developed COMSOL model. It should be noted also that the comparison between the COMSOL model (in which the fracture is considered as a line) and TRACES (in which the fracture is a 2D layer) confirms the results of *Grillo et al. (2010)* about the validity of the technique based on $(n-1)$ dimensional fractures (i.e. average properties over the fracture) for the simulation of SWI in FCAs.

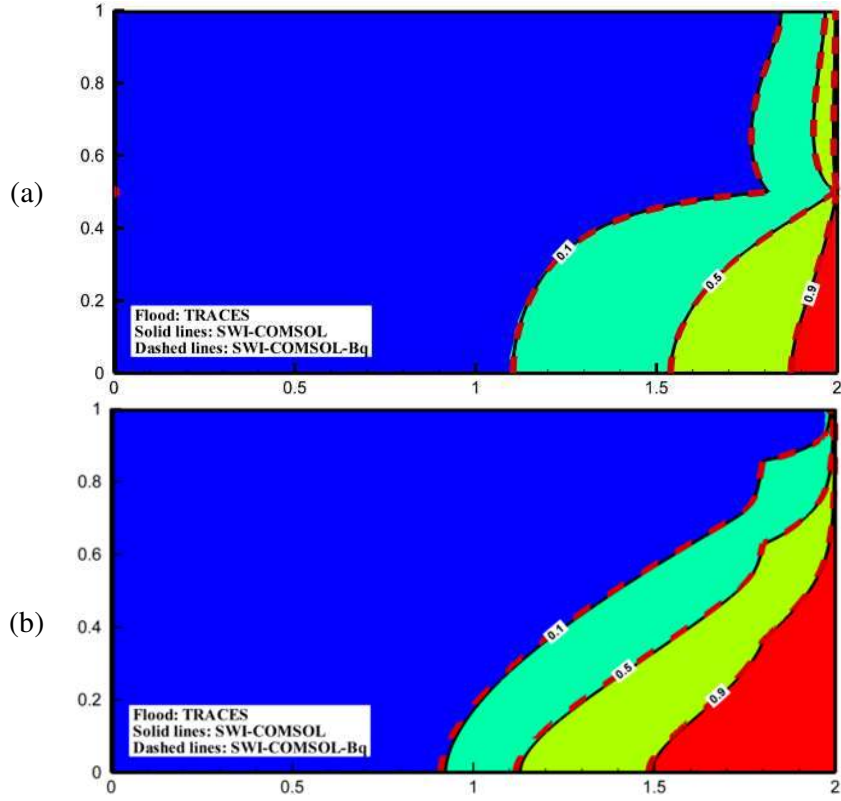


Fig. 4.4. Isochlors obtained using TRACES (in-house code) and COMSOL model (with and without Boussinesq approximation) for the fractured test cases: a) single horizontal fracture and b) single vertical fracture.

4.5. Global sensitivity Analysis: results and discussion

The methodology used to perform GSA is described in the flowchart presented in Fig. 4.5. In this section we present the assumptions and numerical details related to the PCE construction. We also validate the PCE meta-model by comparison against physical COMSOL model and we present the results of the GSA based on the SI's, for both salinity distribution and SWI metrics.

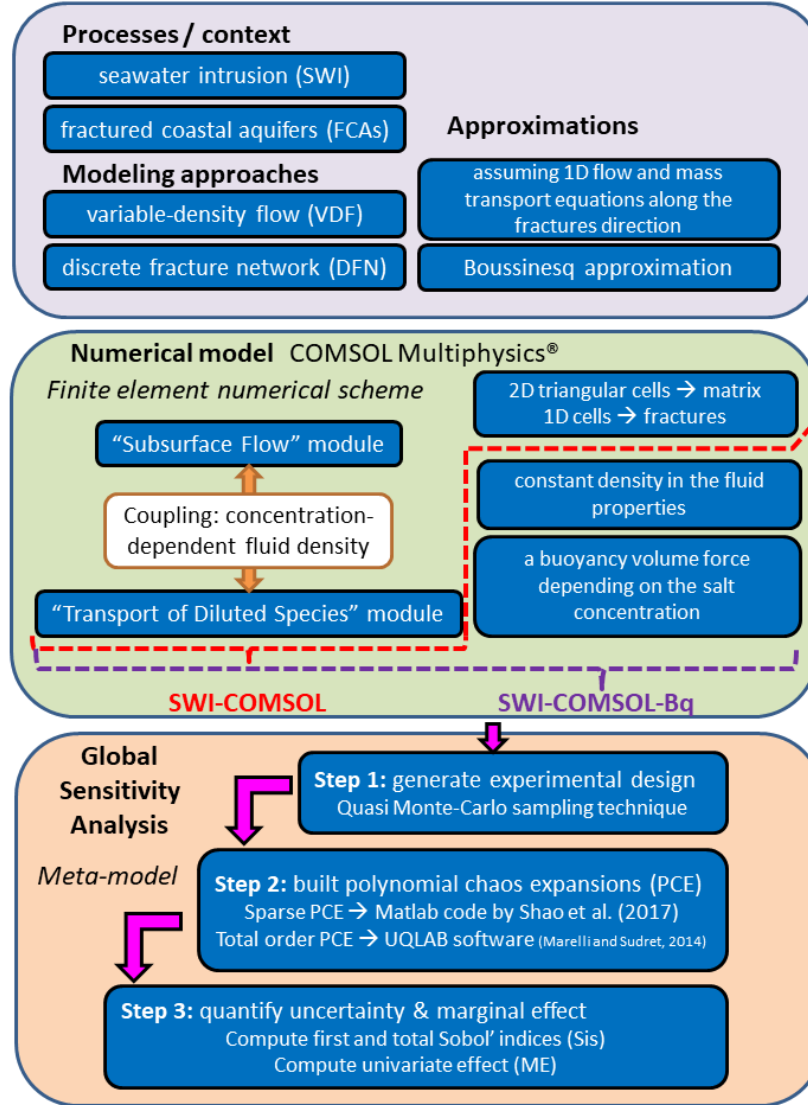


Fig. 4. 5. A flowchart describing the methodology and approaches used to perform the global sensitivity analysis: The first block (in purple) describes the physical processes and the corresponding mathematical models used in this study; The second block (in olive-green) presents the finite element model used to simulate the physical processes (COMSOL with and without Boussinesq approximation); The third block (in orange) describes the approach used to perform global sensitivity analysis (polynomial chaos expansion as meta-model and Sobol's indices as sensitivity metrics).

4.5.1. The single horizontal fracture configuration (SHF)

Several studies showed that, under steady-state condition, the isotropic Henry Problem is governed by six dimensionless quantities which are the gravity number, longitudinal and transverse Peclet numbers, ratio of the fresh water density to the difference between freshwater and saltwater densities, Froude number and the concentration of salt in seawater (*Riva et al., 2015; Fahs et al., 2018*). Uncertainty analysis related to these parameters is performed in *Riva et al. (2015)*. The main goal of our work is to investigate the effect of uncertainties related to the presence of fractures. Thus, for the SHF configuration, we assume that the hydraulic conductivity (K^F), aperture (e^F), depth (d^F) and longitudinal dispersivity (α_L^M) of the fracture are uncertain. For the matrix domain, we only include the longitudinal dispersivity (α_L^M) in our analysis as this parameter is important for the exchange between fracture and matrix domain. The dispersivity ratio (transverse to longitudinal) is set to be 0.1. Other parameters are kept constant. Table 4.3 summarizes the values of the deterministic parameters as well as the range of variability of the uncertain parameters. The values used in this table are similar to *Sebben et al. (2015)*.

We should mention that network connectivity (i.e. how fractures are interconnected) has a clear and large impact on the extent of SWI. However, in the cases investigated in this work, all the fractures are fully connected (abutting and crossing fractures). Thus the effect of network connectivity is not considered. Disconnected cases are not considered because it is not obvious to find well defined parameters (required for GSA) to describe the connectivity. Also, disconnected fractures can lead to discontinuous model outputs for which the PCE surrogate model could not approximate the true system with an acceptable degree of accuracy.

Table 4.3. Values and ranges of variability of the parameters used for the GSA.

| <i>Parameters</i> | <i>Configuration SHF</i> | <i>Configuration NOF</i> |
|---------------------|---|---|
| $\rho_1 [kg/m^3]$ | 1,025 | 1,025 |
| $\rho_0 [kg/m^3]$ | 1,000 | 1,000 |
| $q_d [m^2/s]$ | 6.6×10^{-6} | 6.6×10^{-6} |
| $H [m]$ | 1 | 1 |
| $\ell [m]$ | 2 | 2 |
| $K^M [m/s]$ | 2.49×10^{-5} | 2.49×10^{-5} |
| $K^F [m/s]$ | $[1.17 \times 10^{-1} - 7.65 \times 10^{-1}]$ | $[1.86 \times 10^{-2} - 1.17 \times 10^{-1}]$ |
| $\varepsilon^M [-]$ | 0.2 | 0.2 |
| $\varepsilon^F [-]$ | 1.0 | 1.0 |
| $e^F [m]$ | $[3.8 \times 10^{-4} - 9.7 \times 10^{-4}]$ | $[3.8 \times 10^{-4} - 9.7 \times 10^{-4}]$ |
| $d^F [m]$ | $[0.1 - 0.9]$ | - |
| $\delta^F [m]$ | - | $[0.08 - 0.25]$ |
| $D_m [m^2/s]$ | 10^{-9} | 10^{-9} |
| $\alpha_L^M [m]$ | $[0.05 - 0.3]$ | $[0.05 - 0.3]$ |
| $\alpha_T^M [m]$ | $0.1 \times \alpha_L^M$ | $0.1 \times \alpha_L^M$ |
| $\alpha_L^F [m]$ | $[0.05 - 0.3]$ | $[0.05 - 0.3]$ |
| $\alpha_T^F [m]$ | 0 | 0 |

- PCE construction: Numerical details, orders and accuracy

The uncertain parameters are assumed to be uniformly distributed over their ranges of variability. The PCEs are evaluated using an experimental design consisting of 100 samples. To obtain a deterministic experimental design that covers the parameter space, we use the Quasi-Monte-Carlo sampling technique. A preliminary mesh sensitivity analysis is performed to ensure mesh-independent solutions for all the simulated samples. These simulations were important in order to verify that the GSA results are not affected by numerical artifacts related to the finite element discretization. The mesh sensitivity analysis is performed using the most challenging numerical case that deals with the highest value of K^F and lowest values of α_L^M , α_L^F and e^F . In such a case the advection and buoyancy processes are very important and the corresponding numerical solution could be highly sensitive to the mesh size as it might suffer from unphysical oscillations or numerical diffusion. A mesh-independent solution is achieved

for this case using a grid consisting of about 50,000 elements. This mesh is used for the 100 simulations required for computing the PCE expansions.

For each SWI metric (or model output), the corresponding PCE surrogate model is calculated using the technique described in section 4.3. For the salt concentration distribution (multivariate output), component-wise PCE is constructed on each node of the regular 2D square grid defined for the control points (involving 5,000 control points). The MATLAB code developed by *Shao et al. (2017)* is used to compute the sparse PCE. To give more confidence to the sparse PCE, we also compute total order PCE using the UQLAB software (*Marelli and Sudret, 2014*). As five input variables are considered and 100 samples are available, only third-order polynomial could be reached via the total order PCE expansion. The corresponding optimal number of samples is 56. With the sparse technique, implemented in this work, higher orders can be reached even if the optimal number of samples required for full PCE is not achieved. Sixth order PCE is reached for the salt concentration distribution and all SWI metrics except the width of the mixing zone for which the polynomial order is limited to five. The accuracy of the resulting sparse PCE surrogate model is checked by comparison against the physical COMSOL model. In Fig. 4.6, we compare the values obtained with the sparse PCE with those of DFMM-VDF physical model implemented with COMSOL for parameter inputs corresponding to the experimental design (i.e. used for the PCE construction) and also for new samples. Some examples of the results, precisely the length of saltwater toe (L_{toe}) and the mass of salt persisting in the aquifer (Ms), are plotted in Fig. 4.6. We can observe an excellent match which confirms that the PCE surrogate model reproduces the physical model outputs well.

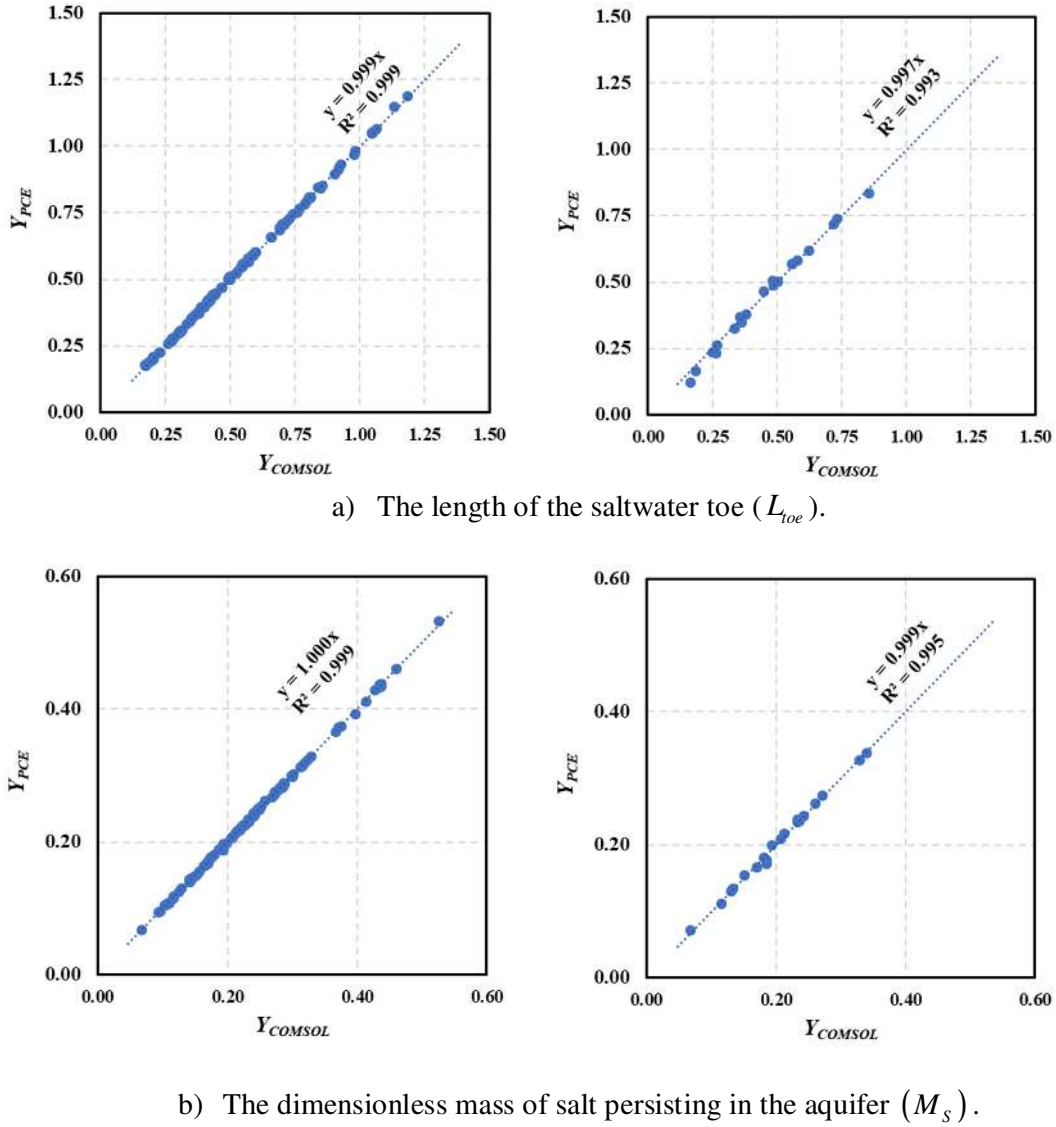


Fig. 4.6. Comparison between the PCE surrogate model and physical (COMSOL) model for the SHF configuration: On the left side, 100 samples used for the experimental design and on the right side, 20 simulations which do not coincide with the experimental design (R^2 is the coefficient of determination).

- *Uncertainty propagation and Marginal Effects (ME)*

Based on the PCE, we calculate the first and total SIs which are used for uncertainty propagation. We also calculate the ME (univariate effect) to obtain a global idea about the impact of the input parameters on the model output. The ME of a certain parameter represents the variability of the model output to this parameter when other parameters are kept constant, at their average values.

The GSA results for the spatial distribution of the salt concentration are illustrated in Fig. 4.7. Fig. 4.7a shows the distribution of the mean concentration based on the PCE expansion. At each node of the mesh used for the control points, the mean value of the salt concentration is calculated as the arithmetic average of the concentrations corresponding to the 100 samples used in the experimental design which are evaluated via the PCE surrogate model. This figure shows that the mean concentration distribution reflects the systematic behavior of SWI. The isochlors are more penetrated at the bottom aquifer due to the saltwater density. This confirms that the PCE surrogate model mimics the full model's response. We also calculate the concentration variance to evaluate how far the concentrations are spread out from their average values (Fig. 4.7b). As expected, the variance is significant in the saltwater wedge. The largest values are located near the aquifer bottom surface where the SWI is usually induced by mixing processes that can be highly sensitive to the model inputs (fracture characteristics and matrix dispersivity). The variance is negligible near the sea-side as the boundary conditions are almost deterministic and the sole acting random parameter is the longitudinal dispersivity that can affect the dispersive entering flux. The sensitivity of the concentration distribution to the uncertain parameters is assessed with the maps of the total SI (Figs 4.7 c-g). The total SI of α_L^M (Fig. 4.7c) shows that the uncertainty related to this parameter affects the concentration distribution at the top aquifer, outside the saltwater wedge. In this zone, the salt transport processes are dominated by the longitudinal dispersion flux as the velocity is toward the sea and it is almost horizontal and parallel to the salt concentration gradient. The zones of largest total SI for K^F and e^F are located within the saltwater wedge toward the low isochlors (Fig. 4.7d and 4.7e). In this region, the mass transfer is mainly related to the advection process which is related to the velocity field. This later is highly depending on the fracture permeability and aperture. The zone of influence of d^F is also located within the saltwater wedge, but toward the aquifer bottom surface and at the vicinity of the high isochlors (Fig. 4.7f). The influence of

α_L^F is limited to the vicinity of the sea boundary where α_L^F can impact the saltwater flux to the aquifer (Fig. 4.7g).

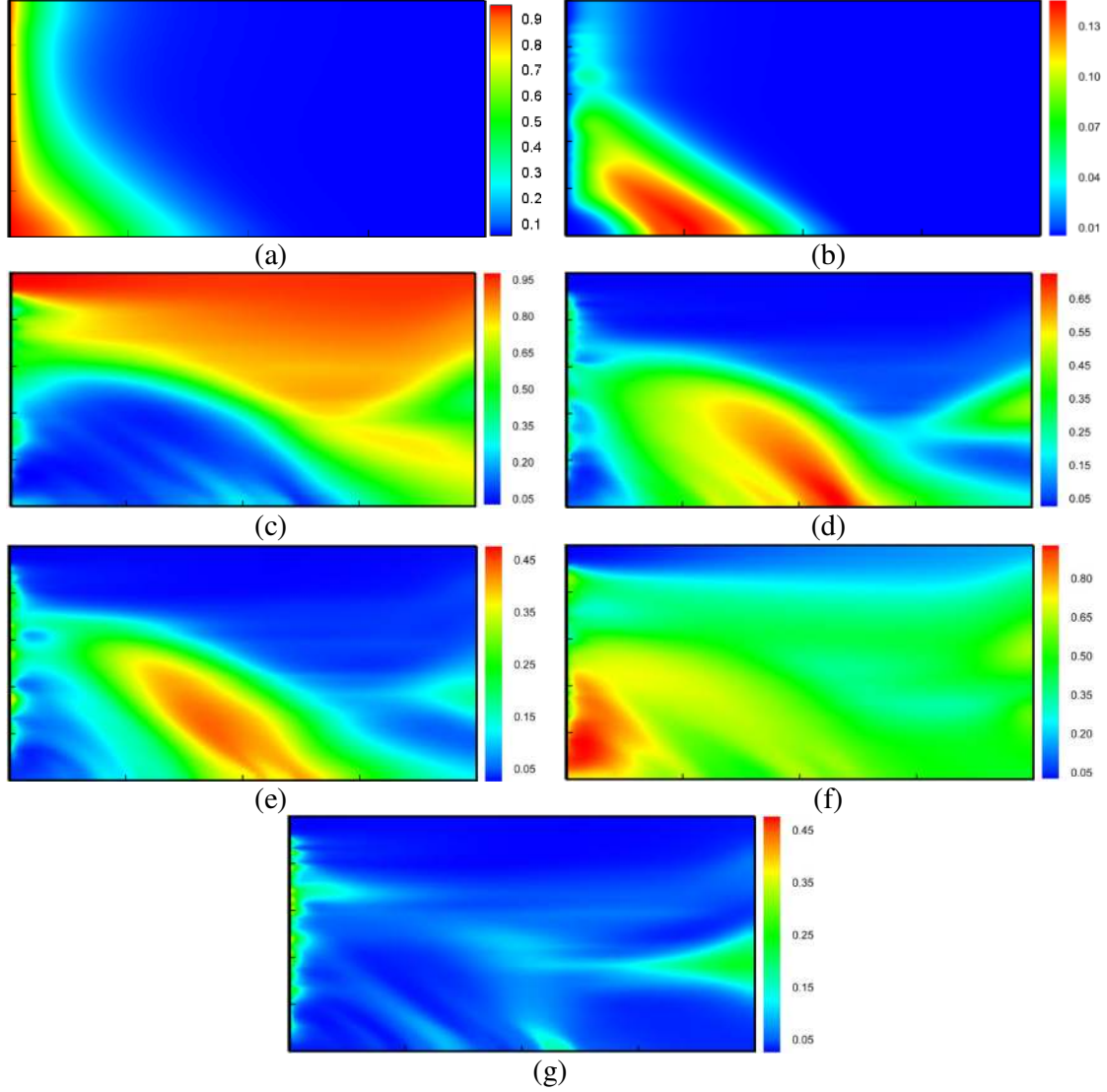


Fig. 4.7. GSA results for the spatial distribution of the salt concentration (SHF configuration): (a) mean salt concentration (b) variance of the salt concentration, (c) total SI of α_L^M , (d) total SI of K^F , (e) total SI of e^F , (f) total SI index of d^F and (g) total SI index of α_L^F .

In the fracture, advection is dominating and dispersion is negligible. It is worthwhile noting that the total SIs count in the overall contribution of a parameter including nonlinearities and interactions. Thus, SIs allow for ranking the parameters according to their importance. It

appears on Figs. 4.7 that d^F , K^F and e^F are the most influential parameters because their total SI are more pronounced in the region where the salt concentration variance is maximum. From the scales of Figs. 4.7 (d-f), it is clear that K^F and e^F are more influential than d^F . Figs. 4.7c shows that the salinity distribution is weakly sensitive to the longitudinal dispersivity of the matrix as in its zone of influence the variance is negligible.

Inspection of the sensitivity of SWI metrics to uncertain parameters is given in Fig. 4.8. This figure represents the bar-plots of the total and first-order SIs of the SWI metrics. As mentioned previously for a further understanding of the uncertainty on SWI metrics related to the imperfect knowledge of input parameters, we also investigate the MEs of the most relevant parameters. These MEs are plotted in Fig. 4.9. The large variability of the SWI metrics (see vertical scales in Figs. 4.9a-j) confirms that the MEs are in agreement with the SIs.

Fig. 4.8a shows that the uncertainty on L_{toe} is mainly due to the effects of d^F and K^F . With a total SI of 0.54, d^F is considered as the most influential parameter. The ME of d^F and K^F on L_{toe} are given in Fig. 4.9a and 4.9b, respectively. Fig. 4.9a shows that L_{toe} decreases with d^F which is coherent with the results of *Sebben et al. (2015)*. Fig. 4.9b shows that L_{toe} increases with K^F . The physical interpretation of this variation is that the increase of K^F heightens the potential of the fracture to constitute a preferential freshwater flow path. This slows down the freshwater flow in the matrix which in turn facilitates SWI and leads to the increase of the penetration length of the saltwater wedge. Fig. 4.8b indicates that the variability of L_s is mainly impacted by α_L^M . This makes sense as L_s measures the salinity dispersion along the aquifer bottom surface which is mainly controlled by α_L^M . L_s is even expected to increase with α_L^M , which is confirmed from the ME in Fig. 4.9c. We can also notice in Fig. 4.8b the slight sensitivity of L_s to d^F . The corresponding ME (Fig. 4.9d) shows that this sensitivity is relatively important for deep fractures ($d^F > 0.6$).

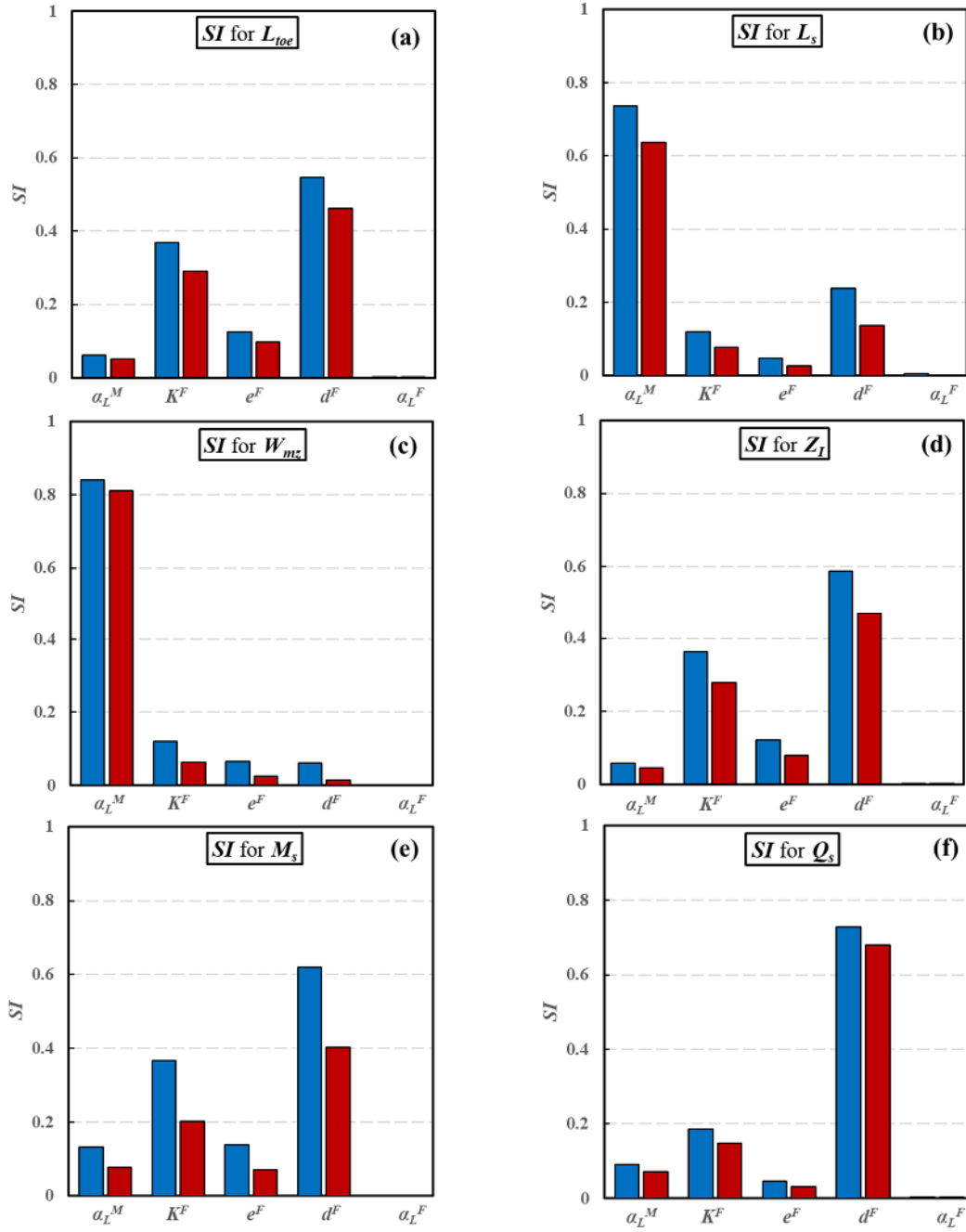


Fig. 4.8. Total (blue) and first order (red) SIs for the SHF configuration: (a) L_{toe} , (b) L_s , (c)

\overline{W}_{mz} , (d) Z_I , (e) M_s and (f) Q_s^{total} .

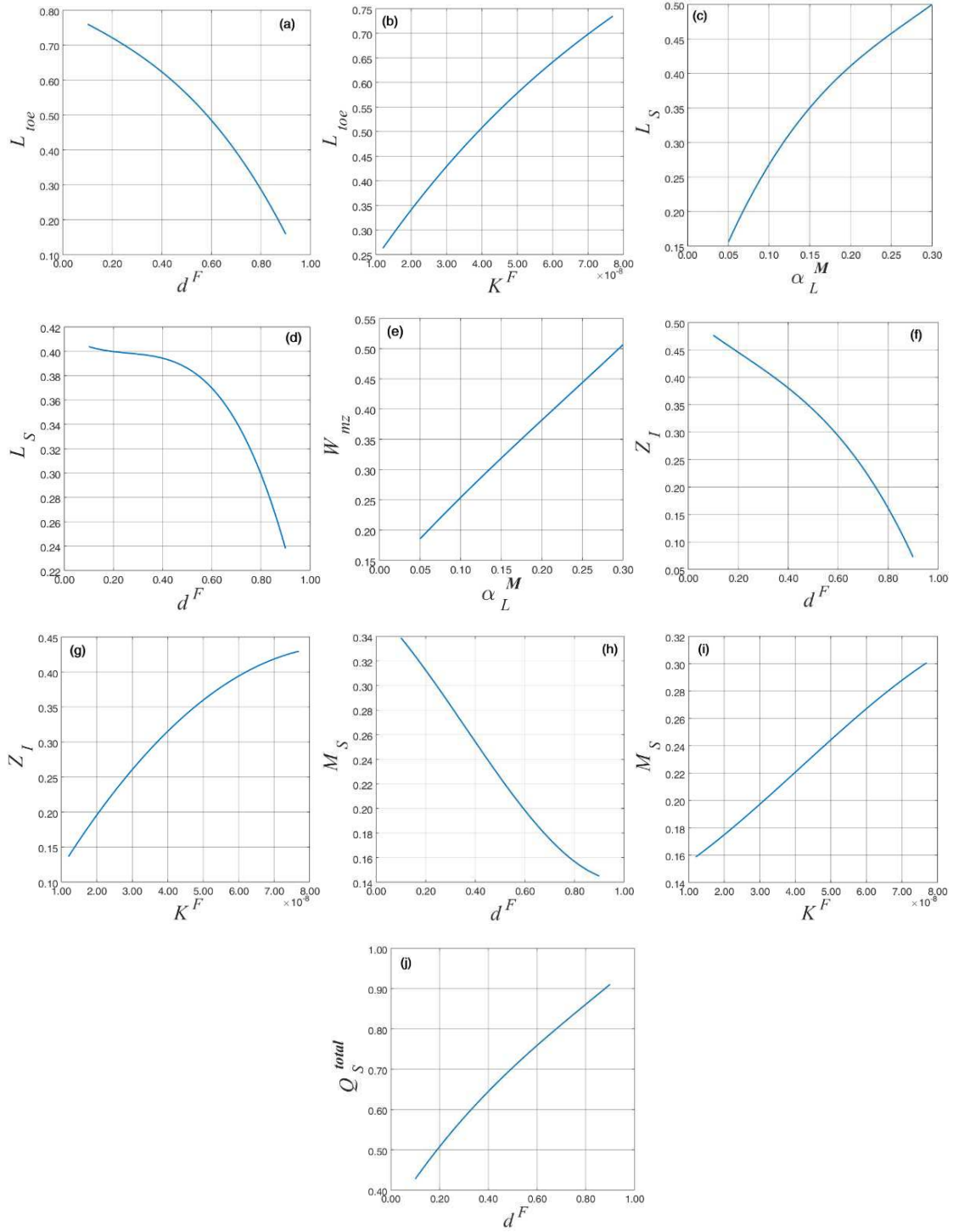


Fig. 4.9. The marginal effects of uncertain parameters on SWI metrics for the SHF configuration.

The SIs for \bar{W}_{mz} are given in Fig. 4.8c. The width of the mixing zone is mainly controlled by the dispersive flux. This is why, α_L^M is the main parameter affecting \bar{W}_{mz} . As expected,

increasing variation of \overline{W}_{mz} against α_L^M can be observed in Fig. 4.9e. For Z_I (Fig. 4.8d), with a total SI of 0.58, d^F is the most important parameter. Fig. 4.9f shows that Z_I decreases with d^F , which is in agreement with the results of *Sebben et al. (2015)*. Variability of Z_I could be also affected by the uncertainty of K^F . The corresponding ME in Fig. 4.9g shows that Z_I increases with K^F . Fig. 4.8e depicts the SIs for the mass of salt persisting in the aquifer (M_s). It indicates that M_s is primarily sensitive to d^F (SI=0.62). It is also sensitive to K^F . ME (Fig. 4.9h) shows that M_s decreases with d^F , which is also consistent with the results *Sebben et al. (2015)*. M_s increases with K^F (Fig. 4.9i). This behavior is related to fact that the increase of K^F enhances the inland extent of the saltwater wedge, as explained in the previous section. Finally, the SIs for Q_s^{total} shows that this output is mainly affected by d^F (Fig. 4.8f). As show in Fig. 4.9j (Q_s^{total}) increases with d^F . In general, the SIs show that the uncertainty associated with α_L^F has no effect on the SWI metrics, which is logical, as salt transport in the fracture is dominated by the advection processes.

4.5.2. The network of orthogonal fractures configuration (NOF)

In this configuration, our goal is to investigate the effect of uncertainty related to the fractures density on the model outputs. Thus, we keep the same uncertain parameters as for the SHF configuration but we replace (d^F) by (δ^F). The latter is considered here as the parameter representing the fracture density. The values of the deterministic parameters and the range of variability of the uncertain inputs are given in Table 4.3. The lowest value of δ^F corresponds to a network with 13 horizontal and 26 vertical fractures. These values are used to obtain the results in affordable CPU time, as denser fractured configurations would require a large number of simulations to construct the PCE and the COMSOL model in this case becomes very CPU time consuming. We should mention that, for this configuration, we reduce the hydraulic conductivity of the fractures. If the same values would have been used as in SHF configuration, freshwater flow would have been so intensive that no SWI would occur.

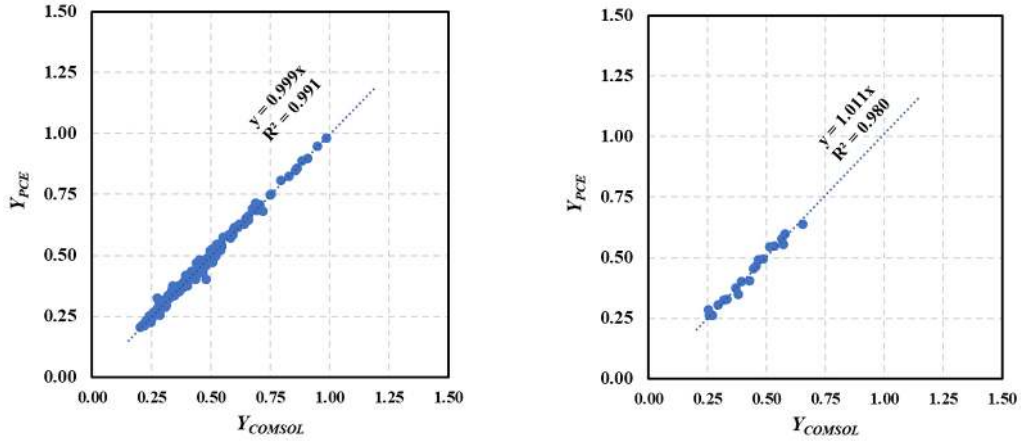
- PCE construction: Numerical details, orders and accuracy

The NOF configuration is more sensitive to the fractures characteristics than SHF configuration. The number of samples is progressively increased until obtaining accurate PCEs. The corresponding experimental design involves 200 samples. The mesh sensitivity analysis for the most challenging cases (the smallest value of δ^F) reveals that mesh-independent

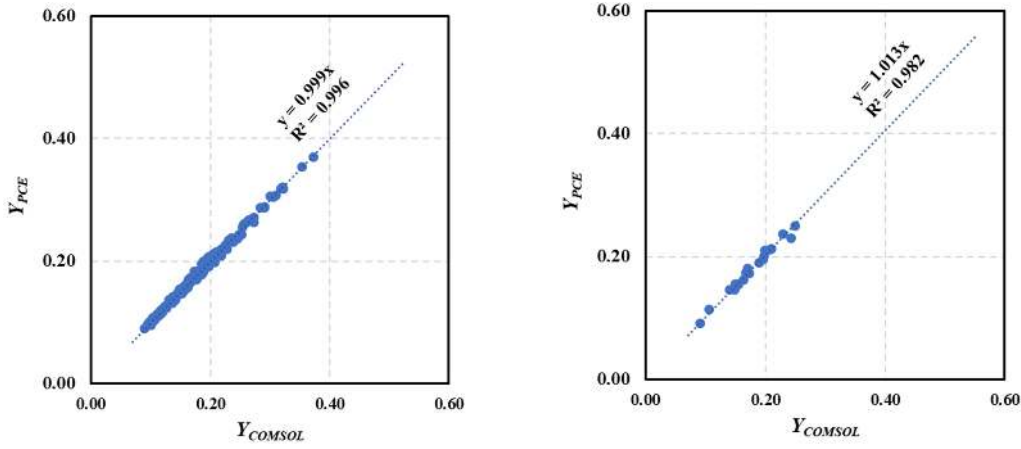
solution can be obtained using a grid of 70,000 elements. As for the SHF configuration, sparse and total PCE are calculated. With 200 samples, order 4 total PCE can be obtained. The optimal number of samples is 126. With the sparse technique, sixth order polynomial is reached for L_{oe} , M_s , Z_I and Q_s^{total} . For L_s and \bar{W}_{mz} orders 4 and 8 are achieved, respectively. Fig. 4.10 shows some comparisons between the sparse PCE surrogate and COMSOL models and highlights the accuracy of the PCE expansions. A good matching is observed both for the input parameters of the experimental design and for new samples. It is relevant to emphasize that this level of accuracy is acceptable to obtain good GSA results with the SIs evaluated using the surrogate model.

- Uncertainty propagation and marginal effects

The distribution of the mean concentration based on the PCE expansion is given in Fig. 4.11a. The mean PCE isochlors emulate the ones obtained using the physical model (Fig. 4.12). They present some discontinuous points where saltwater is pushed toward the sea due to high permeability in the fractures. The spatial map of the concentration variance is plotted in Fig. 4.11b. Compared to the SHF configuration, the zone of significant variance is contracted and concentrated toward the bottom surface of the aquifer near the low mean isochlors. The map of the total SIs of α_L^M (Fig. 4.11c) is quite similar to the one in the SHF configuration but it echoes the presence and influence of fracture network. Fig. 4.11c shows that the zone of influence of α_L^M falls where the concentration variance is negligible. Thus, α_L^M is not an important parameter for salinity distribution. Sensitivity to K^F and e^F are both important (Fig. 4.11d and e). The zone of influence of K^F is discontinuous and mainly located toward the sea boundary in at the bottom of the aquifer. Important values can be observed landward (see Fig. 4.11d) but these values do not express high sensitivity as the concentration variance is negligible in this zone. The sensitivity to the fractures density (δ^F) is given in Fig. 4.11f. This figure shows that uncertainty associated δ^F can mainly affect the salinity distribution within the mixing zone toward the bottom surface. It confirms that δ^F is an influential parameter. Finally, and in contrast to the SHF configuration, α_L^F appears to be an important parameter in the NOF configuration (Fig. 4.11g). It affects mainly salinity distribution around the low isochlors.



a) The length of the saltwater toe (L_{toe})



b) The dimensionless mass of salt persisting in the aquifer (M_s).

Fig. 4.10. Comparison between the PCE surrogate and physical (COMSOL) models for the NOF configuration: On the left side, 200 samples used for the experimental design and on the right side, 20 simulations which do not coincide with the experimental design.

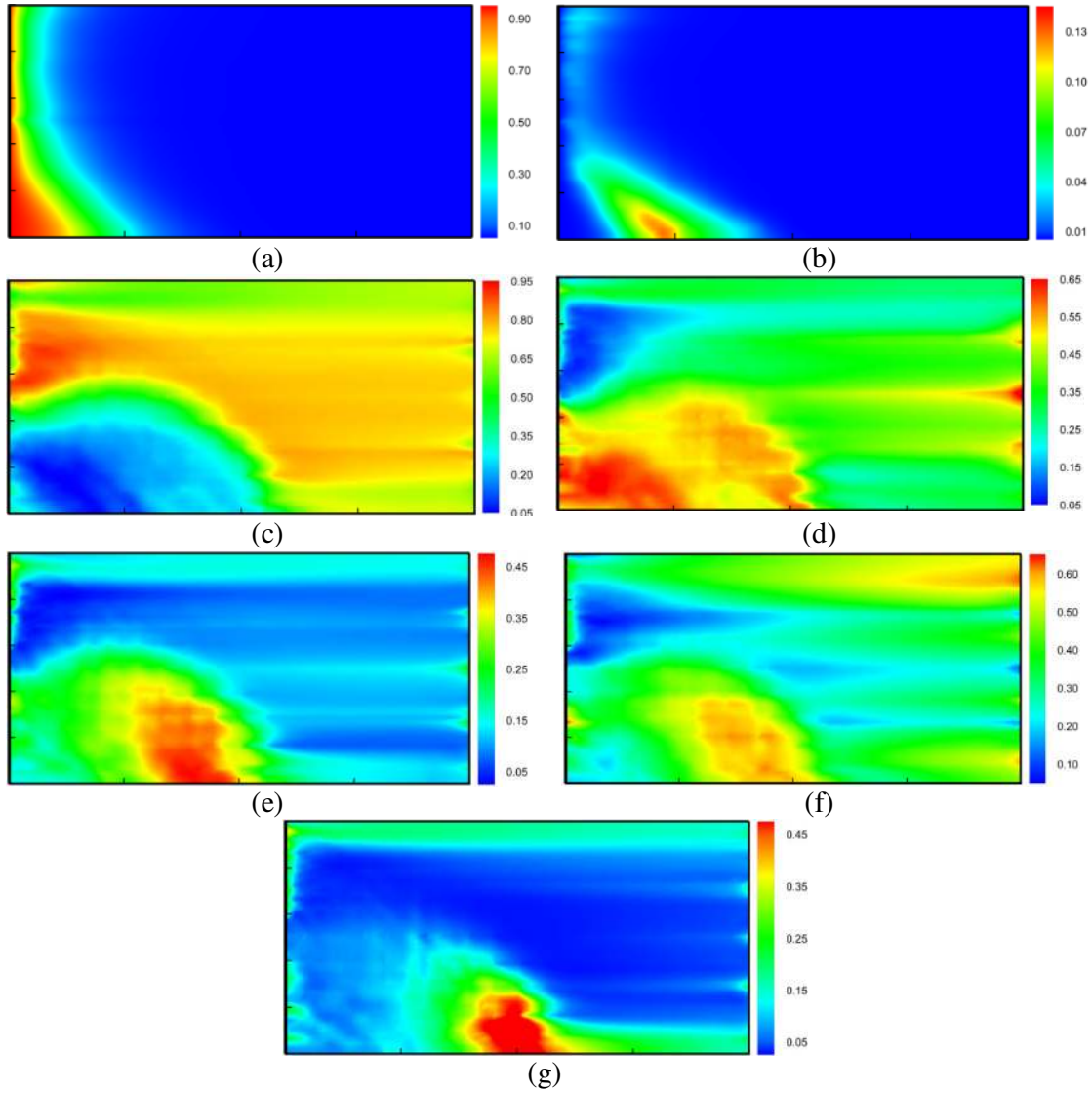


Fig. 4.11. GSA results for the spatial distribution of the salt concentration (NOF configuration): (a) mean salt concentration (b) variance of the salt concentration, (c) total SI of α_L^M , (d) total SI of K^F , (e) total SI of e^F , (f) total SI index of δ^F and (g) total SI index of α_L^F

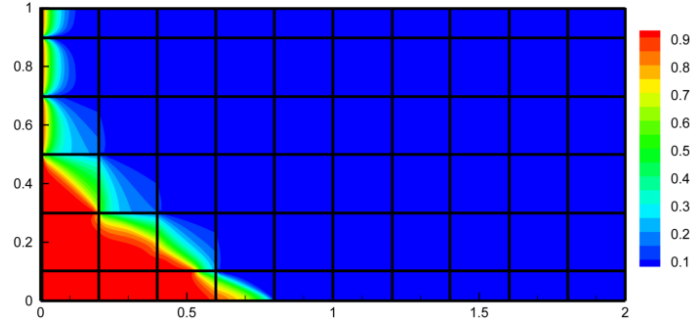


Fig. 4.12. Isochlors distribution for the NOF configuration ($\alpha_L^M = \alpha_L^F = 0.05m$;

$K^F = 0.07m/s$; $e^F = 0.1mm$; $\delta^F = 0.2m$, others parameters are the same as Table 4.3).

The bar-plots in Fig. 4.13 depict the total and first-order SIs for the SWI metrics to the uncertain parameters and Fig. 4.14 gives the MEs of these parameters. In general Fig. 4.14 confirms the results of the SIs as large variations of SWI metrics can be observed with respect to the uncertain parameters. Fig. 4.13a demonstrates that L_{toe} is mainly controlled by K^F and δ^F . The corresponding total SIs are $S_{K^F}^T = 0.52$ and $S_{\delta^F}^T = 0.32$, respectively. Fig. 4.14a shows an increasing variation of L_{toe} against K^F . As for the SHF configuration, this is related to the fact that the increase of K^F concentrates the freshwater flow in the fractures and entails a weaker freshwater flow in the matrix. As consequence, the saltwater wedge expands landward and L_{toe} increases. This behavior can be understood also using the equivalent porous media model which is based on a bulk hydraulic conductivity. As given in *Sebben et al. (2015)*, the bulk equivalent conductivity (K^{eq}) for a network of orthogonal fractures is given by:

$$K^{eq} = \left[\left(K^M + \frac{K^F e^F}{\delta^F} \right)^{-1} + \frac{e^F}{K^F \delta^F} \right]^{-1} \quad (4.20)$$

Eq. (4.20) shows that K^{eq} increases with the increase of K^F . The equivalent gravity number, which compares the buoyancy forces to the inland freshwater flux, is given by (*Fahs et al. 2018*):

$$Ng^{eq} = \frac{K^{eq} . H . (\rho_1 - \rho_0)}{\rho_0 q_d} \quad (4.21)$$

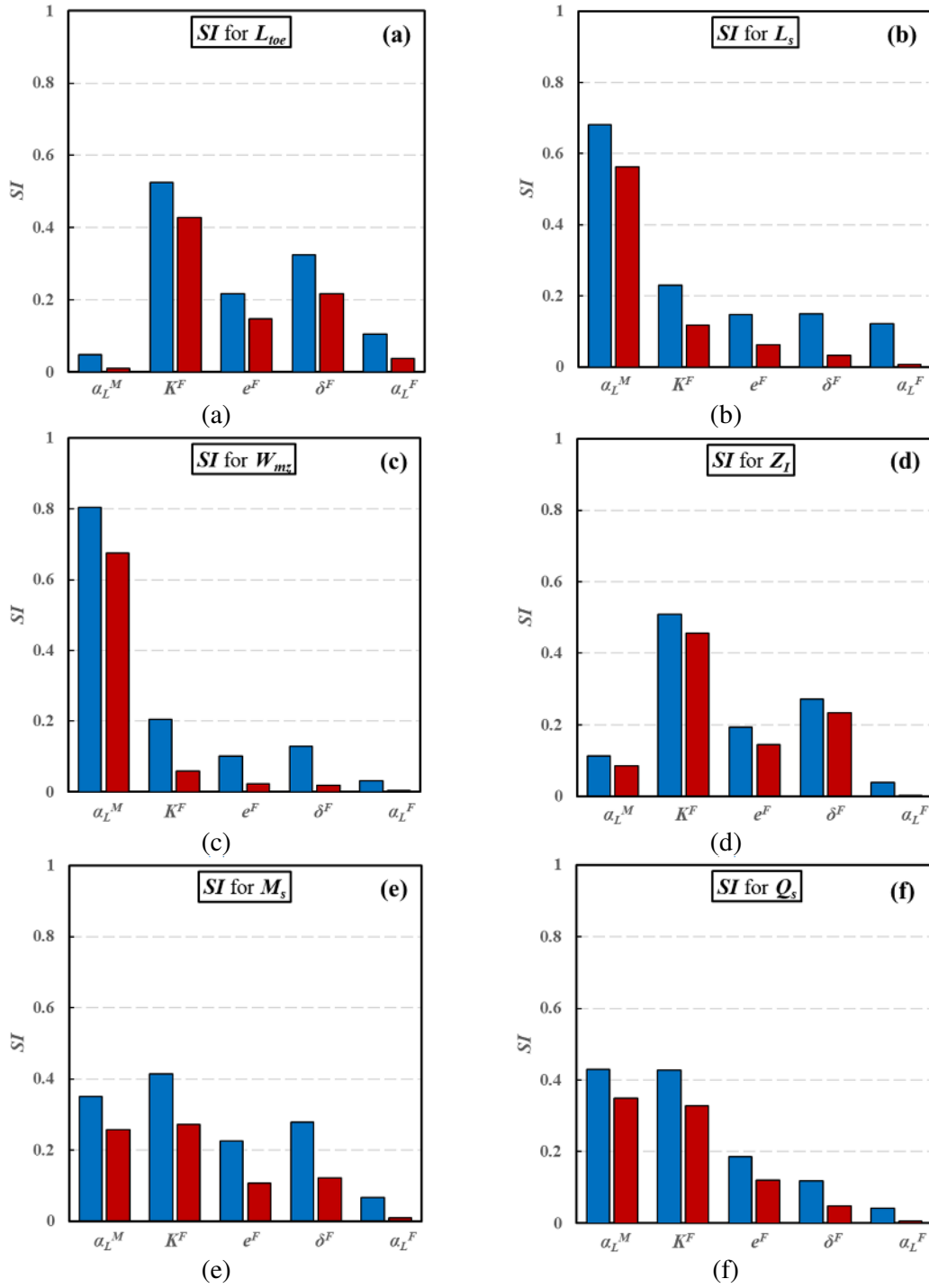


Fig. 4.13. Total (blue) and first order (red) SIs for the NOF configuration: (a) L_{toe} , (b) L_s , (c)

\overline{W}_{mz} , (d) Z_I , (e) M_s and (f) Q_s^{total} .

The increase of K^{eq} leads to the increase of Ng^{eq} . This latter can be interpreted, at constant densities and hydraulic conductivity, as a decrease in the inland freshwater that opposes SWI. This enhances the extend of SWI and leads to the increase of L_{toe} .

Fig. 4.14b shows that L_{toe} decreases with δ^F . In fact, the increase of δ^F corresponds to the reduction of the fracture density. This enhances the freshwater flow in the porous matrix and pushes the saltwater wedge toward the sea. The equivalent bulk hydraulic conductivity model can be also useful in explaining this variation, by reasoning in the same way as for the variation of L_{toe} against K^F . As it is clear from Eq. (4.20), the increase of δ^F (for the average value of K^M, K^F and e^F) corresponds to a decrease in K^{eq} and the related equivalent gravity number. This can be interpreted as an increase of the freshwater flux that lowers the extent of SWI and decreases L_{toe} .

The bar-plots in Figs. 4.13b and 4.13c indicate that, as for the SHF configuration, α_L^M is the most important parameter affecting L_S and \overline{W}_{mz} . The corresponding SIs are calculated to be 0.68 and 0.34, respectively. Figs. 14c and 14d display increasing variation of L_S and \overline{W}_{mz} against α_L^M . This makes sense as L_S and \overline{W}_{mz} are mainly related to the mixing processes which are controlled by α_L^M . Fig. 4.13d shows that, with $S_{K^F}^T = 0.50$ and $S_{\delta^F}^T = 0.27$, K^F and δ^F are the most important parameters affecting Z_I . MEs in Figs. 14e and 14f indicate that Z_I increases with K^F and decreases with δ^F . The reason behind these variations is the enhancement (resp. reduction) in the saltwater wedge extent associated with the variation of K^F (resp. δ^F), explained previously. These results related to the variation of Z_I against δ^F are found to be in agreement with those in *Sebben et al. (2015)*.

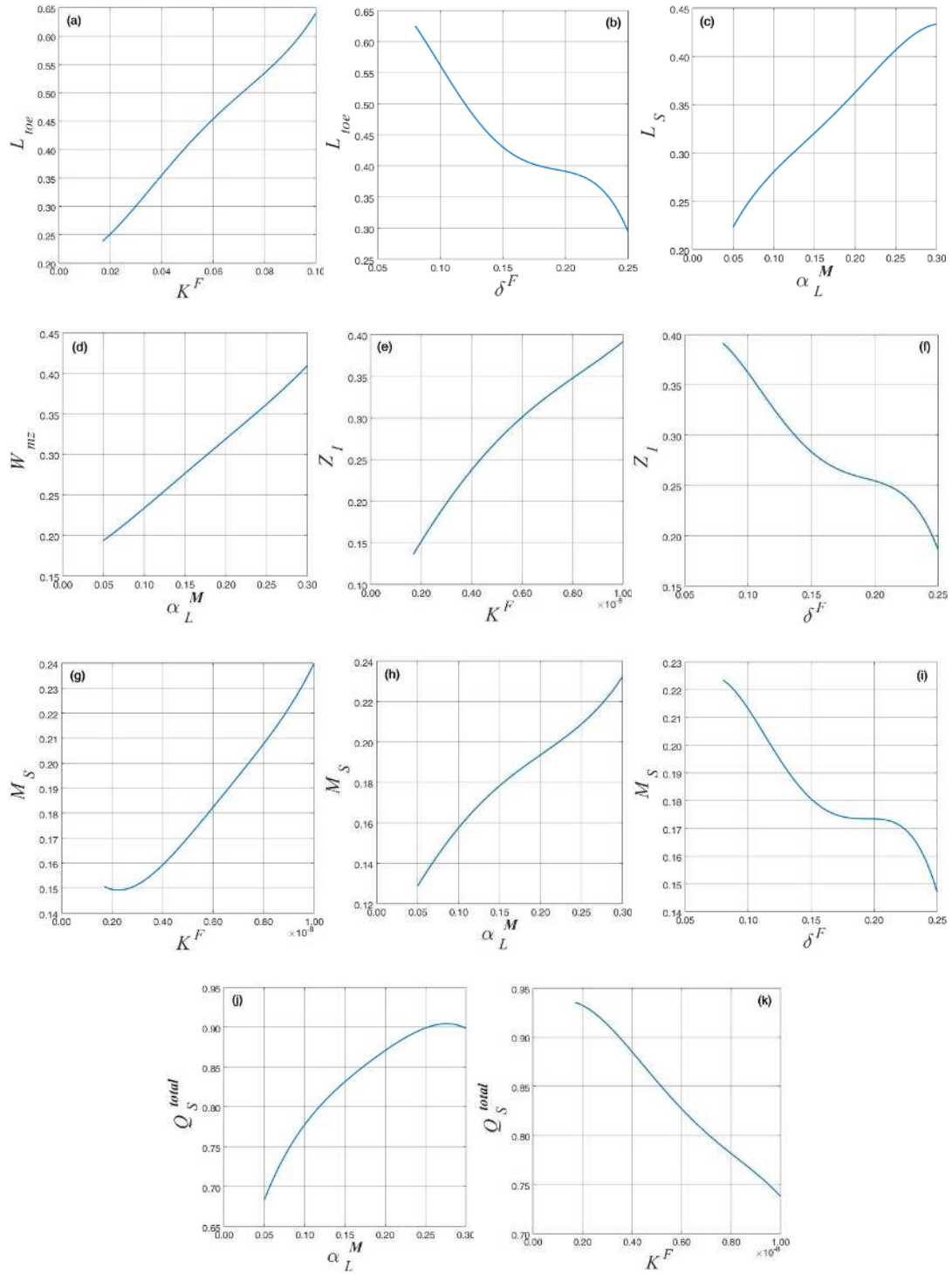


Fig. 4.14. The marginal effects of uncertain parameters on SWI metrics for the NOF configuration.

The dimensionless mass of salt persisting in the aquifer (M_s) appears to be sensitive to all uncertain parameters, except α_L^F (Fig. 4.13e). The total SIs with respect α_L^M , K^F , e^F , δ^F are calculated to be 0.34, 0.41, 0.22 and 0.27, respectively. The MEs show that M_s decreases with δ^F and increases with K^F and α_L^M (Figs. 14g-i). The variation against δ^F and K^F is related to the behavior of the saltwater wedge when these parameters change (see above). The increase of α_L^M pushes the saltwater wedge landward (Fahs *et al.*, 2018) and increases the area of the salted zone as well as the mass of salt persisting in the aquifer. The total flux of saltwater entering the aquifer (Q_s^{total}) is mainly affected by α_L^M , K^F (Fig. 4.13f). The total SIs of these parameters are calculated to be 0.43 and 0.42, respectively. The MEs (Figs. 4.14j and 4.14k) show that Q_s^{total} increases with α_L^M and decreases with K^F . Indeed, Q_s^{total} is advective and dispersive saltwater flux at the sea boundary. The dispersive flux is proportional to α_L^M . This explains why Q_s^{total} increases with α_L^M . The increase of K^F corresponds to the decrease of the gravity number (see above). A lower gravity number indicates less significant effect of the buoyancy forces for which the saltwater velocity decreases and reduces the advective saltwater flux. Finally, it is worth noting that, for the NOF configuration, the SIs for α_L^F are more important than for the SHF configuration. α_L^F appears to be an important parameter, especially for L_{toe} and L_s . In general, physical consistency of the results for both SHF and NOF configuration provides insight on the validity of our analysis based on the PCE as a meta-model.

4.6. Conclusion

In this work, the DFMM model is coupled with the VDF model to simulate SWI in FCAs. The DFMM-VDF model requires the discontinuous description of the fracture characteristics which are usually uncertain. Thus, it is essential, for several practical and theoretical purposes, to understand/quantify how the uncertainties associated with the imperfect knowledge of the fracture characteristics can propagate through the model and introduce uncertainties into the model outputs. Despite the high performance of computer codes for SWI models, run-time of these codes is still high because of the high nonlinearity, dense grids required for fractures and large space and time scales associated with studied domains. Thus the traditional techniques for uncertainty analysis (i.e. Monte-Carlo simulations) cannot be easily applied in this context, as they require a large number of simulations to achieve reliable results. To meet the

computational challenges of traditional techniques, we develop in this work a GSA based on the non-intrusive PCE. In particular, we apply an efficient sparse technique to construct the PCE with a reduced number of model evaluations, based on Kashyap information criterion. In the literature, GSA has been recently applied to SWI but previous studies are limited to homogeneous domain. Two configurations of the fractured Henry Problem, dealing with a single horizontal fracture (SHF) and a network of orthogonal fractures (NOF), are considered as conceptual models. The simulations required to construct the PCE are performed using a finite element model developed in the framework of COMSOL software. Boussinesq approximation is implemented to improve the computational efficiency of the COMSOL model. From technical point of view, this work shows several novelties that are important for the simulation of SWI. It shows the ability of COMSOL to accurately simulate SWI in simple and fractured aquifers. It also proves that the dimension reduction of fractures in the frame of the DFMM model is a valid approach to simulate SWI in FCAs and confirms the validity of the Boussinesq approximation in such a case. Regarding uncertainty analysis, this study presents an efficient (low cost) methodology to understand uncertainty propagation into SWI models. This methodology is generic and can be efficiently applied to real field investigations. In hydrogeological applications, GSA is often applied to investigate uncertainty propagation associated with hydrogeological parameters. This work shows that GSA is generic and can be a valuable tool for different kinds of uncertainties. The GSA results showed that, for the SHF configuration, the uncertainty associated with the fracture hydraulic conductivity and depth is the first sources of uncertainty on the salinity distribution. The spatial distributions of the SIs are given as maps. This represents an important feature of this study as these maps are not only important for uncertainty analysis but also provide relevant locations for measurement required for aquifer characterization. Fracture hydraulic conductivity and depth are also important parameters for the toe position (L_{toe}), thickness of the freshwater discharge zone (Z_I), the mass of salt persisting in the aquifer (M_s) and the flux of saltwater entering the aquifer (Q_s^{total}). The thickness of the saltwater wedge and the width of the mixing zone are mainly controlled by the dispersion coefficient in the matrix. The uncertainty related to the fracture aperture has a slight impact on the SWI metrics. Its major effect is observed on L_{toe} . Uncertainty associated with the fracture dispersion coefficient does not affect in any way the SWI metrics. For the NOF configuration, the imperfect knowledge of fracture hydraulic conductivity and density are the first source of uncertainty of the salinity distribution. However,

it is observed that all the uncertain parameters become important for the salinity distribution, in this case. In contrast to the SHF configuration, in which the dispersion in the fracture is not important, in the NOF configuration the salinity distribution at the aquifer top surface is influenced by this fracture dispersivity. L_{toe} and Z_I are mainly controlled by the fractures density and hydraulic conductivity. As for the SHF configuration, the width of the mixing zone is mainly affected by uncertainty associated with the dispersion coefficient in the matrix. L_s is also majorly affected by the dispersion coefficient in the matrix, but the other uncertain parameters are also influencing it. All the uncertain parameters have distributed effects on M_s and Q_s^{total} .

This work has been the subject of an article published in the Journal of Hydrology in January 2019. (Koohbor *et al.*, 2019). <https://doi.org/10.1016/j.jhydrol.2019.01.052>

4.7. Field case study: Application to Clashnessie Bay, UK

The developed strategy for GSA based on PCE has been applied to a hypothetical two-dimensional case. In order to reflect the actual capabilities of this technique and to investigate the field application of this method, we are interested to apply the developed methodology on a field case study. The field chosen for this application is in Clashnessie Bay, Scotland, UK (see Fig. 4.15). This project is in collaboration with Dr. Jean-Christophe Comte and Dr. Andrés González Quirós from the School of Geosciences, University of Aberdeen, Aberdeen, UK. The main idea behind this project is to evaluate how geophysical field measurement data (i.e. Electrical Resistivity Tomography), simulation and global sensitivity analysis can be coupled together to develop a reliable model for SWI in fractured coastal aquifers at real scale. The contribution of this thesis is in the development of the forward model.



Fig. 4.15. The location of Clashnessie coastal aquifer (image taken from Google Earth)

The chosen field, simply referred to as Clashnessie aquifer from this point forward, is a fractured basement-rock coastal aquifer mainly composed of gneiss from the Lewisian complex, aged Precambrian, intersected by a densely fractured regional fault zone. The domain and the considered boundary conditions for the GSA and parameter estimation is seen in Fig. 4.16a in plan-view (blue rectangle) and in three-dimensional view in Fig. 4.16b. Electrical Resistivity Tomography (ERT) cross-sections have been generated by inversion of the field measurements acquired in 2019 for two lines parallel to the coastline (see lines A-A' and B-B' in Fig. 4.16a) and for one line along the fault zone (line C-C' in Fig.4.16a) (University of Aberdeen unpublished data, 2019). The ERT profiles of each line can be seen in Fig. 4.17.

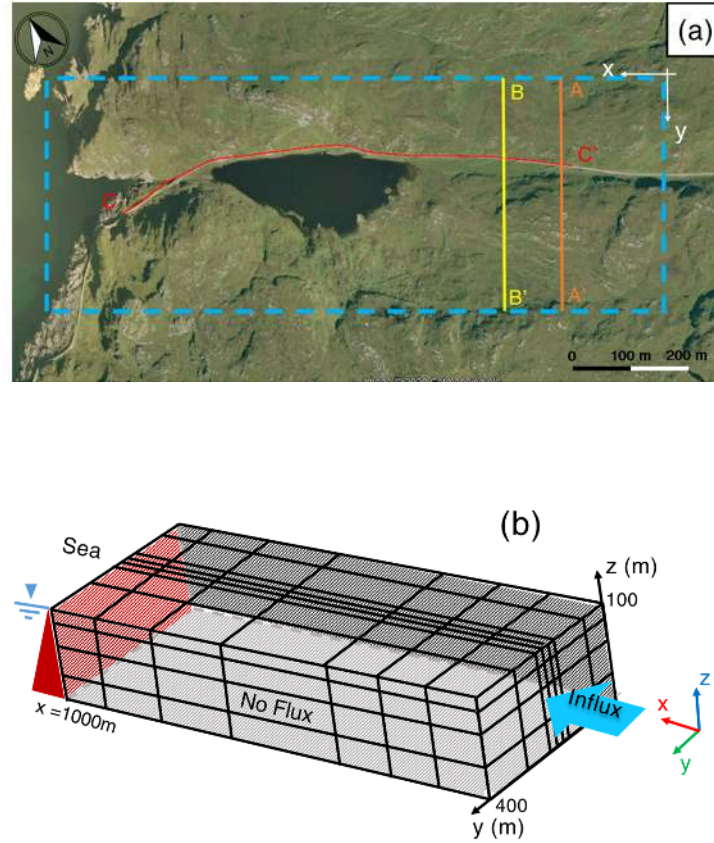


Fig. 4.16. Representation of the (a) domain boundaries in plan-view (image is from Google Earth) and (b) the schematic 3D representation of the problem domain

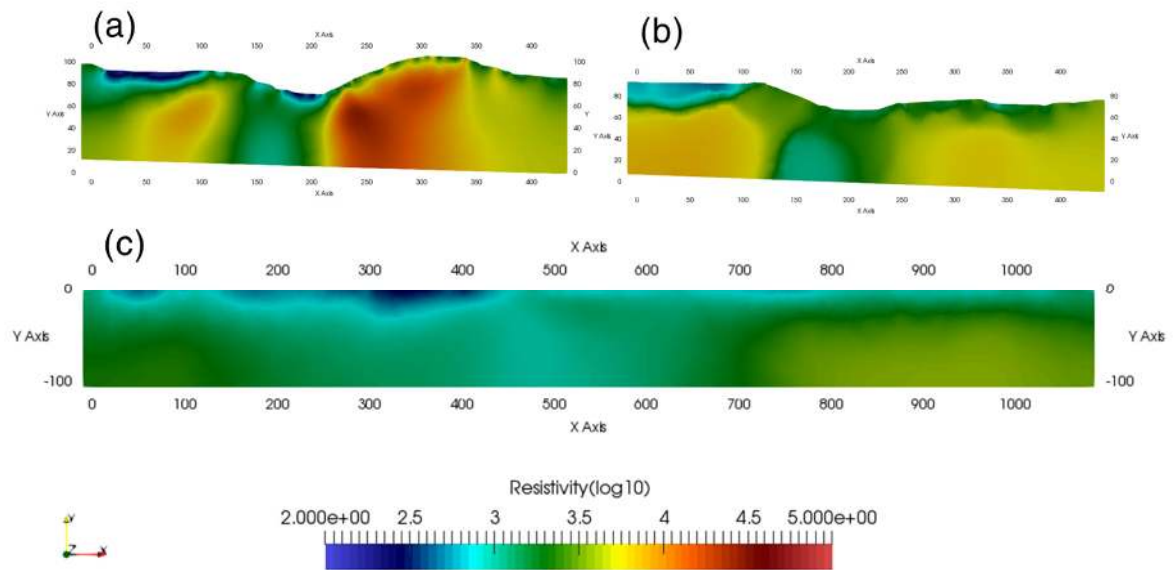


Fig. 4.17. ERT maps for: (a) A-A' line, (b) for B-B' line and (c) for C-C' line (University of Aberdeen, unpublished data, 2019)

Petrophysical relationships (e.g. Archie's law and Waxman-Smith saturation method) are used to obtain an approximation of the bulk porosity of the rocks based on the ERT maps (*Comte et al., 2019; Mezquita Gonzalez and Comte, 2019*). The bulk porosity is then used to give insights about the fracture density and aperture in each region of the investigated domain. Waxman-Smith saturation method is proposed by *Waxman and Smith (1968)* as followed:

$$S_w^n + R_w B Q_v S_w^{n-1} - \frac{\Phi^{-m} R_w}{R_t} = 0 \quad (4.22)$$

Where fractional $S_w [-]$ is water saturation, $\Phi [-]$ is fractional porosity, $n [-]$ and $m [-]$ are saturation and cementation exponents respectively, $R_w [ohm-m]$ is formation water resistivity, $R_t [ohm-m]$ is formation resistivity, $Q_v [meq.ml^{-1}]$ is cation exchange capacity per unit pore volume and $B [ml.meq^{-1}.ohm^{-1}.m^{-1}]$ is the equivalent conductance of the clay counter-ions. Considering that the water-table is close to the ground level in the area of study and the domain is considered saturated ($S_w = 1$) and Eq. (4.22) is then simplified to:

$$R_t = \frac{\Phi^{-m}}{\sigma_w + B Q_v} \quad (4.23)$$

Where $\sigma_w = \frac{1}{R_w} [S.m^{-1}]$ is the water conductivity. Applying logarithm to both sides of Eq. (4.23) and simplifying the equation to have porosity as the main dependent variable we have:

$$\Phi = 10^{\frac{-1}{m}(\log(R_t) + \log(B Q_v))} \quad (4.24)$$

And:

$$Q_v = (CEC) \left(\frac{1-\Phi}{\Phi} \right) d_{rock} \quad (4.25)$$

Where $CEC [meq.gr^{-1}]$ is the cation exchange capacity and $d_{rock} [gr.ml^{-1}]$ is the density of the rock. Bulk porosity of the formation in each region is estimated using Eqs. (4.24) and (4.25) and the values of m , B , CEC and σ_w from the field measurements. The obtained range of values for the bulk porosity are then used to construct a simplified DFMM model with orthogonal fractures to simulate SWI in Clashnessie aquifer. The SWI simulations, performed with COMSOL Multiphysics®, will serve as the input data to construct the PCE surrogate model. The main process of the GSA resembles the idea and the process in *Koohbor et al. (2019)*. This project is ongoing and still in its early phases at this time, the final results are not

obtained. Figs. 4.18 and 4.19 show respectively the fracture network orientation along with the meshing grid and the result of one of the COMSOL simulations only for schematic representation and clarification of the process.

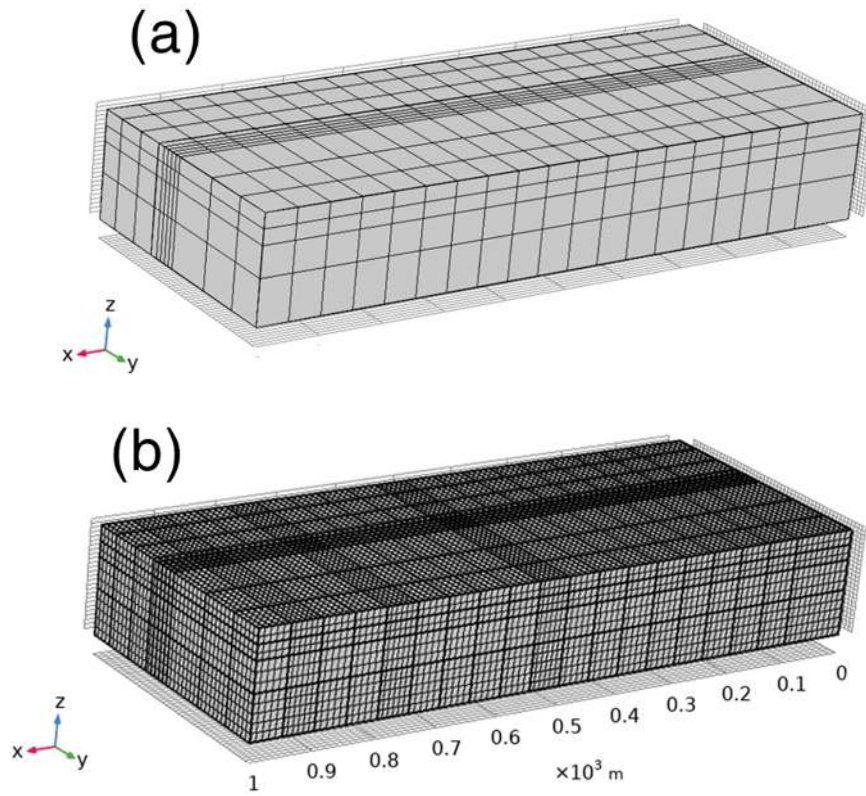


Fig. 4.18. Representation of the: (a) domain and the fracture network orientation and (b) the meshing grid (i.e. approximately 50K hexahedral elements)

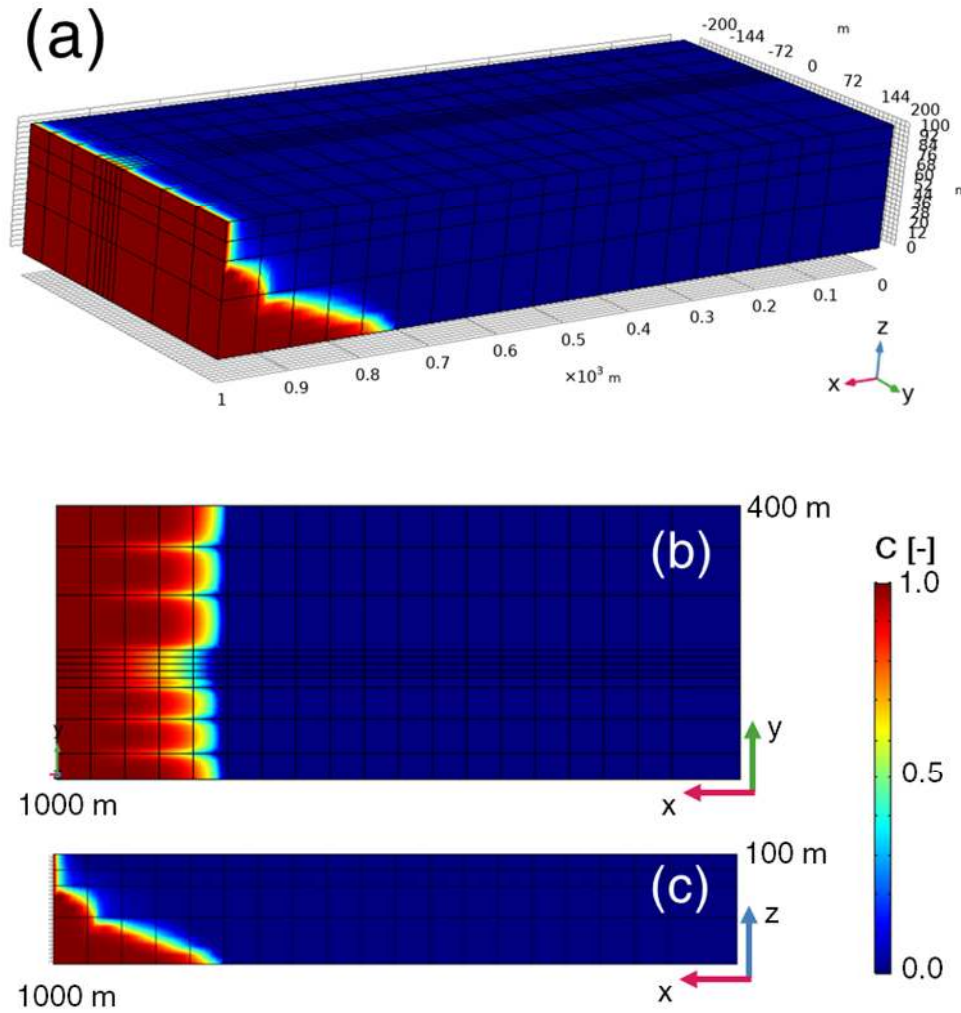


Fig. 4.19. Distribution of salt in an arbitrary case in the domain: (a) 3D-view, (b) x-y (i.e. plan) view at $z=0$ m and (c) x-z (i.e. profile) view at $y=400$ m

Chapter V: An advanced discrete fracture model for variably saturated flow in fractured porous media

5.1. Introduction

Understanding variably saturated flow (VSF) in fractured porous media has great significance to many environmental and geotechnical applications, such as groundwater recharge in karst aquifers, (*Mudarra and Andreo, 2011; de Rooij et al., 2013 de Rooij, 2019*), epikarst (*Chang et al. 2019*) and unconfined chalk aquifers (*Ireson et al, 2009*). VSF in fractured zones has been studied for geological disposal of nuclear waste such as the one at Yucca Mountain in the United States, where an unsaturated zone was assessed to serve as a potential site for the deposition of high-level nuclear wastes (*Hayden et al., 2012; Ye et al., 2007*). Other applications include contaminant transport and infiltration of landfill leachate (*Brouyère, 2006; Ben Abdelghani et al., 2015*), infiltration through unsaturated saprock in hillslopes with shallow fractured shale bedrock (*Guo et al., 2019*), unsaturated flow and contaminant transport in saprolite (*Van der Hoven et al., 2003; Alazard et al., 2016*), water flow in cracked soils and stability of soil slopes with cracks (*Pouya et al., 2013; Wang et al., 2019; Yang and Liu, 2020*), seepage through fissured dams (*Jiang et al., 2014*), tunnel excavation (*Gokdemir et al., 2019*) and protection of structure foundations in contact with water (*Zhao et al. 2019*), among others.

Fractures in the vadose zone typically provide preferential flow pathways. However, they could also act as flow barriers from capillary forces, depending on the degree of saturation (*Cey et al., 2006; Wang and Narasimhan, 1985*). The VSF in fractured porous media involves several coupled and complex processes such as capillary and gravity-driven transient flows, preferential flow in fractures, and fracture-matrix interactions from imbibition and diffusion (*Hoteit, 2013*). Due to these complexities, and despite the broad range of applications, the processes of VSF in fractured porous media are not well-understood. Related experimental studies are scarce and limited to simplified fracture configurations. For instance, *Yang et al. (2019)* presented an experimental study to investigate VSF through a simple T-shaped fracture intersection. *Wang et al. (2017)* investigated the effect of fracture aperture on capillary pressure-saturation relation. *Kordilla et al. (2017)* studied the effect of droplet and rivulet unsaturated flow modes at simple intersecting fractures. Based on experiments, *Tokunaga and Wan (2001)* introduced a new mechanism of VSF in a single fractured domain, named as

“surface-zone flow”, which can appear when the permeability of skin fractures is significantly higher than that of the porous matrix.

Most of the studies related to VSF in fractured domains rely on numerical simulations, which are used for several theoretical and practical purposes. For instance, understanding physical processes (*Liu et al., 2002, 2004*), field studies (*Zhou et al., 2006; Ye et al., 2007; Masciopinto and Caputo, 2011; Kordilla et al., 2012; Ben Abdelghani et al., 2015; Robineau et al., 2018*) and validation of laboratory experiments (*Roels et al., 2003; Malenica et al., 2018*). In applied studies, numerical simulations are considered as an irreplaceable and cost-effective tool for designing, predicting, and uncertainty assessments. Unsaturated flow in porous media is usually described using the Richards’ equation (RE) that combines Darcy’s law and continuity equation which are coupled via constitutive relations expressing permeability and water content as a function of the hydraulic head (*Farthing and Ogden, 2017*). RE is a simplification of the two-phase (water-air) flow model assuming that air remains essentially at atmospheric pressure. This approximation is valid when the effect of air on water flow is negligible (*Szymkiewicz, 2013*). The models used to treat the fractures can be classified into two main categories: the equivalent continuum model (ECM) and the discrete fracture-matrix (DFM) model. With the ECM, the fractured domain is represented by a homogenous porous media with equivalent hydraulic parameters. In this case, RE is used with a specific permeability constitutive relation and retention curve including the effect of fractures. The main drawback of ECM is related to the development of effective retention and permeability curves in the presence of fractures (*Guarracino and Quintana, 2009; Monachesi and Guarracino, 2011; Pouya et al., 2013*). The dual-porosity model, which can be seen as an extension of the ECM, treats the fractured domains as dual interactive continua representing fractures and porous matrix, respectively (*Brouyère, 2006; Kuráží, 2010*). Different hydraulic properties are associated to each continuum. Flow cannot occur in the matrix continuum, which only acts as a source/sink term, while the fracture continuum provides the flow connectivity despite its low storage capacity (*Fahs et al., 2014*). On the other hand, the dual-permeability model is more used than dual-porosity for VSF in fractured domains as it allows for moisture flow in both the fracture and matrix continua (*Kordilla et al., 2012; Robineau et al., 2018*). The dual permeability model requires two sets of constitutive relations for the fracture and matrix domains. Unlike ECM and dual continua models, the DFM model is based on an explicit description of fractures. With DFM model, the hydraulic properties of fractures and their topology are considered explicitly, where the matrix and the fractures are modeled as separate

elements of one continuum. For DFM model, RE is often utilized to simulate flow in both fractures and matrix, but with different constitutive relations and properties for each medium. Examples of utilization of the DFM model for VSF can be found in *Therrien and Sudicky (1996)*, *Masciopinto and Caputo (2011)*, *Ben Abdelghani et al. (2015)*, *Li and Li (2019)* and *Li et al. (2020)*.

ECM provides efficient simulations with relatively low computational costs and complexity. It is relatively simple and straightforward to implement, which is commonly used in real field applications (*Liu et al., 2005*). However, the accuracy of this model is highly dependent on the validity of the equivalent retention curves and constitutive relations in representing the matrix and the fractures (*Liu et al., 2005*). ECM is not suitable for small scale applications or for cases involving a small number of fractures (*Roels et al., 2003*). Further, this method cannot provide a detailed description of the flow dynamics in fractures and fails to reproduce the preferential flow paths encountered in fractured vadose zones (*Liu et al., 2005, 2007*). In many applications, DFM model is more suitable to simulate preferential flow, as fractures are captured in more detail. This model is essential to understand water flow processes in fractures at a small scale (*Cey et al., 2006*). It is also applied at the field scale with a small number of well-defined fractures (*Hirthe and Graf, 2015; Ben Abdelghani et al., 2015*). However, DFM model is computationally expensive and requires detailed information about the fractures. The inefficiency is related to the dense computational meshes and often causes poor convergence due to the high discontinuity between the hydraulic properties of fractures and matrix, particularly in the case of dense fracture networks (*Berre et al., 2019; Nordbotten et al., 2019*). A common approach that significantly alleviates the computational complexity of the DFM model is the hybrid-dimensional technique (*Therrien and Sudicky, 1996; Hoteit and Firoozabadi, 2008; Li et al., 2020*) in which the fractures are considered as co-dimensional interfaces with respect to the full-dimensional elements representing the matrix (i.e., one-dimensional fractures in the two-dimensional matrix elements).

With the continued advancement in new numerical methods and the recent progresses in powerful computational technologies, the DFM model has received an increasing interest due to its robustness in reproducing physical processes of flow and transport in fractured porous media. This results in extensive research on the development of appropriate numerical techniques and schemes that aims at improving the computational performance of the DFM model for saturated flow (*Ahmed et al., 2017; Berre et al., 2019; Nordbotten et al., 2019*). This

study focuses on the use of the DFM model for the simulation of unsaturated flow in vadose fractured zones.

Modeling VSF in explicitly fractured domains (i.e., with the DFM model) remains a computationally challenging task which usually exhibits numerical complexities (*Li and Li, 2019*). The challenges are not only due to the presence of dense fractures and the associated complex geometry, property discontinuities, quality of mesh discretization and poor convergence but also due to the inherent numerical complexities of the RE (*Li and Li, 2019*). It is well-known that the numerical solution of the RE, even in unfractured domains, is one of the most challenging problems in hydrogeology (*Miller et al., 2013*). Numerical difficulties are caused by the mathematical characteristics of this equation that could change from hyperbolic to parabolic, depending on the saturation. Alongside there is strong nonlinearity introduced by the constitutive relationships (*Suk and Park, 2019*). Slow/no-convergence, small time-steps, mass conservation, and numerical oscillations are common numerical issues that are usually encountered in the solutions of RE. Significant efforts have been made in last decades on the development of advanced and appropriate numerical techniques for solving this equation (*Celia et al., 1990; Farthing et al., 2003; Li et al., 2007; Ji et al., 2008; Fahs et al., 2009; Hassane Maina and Ackerer, 2017; Suk and Park, 2019; Ngo-Cong et al., 2020*). The most investigated problems are related to the selection of the primary variable (pressure head, water content or mixed form), mass conservative solution, time and spatial discretization schemes, nonlinear solvers and numerical evaluation of equivalent hydraulic conductivity (*Miller et al., 2013 and references therein*). More details about the numerical solution of RE can be found in recent review papers by Farthing and Ogden (2017) and Zha et al. (2019).

Unlike in unfractured media, numerical solutions of RE in explicitly fractured domains are not well-developed. Most of the existing tools are based on the standard finite element method for space discretization and backward Euler scheme for time integration (*Therrien and Sudick 1996*). These traditional methods may not be suitable to solve the RE equation under complex fractured configurations. This restricts the applicability of the existing models for engineering practice, especially at real scale. Hence, it is important to carry out further studies on the development of robust and efficient numerical techniques to solve the RE in explicitly fractured domains involving complex fracture networks, which is the main objective of this study. This is crucial to improve the capability of current models in developing more realistic simulations and to deal with the growing demand on predicting and understanding the dynamics of aquifers under non-stationary conditions, at large time and space scales. The objective of this study is

to develop a new numerical technique for VSF in fractured porous domains that is not only accurate but also efficient and fast, which is a fundamental challenge of computation water resources.

In this work, we couple advanced numerical techniques for space discretization and time integration to solve the RE in explicitly fractured domains. We consider the head-form of the RE. This form allows for efficient numerical solutions as the pressure-head is used as the only primary variable. However, this approach may lead to non-conservative solutions when it is solved with first-order time integration methods (*Celia et al., 1990; Farthing et al. 2003*). To avoid this problem and to obtain conservative solutions, we use high-order integration techniques, as it is discussed further in this section. Among different existing techniques for space discretization, we use the mixed hybrid finite element (MHFE) method (*Brezzi and Fortin, 1991; Farhloul and Fortin, 2002; Farhloul, 2020*). A review about the use of this method and its advantages (e.g., local mass conservation, ability to intrinsically treat anisotropic domains, consistent velocity field even in highly heterogeneous domains) in simulating groundwater flow can be found in *Younes et al., (2010)*. The MHFE method was initially used to simulate saturated flow in simple porous media (*Younes et al., 1999*). It has been then extended to VSF by *Farthing et al. (2003)*, *Fahs et al. (2009)* and *Belfort et al. (2009)*. As the method deals with the water fluxes and average pressures at the edges of the mesh elements, it is highly suitable for the DFM model with the hybrid-dimensional technique where fractures are defined on the edges of the matrix elements. The method has been extended to the simulation of flow in fractured porous media in *Hoteit and Firoozabadi (2008)*, *Zidane and Firoozabadi (2014, 2018)*, *Chen et al. (2016)*, *Moortgat et al. (2016)* and *Moortgat (2017)*. To our knowledge, the MHFE has been yet applied for VSF in fractured media. One of the objective of this work is to extend this method to VSF in explicitly fractured domains and to evaluate its performance in such an application. Combined with the MHFE, we introduce a new mass-lumping (ML) technique. As the nonlinearity of the RE imposes small time steps, most finite-element-based methods suffer from spurious oscillations related to the discretization of the transient accumulation term (*Hoteit et al., 2002, Elguedj et al., 2009; Scudeler et al., 2016*). This problem has been encountered with the MHFE in *Belfort et al. (2009)*. For RE, the problem of unphysical oscillations is particularly crucial as it leads to a loss of numerical stability that would affect the convergence of the nonlinear solver. *Younes et al. (2006)* developed an ML technique for the MHFE to eliminate unphysical oscillations. *Belfort et al. (2009)* extended the ML technique to VSF in unfractured domains. *Fučík (2019)*

applied the MHFE method to compositional two-phase flow in heterogeneous porous media and showed that ML technique is needed for handling material discontinuities. In this work, we develop an efficient approach to generalize the ML technique to VSF in fractured domains. Besides spatial discretization, selecting an efficient temporal scheme is crucial. Little attention has been devoted to the time integration of groundwater flow in fractured domains (*Moortgat et al., 2016*). This is also true for VSF with the DFM model. Existing numerical models are based on the first-order backward Euler scheme (*Therrien and Sudick 1996*). However, several works show the advantages of higher-order time integration schemes for the simulation of unsaturated flow. *Farthing et al. (2003)* showed that with a higher-order time integration scheme, conservative solutions could be obtained even with the non-conservative form of the RE. *Fahs et al. (2009)* proved that adaptive high order time integration schemes could lead to faster solutions than standard first-order methods. Here, we couple the MHFE and the ML technique to an adaptive high order time integration scheme via the method of lines (MOL) (*Matthews et al., 2004*). This approach permits using a sophisticated ordinary differential equation (ODE) solver for time integration (DLSODIS) that allows, besides high order adaptive time integration, an appropriate time-stepping management and efficient procedure to deal with nonlinearities.

5.2. Governing Equations of VSF in fractured domains

VSF in fractured and porous media is described by the RE, coupling the Darcy-Buckingham's law and the mass conservation equation, as shown below:

$$\mathbf{q}^\beta = -K^\beta (S_e^\beta(h^\beta)) \nabla H^\beta \quad (5.1)$$

$$(c^\beta(h^\beta) + S_s^\beta S_w^\beta(\theta^\beta)) \frac{\partial H^\beta}{\partial t} + \nabla \cdot \mathbf{q}^\beta = f^\beta \quad (5.2)$$

$$H^\beta = h^\beta + z \quad (5.3)$$

Where the superscript $\beta \in \{M, F\}$ is the medium index (M for matrix, and F for fracture), H^β [L] and h^β [L] are, respectively, the piezometric head and pressure head, and z [L] is the elevation. The list of variables and parameters associated with Eqs. (5.1) and (5.2) are provided in Table 5.1.

Table 5.1. Definition of parameters and variables associated with the VSF governing equations.

| Parameter | Definition | Dimension |
|---|----------------------------|-------------|
| K | hydraulic conductivity | $[LT^{-1}]$ |
| $S_e = \frac{\theta - \theta_r}{\theta_s - \theta_r}$ | effective saturation | $[-]$ |
| θ | water content | $[-]$ |
| θ_r | residual water content | $[-]$ |
| θ_s | saturated water content | $[-]$ |
| S_s | specific storage | $[L^{-1}]$ |
| $S_w = \frac{\theta}{\theta_s}$ | relative saturation | $[-]$ |
| $c(h) = \frac{d\theta}{dh}$ | specific moisture capacity | $[L^{-1}]$ |
| f | sink/source term | $[T^{-1}]$ |

We use the standard form of the *van Genuchten (1980)* model for the inter-relation of pressure head and water content, where different properties are considered for the matrix and fractures:

$$S_e^\beta = \frac{\theta^\beta - \theta_r^\beta}{\theta_s^\beta - \theta_r^\beta} = \begin{cases} \frac{1}{\left(1 + |\alpha^\beta h^\beta|^{n^\beta}\right)^{m^\beta}} & h^\beta < 0 \\ 1 & h^\beta \geq 0 \end{cases} \quad (5.4)$$

In the above equation, $\alpha^\beta [L^{-1}]$ and $n^\beta [-]$ are parameters related to the mean pore size and uniformity of mean size distribution of the matrix and fractures, and $m^\beta = 1 - 1/n^\beta$. For conductivity-saturation relationship, the van Genuchten-Mualem model (*Mualem, 1976*) is given by:

$$K^\beta = K_s^\beta \sqrt{(S_e^\beta)} \left(1 - \left(1 - (S_e^\beta)^{1/m^\beta} \right)^{m^\beta} \right)^2 \quad (5.5)$$

5.3. Numerical solution: MHFE method, ML technique, and MOL

We develop a new numerical scheme to solve the system of Eqs. (5.1)-(5.5) using 2D unstructured triangular meshes. The scheme can also be used with other mesh types. As mentioned in the introduction, the fractures are considered with the hybrid-dimensional technique as 1D interfaces of the 2D elements representing the matrix. This approach provides a significant reduction in the complexity of the computational mesh. However, the local density and complexity of the fracture network should be considered; as presented in *Berre et al. (2019)* the complex fracture network causes challenges to the generation of a conforming mesh.

The developed scheme couples the MHFE and ML technique for space discretization with an advanced ODE solver for time integration via the MOL. This method consists of discretizing the space derivatives while maintaining the time derivative in its continuous form. This discretization allows converting the system of partial differential equations into a system of ODEs, which is solved using a sophisticated solver. The main steps of the developed schemes are detailed here.

5.3.1. Trial functions of the MHFE method for the matrix and fractures

Since the matrix and fracture elements exhibit different dimensions, the governing equations are discretized separately, then coupled and solved simultaneously. In the matrix, based on the formulation of MHFE, the total flux across an edge of an element E , referred to as Q^E , is approximated as the following (*Chavent and Jaffré, 2014*) :

$$Q^E = \sum_{i=1}^{nf} Q_i^E \mathbf{w}_i^E \quad (5.6)$$

Where Q_i^E is the flux across edge “ i ” in element E , referred to as ∂E_i . This discretization technique applies to the matrix elements (Fig. 5.1a) and the fracture interfaces (Fig. 5.1b). For fracture edges, element E becomes ∂E , and the edges of the elements become the nodes of the fracture edge. We use the lowest order Raviart-Thomas space (*Raviart and Thomas, 1977*), for which nf is equal to 3 for triangles used for matrix elements, and 2 for the fracture edges.

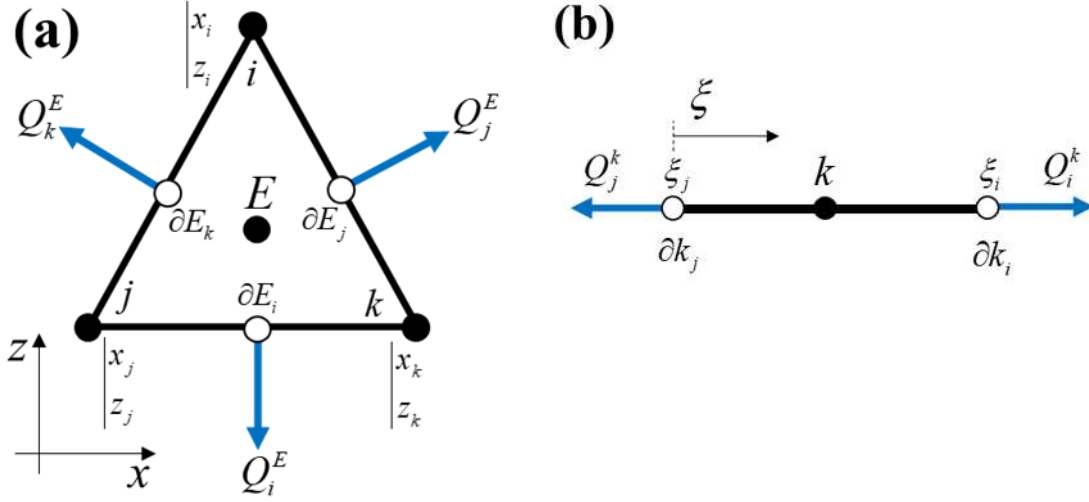


Fig. 5.1. Fluxes across the interfaces of a computational cell: (a) matrix element and (b) fracture edge.

The shape functions, W_i^E for the i^{th} edge of a matrix element (E), when using the lowest order Raviart-Thomas space are:

$$W_i^E = \frac{1}{2|E|} \begin{pmatrix} x - x_i^E \\ z - z_i^E \end{pmatrix}, \quad i = 1, 2, 3 \quad (5.7)$$

where $|E| [L^2]$ is the surface area of the matrix element, and $x_i^E [L]$ and $z_i^E [L]$ are, respectively, the horizontal and vertical coordinates of the opposite node to ∂E_i . The shape functions for the fracture edges are:

$$W_i^k = \frac{1}{\ell} (\xi - \xi_i) \quad i = 1, 2 \quad (5.8)$$

where $\ell [L]$ is the length of the fracture edge and $\xi_i [L]$ is the local coordinates of the opposite element node.

5.3.2. Flux discretization in the matrix elements (MHFE method and ML technique)

Applying the MHFE discretization to Eq. (5.1), using the flux expression from Eq. (5.6) on a matrix element, and then rearranging the two sides of the equation, we obtain the following expression of the fluxes (Younes *et al.*, 2006):

$$Q_i^E = \sum_{j=1}^3 M_{E,ij}^{-1} (H^E - TH_j^E) \quad (5.9)$$

Where H^E and TH_j^E are, respectively, the mean piezometric head in element E and on edge ∂E_j . $M_{E,ij}^{-1}$ is the inverse of the local stiffness matrix obtained as followed:

$$M_{E,ij} = \int_E W_i^E (K^E)^{-1} W_j^E \quad (5.10)$$

Using the mass-lumping scheme presented by *Younes et al. (2006)*, the flux across the edges of the element E are approximated as followed:

$$Q_i^E = \overline{Q_i^E} + \frac{Q_S^E}{3} - \frac{|E|}{3} (c^E + S_s^E S_w^E) \frac{dTH_i^E}{dt} \quad (5.11)$$

where Q_S^E [$L^2 T^{-1}$] is the sink/source term imposed on the matrix element E . $\overline{Q_i^E}$ [$L^2 T^{-1}$] is the flux corresponding to the stationary problem without the sink/source term that can only be expressed as a function of alternated local matrix and traces of the piezometric head:

$$\overline{Q_i^E} = \sum_{j=1}^3 N_{E,ij} TH_j^E \quad (5.12)$$

The local matrix (N_E) has the following form, with the notations written after:

$$N_{E,ij} = \frac{\alpha_{E,i} \alpha_{E,j}}{\alpha_E} - M_{E,ij}^{-1} \quad (5.13)$$

$$\alpha_{E,i} = \sum_{j=1}^3 M_{E,ij}^{-1} \quad \text{and} \quad \alpha_E = \sum_{i=1}^3 \alpha_{E,i} \quad (5.14)$$

5.3.3. Flux discretization for a fracture element

The formulation of MHFE in the fracture element “ k ” is similar to the formulation in the matrix elements (see *Hoteit and Firoozabadi, 2008*). Using the same approach as presented for the discretization in the matrix, fluxes are expressed by the average hydraulic head on the fracture edge and hydraulic head on the fracture nodes (see Fig. 5.1).

$$Q_i^k = \sum_{j=1}^2 M_{k,ij}^{-1} (H^k - TH_j^k) \quad (5.15)$$

$$M_{k,ij} = \int_{\ell} W_i^k (K^k)^{-1} W_j^k \quad (5.16)$$

Applying Eq. (5.15) on Eq. (5.2) for the fracture edges, the continuity equation treated with a finite volume procedure leads to:

$$\varepsilon \ell \left(c^k(h^k) + S_s^k S_w^k(\theta^k) \right) \frac{dH^k}{dt} + \varepsilon \sum_{i=1}^2 Q_i^k = Q_s^k + Q_f^k \quad (5.17)$$

where ε [L] and ℓ [L] refer to the fracture aperture and length, respectively. Q_s^k [L^2T^{-1}] represents the sink/source term inside the fracture, and Q_f^k [L^2T^{-1}] is the matrix–fracture volumetric exchange flux, which is explained in the next section.

5.3.4. Hybridization: mass conservation on edges

Obtaining the global format of the discretized equations requires coupling the flux and piezometric head associated with neighboring elements E and E' having ∂E_i in common. If edge ∂E_i is not a fracture, the continuity of flux and piezometric head is imposed, such that:

$$\begin{cases} Q_i^E + Q_i^{E'} = 0 \\ TH_i^E = TH_i^{E'} \end{cases} \quad (5.18)$$

If ∂E_i coincides with a fracture, the total flux across both sides coming from the adjacent matrix elements defines the matrix-fracture exchange flux Q_f^k , which acts as a sink/source term on the fracture edge. As for the continuity of piezometric heads, the mean heads associated with the matrix edges are equal to the mean head in the fracture element, that is:

$$\begin{cases} Q_i^E + Q_i^{E'} = Q_f^k \\ H^k = TH_i^E = TH_i^{E'} \end{cases} \quad (5.19)$$

For further explanation on the elimination of Q_f^k in the final format of the equations, refer to *Hoteit and Firoozabadi (2008)*.

5.3.5. The new ML technique for fractures

The global matrix corresponding to the discrete system of equations does not necessarily satisfy the M-matrix conditions which requires a non-singular matrix with $m_{ii} > 0$ and $m_{ij} \leq 0$ (*Younes et al., 2006; Hoteit, et al., 2002*). The M-matrix property ensures respecting the discrete maximum principle; in other words, the solution is free from unphysical oscillations. The global matrix obtained by MHFE is symmetric and positive definite but is not, in general, an M-matrix. In order to improve the property of our numerical scheme, we use a combination of two mass-lumping techniques; one for porous matrix elements, as shown in section 5.3.2, and a new technique that we propose for fracture edges. This proposed mass-lumping scheme, applied to the fracture edges, ensures the consistency of the M-matrix property for the combined matrix/fracture system.

To explain the mass-lumping scheme for the fracture edges, the global matrix of the discrete system (resulting from the MHFE method) is decomposed into nine submatrices, including six sub-matrices being pairwise transpose of each other due to the symmetry of the global matrix. The decomposition of the global matrix and different sub-matrices are shown in Fig 5.2.

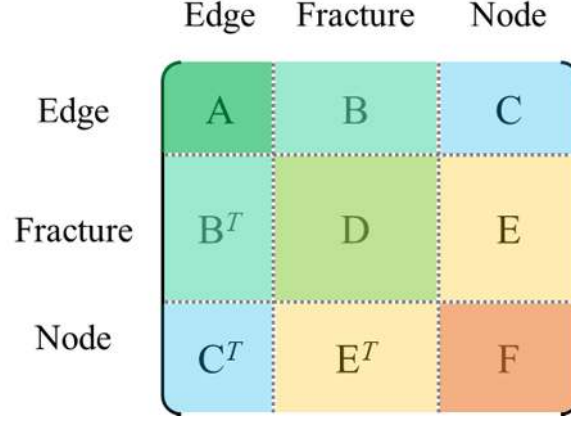


Fig. 5.2. Decomposition of the global matrix into nine sub-matrices.

Matrix (A) is composed of the coefficients associated with flux continuity between adjacent porous matrix elements where interfaces are not fractures. (A) is similar to the one obtained with MHFE in unfractured domains. As the ML technique is used for porous matrix elements, (A) satisfies the M-matrix properties (Younes *et al.*, 2006). Matrix (B) denotes the coefficients associated with the connectivity of the porous matrix and the edges shared with fractures, which are all negative or zero (see Eq. (5.11)). Matrix (C) represents the contribution of fracture nodes on the flux continuity on the unfractured edges. The coefficients of (C) are all zero due to the fact that there is no flow exchange between the fracture nodes and matrix edges. Matrix (D) is also an M-matrix (see Eq. (5.11)), and matrix (E) has all negative or zero components when applying the mass-lumping defined in Eq. (5.11). However, matrix (F), which corresponds to the connectivity and flow exchange between fracture edges, is not necessarily an M-matrix. To get a global matrix satisfying the M-matrix conditions, we propose a numerical integration technique to calculate the stiffness matrix ($M_{k,ij}^{-1}$), such that:

$$M_{k,ij} = \frac{1}{K_f^k \ell^2} \int_0^\ell (\xi - \xi_i)(\xi - \xi_j) d\xi \quad (5.20)$$

K_f^k is the hydraulic conductivity of the fracture element (k). The matrix format of $M_{k,ij}$ is given by:

$$\mathbf{M}_k = \frac{1}{K_f^k \ell^2} \begin{pmatrix} \int_0^\ell (\xi - \xi_i)(\xi - \xi_i) d\xi & \int_0^\ell (\xi - \xi_i)(\xi - \xi_j) d\xi \\ \int_0^\ell (\xi - \xi_j)(\xi - \xi_i) d\xi & \int_0^\ell (\xi - \xi_j)(\xi - \xi_j) d\xi \end{pmatrix} \quad (5.21)$$

The calculation of the integrals in each component of the matrix can be approximated numerically. Fig. 5.3 describes schematically the process. In Fig. 5.3a, the red area represents the integral of the diagonal terms of matrix \mathbf{M}_k (Eq. (5.21)). In Fig. 5.3b, the red area corresponds to the integral for the off-diagonal terms of the \mathbf{M}_k (Eq. (5.21)). Applying the ML technique in the fractures, the red areas are approximated using the rectangular integration as represented with the blue areas. This integration approach results in zero off-diagonal elements for the matrix.

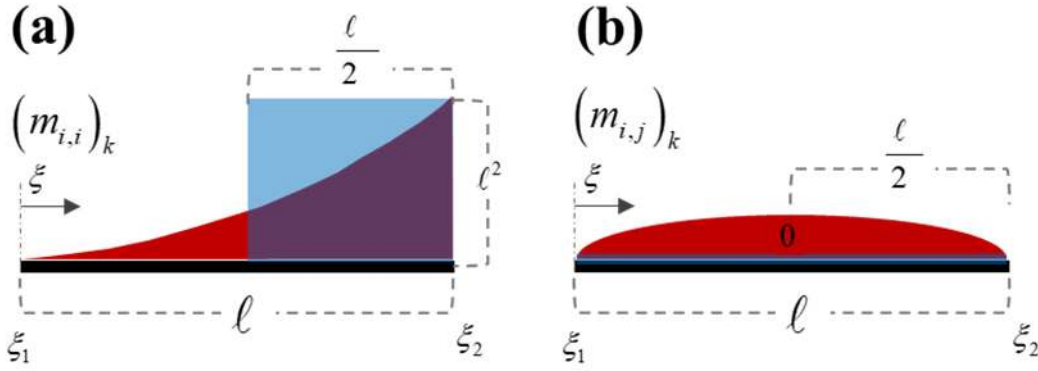


Fig. 5.3. Schematic of the numerical integration of the integrals of the matrix \mathbf{M}_k (Eq. (5.21)): (a) diagonal terms $(m_{i,i})_k$ and (b) off-diagonal terms $(m_{i,j})_k$. Red areas represent the integrals with their analytical expression and blue areas are the corresponding numerical approximation.

Calculating the integral analytically (red surface in Fig. 5.3) leads to a stiffness matrix that does not satisfy the M-matrix properties. However, numerical approximation (the blue surface in Fig. 5.3) leads to the following:

$$\mathbf{M}_k = \frac{\ell}{2K_f^k} \mathbf{I} \quad (5.22)$$

$$\mathbf{M}_k^{-1} = \frac{2K_f^k}{\ell} \mathbf{I} \quad (5.23)$$

Where \mathbf{I} is the identity matrix. The process leads to a diagonal stiffness matrix. Hence, sub-matrix \mathbf{F} satisfies M-matrix condition that guarantees stable solution in each time step. The validity of the results is demonstrated in the following sections.

5.3.6. High-order adaptive time integration

The system of differential equations obtained by coupling the discretized fluxes in the matrix and fracture elements leads to a system of temporal ODEs. In this work, we solve this system using the advanced solver DLSODIS (Double precision Livermore Solver for Ordinary Differential equations – Implicit form and Sparse matrix), which is a public domain solver (Hindmarsh, 1980; Seager and Balsa, 1982). The solver is based on the backward differentiation formula (BDF). It has the advantage of using a high-order time integration scheme. Both variable time step sizes and variable integration orders are used to reach accurate solutions with optimized CPU time. The integration order variability makes this solver highly accurate when compared to conventional constant order solvers. In particular, for VSF, and as shown in Farthing et al. (2003) and Fahs et al. (2009), high order schemes lead to accurate mass balance even with the non-conservative form of RE. The variability of time step size allows reducing the calculation time and therefore results in exceptional efficiency improvement. The accuracy of DLSODIS is controlled by various tolerances related to the relative and absolute errors, which are set to 10^{-6} in this work. The time step size is changed and adapted periodically by the solver to honor the imposed tolerances. The algebraic nonlinear system, resulting from the temporal integration of each time-step, is solved using a modified Newton iteration scheme (Radhakrishnan and Hindmarsh, 1993) where the Jacobian matrix is calculated numerically using a finite difference approximation and a column grouping technique of Curtis et al. (1974).

5.4. Results: Verification and advantages of the new developed numerical scheme

5.4.1. Verifications: Fractured Vauclin test case

The developed numerical scheme, based on the combination of the MHFE method, ML technique, and MOL, was implemented in a FORTRAN code. The main goal of this section is to verify the correctness of this code. Thus, we consider a computationally simple example in order to avoid numerical artifacts. The example is inspired by the laboratory experiments of Vauclin et al. (1979), dealing with water table recharge. This example is accepted as a standard

benchmark for VSF as it provides reliable experimental data with simple boundary conditions. The laboratory experiments of *Vauclin et al. (1979)* deals with unfractured homogenous soil. We adopted four fractured examples by assuming the same configuration (geometry, dimensions and boundary conditions) and by embedding in the domain i) a single vertical fracture, ii) a single horizontal fracture, iii) a single inclined fracture and iv) a network of fractures similar to the ones encountered in karst aquifers. The original experimental setup of *Vauclin et al. (1979)* consists of a rectangular soil slab ($600\text{cm} \times 200\text{cm}$). A constant influx of 355 cm/day is applied over a width of 100cm in the center-top of the domain. Initially, the water table is located at 65cm from the bottom surface. Because of the symmetry, only the right half of the domain is considered and the axis of symmetry acts as an impermeable boundary on the left. The rest of the boundary and initial conditions are similar to the original experiment. The hydrological properties of the porous matrix are obtained from (*Clement et al., 1994*), whereas the fracture properties are selected from (*Fairley et al., 2004; Kuráží et al., 2010*). The matrix and fracture parameters are provided in Table 5.2. Effects of these parameters on VSF in fractured domain is beyond the scope of the study. The most computationally challenging values are considered with an emphasis of their high hydrodynamic conduction of fractures compared to the soil matrix.

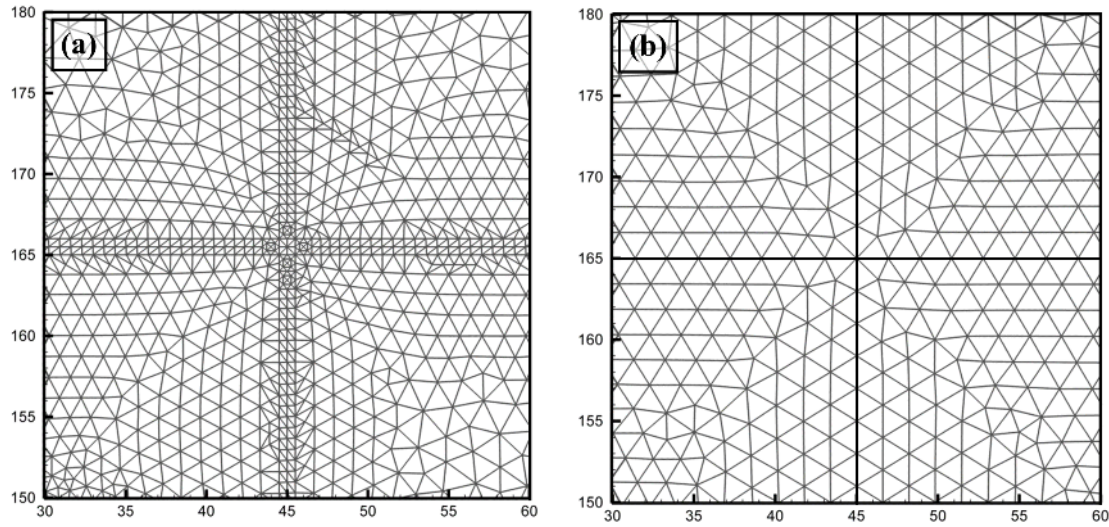
Table 5.2. Parameters used for the verification examples: Vauclin experiments and infiltration in dry soil (ε is the fractures aperture).

| Parameter | Fractured Vauclin | | Infiltration in dry soil | |
|--------------------|-------------------|------------|--------------------------|------------|
| | Matrix | Fracture | Matrix | Fracture |
| θ_r | 0.01 | 0.0001 | 0.01 | 0.001 |
| θ_s | 0.3 | 1.0 | 0.399 | 0.8 |
| $\alpha (cm^{-1})$ | 0.033 | 0.01 | 0.014 | 0.001 |
| n | 4.1 | 1.5 | 1.6 | 1.5 |
| $K_s (cm. s^{-1})$ | 0.00972 | 0.32000 | 0.00053 | 0.01157 |
| $S_s (cm^{-1})$ | 10^{-10} | 10^{-10} | 10^{-10} | 10^{-10} |
| $\varepsilon (cm)$ | - | 1 | - | 1 |

Our developed code, based on the MHFE method, ML technique (for both fractures and matrix) and the hybrid-dimensional technique (1D fractures and 2D porous matrix) is referred to as MH-Lump-1D/2D. This code is verified here by comparison against an in-house code based on the MHFE method and dealing with VSF in unfractured domains. The in-house code has been validated against experimental data in *Fahs et al. (2009)*. In this in-house code, both matrix and fractures are considered as 2D elements. Thus, this second code is referred as MH-2D/2D. An example of the difference between the computational mesh used in MH-Lump-1D/2D and MH-2D/2D is given in Fig. 5.4. For more confidence in the correctness of the newly developed code (MH-Lump-1D/2D), we compare it against a finite element solution from COMSOL Multiphysics. This software provides a tool to simulate fractured porous media based on the hybrid-dimensional technique. However, when this tool is used for VSF, the fractures are always assumed as saturated, which is not the case in our examples. Thus, as in the code MH-2D/2D, we consider the fractures as 2D elements in COMSOL. The COMSOL model is denoted as COMSOL-2D/2D. The numerical codes used for verifications and summary about corresponding numerical techniques are given in Table 5.3. In all codes including the COMSOL model, the time integration is performed in the same manner, using the BDF method with variable order.

Table 5.3. Specification of different numerical codes used for verifications. (FE: denotes the standard finite element method). BDF method is used in all codes for time integration.

| <i>Code name</i> | <i>Implemented numerical techniques</i> | | | |
|------------------|---|------------------------|----------------------------|-------------------------|
| | Fractures representation | Spatial discretization | ML technique for fractures | ML technique for matrix |
| MH-Lump-1D/2D | 1D | MHFE | Yes | Yes |
| MH-2D/2D | 2D | MHFE | Not applicable | Yes |
| COMSOL-2D/2D | 2D | FE | Not applicable | No |
| MH-Cons-1D/2D | 1D | MHFE | No | Yes |

**Fig. 5.4.** Mesh used in (a) the code MH-2D/2D and COMSOL-2D/2D and (b) in the new code MH-Lump-1D/2D.

The simulations are performed for one hour of recharge for all cases. The computational meshes used in the simulations with the code MH-Lump-1D/2D consist of about 17K elements for the cases of horizontal, vertical, and inclined fracture, and about 40K elements for the fracture network configuration. With the same level of refinement in the matrix, the corresponding computational meshes used for the codes MH-2D/2D and COMSOL-2D/2D consist of about 20K elements, for the first three cases, and about 80K elements for the fracture network case. The numbers of elements in the 1D/2D and 2D/2D models show that the hybrid-dimensional technique allows for a significant reduction in the mesh density as it avoids local

refinements within the fractures. The gain is more pronounced for dense fracture networks. The computational grids for all cases were generated using the COMSOL meshing tool.

Fig. 5.5 shows the contour map of the volumetric water content (θ) for different test cases after one hour ($t = 1hr$). This figure shows that, in the case of a single fracture, the higher water table is observed for the vertical fracture (Fig. 5.5a). This behavior makes sense as the vertical preferential flow occurring in the fracture, driven by gravity and capillarity, enhances the water table recharge. The lowest water table is observed in the case of horizontal fracture in which the horizontal preferential flow moves water away from the water table and slow down the water recharge rate (Fig. 5.5b). In the case of the inclined fracture, the inclination decreases the vertical component of the preferential flow and increases its horizontal components. Thus, it is expected that the water table, in this case, falls in the middle between the vertical and horizontal cases (Fig. 5.5c). The case dealing with the schematic karst network leads to the highest water table among all cases (Fig. 5.5d). This behavior is a result of the multiple vertical fractures that could recharge the water table faster than the other cases. In the case of a single vertical fracture, as the fracture is quickly saturated, water exchange with the surrounding matrix is significant. Hence, Fig. 5.5a and 5.5d show a high level of water saturation around the fractures in the case of a single vertical fracture and fracture network.

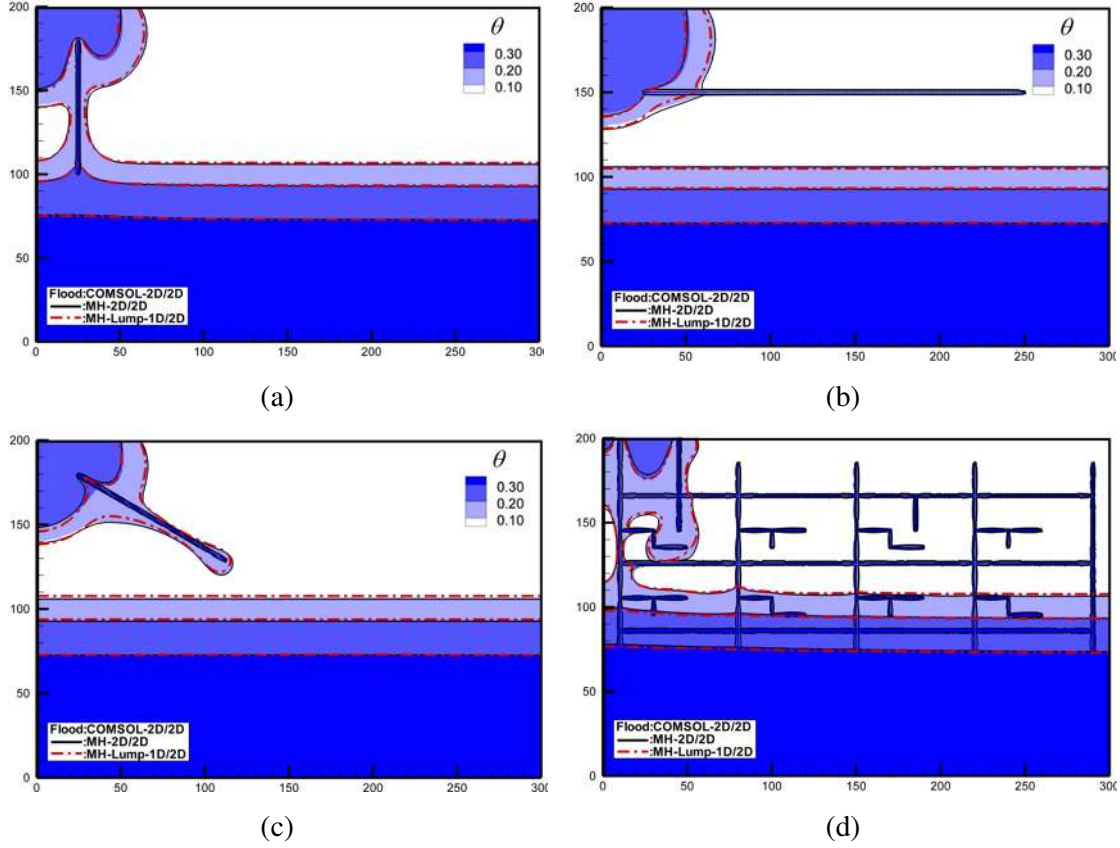


Fig. 5.5. Water content maps at $t=1h$ for the 4 fractured examples of the Vauclin test case. The results are obtained using the codes MH-Lump-1D/2D, MH-2D/2D, and COMSOL-2D/2D: (a) a single vertical fracture, (b) a single horizontal fracture, (c) a single inclined fracture and (d) schematic karst network.

Finally, Fig. 5.5 shows overall excellent agreement between the three codes, which gives confidence in the correctness of our code (MH-Lump-1D/2D). Some minor discrepancies can be observed at the water front, which are related to dissimilarities of the mesh size in 2D/2D and 1D/2D refinements near the fractures. These differences can be reduced by further refining the mesh near the fractures.

5.4.2. Advantages of the ML technique for fractures

The advantages of the ML technique for VSF in unfractured domains is discussed in *Belfort et al. (2009)*. *Fahs et al. (2009)* showed that, besides stable solutions and good convergence properties, the ML technique allows for solving RE in unfractured domains in an efficient manner, using high order time integration scheme. In fractured domains, the ML technique is

applied for unsaturated flow, in this work, for the first time. For saturated flow, this technique may not be critical, as the saturated flow does not require small time steps, for which numerical instabilities could appear. For VSF, small time steps should be used to guarantee the convergence of the nonlinear solver. Thus, spurious oscillations may affect both the accuracy and convergence rate of the solutions. An essential contribution of this work is the development of the ML technique for the DFM model. For the matrix, we apply the same ML technique as developed in *Fahs et al. (2009)* for unfractured domains. The major contribution of this work is in the development of the ML technique for the fractures. In section 5.3.5, we investigate the stability of the corresponding solutions via a theoretical analysis based on the M-matrix property. The main goal of this section is to verify the stability of the developed ML technique (particularly for fractures) and to investigate its advantages via numerical experiments. To do so, we consider the newly developed code MH-Lump-1D/2D in which the ML technique is implemented for the matrix and fractures and a modified version, called MH-Cons-1D/2D, in which ML technique is used only for the matrix. To compare these models, we consider the challenging case of infiltration in dry soil with imposed heads at the top and bottom surfaces (*Huang et al. 1996; Ngo-Cong et al., 2020*). Besides the nonlinearity related to RE, this problem involves an extremely moving sharp front that cannot be captured numerically without introducing dense grids and small time steps. The later causes unphysical oscillations and convergence difficulties. In contrast to the imposed flux boundary condition, the Dirichlet boundary conditions imposed at the soil top surface compound the numerical difficulties as they require an appropriate approach for the evaluation of the equivalent hydraulic conductivity (*Belfort et al., 2013*). This problem has been widely investigated in the literature and the common question is to develop an accurate solution (*Forsyth and Pruess, 1995; Huang et al., 2002; Arico et al., 2012; Younes et al., 2013; List and Radu, 2016; Islam et al., 2017; Zha et al., 2017; Ngo-Cong et al., 2020*). All the exiting studies suggested appropriate numerical solutions for unfractured domains. Simulations of problems dealing with infiltration in dry fractured soil are not well developed in the literature. The results presented here can serve as a benchmark for code verification.

The geometry is inspired by a real fractured outcrop corresponding to a fractured aquifer in Jeita, Lebanon (Fig. 5.6a). Boundary conditions and soil parameters are similar to Huang et al (1996). Constant pressure heads of -10 cm and -1000 cm are imposed at the top and bottom boundaries of the domain, respectively, and an initial pressure head of -1000 cm representing a highly dry soil is assumed. Side boundaries are assumed impermeable. The hydraulic

parameters of the matrix and fractures are given in Table 5.2. Fig. 5.6b shows the 1D/2D mesh gridding consisting of 1626 triangular elements for the matrix and 272 linear elements for fractures. The duration of the simulation is set to be 3.2×10^4 s (about 9 hours).

The MH-Cons-1D/2D code had convergence difficulties after 3 hours of simulation. A close look at the results at this time shows that the waterfront reaches the fractures (Fig. 5.6c). Spurious oscillations appear mostly near the fractures. Incoherent results can be observed with pressure head beyond physics (below -1000cm). These oscillations cause the convergence of the nonlinear solver to fail as the system of equations becomes ill-conditioned. The MH-Lump-1D/2D code runs without any convergence problems for the entire simulation duration. The results at $t=3$ h are given in Fig. 5.6d. This figure shows a stable solution free from spurious oscillations. With further advancement of time, fast preferential flow in the dry soil can be noticed along with all the fracture elements (Fig. 5.6e). The demonstration of actual flow in the matrix and fractures can give better insights about the general direction of the flow and conductive behavior of the fractures (see Fig. 5.6f).

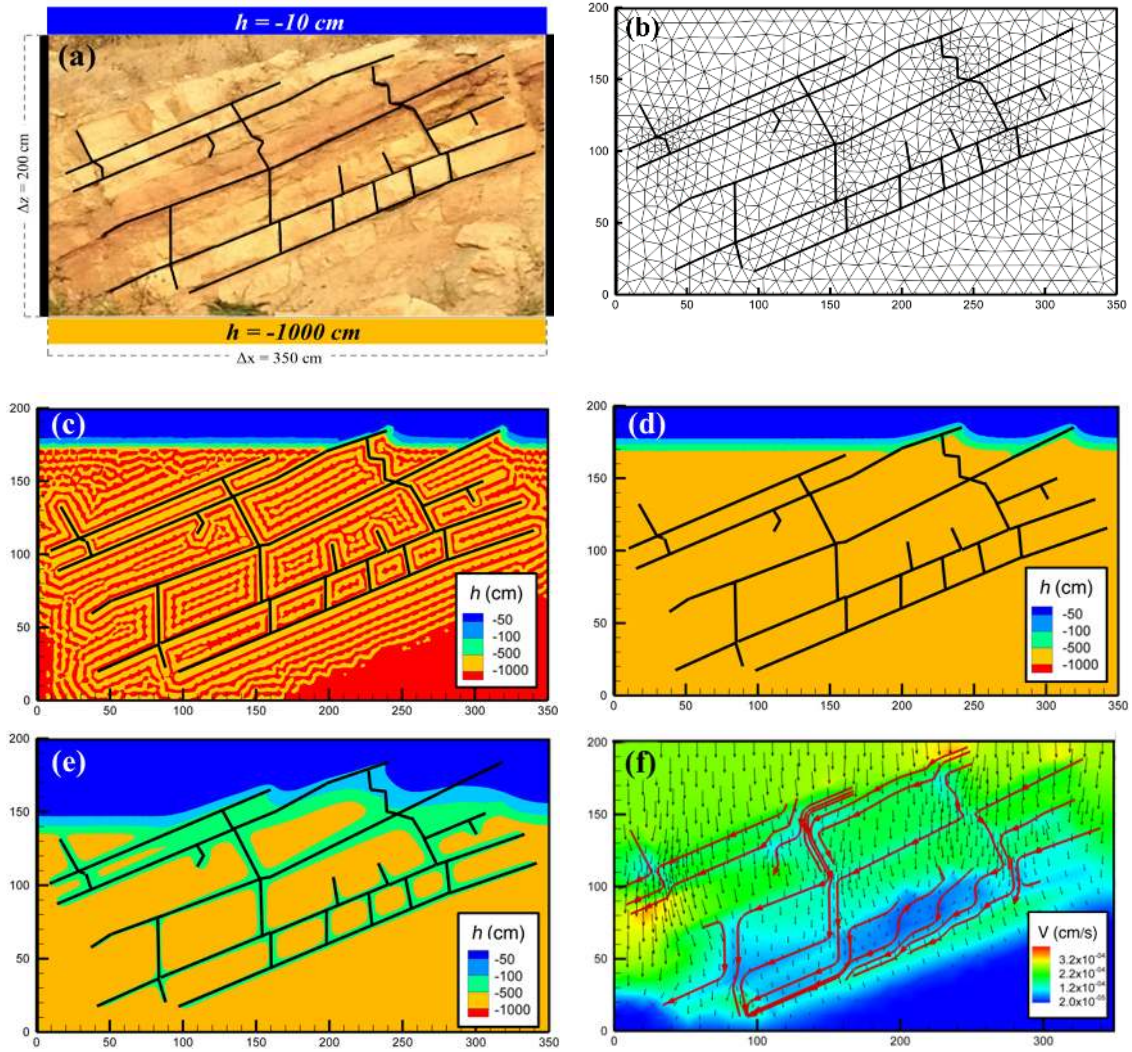


Fig. 5.6. The test case of infiltration in fractured dry soil: (a) synthetic description of the problem: Geometry, fracture network, and boundary conditions, (b) example of computational mesh, (c) pressure head map at $t=3h$ with the MH-Cons-1D/2D code (without ML in fractures), (d) pressure head map at $t=3h$ with the MH-Lump-1D/2D code (with ML in fractures), (e) pressure head map at $t=9h$ with the MH-Lump-1D/2D code and (f) corresponding simultaneous representation of the velocity field, velocity magnitude and the streamlines in fractures.

We also investigate the effect of the ML technique in fractures on the performance of the numerical models. Thus, we compare the CPU time of the MH-Lump-1D/2D and MH-Cons-1D/2D codes for different levels of mesh refinement. It should be mentioned that the computer

system used for all the simulations (in this section and other sections) has an Intel® Core™ i7-6700 CPU at 3.4 GHz with 16 GB (2×8GB) of installed memory (RAM). Fig. 5.7 gives the variation of the CPU for both codes versus the number of elements of the computational grids. It shows that the ML technique in fractures allows for a significant reduction in CPU time by 2 orders of magnitude, whatever the level of mesh refinement. This gain in CPU time is mainly related to the better convergence properties of our proposed scheme.

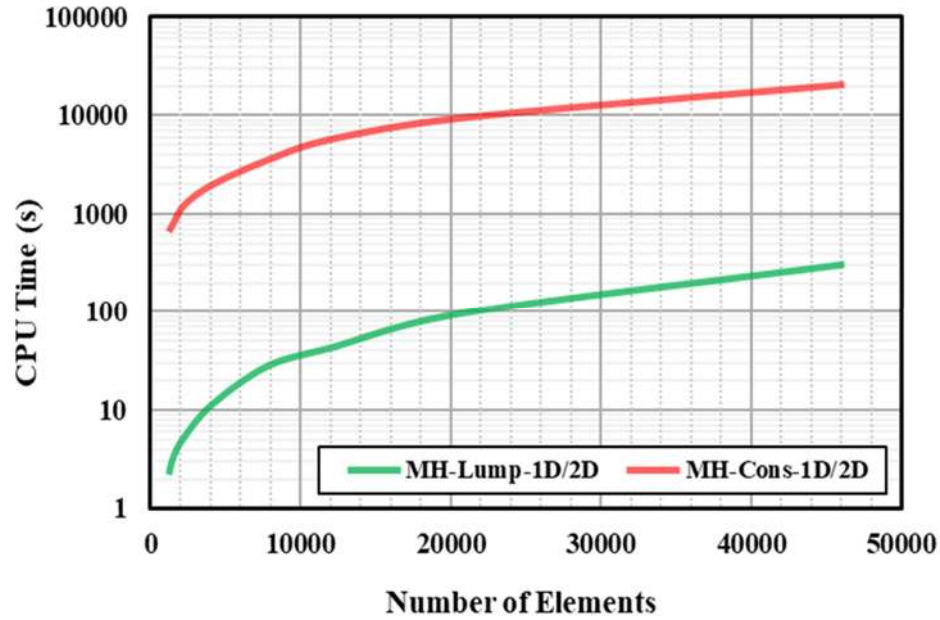


Fig. 5.7. CPU time vs. the number of elements of the computational mesh for both MH-Lump-1D/2D and MH-Cons-1D/2D codes.

5.5. Results: Field Scale Applications

5.5.1. Objectives and overall presentation of the site

This section aims at demonstrating the applicability of the proposed numerical scheme in simulating real field cases. Thus, we use our code (MH-Lump-1D/2D) to investigate the effect of climate change on groundwater resources in a karst aquifer/spring system in El Assal, Lebanon. In particular, we use this code to evaluate the effect of a fracture network on the hydrodynamics behavior of the aquifer and the predictions of groundwater resources under potential impact of climate change. This field application demonstrates the capability of the developed scheme to perform simulations at not only large spatial scale, that extends for kilometers, but also for large time scale, which includes predictions of climate-change effects

over a period of 80 years. It is also essential to show the performance of the new scheme in simulating water-table dynamics under highly variable recharge conditions.

El Assal karst spring is located at 1552 m (above sea level) in Mount Lebanon-Lebanon about 50 km from Beirut (Fig. 5.8a). Its catchment area of about 12 km² is delineated based on tracer test experiments. The aquifer is composed of three zones of highly fissured, thinly layered basal dolostone overlain by dolomitic limestone, and limestone of Albian to Cenomanian age. The spring emerges at the top of the underlying marls and volcanics of Aptian age. The catchment is characterized by a thick unsaturated zone (over 400 m). Dolines were mapped on the catchment to determine zones of point source infiltration. Disturbed representative soil samples were collected from different locations to determine the hydraulic properties such as particle size distribution and hydraulic conductivity at saturation. Fractures were mapped in the field along distinct sections. The recharge area is located between 1600 m and 2200 m elevation and is mostly dominated by snowmelt. The annual discharge of the spring ranges between 15-22 Mm³ based on high-resolution monitoring since 2014 with maxima reaching 2 m³/s following snowmelt and minimum flow rates of 0.24m³/s during recession periods. The spring provides downstream villages in the Kesrouane district with about 24,000 m³ (0.28 m³/s) of water daily for domestic use and is an essential historic spring in the region. Further information about the El Assal karst aquifer/spring system including the domain geometry and characterization (e.g., soil and aquifer hydraulic parameters) is discussed by *Doummar et al. (2018)*. Fig. 5.8b shows the schematic profile of El Assal karst aquifer used as the domain of simulation. The calibrations of the aquifer properties are out of the scope of this study. The parameters of the porous matrix are used as in *Doummar et al. (2018)*, where the aperture of the fractures is assumed to be 1cm. The saturated hydraulic conductivity of the fractures was calculated using the cubic law and the other parameters were assumed to be similar to the one for the case of infiltration in dry soil (see Table 5.2).

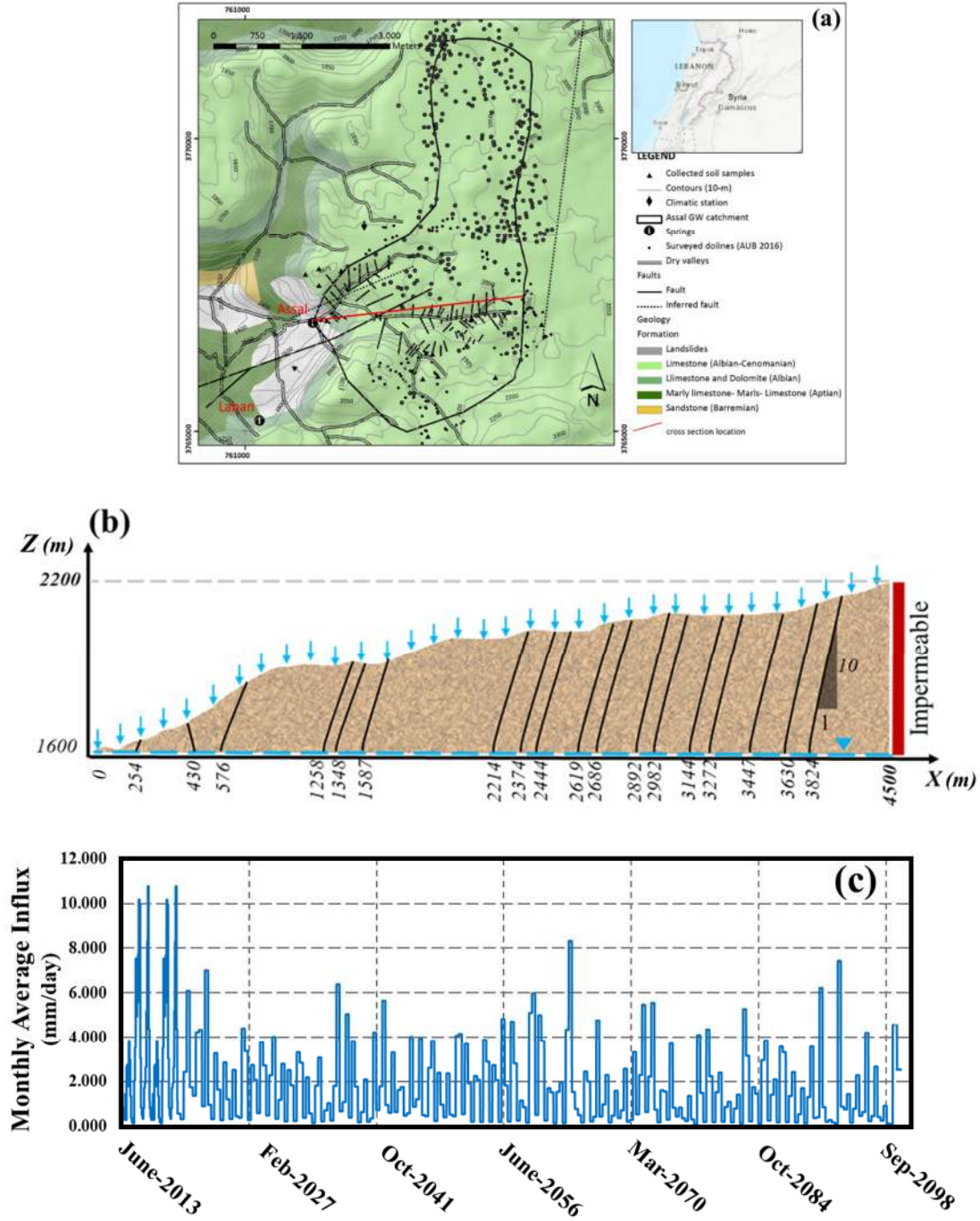


Fig. 5.8. Representation of: (a) the location of the El Assal karst aquifer, (b) schematic domain used to simulate the aquifer and (c) the monthly average recharge projection used for the simulations from 2013 to 2099. Time zero is June 1st, 2013.

5.5.2. Methodology for simulation and analysis

The domain is discretized using a triangular grid consisting of about 140K elements. No-flow boundary conditions are assumed at the right inland side and at the bottom surface representing the initial water table. On the left side, the spring is simulated by imposing a nodal zero pressure head. The site is firstly simulated from 2013 to 2019 using real historical data (June 1st, 2013 to May 29th, 2019), in order to understand groundwater flow dynamics in the aquifer under three regimes of recharge including snowmelt, precipitation and dry periods. We then simulate the site with predicted precipitations for 2019-2099 (starting from June 1st, 2019) in order to evaluate future responses of the spring discharge variations caused by climate change. We extract daily recharge time series (2019-2099) from the calibrated integrated model in *Doummar et al.* (2018), where precipitation predictions are obtained from the IPSL_CM5 GCM (5th phase of the Coupled Model Intercomparison Project; Dufresne et al., 2013; Global Climatic Model) for Lebanon with a resolution of 0.25° based on the AgMERRA dataset (Ruane et al., 2015). In *Doummar et al.* (2018), the scenario RCP 6.0 was adopted, reflecting a stabilization of the radiative forcing value without overshoot pathway at 6 W/m² after 2100. Projected raw data were corrected to account for the elevation of the catchment area (1500-2200 m), using a constant lapse rate for T (-0.24 °C) and P (+5.5%) per 100 m elevation. For all simulations, we consider monthly averaged recharge variation. The results of simulations are analysed using the spatial maps of water content (θ) and three scalar metrics which are i) the dimensionless average saturation of the aquifer (V_m), ii) the maximum water table elevation (H_0) and iii) the discharge rate at the spring outlet (q_{out}). The mathematical expressions of the metrics are stated as follows:

$$V_m = \frac{1}{|\Omega|} \int_{\Omega} S_e \, d\Omega \quad (5.24)$$

($|\Omega|$ is the area of the aquifer and S_e is the element effective saturation defined in Table 5.1)

$$H_0 = \max_{h(x,y,t)=0} (H(x, y, t)) \quad (5.25)$$

$$q_{out} = -K \nabla H \Big|_{x=0} \quad (5.26)$$

5.5.3. Simulations with real data from 2013 to 2019

We simulate the aquifer using data from June 1st, 2013 to May 29th, 2019. Initially, the domain is assumed to be at hydrostatic equilibrium. For this period, real recharge data are used for 2013-2016, and similar data trends are imposed for 2016-2019, since data for this period are not available. To investigate the effect of fractures on the groundwater dynamics, we simulate

the aquifer using 2 models, using the code MH-Lump-1D/2D. The first model considers the fracture network while the second one assumes the domain as homogenous with no fractures. The corresponding maps of water content at the end of May 2019 are represented in Fig. 5.9. In general, similar profiles can be observed on the right side of the aquifer, where fractures do not exist. A dry zone can be observed between the two wet zones at the top and bottom. The appearance of this zone is due to the dry-wet cycle of the recharge process. During a dry period, water saturation at the top aquifer decreases, and then during the recharge period, the upper surface is rapidly saturated. Still in the right part of the aquifer, but shifted left, where fractures occur, we observe that the fracture network does not have a dominant trend on the saturation distribution. Being highly permeable relative to the matrix, fractures tend to conduct the flow faster than the adjacent matrix. This leads to high dry zones around the fractures, which are visible on the top of Fig. 5.9a. Around the centre of the aquifer, the preferential flow in the fractures enhances water infiltration and expands horizontally towards the dry zone at the middle depth of the aquifer. On the left side, the fractures have a more dominant effect, contrasting to the results of the unfractured model, where a high saturation zone can be observed near the top surface.

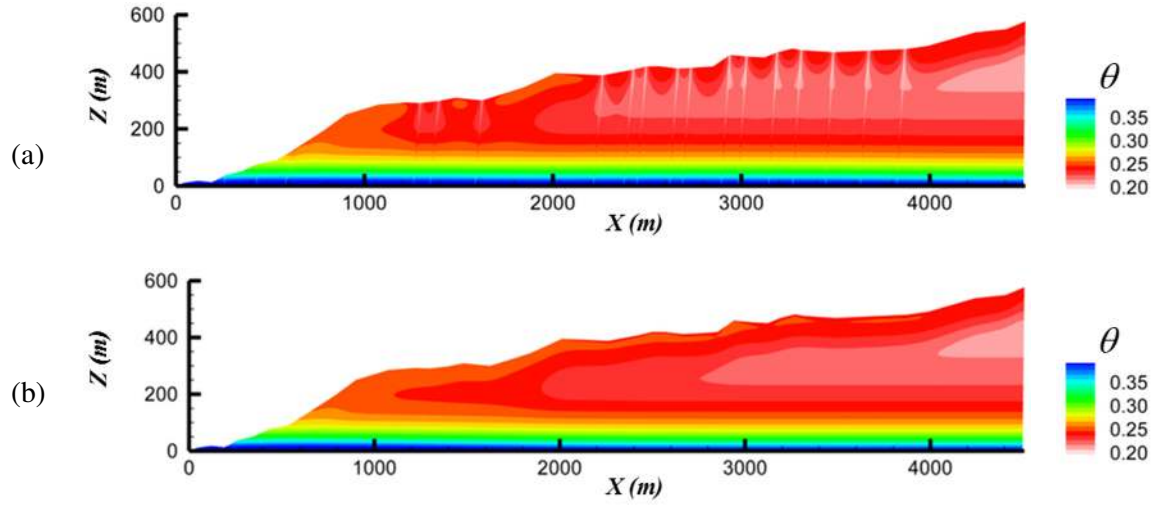


Fig. 5.9. Maps of aquifer water content at the end of the simulation 2013-2019 (end of May 2019): (a) by considering the fracture network and (b) by neglecting the fractures.

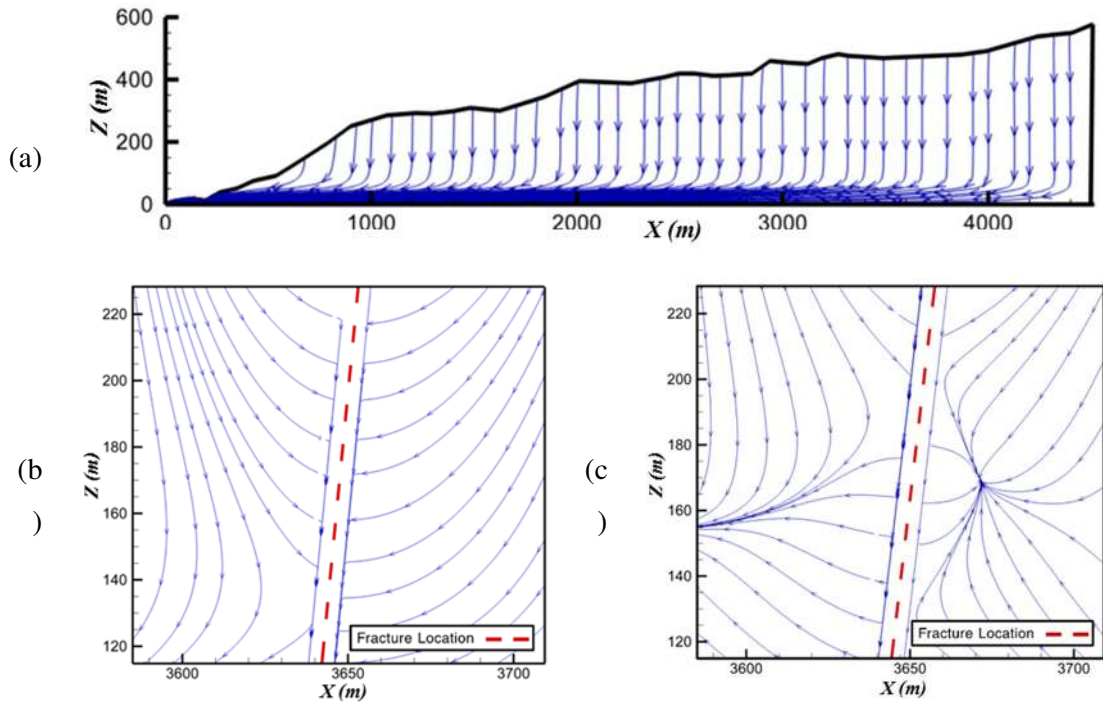


Fig. 5.10. Flow streamlines maps for: (a) The far-field flow direction in the aquifer, (b) Flow direction around fractures and (c) Flow around stagnation points.

The main streamlines of groundwater flow in the aquifer with the fracture network is shown in Fig. 5.10. Vertical infiltration can be observed in the unsaturated zone. Near the water table, the groundwater flow is horizontal towards the spring (Fig. 5.10a). It can be seen that flow generally tends to be absorbed and then travel through fractures (Fig. 5.10b). In some instances, when a local maximum in the recharge distribution occurs and is followed by a relatively dry period, certain points appear near the fractured region which tends to absorb water and create stagnant points nearby (Fig. 5.10c). This behavior is mostly due to the fact that the water is drained faster in the fracture than in the porous matrix, resulting in higher conductivity (i.e., higher saturation) in the stagnant points compared to their adjacent points in the fracture.

Fig. 5.11 depicts the time variations of the scalar metrics (V_m , H_0 , and q_{out}) using both the fractured and unfractured models. Fig. 5.11a confirms that there is a slight gap between both models regarding V_m but in general, less amount of water is obtained with the fractured model. Referring to Fig. 5.11b, we can see that the level of the water table is significantly affected by the fractures, which is coherent with the results discussed in Fig. 5.9. Fig. 5.11c shows that the fractured model leads to higher water flux at the spring outlet compared to the non-fracture model. These results indicate that the fracture network enhances water infiltration in the aquifer. This increases the water discharge through the spring and decreases the amount of water stored in the unsaturated part of the aquifer. The results of Fig. 5.11c are coherent with the ones in Fig. 5.11a. As in both models, fractured and unfractured, the amount of influx from the recharge is the same, and more water is discharged with the fracture model (Fig. 5.11c), which should lead to less retention of water in the aquifer with this fracture model. This behavior is observed in Fig. 5.10a, which shows less amount of stored water with the fractured model than the unfractured one.

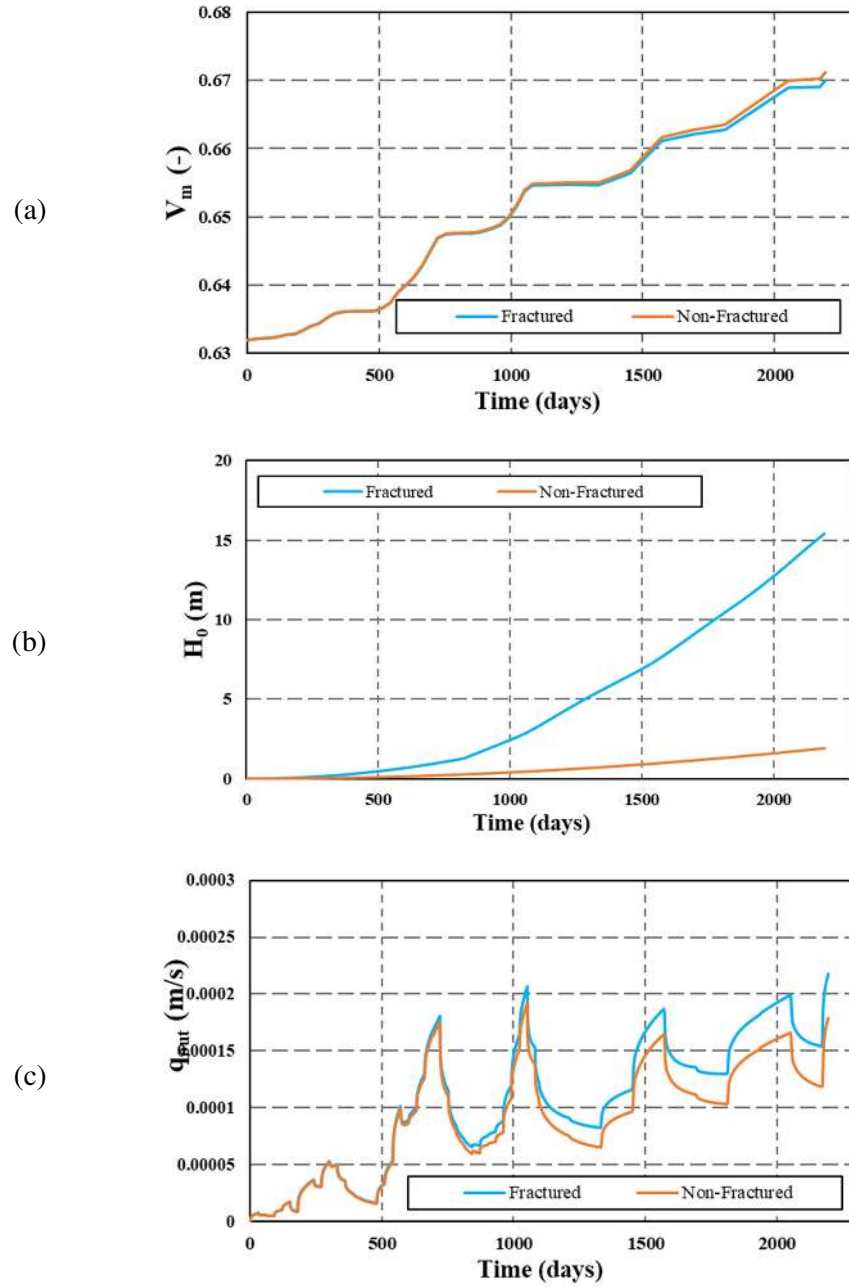


Fig. 5.11. Temporal distribution of (a) V_m (average amount of available water), (b) H_0 (maximum level of the water table), and (c) q_{out} (spring outlet discharge). Simulations from 2013 to 2019 (using real data) with both fractured (blue curves) and non-fractured (orange curves) models. Time zero represents June 1st, 2013.

5.5.4. Predictions under climate change from 2019 to 2099

In this section, we investigate the effect of fractures on the predictions of water resources in the El Assal aquifer under different scenarios reflecting climate-change conditions. Here we investigate the effect of neglecting the fractures on the predicted results. Thus, we simulate the aquifer with the predicted recharge from June 1st, 2019 until 2099. We started the simulation with hydrostatic equilibrium on June 1st, 2013. We run the models from 2013 until the end of May 2019 using real data (as in the previous section). We follow with predictions (since June 2019), where we consider recharge under climate change. The aquifer is simulated using 3 models. The first model, named F/NCC, considers the fracture network but neglects the effects of climate change on recharge. In this model, we assume that the recharge distribution of 2013-2019 occurs over the next eighty years, up to 2099. The second model, named F/CC, considers the fracture network and assumes variable recharge due to the effect of climate change (as in Fig. 5.8c). The last model neglects the fracture network (i.e., considers the domain as homogenous) and assumes variable recharge due to climate change. This model is denoted by NF/CC.

The results of the three models, regarding the map of water saturation, are presented in Fig. 5.12. At first glance, the water content and the saturated zone are higher in the model with neglected variations of recharge due to climate change, as expected. With climate change effects, the fracture model leads to a lower water table than the homogenous model. This is expected as the preferential flow in the fracture network enhances water infiltration through the unsaturated zone. Investigating further through the transient behavior of the proposed metrics, we can obtain better insights as shown in Fig. 5.13. In this figure, the effect of climate change reduces the amount of available water in the aquifer as well as the water discharge at the spring outlet. This is observed from the differences between the model with neglected climate change effects (red curves) and the models with these effects (blue and orange curves). Under climate change conditions, we can observe two regimes of time variation. Starting from hydrostatic equilibrium in 2020, during the first 40 years (from 2020 to 2060), the amount of water available in the aquifer, the water level table and the discharge flux at the spring will increase. After 2060, these metrics will exhibit a decreasing variation with time indicating less availability in water resources due to climate change. The general patterns of the results of the models F/CC and NF/CC indicate that neglecting fractures leads to an overestimation of the available water resources in the aquifer. The difference in the estimated amount of available water with both F/CC and NF/CC models is evident from early time and continues during all

the simulated period. The level of the water table is slightly sensitive to fractures. Neglecting fractures in the model would lead to some periods where the level of the water table is overestimated and other periods where it is underestimated. This effect is also observed for the water discharge in the spring.

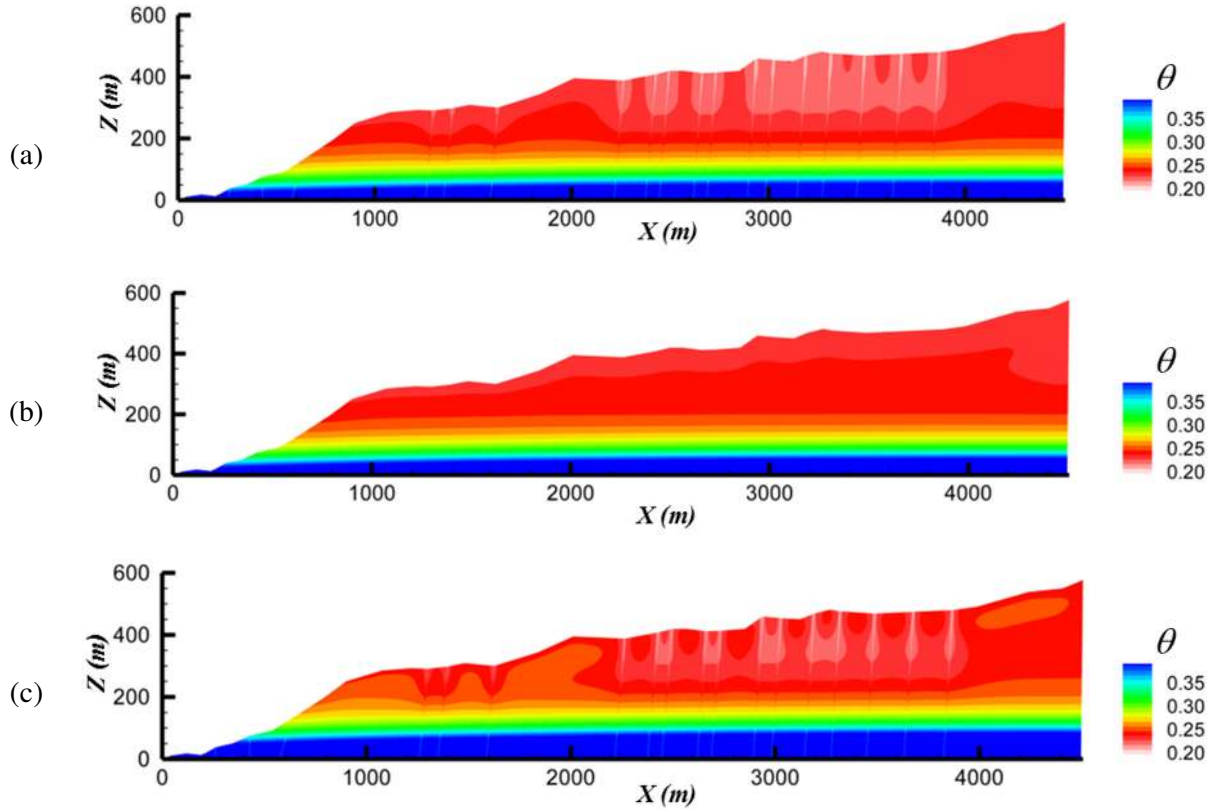


Fig. 5.12. Spatial distribution of aquifer water content in 2099: (a) F/CC model including fracture network and climate change effect on recharge, (b) NF/CC model, ignoring fracture network and considering climate change effect on recharge and c) F/NCC model, considering fracture network and ignoring climate change effect. Time zero is January 1st, 2020.

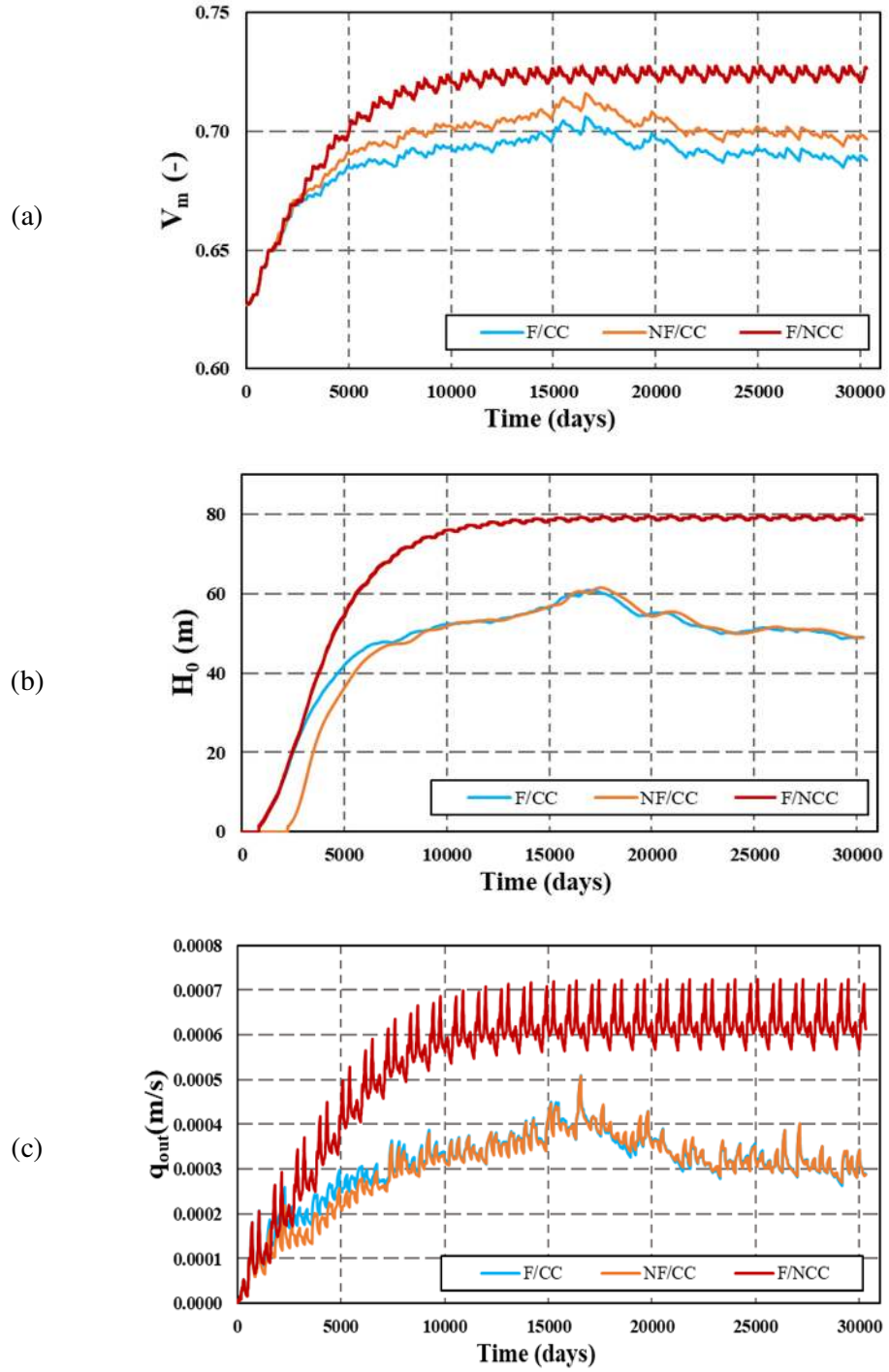


Fig. 5.13. Temporal distribution of (a) V_m , (b) H_0 , and (c) q_{out} for 2012-2099 period with the three models: F/CC (blue curves), NF/CC (orange curves) and F/NCC (red curves).

As the spring outlet discharges the most important metric, we explore more the variability of this metric in Fig. 5.14. For the period 0-7000 days (until 2033), it is clear that the discharge flux estimated with the fractured model is higher than the one with the unfractured model. Thus we focus the analysis in Fig. 5.14 on the period 2033-2099. This figure shows, simultaneously, the normalized distribution of the projected recharge (normalized using the maximum recharge value) along with the normalized difference between spring outlet discharge of the F/CC and NF/CC models (Δq_{out}). Both recharge and Δq_{out} are normalized using the maximum value of the recharge influx. It can be observed that the higher variability in the recharge distribution results in higher variability of Δq_{out} and higher inaccuracy in the prediction of the outlet discharge. The other interesting observation is the delay in the response of the system at approximately 20000 days (late 2060). This point corresponds to the high recharge influx at 17000 days (early 2060). We presume that this delay is due to the high fluctuation of the recharge at this period, which results in high dry soil in the next dry season and saturated fractures. Saturated fractures (i.e. highly permeable fractures) tend to absorb the flow from the nearby matrix, resulting in much slower flow in the soil and a slower response of the spring. In other words, the fractures act as a sink for the flow, which impacts the flow locally in the aquifer, resulting in a lag-time between the recharge event and the spring discharge response. This lag-time can grow over time due to the increase of variation of the recharge caused by the climate-change.

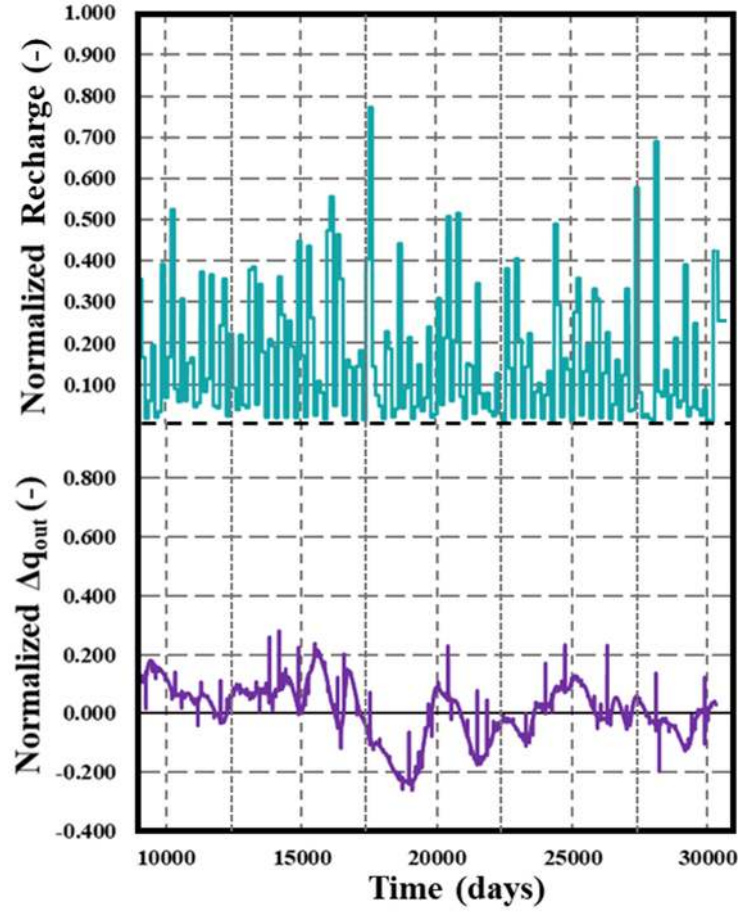


Fig. 5.14. Figure exploring the effect of fractures on the predicted spring outlet discharge under climate change effects; Δq_{out} represents the normalized difference between the spring outlet discharge estimated, respectively, with the F/CC (with fractures) and NF/CC (without fractures) models. Both recharge and Δq_{out} are normalized against the maximum value of the recharge influx.

5.6. Conclusion

Simulation of the VSF in a discretely fractured domain is a computationally challenging problem, which requires solving the RE in the matrix and dense fracture networks involving complicated geometry and discontinuities in the hydraulic properties. The presence of fractures adds complexity to the RE solution, which is already a challenging task without fractures. Existing numerical models of VSF in discrete fractured domains are limited to standard numerical techniques that limit their applications in field studies. We develop a new numerical scheme for solving RE in discrete fractured domains by combining advanced techniques for space and time discretization.

The fracture network is considered via the hybrid-dimensional technique (1D fractures in a 2D matrix). For the space discretization, we extend the MHFE to deal with VSF in fractured vadose zones. We develop a new ML technique for the fractures to improve the performance and the robustness of the method in simulating preferential flow in dense fracture networks. For time integration, while existing numerical models for flow and transport in fractured domains deal with standard backward Euler first-order method, we use a sophisticated technique based on adaptive high order technique with accurate adaptive time-stepping procedure. We use the MOL to couple MHFE method, ML technique for fractures, and high order adaptive technique. The MHFE method is used for VSF in fractured media for the first time.

The new proposed numerical scheme is implemented in a FORTRAN code and validated against COMSOL Multiphysics on a case dealing with water table recharge. We show the stability of our scheme based on the M-matrix property. We also highlight its advantages and performance by comparing it against other standard numerical techniques in simulating a challenging case of water infiltration in dry soil under imposed pressure heads. The results show that the suggested ML technique eliminates all numerical oscillations and improves the convergence of the nonlinear solver, leading to a significant reduction in computational time.

The proposed scheme is then used to investigate the effect of climate change on groundwater resources in a karst aquifer/spring system in El Assal, Lebanon. This application shows the performance of the proposed scheme in simulating problems with large time and space scales under variable recharge conditions. The simulations are performed with a computational mesh consisting of about 140K elements, for a duration of about 87 years and under high variable recharge conditions (snowmelt, rain, and dry periods). The corresponding CPU time is less than 1 hour. The results show that neglecting the fracture network in the aquifer would lead to

an overestimation of the amount of available water as well as the groundwater discharge through the spring outlet.

The proposed scheme is generic and can be extended to other applications. The developed ML technique for fractures and the procedure used for time integration can be applied for other finite element-based methods. The application to the El Assal aquifer can also be extended to model more detailed analyses aiming at determining the parameters of the matrix and fractures, based on available observation data. This model has the features to be coupled with an optimization procedure to calibrate simulations with field observations. The proposed scheme can be extended to 3D, which is an ongoing task of this work.

This work has been the subject of an article published in the journal of Advances in Water Resources on May 2020. (*Koohbor et al., 2020*).

<https://doi.org/10.1016/j.jhydrol.2019.01.052>

Chapter VI: Conclusion and perspectives

6.1. General conclusion

The context of this work addresses the numerical modeling of flow and mass transport in fractured porous media with a focus on two applications: Seawater Intrusion in coastal aquifers and variably saturated flow in fractured vadose zones. The main objective of this work is to improve the efficiency and accuracy of the numerical models in order to enhance their capacity in representing more complex and realistic configurations. There has been a significant part dedicated to the development of semi-analytical solutions that can be used for the assessment of newly developed numerical codes and models and they are helpful for understanding physical processes. There has been also a development of an efficient technique, based on surrogate modeling, to investigate the uncertainties related to fractures on seawater intrusion. We also contribute an efficient and advanced numerical scheme that is more efficient than existing schemes, for the simulation of variably saturated flow in fractured domains. Real field applications have been developed to highlight the capacities of the developed techniques.

The Henry problem is the only existing semi-analytical solution for seawater intrusion with the variable density flow model. We improved the realism of this solution by extending it to velocity-dependent dispersion in anisotropic and stratified (i.e. layered heterogeneity) coastal aquifers. This makes it one of the most general and comprehensive solutions proposed for the Henry problem. As the first existing semi-analytical solution, the new one is based on the Fourier series method. We present a new implementation of the methods to deal with dispersion, anisotropy and heterogeneity. An efficient nonlinear solver is used to obtain accurate solutions even in the case of narrow mixing zones. We provided high-quality data for several quantitative metrics of seawater intrusion that can be effectively used in further studies for benchmarking numerical schemes. All the metrics have been calculated analytically using the Fourier series. We used the developed solution to give better insights on the combined effects of anisotropy and heterogeneity on seawater intrusion processes and relevant metrics.

We show that at a constant gravity number, decreasing anisotropy ratio (i.e. $r_k = K_z/K_x$) leads to further intrusion of saltwater. The semi-analytical solution shows that anisotropy leads to a wider mixing zone and intensifies the saltwater flux entering the aquifer. We discuss and explain some contradictory results in the literature with the aid of the proposed solution. The

contradictory results were related to the way in which the anisotropy ratio was changed and its effect on the gravity number. We also show that the width of the mixing zone is sensitive to the rate of stratification. This sensitivity is augmented in highly anisotropic aquifers. The stratification rate and anisotropy have complementary effects on all SWI metrics, except for the depth of the discharge zone.

We were also interested in contaminant transport in coastal aquifers subject to seawater intrusion. From a computational point of view, this is a complex issue due to the space and time variability of the velocity field, which is affected by the salinity of the sea. Analytical solutions for this case and in general for contaminant transport in non-uniform velocity fields are scarce. Existing solutions are based on significant simplifications (low density contrast) which are not representative of real field conditions. Thus, we extended the semi-analytical solution of the Henry problem to deal with contaminant transport in coastal aquifer under seawater intrusion. We considered two cases inspired by field configurations, dealing with contaminant infiltration from the top surface of the aquifer or upstream inland contamination induced by a regional flow. The semi-analytical solution is obtained using the Fourier series method. We evaluated analytically several metrics characterizing the contaminant transport as the Sherwood number, the mass flux, among others. The developed semi-analytical solutions can be considered as a benchmark not only for contaminant transport in coastal aquifers but also in a variable-velocity field.

We also used the semi-analytical solution to understand the processes of contaminant transport in coastal aquifers. Our results showed that, in the case of contaminant infiltration from the top surface of the aquifer, seawater intrusion limits the spread of the contaminant in the aquifer by contracting the contaminated zone. However, the intensification of seawater intrusion does not have significant effects on the discharged contaminant flux into the sea. For the landward contamination scenario, moderate seawater intrusion affects mainly the spatial distribution of the contamination plume while extreme seawater intrusion can increase the contaminant discharge flux to the sea. The proposed semi-analytical solution helps to fill some gaps in the literature of benchmarking contaminant transport under variable velocity fields and the findings give insights on the quality management of the freshwater resorts in coastal aquifers.

We also investigated seawater intrusion in fractured coastal aquifers. The most reliable model to deal with seawater, in this case, is based on the coupling between the variable-density flow and the Discrete Fracture Network in which the fractures are considered explicitly. However,

this model requires a detailed and explicit description of fractures. Thus, the uncertainty of fracture topology and hydrodynamic properties may impose major uncertainty on the results of this model. Thus, we developed an efficient strategy to investigate uncertainty propagation in this case. Our strategy is based on the global sensitivity analysis via the Sobol indices. The evaluation of these indices requires a large number of simulations that cannot be performed using the variable density flow model due to the high required CPU time. We suggest a strategy based on surrogate modeling. An optimal number of simulations developed using the variable density flow model. This model has been developed using COMSOL Multiphysics. These simulations are used to build a surrogate model based on the polynomial chaos expansion. A new sparse polynomial chaos expansion technique is used to allow for high polynomial orders at low computation costs. The surrogate model is used to obtain the Sobol' indices. From a technical point of view, an important feature of this work is the generation of the strategy based on surrogate modeling to deal with fractures uncertainties. Coupling COMSOL with global sensitivity analysis is also an important outcome that has been never developed in the context of seawater intrusion and in general in applications related to flow and transport in porous media. The findings provide technical support for both preliminary studies and post-processing of monitoring, controlling and prevention of seawater intrusion in fractured coastal aquifers.

The performance and robustness of the developed strategy for uncertainty analysis have been evaluated on the hypothetical case of the fractured Henry problem. Two scenarios were considered in this study: (i) single horizontal fracture with changing location and (ii) network of orthogonal fractures with changing density. The proposed strategy was applied to both scenarios in parallel. We show that fracture hydraulic conductivity is the first source of uncertainty on the salinity distribution. The imperfect knowledge of fracture location and density affects mainly the toe position and the total flux of saltwater entering the aquifer. Marginal effects based on the polynomial chaos expansion are used to understand the effects of fracture characteristics on seawater intrusion. An initial step behind application at real scale is under development on the coastal aquifer of Clashnessie Bay, UK at the northwestern Scotland. This thesis presents the first results of the 3D forward seawater intrusion model.

In the last part of the thesis, we were interested in the simulation of variably saturated flow in fractured domains with the Discrete Fracture/Matrix model which remains a computationally challenging problem. This challenge comes partly from the nonlinear nature of the flow model (Richards' equation for unsaturated flow) and partly from the geometrical and hydrodynamic complexities imposed by the fractures. Most existing techniques are based on the standard

finite element method with a backward Euler scheme for time integration. We developed a hybrid-dimension technique with advanced and appropriate techniques for space and time discretization. The proposed scheme is accurate and computationally more efficient comparing with most conventional methods and schemes used to simulate flow in variably saturated flow in fractured porous media. The developed scheme is based on the mixed hybrid finite element method for space discretization and the method of lines for time integration. We suggest a new mass lumping procedure for the mixed hybrid finite element method to deal with spurious oscillations related to flow in fractures. While existing numerical schemes are based on first-order time integration schemes, the method of lines allows for using higher-order time integration. It allows also the use of an accurate adaptive time-stepping procedure based on error control. The combination of the mass lumping technique with the method of lines significantly improves the computational performance and robustness of the simulations. The accuracy of the proposed scheme is validated by comparing the results on common benchmark and by comparison to the conventional software package (i.e. COMSOL Multiphysics®). The applicability of the newly developed scheme is demonstrated in a study concerning the effect of climate change on the temporal response of a karst aquifer/spring system in El Assal, Lebanon. Simulations are performed to predict the aquifer metrics (e.g. spring recharge) for 80 years, up to 2099. It was shown that neglecting the presence of fractures in the domain will result in considerable misestimating of the available amount of groundwater. This study demonstrates the performance of our proposed scheme to deal with field case studies involving large periods of time. The proposed numerical scheme is generic for Discrete Fracture/Matrix models with any finite element method and can be extended to other applications as well as showing perspective to be applied to other field case studies.

6.2. Perspective

The topics discussed in this work show promises and potential for future assessment. We propose some suggestions, however, the potential research foci are not limited to the following:

1. There is a scarcity of benchmarks and closed-form analytical solutions for seawater intrusion in fractured coastal aquifers. The Fourier series solution can be applied to develop a semi-analytical solution for cases involving simple fractured scenarios of the Henry problem.
2. The semi-analytical solution for contaminant transport in coastal aquifers has been developed for tracer contaminants that do not affect the fluid density. It would be

interesting to extend the study to dense plume migration. This will provide a new benchmark for contaminant transport in coastal aquifers under more realistic conditions and provide better understating on the effect of seawater intrusion on dense plume migration.

3. The methodology of uncertainty analysis for seawater intrusion in fractured coastal aquifers has been applied to a series of 2D theoretical configurations. The extension of a 3D case and real field study is an ongoing research topic. Testing other machine learning techniques as a surrogate model (other than polynomial chaos expansion) is worth investigating.
4. We suggest that the new developed numerical scheme for variably saturated flow could be generalized to 3D domains. The developed model could be helpful in investigating the validity of the Richards' equation to deal with fractured domains. Its validity for unfractured domains has been widely discussed in the literature. However, to the best of our knowledge the validity for fractured domains has never been addressed.

Chapitre VI : conclusion et perspectives

6.1. Conclusion générale

Le travail retranscrit dans ce mémoire de thèse se place dans le contexte de la modélisation numérique des écoulements et du transport de masse en milieux poreux fracturés et se concentre sur deux applications principales : l'intrusion saline dans les aquifères côtiers et l'écoulement variablement saturé en zone vadose fracturée. L'objectif principal des études conduites a consisté à améliorer l'efficacité et la précision des modèles numériques afin d'accroître leur capacité à représenter des configurations toujours plus complexes et réalistes. Une partie importante a été consacrée au développement de solutions semi-analytiques pouvant être utilisées pour l'évaluation de codes et de modèles numériques nouvellement développés et qui sont également utiles pour comprendre les processus physiques en jeu. Une technique efficace, basée sur la modélisation de substitution (i.e. la construction d'un métamodèle), a également été mise au point pour étudier les incertitudes liées aux fractures sur l'intrusion saline. Notre contribution concerne également l'élaboration d'un schéma numérique efficace et avancé, plus performant que les schémas existants, pour la simulation des écoulements variablement saturés dans les domaines fracturés. Des applications réelles basées sur des données de terrain ont été construites et testées pour souligner les capacités des techniques développées.

Seul le problème de Henry dispose d'une solution semi-analytique pour modéliser l'intrusion saline avec le modèle d'écoulement densitaire. Le travail réalisé durant la thèse, et retranscrit dans ce mémoire, a permis d'améliorer le réalisme de cette solution par la prise en compte d'une dispersion dépendant de la vitesse et en considérant un domaine anisotrope et stratifié (i.e. l'aquifère côtier est décrit par une hétérogénéité de couches). Cette approche aboutit à l'une des solutions les plus générales et les plus complètes proposées pour le problème de Henry. Dans la continuité des travaux réalisés précédemment au laboratoire, la nouvelle solution est basée sur la méthode de décomposition en séries de Fourier. Une nouvelle implémentation de la méthode a donc été présentée dans ce mémoire pour traiter la dispersion, l'anisotropie et l'hétérogénéité. Un solveur non linéaire efficace est utilisé pour obtenir des solutions précises, y compris dans le cas de zones de mélange étroites. Des résultats de grande précision sur l'intrusion saline ont été obtenus pour plusieurs variables et indicateurs quantitatifs et pourront être utilisés efficacement dans des études ultérieures destinées à la validation et/ou à l'inter-comparaison de schémas numériques. Tous les indicateurs ont été calculés analytiquement en utilisant les séries de Fourier. Et la solution développée a permis de mieux comprendre les

effets combinés de l'anisotropie et de l'hétérogénéité sur les processus d'intrusion d'eau de mer, et de bien renseigner les indicateurs pertinents qui caractérisent ce problème.

Ainsi, il a été démontré dans ce travail qu'à nombre de gravité constant, la diminution du rapport d'anisotropie (i.e. $r_k = K_z/K_x$) entraîne une intrusion d'eau salée plus importante. La solution semi-analytique montre également que l'anisotropie conduit à une zone de mélange plus large et intensifie le flux d'eau salée entrant dans l'aquifère. En outre, l'origine de certains résultats contradictoires évoqués dans la littérature a pu être expliquée de manière cohérente à l'aide de la solution proposée. Les contradictions relèvent en fait de la manière dont le rapport d'anisotropie a été modifié et de l'effet de ce changement sur l'indice de gravité. Ce travail a également montré que la largeur de la zone de mélange est sensible au taux de stratification. Cette sensibilité augmente avec l'anisotropie des aquifères. Le taux de stratification et l'anisotropie ont des effets complémentaires équivalents sur tous les indicateurs caractérisant l'intrusion saline, exception faite de la profondeur de la zone de déversement des eaux souterraines dans la mer (qui est affectée dans un sens opposé).

Nous nous sommes également intéressés au transport des contaminants dans les aquifères côtiers soumis à l'intrusion saline. D'un point de vue calculatoire, il s'agit d'un problème complexe en raison de la variabilité, dans l'espace et le temps, du champ de vitesse qui est affecté par la concentration en sel. Les solutions analytiques, dans cette configuration, sont rares, ce qui est également le cas d'une manière générale, s'agissant du transport de contaminants soumis à des champs de vitesse non uniformes. Et par ailleurs, les solutions existantes sont basées sur des simplifications importantes (par exemple un faible contraste de densité) qui ne sont dès lors pas représentatives des conditions réelles in-situ. Ainsi, une solution semi-analytique du problème de Henry a été améliorée pour traiter le transport de contaminants dans les aquifères côtiers soumis à l'intrusion d'eau de mer. Deux applications, inspirées de configurations de terrain, ont été réalisées ; la première traite de l'infiltration de contaminants depuis la surface de l'aquifère et la seconde application examine la contamination induite par un flux régional, à l'intérieur de l'aquifère, en amont de l'interface avec l'eau de mer. La solution semi-analytique proposée est obtenue par la méthode de décomposition en séries de Fourier. Plusieurs critères ont été évalués analytiquement afin de caractériser le transport de contaminant, comme par exemple le nombre de Sherwood ou le flux de masse. Les solutions semi-analytiques développées dans le cadre de cette thèse peuvent servir de références pour le transport de contaminants, non seulement dans les aquifères côtiers mais aussi, et plus généralement, dans les systèmes à champ de vitesse variable.

Le développement d'une solution semi-analytique a également permis de mieux comprendre les processus de transport de contaminants dans les aquifères côtiers. En effet, les résultats ont montré que, dans le cas d'une infiltration de contaminant à partir de la surface de l'aquifère, l'intrusion saline limite la propagation du contaminant dans l'aquifère en contractant la zone contaminée. Cependant, l'intensification de l'intrusion d'eau de mer n'a pas d'effets significatifs sur le flux de contaminants rejeté dans la mer. Pour le second scénario présentant une contamination interne de l'aquifère en amont de l'interface eau douce / eau de mer, l'intrusion modérée de l'eau de mer affecte principalement la distribution spatiale du panache de contamination, tandis qu'une forte intrusion saline peut augmenter le flux de contaminants rejeté dans la mer. La solution semi-analytique proposée comble un certain manque d'information fournie par la littérature pour l'évaluation comparative du transport de contaminants dans des situations de champs de vitesse variable et les résultats qui en découlent donnent par ailleurs des indications précieuses pour la gestion des ressources d'eau douce au sein des aquifères côtiers.

Une partie de ce travail de thèse s'est également intéressée à l'intrusion saline dans les aquifères côtiers fracturés. L'un des modèles les plus fiables pour aborder la dynamique de l'intrusion saline, dans ce cas, est basé sur l'écoulement densitaire appliqué à un réseau de fractures discrètes dans lequel les fractures sont prises en compte de manière explicite. Toutefois, cette approche nécessite une description détaillée et explicite des fractures. Subséquemment, l'incertitude en entrée sur la topologie des fractures et les propriétés hydrodynamiques peut provoquer une incertitude importante sur les résultats de ce modèle. Une stratégie efficace pour étudier la propagation de l'incertitude dans cette configuration a ainsi été élaborée. Celle-ci est basée sur l'analyse de sensibilité globale via les indices de Sobol. L'évaluation de ces indices nécessite un grand nombre de simulations qui, réalisées à l'aide du modèle d'écoulement densitaire, requerraient un temps CPU élevé. Aussi, le recours à un modèle de substitution a été réalisé avec succès puisqu'il permet d'optimiser le nombre de simulations opérées avec le modèle d'écoulement densitaire. Le modèle de base a été développé en utilisant COMSOL Multiphysics dont les simulations sont ensuite utilisées pour construire le modèle de substitution basé sur un développement en polynômes du chaos. Une nouvelle technique d'expansion a été implémentée afin d'optimiser le compromis entre l'ordre polynomial, la précision et le temps de calcul. Le modèle de substitution est ensuite utilisé pour obtenir les indices de sensibilité de Sobol. D'un point de vue technique, une avancée significative de ce travail porte sur la mise en œuvre de la stratégie de substitution pour déterminer et analyser les

incertitudes du modèle d'écoulement densitaire en milieu fracturé. Le couplage de COMSOL avec l'analyse de sensibilité globale constitue aussi une démarche novatrice, jamais entreprise dans le contexte de l'intrusion saline, et plus généralement pour aborder les applications d'écoulement et de transport en milieux poreux. La méthodologie et les résultats présentés fournissent un cadre technique pour les études préliminaires et le post-traitement associé au suivi, au contrôle et à la prévention de l'intrusion saline dans les aquifères côtiers fracturés.

Au niveau applicatif, les performances et la robustesse de la stratégie développée pour l'analyse d'incertitudes ont été évaluées sur le cas synthétique du problème de Henry fracturé. Deux scénarios ont été investigués dans cette étude : le premier considère une unique fracture horizontale avec changement de localisation tandis que le second s'appuie sur un réseau de fractures orthogonales avec changement de densité. La stratégie évoquée ci-avant a été appliquée aux deux scénarios en parallèle. Il a ainsi été montré que la conductivité hydraulique des fractures est la première source d'incertitude sur la distribution de salinité. La connaissance imparfaite de la localisation et de la densité de fractures affecte principalement la position de l'extrémité du biseau salé et le flux total d'eau salée entrant dans l'aquifère. Les effets marginaux, calculés à partir des polynômes du chaos, ont été utilisés pour comprendre les répercussions des caractéristiques des fractures sur l'intrusion d'eau de mer. Enfin, une première étape vers l'application à l'échelle réelle a été franchie dans cette thèse avec le développement d'un modèle de l'aquifère côtier de la baie de Clashnessie, au Royaume-Uni, dans le nord-ouest de l'Écosse. Les premiers résultats 3D du modèle direct d'intrusion saline ont aussi été présentés.

La dernière partie de ce mémoire de thèse a été consacrée à la simulation des écoulements variablement saturés, dans des domaines fracturés, avec le modèle à réseau de fractures discrètes, problème dont les difficultés sur le plan numérique et informatique ont été par ailleurs soulignées. Le challenge tient pour partie à la nature non linéaire du modèle d'écoulement (équation de Richards pour l'écoulement non saturé) et également à la complexité géométrique et au contraste hydrodynamique imposés par les fractures. La plupart des techniques existantes sont basées sur la méthode standard des éléments finis avec un schéma d'Euler implicite (i.e. schéma amont d'ordre 1) pour l'intégration temporelle.

Une approche à dimension hybride (i.e. fractures 1D et matrice 2D) a été développée et combinée à des techniques avancées de discrétisations en espace et en temps. Le schéma proposé est précis et plus efficace sur le plan du calcul que la plupart des méthodes et schémas

conventionnels utilisés pour simuler l'écoulement en milieu poreux fracturé variablement saturé. Il est basé sur la méthode des éléments finis mixtes hybrides (EFMH) pour la discrétisation spatiale et la méthode des lignes pour l'intégration en temps. Une nouvelle procédure de condensation de la masse pour la méthode EFMH a été élaborée afin d'éviter les oscillations parasites liées à l'écoulement dans les fractures. Alors que les schémas numériques existants sont basés sur des formules d'intégration temporelle du premier ordre, la méthode des lignes permet d'utiliser une intégration temporelle d'ordre supérieur. Elle permet également l'utilisation d'une procédure précise d'adaptation du pas de temps basée sur le contrôle des erreurs en cours de simulation. La combinaison de la technique de condensation de la masse avec la méthode des lignes améliore considérablement les performances de calcul et la robustesse des simulations. Le schéma proposé a été validé, et sa précision évaluée, en comparant, pour un problème de référence défini, les résultats des simulations opérées également avec un progiciel classique (i.e. COMSOL Multiphysics®) et/ou avec un modèle sans réduction de dimension.

L'applicabilité du nouveau schéma développé a été démontrée dans le cadre d'une étude concernant l'effet du changement climatique sur la réponse temporelle d'un aquifère fracturé à El Assal, au Liban. Des simulations ont été réalisées pour évaluer certains indicateurs hydrologiques de l'aquifère (par exemple, la recharge de nappe) sur 80 ans, jusqu'en 2099. Il a été établi que le fait de négliger la présence de fractures dans le domaine entraînerait une mauvaise estimation de la quantité d'eau souterraine disponible. Dans ce contexte, cette étude a démontré la performance du schéma proposé pour traiter des études de terrain impliquant de longues périodes de temps. Le schéma numérique proposé est générique pour les modèles de réseaux de fractures discrètes résolus avec n'importe quelle méthode d'éléments finis et il peut ainsi être étendu à d'autres applications, ou s'inscrire en perspectives sur d'autres cas de terrain.

6.2. Perspectives

Les thèmes abordés dans ce mémoire sont prometteurs et offrent différentes orientations possibles pour de futurs travaux de recherche. Quelques suggestions sont ainsi proposées dans les paragraphes suivants, sans que cela n'en fasse une liste exhaustive des axes de recherche envisageables.

5. La problématique de l'intrusion saline dans les aquifères côtiers fracturés ne dispose pas de solution exacte, analytique ou semi-analytique. Le développement en séries de Fourier pourrait être appliqué pour construire une solution semi-analytique au problème de Henry présentant des configurations avec des fractures simples.
6. La solution semi-analytique pour le transport de contaminants dans les aquifères côtiers ne prend pas en compte l'effet du contaminant sur la densité du fluide. Aussi, il serait intéressant d'étendre l'étude analytique à la migration de panache dense. Cela permettrait de disposer d'une solution de référence pour simuler le transport de contaminants dans les aquifères côtiers dans des conditions plus réalistes et ainsi de mieux estimer l'effet de l'intrusion saline sur la migration d'un panache dense.
7. La méthodologie de l'analyse d'incertitudes pour l'intrusion saline dans les aquifères côtiers fracturés a été appliquée à une série de configurations théoriques 2D. Son extension à un cas 3D et une étude réelle de terrain constitue un sujet de recherche en cours. Des tests avec d'autres techniques d'apprentissage machine en tant que modèle de substitution (à comparer avec la décomposition en polynômes du chaos) méritent certainement une attention particulière.
8. Le nouveau schéma numérique développé pour les écoulements variablement saturés en milieux poreux fracturés pourrait être généralisé aux domaines 3D. Par ailleurs, ce modèle pourrait être utile pour étudier la validité de l'équation de Richards dans ce contexte particulier. Cette question a été largement discutée dans la littérature pour les domaines non fracturés. Cependant, à notre connaissance, la question de la validité n'a jamais été abordée pour les domaines fracturés.

References

- Abarca, E., Carrera, J., Sánchez-Vila, X., Dentz, M., 2007. Anisotropic dispersive Henry problem. *Advances in Water Resources* 30, 913–926. <https://doi.org/10.1016/j.advwatres.2006.08.005>
- Abd-Elhamid, H.F., Javadi, A.A., 2011. A density-dependant finite element model for analysis of saltwater intrusion in coastal aquifers. *Journal of Hydrology* 401, 259–271. <https://doi.org/10.1016/j.jhydrol.2011.02.028>
- Ahmed, R., Edwards, M.G., Lamine, S., Huisman, B.A.H., Pal, M., 2017. CVD-MPFA full pressure support, coupled unstructured discrete fracture–matrix Darcy-flux approximations. *Journal of Computational Physics* 349, 265–299. <https://doi.org/10.1016/j.jcp.2017.07.041>
- Alazard, M., Boisson, A., Maréchal, J.-C., Perrin, J., Dewandel, B., Schwarz, T., Pettenati, M., Picot-Colbeaux, G., Kloppman, W., Ahmed, S., 2016. Investigation of recharge dynamics and flow paths in a fractured crystalline aquifer in semi-arid India using borehole logs: implications for managed aquifer recharge. *Hydrogeol J* 24, 35–57. <https://doi.org/10.1007/s10040-015-1323-5>
- Alberti, L., La Licata, I., Cantone, M., 2017. Saltwater Intrusion and Freshwater Storage in Sand Sediments along the Coastline: Hydrogeological Investigations and Groundwater Modeling of Nauru Island. *Water* 9, 788. <https://doi.org/10.3390/w9100788>
- Alhama Manteca, I., Alcaraz, M., Trigueros, E., Alhama, F., 2014. Dimensionless characterization of salt intrusion benchmark scenarios in anisotropic media. *Applied Mathematics and Computation* 247, 1173–1182. <https://doi.org/10.1016/j.amc.2014.09.033>
- Al-Khoury, R., 2012. Computational modeling of shallow geothermal systems, Multiphysics modeling. CRC Press, Boca Raton, [Fla.].
- Ameli, A.A., Craig, J.R., 2014. Semianalytical series solutions for three-dimensional groundwater-surface water interaction. *Water Resources Research* 50, 3893–3906. <https://doi.org/10.1002/2014WR015394>
- Anwar, N., Robinson, C., Barry, D.A., 2014. Influence of tides and waves on the fate of nutrients in a nearshore aquifer: Numerical simulations. *Advances in Water Resources* 73, 203–213. <https://doi.org/10.1016/j.advwatres.2014.08.015>
- Arfib, B., Charlier, J.-B., 2016. Insights into saline intrusion and freshwater resources in coastal karstic aquifers using a lumped Rainfall–Discharge–Salinity model (the Port-Miou brackish spring, SE France). *Journal of Hydrology* 540, 148–161. <https://doi.org/10.1016/j.jhydrol.2016.06.010>
- Aricò, C., Sinagra, M., Tucciarelli, T., 2012. The MAST-edge centred lumped scheme for the flow simulation in variably saturated heterogeneous porous media. *Journal of Computational Physics* 231, 1387–1425. <https://doi.org/10.1016/j.jcp.2011.10.012>
- Ataie-Ashtiani, B., 2007. MODSharp: Regional-scale numerical model for quantifying groundwater flux and contaminant discharge into the coastal zone. *Environmental Modelling & Software* 22, 1307–1315. <https://doi.org/10.1016/j.envsoft.2006.07.005>

- Ataie-Ashtiani, B., Werner, A.D., Simmons, C.T., Morgan, L.K., Lu, C., 2013. How important is the impact of land-surface inundation on seawater intrusion caused by sea-level rise? *Hydrogeology Journal* 21, 1673–1677. <https://doi.org/10.1007/s10040-013-1021-0>
- Bakalowicz, M., El Hakim, M., El-Hajj, A., 2008. Karst groundwater resources in the countries of eastern Mediterranean: the example of Lebanon. *Environmental Geology* 54, 597–604. <https://doi.org/10.1007/s00254-007-0854-z>
- Bakhtyar, R., Brovelli, A., Barry, D.A., Robinson, C., Li, L., 2013. Transport of variable-density solute plumes in beach aquifers in response to oceanic forcing. *Advances in Water Resources* 53, 208–224. <https://doi.org/10.1016/j.advwatres.2012.11.009>
- Barragán, J.M., de Andrés, M., 2015. Analysis and trends of the world's coastal cities and agglomerations. *Ocean & Coastal Management* 114, 11–20. <https://doi.org/10.1016/j.ocecoaman.2015.06.004>
- Bear, J., Cheng, A.H.-D., Sorek, S., Ouazar, D., Herrera, I. (Eds.), 1999. *Seawater Intrusion in Coastal Aquifers — Concepts, Methods and Practices, Theory and Applications of Transport in Porous Media*. Springer Netherlands, Dordrecht. <https://doi.org/10.1007/978-94-017-2969-7>
- Beaujean, J., Nguyen, F., Kemna, A., Antonsson, A., Engesgaard, P., 2014. Calibration of seawater intrusion models: Inverse parameter estimation using surface electrical resistivity tomography and borehole data. *Water Resources Research* 50, 6828–6849. <https://doi.org/10.1002/2013WR014020>
- Belfort, B., Ramasomanana, F., Younes, A., Lehmann, F., 2009. An Efficient Lumped Mixed Hybrid Finite Element Formulation for Variably Saturated Groundwater Flow. *Vadose Zone Journal* 8, 352–362. <https://doi.org/10.2136/vzj2008.0108>
- Belfort, B., Younes, A., Fahs, M., Lehmann, F., 2013. On equivalent hydraulic conductivity for oscillation-free solutions of Richard's equation. *Journal of Hydrology* 505, 202–217. <https://doi.org/10.1016/j.jhydrol.2013.09.047>
- Ben Abdelghani, F., Aubertin, M., Simon, R., Therrien, R., 2015. Numerical simulations of water flow and contaminants transport near mining wastes disposed in a fractured rock mass. *International Journal of Mining Science and Technology* 25, 37–45. <https://doi.org/10.1016/j.ijmst.2014.11.003>
- Berkowitz, B., 2002. Characterizing flow and transport in fractured geological media: A review. *Advances in Water Resources* 25, 861–884. [https://doi.org/10.1016/S0309-1708\(02\)00042-8](https://doi.org/10.1016/S0309-1708(02)00042-8)
- Berre, I., Doster, F., Keilegavlen, E., 2019. Flow in Fractured Porous Media: A Review of Conceptual Models and Discretization Approaches. *Transp Porous Med* 130, 215–236. <https://doi.org/10.1007/s11242-018-1171-6>
- Blatman, G., Sudret, B., 2011. Adaptive sparse polynomial chaos expansion based on least angle regression. *Journal of Computational Physics* 230, 2345–2367. <https://doi.org/10.1016/j.jcp.2010.12.021>
- BniLam, N., Al-Khoury, R., 2017. A spectral element model for nonhomogeneous heat flow in shallow geothermal systems. *International Journal of Heat and Mass Transfer* 104, 703–717. <https://doi.org/10.1016/j.ijheatmasstransfer.2016.08.055>

- Bolster, D.T., Tartakovsky, D.M., Dentz, M., 2007. Analytical models of contaminant transport in coastal aquifers. *Advances in Water Resources* 30, 1962–1972. <https://doi.org/10.1016/j.advwatres.2007.03.007>
- Boufadel, M.C., Suidan, M.T., Venosa, A.D., 1999. A numerical model for density-and-viscosity-dependent flows in two-dimensional variably saturated porous media. *Journal of Contaminant Hydrology* 37, 1–20. [https://doi.org/10.1016/S0169-7722\(98\)00164-8](https://doi.org/10.1016/S0169-7722(98)00164-8)
- Brezzi, F., Fortin, M. (Eds.), 1991. *Mixed and Hybrid Finite Element Methods*, Springer Series in Computational Mathematics. Springer New York, New York, NY. <https://doi.org/10.1007/978-1-4612-3172-1>
- Brouyère, S., 2006. Modelling the migration of contaminants through variably saturated dual-porosity, dual-permeability chalk. *Journal of Contaminant Hydrology* 82, 195–219. <https://doi.org/10.1016/j.jconhyd.2005.10.004>
- Bruggeman, G.A., 1999. *Analytical Solutions of Geohydrological Problems*. Elsevier, Burlington.
- Burdakov, O., Kapyrin, I., Vassilevski, Y., 2012. Monotonicity recovering and accuracy preserving optimization methods for postprocessing finite element solutions. *Journal of Computational Physics* 231, 3126–3142. <https://doi.org/10.1016/j.jcp.2011.12.041>
- Burrows, W., Doherty, J., 2015. Efficient Calibration/Uncertainty Analysis Using Paired Complex/Surrogate Models. *Groundwater* 53, 531–541. <https://doi.org/10.1111/gwat.12257>
- Carrera, J., Hidalgo, J.J., Slooten, L.J., Vázquez-Suñé, E., 2010. Computational and conceptual issues in the calibration of seawater intrusion models. *Hydrogeol J* 18, 131–145. <https://doi.org/10.1007/s10040-009-0524-1>
- Celia, M.A., Bouloutas, E.T., Zarba, R.L., 1990. A general mass-conservative numerical solution for the unsaturated flow equation. *Water Resour. Res.* 26, 1483–1496. <https://doi.org/10.1029/WR026i007p01483>
- Cey, E., Rudolph, D., Therrien, R., 2006. Simulation of groundwater recharge dynamics in partially saturated fractured soils incorporating spatially variable fracture apertures. *Water Resour. Res.* 42. <https://doi.org/10.1029/2005WR004589>
- Chang, C.-M., Yeh, H.-D., 2010. Spectral approach to seawater intrusion in heterogeneous coastal aquifers. *Hydrol. Earth Syst. Sci.* 14, 719–727. <https://doi.org/10.5194/hess-14-719-2010>
- Chang, S.W., Clement, T.P., 2013. Laboratory and numerical investigation of transport processes occurring above and within a saltwater wedge. *Journal of Contaminant Hydrology* 147, 14–24. <https://doi.org/10.1016/j.jconhyd.2013.02.005>
- Chang, S.W., Clement, T.P., Simpson, M.J., Lee, K.-K., 2011. Does sea-level rise have an impact on saltwater intrusion? *Advances in Water Resources* 34, 1283–1291. <https://doi.org/10.1016/j.advwatres.2011.06.006>
- Chang, Y., Wu, J., Jiang, G., Liu, L., Reimann, T., Sauter, M., 2019. Modelling spring discharge and solute transport in conduits by coupling CFPv2 to an epikarst reservoir for a karst aquifer. *Journal of Hydrology* 569, 587–599. <https://doi.org/10.1016/j.jhydrol.2018.11.075>

- Chavent, G., Jaffre, J., 2014. *Mathematical Models and Finite Elements for Reservoir Simulation: Single Phase, Multiphase and Multicomponent Flows through Porous Media*. Elsevier Science, Burlington.
- Chen, B.-F., Hsu, S.-M., 2004. Numerical Study of Tidal Effects on Seawater Intrusion in Confined and Unconfined Aquifers by Time-Independent Finite-Difference Method. *J. Waterway, Port, Coastal, Ocean Eng.* 130, 191–206. [https://doi.org/10.1061/\(ASCE\)0733-950X\(2004\)130:4\(191\)](https://doi.org/10.1061/(ASCE)0733-950X(2004)130:4(191))
- Chen, H., Salama, A., Sun, S., 2016. Adaptive mixed finite element methods for Darcy flow in fractured porous media. *Water Resour. Res.* 52, 7851–7868. <https://doi.org/10.1002/2015WR018450>
- Chen, J.-S., Hsu, S.-Y., Li, M.-H., Liu, C.-W., 2016a. Assessing the performance of a permeable reactive barrier–aquifer system using a dual-domain solute transport model. *Journal of Hydrology* 543, 849–860. <https://doi.org/10.1016/j.jhydrol.2016.11.002>
- Chen, J.-S., Lai, K.-H., Liu, C.-W., Ni, C.-F., 2012. A novel method for analytically solving multi-species advective–dispersive transport equations sequentially coupled with first-order decay reactions. *Journal of Hydrology* 420–421, 191–204. <https://doi.org/10.1016/j.jhydrol.2011.12.001>
- Chen, J.-S., Liang, C.-P., Liu, C.-W., Li, L.Y., 2016b. An analytical model for simulating two-dimensional multispecies plume migration. *Hydrology and Earth System Sciences* 20, 733–753. <https://doi.org/10.5194/hess-20-733-2016>
- Chen, K., Zhan, H., Zhou, R., 2016. Subsurface solute transport with one-, two-, and three-dimensional arbitrary shape sources. *Journal of Contaminant Hydrology* 190, 44–57. <https://doi.org/10.1016/j.jconhyd.2016.04.004>
- Chen, Z., 2007. *Reservoir simulation: mathematical techniques in oil recovery*, CBMS-NSF regional conference series in applied mathematics. SIAM/Society for Industrial and Applied Mathematics, Philadelphia, PA.
- Chen, Z., Auler, A.S., Bakalowicz, M., Drew, D., Griger, F., Hartmann, J., Jiang, G., Moosdorf, N., Richts, A., Stevanovic, Z., Veni, G., Goldscheider, N., 2017. The World Karst Aquifer Mapping project: concept, mapping procedure and map of Europe. *Hydrogeology Journal* 25, 771–785. <https://doi.org/10.1007/s10040-016-1519-3>
- Ciriello, V., Federico, V.D., Riva, M., Cadini, F., Sanctis, J.D., Zio, E., Guadagnini, A., 2013. Polynomial chaos expansion for global sensitivity analysis applied to a model of radionuclide migration in a randomly heterogeneous aquifer. *Stochastic Environmental Research and Risk Assessment* 27, 945–954. <https://doi.org/10.1007/s00477-012-0616-7>
- Class, H., Ebigbo, A., Helmig, R., Dahle, H.K., Nordbotten, J.M., Celia, M.A., Audigane, P., Darcis, M., Ennis-King, J., Fan, Y., Flemisch, B., Gasda, S.E., Jin, M., Krug, S., Labregere, D., Naderi Beni, A., Pawar, R.J., Sbai, A., Thomas, S.G., Trenty, L., Wei, L., 2009. A benchmark study on problems related to CO₂ storage in geologic formations: Summary and discussion of the results. *Comput Geosci* 13, 409–434. <https://doi.org/10.1007/s10596-009-9146-x>
- Clement, T.P., Wise, W.R., Molz, F.J., 1994. A physically based, two-dimensional, finite-difference algorithm for modeling variably saturated flow. *Journal of Hydrology* 161, 71–90. [https://doi.org/10.1016/0022-1694\(94\)90121-X](https://doi.org/10.1016/0022-1694(94)90121-X)
- Collet, I., Engelbert, A., 2013. Coastal regions: people living along the coastline, integration of NUTS 2010 and latest population grid [WWW Document]. URL

<http://ec.europa.eu/eurostat/web/products-statistics-in-focus/-/KS-SF-13-030> (accessed 3.9.17).

- Comte, J.-C., Ofterdinger, U., Legchenko, A., Caulfield, J., Cassidy, R., Mézquita González, J.A., 2019. Catchment-scale heterogeneity of flow and storage properties in a weathered/fractured hard rock aquifer from resistivity and magnetic resonance surveys: implications for groundwater flow paths and the distribution of residence times. *Geological Society, London, Special Publications* 479, 35–58. <https://doi.org/10.1144/SP479.11>
- Cox, M.E., Hillier, J., Foster, L., Ellis, R., 1996. Effects Of A Rapidly Urbanising Environment On Groundwater, Brisbane, Queensland, Australia. *Hydrogeology Journal* 4, 30–47. <https://doi.org/10.1007/s100400050084>
- Craig, J.R., Heidlauf, T., 2009. Coordinate mapping of analytical contaminant transport solutions to non-uniform flow fields. *Advances in Water Resources* 32, 353–360. <https://doi.org/10.1016/j.advwatres.2008.11.013>
- Crestaux, T., Le Maître, O., Martinez, J.-M., 2009. Polynomial chaos expansion for sensitivity analysis. *Reliability Engineering & System Safety* 94, 1161–1172. <https://doi.org/10.1016/j.ress.2008.10.008>
- Curtis, A.R., Powell, M.J.D., Reid, J.K., 1974. On the Estimation of Sparse Jacobian Matrices. *IMA Journal of Applied Mathematics* 13, 117–119. <https://doi.org/10.1093/imamat/13.1.117>
- Dagan, G., Zeitoun, D.G., 1998. Seawater-freshwater interface in a stratified aquifer of random permeability distribution. *Journal of Contaminant Hydrology* 29, 185–203. [https://doi.org/10.1016/S0169-7722\(97\)00013-2](https://doi.org/10.1016/S0169-7722(97)00013-2)
- Dai, H., Chen, X., Ye, M., Song, X., Zachara, J.M., 2017. A geostatistics-informed hierarchical sensitivity analysis method for complex groundwater flow and transport modeling. *Water Resources Research* 53, 4327–4343. <https://doi.org/10.1002/2016WR019756>
- Davis, T.A., 2004. Algorithm 832: UMFPACK V4.3: an unsymmetric-pattern multifrontal method. *ACM Transactions on Mathematical Software* 30, 196–199. <https://doi.org/10.1145/992200.992206>
- De Rocquigny, E., 2012. *Modelling Under Risk and Uncertainty: An Introduction to Statistical, Phenomenological and Computational Methods*. John Wiley & Sons.
- De Rooij, R., 2019. Improving accuracy and efficiency in discrete-continuum karst models. *Environ Earth Sci* 78, 115. <https://doi.org/10.1007/s12665-019-8115-5>
- De Rooij, R., Perrochet, P., Graham, W., 2013. From rainfall to spring discharge: Coupling conduit flow, subsurface matrix flow and surface flow in karst systems using a discrete-continuum model. *Advances in Water Resources* 61, 29–41. <https://doi.org/10.1016/j.advwatres.2013.08.009>
- Dell’Oca, A., Riva, M., Guadagnini, A., 2017. Moment-based metrics for global sensitivity analysis of hydrological systems. *Hydrol. Earth Syst. Sci.* 21, 6219–6234. <https://doi.org/10.5194/hess-21-6219-2017>
- Deman, G., Konakli, K., Sudret, B., Kerrou, J., Perrochet, P., Benabderrahmane, H., 2016. Using sparse polynomial chaos expansions for the global sensitivity analysis of groundwater lifetime expectancy in a multi-layered hydrogeological model. *Reliability Engineering & System Safety* 147, 156–169. <https://doi.org/10.1016/j.ress.2015.11.005>

- Deng, B., Wang, J., 2017. Saturated-unsaturated groundwater modeling using 3D Richards equation with a coordinate transform of nonorthogonal grids. *Applied Mathematical Modelling* 50, 39–52. <https://doi.org/10.1016/j.apm.2017.05.021>
- Diaz Viera, M.A. (Ed.), 2012. *Mathematical and numerical modeling in porous media: applications in geosciences, Multiphysics modeling*. CRC Press ; Balkema, Boca Raton : Leiden.
- Diersch, H.-J.G., Kolditz, O., 2002. Variable-density flow and transport in porous media: approaches and challenges. *Advances in Water Resources* 25, 899–944. [https://doi.org/10.1016/S0309-1708\(02\)00063-5](https://doi.org/10.1016/S0309-1708(02)00063-5)
- Dietrich, P., Helmig, R., Sauter, M., Hötzl, H., Köngeter, J., Teutsch, G. (Eds.), 2005. *Flow and Transport in Fractured Porous Media*. Springer-Verlag, Berlin Heidelberg.
- Dokou, Z., Karatzas, G.P., 2012. Saltwater intrusion estimation in a karstified coastal system using density-dependent modelling and comparison with the sharp-interface approach. *Hydrological Sciences Journal* 57, 985–999. <https://doi.org/10.1080/02626667.2012.690070>
- Dose, E.J., Stoeckl, L., Houben, G.J., Vacher, H.L., Vassolo, S., Dietrich, J., Himmelsbach, T., 2014. Experiments and modeling of freshwater lenses in layered aquifers: Steady state interface geometry. *Journal of Hydrology* 509, 621–630. <https://doi.org/10.1016/j.jhydrol.2013.10.010>
- Doummar, J., Hassan Kassem, A., Gurdak, J.J., 2018. Impact of historic and future climate on spring recharge and discharge based on an integrated numerical modelling approach: Application on a snow-governed semi-arid karst catchment area. *Journal of Hydrology* 565, 636–649. <https://doi.org/10.1016/j.jhydrol.2018.08.062>
- Dufresne, J.-L., Foujols, M.-A., Denvil, S., Caubel, A., Marti, O., Aumont, O., Balkanski, Y., Bekki, S., Bellenger, H., Benshila, R., Bony, S., Bopp, L., Braconnot, P., Brockmann, P., Cadule, P., Cheruy, F., Codron, F., Cozic, A., Cugnet, D., de Noblet, N., Duvel, J.-P., Ethé, C., Fairhead, L., Fichefet, T., Flavoni, S., Friedlingstein, P., Grandpeix, J.-Y., Guez, L., Guilyardi, E., Hauglustaine, D., Hourdin, F., Idelkadi, A., Ghattas, J., Joussaume, S., Kageyama, M., Krinner, G., Labetoulle, S., Lahellec, A., Lefebvre, M.-P., Lefevre, F., Levy, C., Li, Z.X., Lloyd, J., Lott, F., Madec, G., Mancip, M., Marchand, M., Masson, S., Meurdesoif, Y., Mignot, J., Musat, I., Parouty, S., Polcher, J., Rio, C., Schulz, M., Swingedouw, D., Szopa, S., Talandier, C., Terray, P., Viovy, N., Vuichard, N., 2013. Climate change projections using the IPSL-CM5 Earth System Model: from CMIP3 to CMIP5. *Clim Dyn* 40, 2123–2165. <https://doi.org/10.1007/s00382-012-1636-1>
- Durran, D.R., 1999. *Numerical Methods for Wave Equations in Geophysical Fluid Dynamics*, Texts in Applied Mathematics. Springer New York, New York, NY. <https://doi.org/10.1007/978-1-4757-3081-4>
- Elguedj, T., Gravouil, A., Maigre, H., 2009. An explicit dynamics extended finite element method. Part 1: Mass lumping for arbitrary enrichment functions. *Computer Methods in Applied Mechanics and Engineering* 198, 2297–2317. <https://doi.org/10.1016/j.cma.2009.02.019>
- Emami-Meybodi, H., Hassanzadeh, H., 2015. Two-phase convective mixing under a buoyant plume of CO₂ in deep saline aquifers. *Advances in Water Resources* 76, 55–71. <https://doi.org/10.1016/j.advwatres.2014.11.011>

- Emami-Meybodi, H., Hassanzadeh, H., Ennis-King, J., 2015. CO₂ dissolution in the presence of background flow of deep saline aquifers: CO₂ dissolution in the presence of background flow. *Water Resources Research* 51, 2595–2615. <https://doi.org/10.1002/2014WR016659>
- Esfandiar, B., Porta, G., Perotto, S., Guadagnini, A., 2015. Impact of space-time mesh adaptation on solute transport modeling in porous media. *Water Resources Research* 51, 1315–1332. <https://doi.org/10.1002/2014WR016569>
- Essaid, H.I., 1990. A multilayered sharp interface model of coupled freshwater and saltwater flow in coastal systems: Model development and application. *Water Resour. Res.* 26, 1431–1454. <https://doi.org/10.1029/WR026i007p01431>
- Fahs, H., Hayek, M., Fahs, M., Younes, A., 2014. An efficient numerical model for hydrodynamic parameterization in 2D fractured dual-porosity media. *Advances in Water Resources* 63, 179–193. <https://doi.org/10.1016/j.advwatres.2013.11.008>
- Fahs, M., Ataie-Ashtiani, B., Younes, A., Simmons, C.T., Ackerer, P., 2016. The Henry problem: New semianalytical solution for velocity-dependent dispersion. *Water Resources Research* 52, 7382–7407. <https://doi.org/10.1002/2016WR019288>
- Fahs, M., Koohbor, B., Belfort, B., Ataie-Ashtiani, B., Simmons, C., Younes, A., Ackerer, P., 2018. A Generalized Semi-Analytical Solution for the Dispersive Henry Problem: Effect of Stratification and Anisotropy on Seawater Intrusion. *Water* 10, 230. <https://doi.org/10.3390/w10020230>
- Fahs, M., Younes, A., Lehmann, F., 2009. An easy and efficient combination of the Mixed Finite Element Method and the Method of Lines for the resolution of Richards' Equation. *Environmental Modelling & Software* 24, 1122–1126. <https://doi.org/10.1016/j.envsoft.2009.02.010>
- Fahs, M., Younes, A., Makradi, A., 2015. A Reference Benchmark Solution for Free Convection in A Square Cavity Filled with A Heterogeneous Porous Medium. *Numerical Heat Transfer, Part B: Fundamentals* 67, 437–462. <https://doi.org/10.1080/10407790.2014.977183>
- Fahs, M., Younes, A., Mara, T.A., 2014. A new benchmark semi-analytical solution for density-driven flow in porous media. *Advances in Water Resources* 70, 24–35. <https://doi.org/10.1016/j.advwatres.2014.04.013>
- Fairley, J.P., Podgorney, R.K., Wood, T.R., 2004. Unsaturated Flow through a Small Fracture-Matrix Network: Part 2. Uncertainty in Modeling Flow Processes. *Vadose Zone Journal* 3, 101–108. <https://doi.org/10.2113/3.1.101>
- Fajraoui, N., Fahs, M., Younes, A., Sudret, B., 2017. Analyzing natural convection in porous enclosure with polynomial chaos expansions: Effect of thermal dispersion, anisotropic permeability and heterogeneity. *International Journal of Heat and Mass Transfer* 115, 205–224. <https://doi.org/10.1016/j.ijheatmasstransfer.2017.07.003>
- Fajraoui, N., Mara, T.A., Younes, A., Bouhlila, R., 2012. Reactive Transport Parameter Estimation and Global Sensitivity Analysis Using Sparse Polynomial Chaos Expansion. *Water, Air, & Soil Pollution* 223, 4183–4197. <https://doi.org/10.1007/s11270-012-1183-8>
- Fajraoui, N., Ramasomanana, F., Younes, A., Mara, T.A., Ackerer, P., Guadagnini, A., 2011. Use of global sensitivity analysis and polynomial chaos expansion for interpretation of

- nonreactive transport experiments in laboratory-scale porous media. *Water Resources Research* 47. <https://doi.org/10.1029/2010WR009639>
- Farhloul, M., 2020. Mixed finite element methods for the Oseen problem. *Numer Algor.* <https://doi.org/10.1007/s11075-020-00879-9>
- Farhloul, M., Fortin, M., 2002. Review and complements on mixed-hybrid finite element methods for fluid flows. *Journal of Computational and Applied Mathematics* 140, 301–313. [https://doi.org/10.1016/S0377-0427\(01\)00520-9](https://doi.org/10.1016/S0377-0427(01)00520-9)
- Farthing, M.W., Kees, C.E., Miller, C.T., 2003. Mixed finite element methods and higher order temporal approximations for variably saturated groundwater flow. *Advances in Water Resources* 26, 373–394. [https://doi.org/10.1016/S0309-1708\(02\)00187-2](https://doi.org/10.1016/S0309-1708(02)00187-2)
- Farthing, M.W., Ogden, F.L., 2017. Numerical Solution of Richards' Equation: A Review of Advances and Challenges. *Soil Science Society of America Journal* 81, 1257–1269. <https://doi.org/10.2136/sssaj2017.02.0058>
- Felisa, G., Ciriello, V., Di Federico, V., 2013. Saltwater Intrusion in Coastal Aquifers: A Primary Case Study along the Adriatic Coast Investigated within a Probabilistic Framework. *Water* 5, 1830–1847. <https://doi.org/10.3390/w5041830>
- Fidelibus, M.D., Calò, G., Tinelli, R., Tulipano, L., 2011. Salt ground waters in the Salento karstic coastal aquifer (Apulia, Southern Italy), in: *Advances in the Research of Aquatic Environment, Environmental Earth Sciences*. Springer, Berlin, Heidelberg, pp. 407–415. https://doi.org/10.1007/978-3-642-19902-8_48
- Finkel, M., Grathwohl, P., Cirpka, O.A., 2016. A travel time-based approach to model kinetic sorption in highly heterogeneous porous media via reactive hydrofacies. *Water Resources Research* 52, 9390–9411. <https://doi.org/10.1002/2016WR019147>
- Firoozabadi, A., Myint, P.C., 2010. Prospects for subsurface CO₂ sequestration. *AIChE J.* 56, 1398–1405. <https://doi.org/10.1002/aic.12287>
- Fischer, P., Jardani, A., Cardiff, M., Lecoq, N., Jourde, H., 2018. Hydraulic analysis of harmonic pumping tests in frequency and time domains for identifying the conduits networks in a karstic aquifer. *Journal of Hydrology* 559, 1039–1053. <https://doi.org/10.1016/j.jhydrol.2018.03.010>
- Forsyth, P.A., Wu, Y.S., Pruess, K., 1995. Robust numerical methods for saturated-unsaturated flow with dry initial conditions in heterogeneous media. *Advances in Water Resources* 18, 25–38. [https://doi.org/10.1016/0309-1708\(95\)00020-J](https://doi.org/10.1016/0309-1708(95)00020-J)
- Fučík, R., Klinkovský, J., Solovský, J., Oberhuber, T., Mikyška, J., 2019. Multidimensional mixed-hybrid finite element method for compositional two-phase flow in heterogeneous porous media and its parallel implementation on GPU. *Computer Physics Communications* 238, 165–180. <https://doi.org/10.1016/j.cpc.2018.12.004>
- Gardner, W. R. Some Steady-state solutions of the unsaturated moisture flow equation with application to evaporation from water table. *Soil Science* **1958**, 85, 228.
- Geng, X., Boufadel, M.C., Cui, F., 2016. Numerical modeling of subsurface release and fate of benzene and toluene in coastal aquifers subjected to tides. *Journal of Hydrology*. <https://doi.org/10.1016/j.jhydrol.2016.10.039>
- Ghezzehei, T.A., Kneafsey, T.J., Su, G.W., 2007. Correspondence of the Gardner and van Genuchten-Mualem relative permeability function parameters: GARDNER AND VAN

- GENUCHTEN-MUALEM MODELS. Water Resour. Res. 43. <https://doi.org/10.1029/2006WR005339>
- Gokdemir, C., Rubin, Y., Li, X., Li, Y., Xu, H., 2019. Vulnerability analysis method of vegetation due to groundwater table drawdown induced by tunnel drainage. *Advances in Water Resources* 133, 103406. <https://doi.org/10.1016/j.advwatres.2019.103406>
- González, J.A.M., Comte, J., 2019. Sensitivity and Uncertainty of Petrophysical Models to Predict Storage Properties in Weathered/Fractured Hard-Rock Aquifers, in: 25th European Meeting of Environmental and Engineering Geophysics. Presented at the 25th European Meeting of Environmental and Engineering Geophysics, European Association of Geoscientists & Engineers, The Hague, Netherlands, pp. 1–5. <https://doi.org/10.3997/2214-4609.201902380>
- Goswami, R.R., Clement, T.P., 2007. Laboratory-scale investigation of saltwater intrusion dynamics: DYNAMICS OF SALTWATER INTRUSION. *Water Resour. Res.* 43. <https://doi.org/10.1029/2006WR005151>
- Gotovac, H., Andricevic, R., Gotovac, B., 2007. Multi-resolution adaptive modeling of groundwater flow and transport problems. *Advances in Water Resources* 30, 1105–1126. <https://doi.org/10.1016/j.advwatres.2006.10.007>
- Grillo, A., Logashenko, D., Stichel, S., Wittum, G., 2010. Simulation of density-driven flow in fractured porous media. *Advances in Water Resources* 33, 1494–1507. <https://doi.org/10.1016/j.advwatres.2010.08.004>
- Guarracino, L., Quintana, F., 2009. A constitutive model for water flow in unsaturated fractured rocks. *Hydrol. Process.* 23, 697–701. <https://doi.org/10.1002/hyp.7169>
- Guevara Morel, C.R., van Reeuwijk, M., Graf, T., 2015. Systematic investigation of non-Boussinesq effects in variable-density groundwater flow simulations. *Journal of Contaminant Hydrology* 183, 82–98. <https://doi.org/10.1016/j.jconhyd.2015.10.004>
- Guo, L., Lin, H., Fan, B., Nyquist, J., Toran, L., Mount, G.J., 2019. Preferential flow through shallow fractured bedrock and a 3D fill-and-spill model of hillslope subsurface hydrology. *Journal of Hydrology* 576, 430–442. <https://doi.org/10.1016/j.jhydrol.2019.06.070>
- Hardyanto, W., Merkel, B., 2007. Introducing probability and uncertainty in groundwater modeling with FEMWATER-LHS. *Journal of Hydrology* 332, 206–213. <https://doi.org/10.1016/j.jhydrol.2006.06.035>
- Hassane Maina, F., Ackerer, P., 2017. Ross scheme, Newton–Raphson iterative methods and time-stepping strategies for solving the mixed form of Richards’ equation. *Hydrol. Earth Syst. Sci.* 21, 2667–2683. <https://doi.org/10.5194/hess-21-2667-2017>
- Hayden, K.M., Telyakovskiy, A.S., Wheatcraft, S.W., 2012. A note on free-surface films in fractures. *Advances in Water Resources* 49, 72–75. <https://doi.org/10.1016/j.advwatres.2012.06.012>
- Hayek, M., Kosakowski, G., Jakob, A., Churakov, S.V., 2012. A class of analytical solutions for multidimensional multispecies diffusive transport coupled with precipitation-dissolution reactions and porosity changes. *Water Resources Research* 48, WR3525. <https://doi.org/10.1029/2011WR011663>
- Held, R., Attinger, S., Kinzelbach, W., 2005. Homogenization and effective parameters for the Henry problem in heterogeneous formations: EFFECTIVE PARAMETERS FOR

- HETEROGENEOUS HENRY PROBLEM. Water Resour. Res. 41.
<https://doi.org/10.1029/2004WR003674>
- Helmig, R., Hassanizadeh, S.M., Dahle, H.K., 2016. Foreword: NUPUS: Porous Media Research Has Got a Brand Name. Transp Porous Med 114, 235–236.
<https://doi.org/10.1007/s11242-016-0736-5>
- Henry, H., 1964. Effects of dispersion on salt encroachment in coastal aquifer. U.S. Geol. Surv. Water Supply Pap. 1613, C70–C84.
- Herckenrath, D., Langevin, C.D., Doherty, J., 2011. Predictive uncertainty analysis of a saltwater intrusion model using null-space Monte Carlo: ANALYSIS OF A SALTWATER INTRUSION MODEL. Water Resour. Res. 47.
<https://doi.org/10.1029/2010WR009342>
- Hindmarsh, A.C., 1980. LSODE and LSODI, two new initial value ordinary differential equation solvers. SIGNUM Newsl. 15, 10–11. <https://doi.org/10.1145/1218052.1218054>
- Hirthe, E.M., Graf, T., 2015. Fracture network optimization for simulating 2D variable-density flow and transport. Advances in Water Resources 83, 364–375.
<https://doi.org/10.1016/j.advwatres.2015.07.001>
- Homma, T., Saltelli, A., 1996. Importance measures in global sensitivity analysis of nonlinear models. Reliability Engineering & System Safety 52, 1–17. [https://doi.org/10.1016/0951-8320\(96\)00002-6](https://doi.org/10.1016/0951-8320(96)00002-6)
- Hoteit, H., 2013. Modeling diffusion and gas–oil mass transfer in fractured reservoirs. Journal of Petroleum Science and Engineering 105, 1–17.
<https://doi.org/10.1016/j.petrol.2013.03.007>
- Hoteit, H., Firoozabadi, A., 2008. An efficient numerical model for incompressible two-phase flow in fractured media. Advances in Water Resources 31, 891–905.
<https://doi.org/10.1016/j.advwatres.2008.02.004>
- Hoteit, H., Mosé, R., Philippe, B., Ackerer, Ph., Erhel, J., 2002. The maximum principle violations of the mixed-hybrid finite-element method applied to diffusion equations. Int. J. Numer. Meth. Engng. 55, 1373–1390. <https://doi.org/10.1002/nme.531>
- Houben, G.J., Stoeckl, L., Mariner, K.E., Choudhury, A.S., 2018. The influence of heterogeneity on coastal groundwater flow - physical and numerical modeling of fringing reefs, dykes and structured conductivity fields. Advances in Water Resources 113, 155–166. <https://doi.org/10.1016/j.advwatres.2017.11.024>
- Hu, C., Youn, B.D., 2011. Adaptive-sparse polynomial chaos expansion for reliability and design of complex engineering systems. Structural and Multidisciplinary Optimization 43, 419–442. <https://doi.org/10.1007/s00158-010-0568-9>
- Huang, K., Mohanty, B.P., van Genuchten, M.Th., 1996. A new convergence criterion for the modified Picard iteration method to solve the variably saturated flow equation. Journal of Hydrology 178, 69–91. [https://doi.org/10.1016/0022-1694\(95\)02799-8](https://doi.org/10.1016/0022-1694(95)02799-8)
- Huang, W., Zheng, L., Zhan, X., 2002. Adaptive moving mesh methods for simulating one-dimensional groundwater problems with sharp moving fronts. Int. J. Numer. Meth. Engng. 54, 1579–1603. <https://doi.org/10.1002/nme.482>
- Huyakorn, P.S., Andersen, P.F., Mercer, J.W., White, H.O., 1987. Saltwater intrusion in aquifers: Development and testing of a three-dimensional finite element model. Water Resour. Res. 23, 293–312. <https://doi.org/10.1029/WR023i002p00293>

- IOC/UNESCO, IMO, FAO, UNDP., 2011. A Blueprint for Ocean and Coastal Sustainability, IOC/UNESCO. Paris.
- Iooss, B., Lemaître, P., 2015. A Review on Global Sensitivity Analysis Methods, in: Dellino, G., Meloni, C. (Eds.), *Uncertainty Management in Simulation-Optimization of Complex Systems*. Springer US, Boston, MA, pp. 101–122. https://doi.org/10.1007/978-1-4899-7547-8_5
- Ireson, A.M., Mathias, S.A., Wheeler, H.S., Butler, A.P., Finch, J., 2009. A model for flow in the chalk unsaturated zone incorporating progressive weathering. *Journal of Hydrology* 365, 244–260. <https://doi.org/10.1016/j.jhydrol.2008.11.043>
- Islam, M., Hye, A., Mamun, A., 2017. Nonlinear Effects on the Convergence of Picard and Newton Iteration Methods in the Numerical Solution of One-Dimensional Variably Saturated–Unsaturated Flow Problems. *Hydrology* 4, 50. <https://doi.org/10.3390/hydrology4040050>
- Jamshidzadeh, Z., Tsai, F.T.-C., Mirbagheri, S.A., Ghasemzadeh, H., 2013. Fluid dispersion effects on density-driven thermohaline flow and transport in porous media. *Advances in Water Resources* 61, 12–28. <https://doi.org/10.1016/j.advwatres.2013.08.006>
- Javadi, A., Hussain, M., Sherif, M., Farmani, R., 2015. Multi-objective Optimization of Different Management Scenarios to Control Seawater Intrusion in Coastal Aquifers. *Water Resour Manage* 29, 1843–1857. <https://doi.org/10.1007/s11269-015-0914-1>
- Javadi, A.A., Abd-Elhamid, H.F., Farmani, R., 2012. A simulation-optimization model to control seawater intrusion in coastal aquifers using abstraction/recharge wells: A SIMULATION-OPTIMIZATION MODEL TO CONTROL SEAWATER INTRUSION. *Int. J. Numer. Anal. Meth. Geomech.* 36, 1757–1779. <https://doi.org/10.1002/nag.1068>
- Jerbi, C., Fournio, A., Noetinger, B., Delay, F., 2017. A new estimation of equivalent matrix block sizes in fractured media with two-phase flow applications in dual porosity models. *Journal of Hydrology* 548, 508–523. <https://doi.org/10.1016/j.jhydrol.2017.03.028>
- Ji, S.-H., Park, Y.-J., Sudicky, E.A., Sykes, J.F., 2008. A generalized transformation approach for simulating steady-state variably-saturated subsurface flow. *Advances in Water Resources* 31, 313–323. <https://doi.org/10.1016/j.advwatres.2007.08.010>
- Jia, W., McPherson, B.J., Pan, F., Xiao, T., Bromhal, G., 2016. Probabilistic analysis of CO₂ storage mechanisms in a CO₂-EOR field using polynomial chaos expansion. *International Journal of Greenhouse Gas Control* 51, 218–229. <https://doi.org/10.1016/j.ijggc.2016.05.024>
- Jiang, Q., Ye, Z., Zhou, C., 2014. A numerical procedure for transient free surface seepage through fracture networks. *Journal of Hydrology* 519, 881–891. <https://doi.org/10.1016/j.jhydrol.2014.07.066>
- Jiang, X.-W., Wan, L., Wang, X.-S., Ge, S., Liu, J., 2009. Effect of exponential decay in hydraulic conductivity with depth on regional groundwater flow. *Geophys. Res. Lett.* 36, L24402. <https://doi.org/10.1029/2009GL041251>
- Jiao, J., Post, V., 2019. *Coastal Hydrogeology*, 1st ed. Cambridge University Press. <https://doi.org/10.1017/9781139344142>
- Juanes, R., Class, H., 2013. Special issue on computational methods in geologic CO₂ sequestration. *Advances in Water Resources* 62, 353–355. <https://doi.org/10.1016/j.advwatres.2013.10.012>

- Kacimov, A.R., 2001. Analytical solution to a sharp interface problem in a vortex-generated flow. *Water Resour. Res.* 37, 3387–3391. <https://doi.org/10.1029/2001WR000384>
- Kacimov, A.R., Obnosov, Yu.V., Sherif, M.M., Perret, J.S., 2006. Analytical Solution to a Seawater Intrusion Problem with a Fresh Water Zone Tapering to a Triple Point. *J Eng Math* 54, 197–210. <https://doi.org/10.1007/s10665-006-9030-9>
- Kalejaiye, B.O., Cardoso, S.S.S., 2005. Specification of the dispersion coefficient in the modeling of gravity-driven flow in porous media. *Water Resources Research* 41, n/a-n/a. <https://doi.org/10.1029/2004WR003925>
- Kerrou, J., Renard, P., 2010. A numerical analysis of dimensionality and heterogeneity effects on advective dispersive seawater intrusion processes. *Hydrogeol J* 18, 55–72. <https://doi.org/10.1007/s10040-009-0533-0>
- Ketabchi, H., Mahmoodzadeh, D., Ataie-Ashtiani, B., Simmons, C.T., 2016. Sea-level rise impacts on seawater intrusion in coastal aquifers: Review and integration. *Journal of Hydrology* 535, 235–255. <https://doi.org/10.1016/j.jhydrol.2016.01.083>
- Khalili, N., Russell, A., Khoshghalb, A. (Eds.), 2014. *Unsaturated Soils: Research & Applications*, 0 ed. CRC Press. <https://doi.org/10.1201/b17034>
- Konakli, K., Sudret, B., 2016. Global sensitivity analysis using low-rank tensor approximations. *Reliability Engineering & System Safety* 156, 64–83. <https://doi.org/10.1016/j.ress.2016.07.012>
- Konz, M., Younes, A., Ackerer, P., Fahs, M., Huggenberger, P., Zechner, E., 2009. Variable-density flow in heterogeneous porous media — Laboratory experiments and numerical simulations. *Journal of Contaminant Hydrology* 108, 168–175. <https://doi.org/10.1016/j.jconhyd.2009.07.005>
- Koohbor, B., Fahs, M., Ataie-Ashtiani, B., Belfort, B., Simmons, C.T., Younes, A., 2019. Uncertainty analysis for seawater intrusion in fractured coastal aquifers: Effects of fracture location, aperture, density and hydrodynamic parameters. *Journal of Hydrology* 571, 159–177. <https://doi.org/10.1016/j.jhydrol.2019.01.052>
- Koohbor, B., Fahs, M., Ataie-Ashtiani, B., Simmons, C.T., Younes, A., 2018. Semianalytical solutions for contaminant transport under variable velocity field in a coastal aquifer. *Journal of Hydrology* 560, 434–450. <https://doi.org/10.1016/j.jhydrol.2018.03.048>
- Koohbor, B., Fahs, M., Hoteit, H., Doummar, J., Younes, A., Belfort, B., 2020. An advanced discrete fracture model for variably saturated flow in fractured porous media. *Advances in Water Resources* 103602. <https://doi.org/10.1016/j.advwatres.2020.103602>
- Kopp, A., Binning, P.J., Johannsen, K., Helmig, R., Class, H., 2010. A contribution to risk analysis for leakage through abandoned wells in geological CO₂ storage. *Advances in Water Resources* 33, 867–879. <https://doi.org/10.1016/j.advwatres.2010.05.001>
- Kordilla, J., Noffz, T., Dentz, M., Geyer, T., Tartakovsky, A.M., 2017. Effect of Unsaturated Flow Modes on Partitioning Dynamics of Gravity-Driven Flow at a Simple Fracture Intersection: Laboratory Study and Three-Dimensional Smoothed Particle Hydrodynamics Simulations: FLOW IN UNSATURATED FRACTURED MEDIA. *Water Resour. Res.* 53, 9496–9518. <https://doi.org/10.1002/2016WR020236>
- Kordilla, J., Sauter, M., Reimann, T., Geyer, T., 2012. Simulation of saturated and unsaturated flow in karst systems at catchment scale using a double continuum approach. *Hydrol. Earth Syst. Sci.* 16, 3909–3923. <https://doi.org/10.5194/hess-16-3909-2012>

- Kuang, X., Jiao, J.J., 2014. An integrated permeability-depth model for Earth's crust: Permeability of Earth's crust. *Geophys. Res. Lett.* 41, 7539–7545. <https://doi.org/10.1002/2014GL061999>
- Kuráň, M., Mayer, P., Lepš, M., Trpkošová, D., 2010. An adaptive time discretization of the classical and the dual porosity model of Richards' equation. *Journal of Computational and Applied Mathematics* 233, 3167–3177. <https://doi.org/10.1016/j.cam.2009.11.056>
- Laabidi, E., Bouhlila, R., 2015. Nonstationary porosity evolution in mixing zone in coastal carbonate aquifer using an alternative modeling approach. *Environ Sci Pollut Res* 22, 10070–10082. <https://doi.org/10.1007/s11356-015-4207-2>
- Langevin, C.D., Dausman, A.M., Sukop, M.C., 2010. Solute and Heat Transport Model of the Henry and Hilleke Laboratory Experiment. *Ground Water* 48, 757–770. <https://doi.org/10.1111/j.1745-6584.2009.00596.x>
- Langevin, C.D., Guo, W., 2006. MODFLOW/MT3DMS-Based Simulation of Variable-Density Ground Water Flow and Transport. *Ground Water* 44, 339–351. <https://doi.org/10.1111/j.1745-6584.2005.00156.x>
- Le Gratiet, L., Marelli, S., Sudret, B., 2017. Metamodel-Based Sensitivity Analysis: Polynomial Chaos Expansions and Gaussian Processes, in: Ghanem, R., Higdon, D., Owhadi, H. (Eds.), *Handbook of Uncertainty Quantification*. Springer International Publishing, Cham, pp. 1289–1325. https://doi.org/10.1007/978-3-319-12385-1_38
- Leij, F.J., Dane, J.H., 1990. Analytical solutions of the one-dimensional advection equation and two- or three-dimensional dispersion equation. *Water Resources Research* 26, 1475–1482. <https://doi.org/10.1029/WR026i007p01475>
- Li, H., Farthing, M.W., Dawson, C.N., Miller, C.T., 2007. Local discontinuous Galerkin approximations to Richards' equation. *Advances in Water Resources* 30, 555–575. <https://doi.org/10.1016/j.advwatres.2006.04.011>
- Li, X., Chen, X., Hu, B.X., Navon, I.M., 2013. Model reduction of a coupled numerical model using proper orthogonal decomposition. *Journal of Hydrology* 507, 227–240. <https://doi.org/10.1016/j.jhydrol.2013.09.011>
- Li, X., Li, D., 2019. A numerical procedure for unsaturated seepage analysis in rock mass containing fracture networks and drainage holes. *Journal of Hydrology* 574, 23–34. <https://doi.org/10.1016/j.jhydrol.2019.04.014>
- Li, X., Li, D., Xu, Y., Feng, X., 2020. A DFN based 3D numerical approach for modeling coupled groundwater flow and solute transport in fractured rock mass. *International Journal of Heat and Mass Transfer* 149, 119179. <https://doi.org/10.1016/j.ijheatmasstransfer.2019.119179>
- List, F., Radu, F.A., 2016. A study on iterative methods for solving Richards' equation. *Comput Geosci* 20, 341–353. <https://doi.org/10.1007/s10596-016-9566-3>
- Liu, H.H., Bodvarsson, G.S., Finsterle, S., 2002. A note on unsaturated flow in two-dimensional fracture networks. *Water Resour. Res.* 38, 15-1-15-9. <https://doi.org/10.1029/2001WR000977>
- Liu, H.H., Salve, R., Wang, J.S., Bodvarsson, G.S., Hudson, D., 2004. Field investigation into unsaturated flow and transport in a fault: model analyses. *Journal of Contaminant Hydrology* 74, 39–59. <https://doi.org/10.1016/j.jconhyd.2004.02.004>

- Liu, H.H., Zhang, R., Bodvarsson, G.S., 2005. An active region model for capturing fractal flow patterns in unsaturated soils: Model development. *Journal of Contaminant Hydrology* 80, 18–30. <https://doi.org/10.1016/j.jconhyd.2005.07.002>
- Liu, M., Meakin, P., Huang, H., 2007. Dissipative particle dynamics simulation of fluid motion through an unsaturated fracture and fracture junction. *Journal of Computational Physics* 222, 110–130. <https://doi.org/10.1016/j.jcp.2006.07.017>
- Liu, Y., Mao, X., Chen, J., Barry, D.A., 2014. Influence of a coarse interlayer on seawater intrusion and contaminant migration in coastal aquifers: INFLUENCE OF COARSE INTERLAYER ON FLOW AND TRANSPORT IN COASTAL AQUIFER. *Hydrol. Process.* 28, 5162–5175. <https://doi.org/10.1002/hyp.10002>
- Llopis-Albert, C., Merigó, J.M., Xu, Y., 2016. A coupled stochastic inverse/sharp interface seawater intrusion approach for coastal aquifers under groundwater parameter uncertainty. *Journal of Hydrology* 540, 774–783. <https://doi.org/10.1016/j.jhydrol.2016.06.065>
- Lu, C., Chen, Y., Zhang, C., Luo, J., 2013. Steady-state freshwater–seawater mixing zone in stratified coastal aquifers. *Journal of Hydrology* 505, 24–34. <https://doi.org/10.1016/j.jhydrol.2013.09.017>
- Lu, C., Kitanidis, P.K., Luo, J., 2009. Effects of kinetic mass transfer and transient flow conditions on widening mixing zones in coastal aquifers. *Water Resources Research* 45, n/a–n/a. <https://doi.org/10.1029/2008WR007643>
- Lu, C., Xin, P., Li, L., Luo, J., 2015. Seawater intrusion in response to sea-level rise in a coastal aquifer with a general-head inland boundary. *Journal of Hydrology* 522, 135–140. <https://doi.org/10.1016/j.jhydrol.2014.12.053>
- MacAllister, D., Jackson, M.D., Butler, A.P., Vinogradov, J., 2018. Remote Detection of Saline Intrusion in a Coastal Aquifer Using Borehole Measurements of Self-Potential. *Water Resources Research* 54, 1669–1687. <https://doi.org/10.1002/2017WR021034>
- Maina, F.Z., Guadagnini, A., 2018. Uncertainty Quantification and Global Sensitivity Analysis of Subsurface Flow Parameters to Gravimetric Variations During Pumping Tests in Unconfined Aquifers. *Water Resources Research* 54, 501–518. <https://doi.org/10.1002/2017WR021655>
- Malenica, L., Gotovac, H., Kamber, G., Simunovic, S., Allu, S., Divic, V., 2018. Groundwater Flow Modeling in Karst Aquifers: Coupling 3D Matrix and 1D Conduit Flow via Control Volume Isogeometric Analysis—Experimental Verification with a 3D Physical Model. *Water* 10, 1787. <https://doi.org/10.3390/w10121787>
- Marelli, S., Sudret, B., 2014. UQLab: A Framework for Uncertainty Quantification in Matlab. *American Society of Civil Engineers*, pp. 2554–2563. <https://doi.org/10.1061/9780784413609.257>
- Marion, P., Najib, K., Rosier, C., 2014. Numerical simulations for a seawater intrusion problem in a free aquifer. *Applied Numerical Mathematics* 75, 48–60. <https://doi.org/10.1016/j.apnum.2012.11.003>
- Masciopinto, C., Caputo, M.C., 2011. Modeling Unsaturated-Saturated Flow and Nickel Transport in Fractured Rocks. *Vadose Zone Journal* 10, 1045–1057. <https://doi.org/10.2136/vzj2010.0087>

- Masciopinto, C., Liso, I., Caputo, M., De Carlo, L., 2017. An Integrated Approach Based on Numerical Modelling and Geophysical Survey to Map Groundwater Salinity in Fractured Coastal Aquifers. *Water* 9, 875. <https://doi.org/10.3390/w9110875>
- Matthews, C.J., Braddock, R.D., Sander, G.C., 2004. Modeling Flow Through a One-Dimensional Multi-Layered Soil Profile Using the Method of Lines. *Environmental Modeling & Assessment* 9, 103–113. <https://doi.org/10.1023/B:ENMO.0000032092.10546.c6>
- May, D.A., 2014. Numerical Modelling in Geosciences, Short-course on Numerical Modelling, National Observatory of Athens.
- Mehdizadeh, S.S., Werner, A.D., Vafaie, F., Badaruddin, S., 2014. Vertical leakage in sharp-interface seawater intrusion models of layered coastal aquifers. *Journal of Hydrology* 519, 1097–1107. <https://doi.org/10.1016/j.jhydrol.2014.08.027>
- Mehnert, E., Jennings, A.A., 1985. The effect of salinity-dependent hydraulic conductivity on saltwater intrusion episodes. *Journal of Hydrology* 80, 283–297. [https://doi.org/10.1016/0022-1694\(85\)90122-2](https://doi.org/10.1016/0022-1694(85)90122-2)
- Meng, J., Li, H., 2017. Efficient Uncertainty Quantification for Unconfined Flow in Heterogeneous Media with the Sparse Polynomial Chaos Expansion. *Transport in Porous Media*. <https://doi.org/10.1007/s11242-017-0974-1>
- Michael, H.A., Russoniello, C.J., Byron, L.A., 2013. Global assessment of vulnerability to sea-level rise in topography-limited and recharge-limited coastal groundwater systems: GLOBAL ASSESSMENT OF VULNERABILITY TO SEA-LEVEL RISE. *Water Resour. Res.* 49, 2228–2240. <https://doi.org/10.1002/wrcr.20213>
- Miller, C.T., Dawson, C.N., Farthing, M.W., Hou, T.Y., Huang, J., Kees, C.E., Kelley, C.T., Langtangen, H.P., 2013. Numerical simulation of water resources problems: Models, methods, and trends. *Advances in Water Resources* 51, 405–437. <https://doi.org/10.1016/j.advwatres.2012.05.008>
- Miller, K.L., Berg, S.J., Davison, J.H., Sudicky, E.A., Forsyth, P.A., 2018. Efficient uncertainty quantification in fully-integrated surface and subsurface hydrologic simulations. *Advances in Water Resources* 111, 381–394. <https://doi.org/10.1016/j.advwatres.2017.10.023>
- Monachesi, L.B., Guarracino, L., 2011. A Fractal Model for Predicting Water and Air Permeabilities of Unsaturated Fractured Rocks. *Transp Porous Med* 90, 779–789. <https://doi.org/10.1007/s11242-011-9815-9>
- Moortgat, J., 2017. Adaptive implicit finite element methods for multicomponent compressible flow in heterogeneous and fractured porous media. *Water Resour. Res.* 53, 73–92. <https://doi.org/10.1002/2016WR019644>
- Moortgat, J., Amooie, M.A., Soltanian, M.R., 2016. Implicit finite volume and discontinuous Galerkin methods for multicomponent flow in unstructured 3D fractured porous media. *Advances in Water Resources* 96, 389–404. <https://doi.org/10.1016/j.advwatres.2016.08.007>
- Mozafari, B., Fahs, M., Ataie-Ashtiani, B., Simmons, C.T., Younes, R., 2018. On the use of COMSOL Multiphysics for seawater intrusion in fractured coastal aquifers. *E3S Web of Conferences* 54, 00020. <https://doi.org/10.1051/e3sconf/20185400020>

- Mualem, Y., 1976. A new model for predicting the hydraulic conductivity of unsaturated porous media. *Water Resour. Res.* 12, 513–522. <https://doi.org/10.1029/WR012i003p00513>
- Mudarra, M., Andreo, B., 2011. Relative importance of the saturated and the unsaturated zones in the hydrogeological functioning of karst aquifers: The case of Alta Cadena (Southern Spain). *Journal of Hydrology* 397, 263–280. <https://doi.org/10.1016/j.jhydrol.2010.12.005>
- Mugunthan, P., Russell, K.T., Gong, B., Riley, M.J., Chin, A., McDonald, B.G., Eastcott, L.J., 2017. A Coupled Groundwater-Surface Water Modeling Framework for Simulating Transition Zone Processes. *Groundwater* 55, 302–315. <https://doi.org/10.1111/gwat.12475>
- Najib, K., Rosier, C., 2011. On the global existence for a degenerate elliptic–parabolic seawater intrusion problem. *Mathematics and Computers in Simulation* 81, 2282–2295. <https://doi.org/10.1016/j.matcom.2010.12.026>
- Nassar, M.K., Ginn, T.R., 2014. Impact of numerical artifact of the forward model in the inverse solution of density-dependent flow problem. *Water Resources Research* 50, 6322–6338. <https://doi.org/10.1002/2013WR014672>
- Ngo-Cong, D., Mai-Duy, N., Antille, D.L., van Genuchten, M.Th., 2020. A control volume scheme using compact integrated radial basis function stencils for solving the Richards equation. *Journal of Hydrology* 580, 124240. <https://doi.org/10.1016/j.jhydrol.2019.124240>
- Nick, H.M., Raoof, A., Centler, F., Thullner, M., Regnier, P., 2013. Reactive dispersive contaminant transport in coastal aquifers: Numerical simulation of a reactive Henry problem. *Journal of Contaminant Hydrology* 145, 90–104. <https://doi.org/10.1016/j.jconhyd.2012.12.005>
- Nield, D.A., Bejan, A., 2013. *Convection in porous media*, 4th ed. ed. Springer Science+Business Media, New York.
- Nield, D.A., Kuznetsov, A.V., 2012. The Effect of Strong Heterogeneity and Strong Throughflow on the Onset of Convection in a Porous Medium: Non-Periodic Global Variation. *Transport in Porous Media* 91, 927–938. <https://doi.org/10.1007/s11242-011-9881-z>
- Njue, C.N., Cundy, A.B., Smith, M., Green, I.D., Tomlinson, N., 2012. Assessing the impact of historical coastal landfill sites on sensitive ecosystems: A case study from Dorset, Southern England. *Estuarine, Coastal and Shelf Science* 114, 166–174. <https://doi.org/10.1016/j.ecss.2012.08.022>
- Nordbotten, J.M., Boon, W.M., Fumagalli, A., Keilegavlen, E., 2019. Unified approach to discretization of flow in fractured porous media. *Comput Geosci* 23, 225–237. <https://doi.org/10.1007/s10596-018-9778-9>
- Oude Essink, G.H.P., van Baaren, E.S., de Louw, P.G.B., 2010. Effects of climate change on coastal groundwater systems: A modeling study in the Netherlands. *Water Resour. Res.* 46, 2009WR008719. <https://doi.org/10.1029/2009WR008719>
- Oz, I., Shalev, E., Yechieli, Y., Gvirtzman, H., 2015. Saltwater circulation patterns within the freshwater–saltwater interface in coastal aquifers: Laboratory experiments and numerical modeling. *Journal of Hydrology* 530, 734–741. <https://doi.org/10.1016/j.jhydrol.2015.10.033>

- Parker, J.C., Kim, U., 2015. An upscaled approach for transport in media with extended tailing due to back-diffusion using analytical and numerical solutions of the advection dispersion equation. *Journal of Contaminant Hydrology* 182, 157–172. <https://doi.org/10.1016/j.jconhyd.2015.09.008>
- Perriquet, M., Leonardi, V., Henry, T., Jourde, H., 2014. Saltwater wedge variation in a non-anthropogenic coastal karst aquifer influenced by a strong tidal range (Burren, Ireland). *Journal of Hydrology* 519, 2350–2365. <https://doi.org/10.1016/j.jhydrol.2014.10.006>
- Pistiner, A., Shapiro, M., 1993. A model for a moving interface in a layered coastal aquifer. *Water Resour. Res.* 29, 329–340. <https://doi.org/10.1029/92WR01901>
- Pokhrel, Y.N., Koirala, S., Yeh, P.J.-F., Hanasaki, N., Longuevergne, L., Kanae, S., Oki, T., 2015. Incorporation of groundwater pumping in a global Land Surface Model with the representation of human impacts. *Water Resour. Res.* 51, 78–96. <https://doi.org/10.1002/2014WR015602>
- Pool, M., Carrera, J., Dentz, M., Hidalgo, J.J., Abarca, E., 2011. Vertical average for modeling seawater intrusion: VERTICAL AVERAGE FOR MODELING SEAWATER INTRUSION. *Water Resour. Res.* 47. <https://doi.org/10.1029/2011WR010447>
- Pool, M., Post, V.E.A., Simmons, C.T., 2015. Effects of tidal fluctuations and spatial heterogeneity on mixing and spreading in spatially heterogeneous coastal aquifers. *Water Resour. Res.* 51, 1570–1585. <https://doi.org/10.1002/2014WR016068>
- Post, V.E.A., Vandenbohede, A., Werner, A.D., Maimun, Teubner, M.D., 2013. Groundwater ages in coastal aquifers. *Advances in Water Resources* 57, 1–11. <https://doi.org/10.1016/j.advwatres.2013.03.011>
- Pouya, A., Vu, M.-N., Ghabezloo, S., Bendjeddou, Z., 2013. Effective permeability of cracked unsaturated porous materials. *International Journal of Solids and Structures* 50, 3297–3307. <https://doi.org/10.1016/j.ijsolstr.2013.05.027>
- Prasad, A., Simmons, C.T., 2005. Using quantitative indicators to evaluate results from variable-density groundwater flow models. *Hydrogeol J* 13, 905–914. <https://doi.org/10.1007/s10040-004-0338-0>
- Qin, R., Wu, Y., Xu, Z., Xie, D., Zhang, C., 2013. Numerical modeling of contaminant transport in a stratified heterogeneous aquifer with dipping anisotropy. *Hydrogeol J* 21, 1235–1246. <https://doi.org/10.1007/s10040-013-0999-7>
- Qu, W., Li, H., Wan, L., Wang, X., Jiang, X., 2014. Numerical simulations of steady-state salinity distribution and submarine groundwater discharges in homogeneous anisotropic coastal aquifers. *Advances in Water Resources* 74, 318–328. <https://doi.org/10.1016/j.advwatres.2014.10.009>
- Radhakrishnan, K., Hindmarsh, A.C., 1993. Description and use of LSODE, the Livmore Solver for Ordinary Differential Equations (No. UCRL-ID-113855, 15013302). <https://doi.org/10.2172/15013302>
- Rajabi, M.M., Ataie-Ashtiani, B., 2014. Sampling efficiency in Monte Carlo based uncertainty propagation strategies: Application in seawater intrusion simulations. *Advances in Water Resources* 67, 46–64. <https://doi.org/10.1016/j.advwatres.2014.02.004>
- Rajabi, M.M., Ataie-Ashtiani, B., Janssen, H., 2015a. Efficiency enhancement of optimized Latin hypercube sampling strategies: Application to Monte Carlo uncertainty analysis and

- meta-modeling. *Advances in Water Resources* 76, 127–139. <https://doi.org/10.1016/j.advwatres.2014.12.008>
- Rajabi, M.M., Ataie-Ashtiani, B., Simmons, C.T., 2015b. Polynomial chaos expansions for uncertainty propagation and moment independent sensitivity analysis of seawater intrusion simulations. *Journal of Hydrology* 520, 101–122. <https://doi.org/10.1016/j.jhydrol.2014.11.020>
- Ramasomanana, F., Fahs, M., Baalousha, H.M., Barth, N., Ahzi, S., 2018. An Efficient ELLAM Implementation for Modeling Solute Transport in Fractured Porous Media. *Water, Air, & Soil Pollution* 229, 46. <https://doi.org/10.1007/s11270-018-3690-8>
- Ranjan, P., Kazama, S., Sawamoto, M., 2006. Effects of climate change on coastal fresh groundwater resources. *Global Environmental Change* 16, 388–399. <https://doi.org/10.1016/j.gloenvcha.2006.03.006>
- Raviart, P.A., Thomas, J.M., 1977. A mixed finite element method for 2-nd order elliptic problems, in: Galligani, I., Magenes, E. (Eds.), *Mathematical Aspects of Finite Element Methods*. Springer Berlin Heidelberg, Berlin, Heidelberg, pp. 292–315. <https://doi.org/10.1007/BFb0064470>
- Reilly, T.E., Goodman, A.S., 1985. Quantitative analysis of saltwater-freshwater relationships in groundwater systems—A historical perspective. *Journal of Hydrology* 80, 125–160. [https://doi.org/10.1016/0022-1694\(85\)90078-2](https://doi.org/10.1016/0022-1694(85)90078-2)
- Ren, F., Ma, G., Wang, Y., Li, T., Zhu, H., 2017. Unified pipe network method for simulation of water flow in fractured porous rock. *Journal of Hydrology* 547, 80–96. <https://doi.org/10.1016/j.jhydrol.2017.01.044>
- Riva, M., Guadagnini, A., Dell’Oca, A., 2015. Probabilistic assessment of seawater intrusion under multiple sources of uncertainty. *Advances in Water Resources* 75, 93–104. <https://doi.org/10.1016/j.advwatres.2014.11.002>
- Robineau, T., Tognelli, A., Goblet, P., Renard, F., Schaper, L., 2018. A double medium approach to simulate groundwater level variations in a fissured karst aquifer. *Journal of Hydrology* 565, 861–875. <https://doi.org/10.1016/j.jhydrol.2018.09.002>
- Roels, S., Vandersteen, K., Carmeliet, J., 2003. Measuring and simulating moisture uptake in a fractured porous medium. *Advances in Water Resources* 26, 237–246. [https://doi.org/10.1016/S0309-1708\(02\)00185-9](https://doi.org/10.1016/S0309-1708(02)00185-9)
- Ruane, A.C., Goldberg, R., Chryssanthacopoulos, J., 2015. Climate forcing datasets for agricultural modeling: Merged products for gap-filling and historical climate series estimation. *Agricultural and Forest Meteorology* 200, 233–248. <https://doi.org/10.1016/j.agrformet.2014.09.016>
- Saltelli, A., 2002. Making best use of model evaluations to compute sensitivity indices. *Computer Physics Communications* 145, 280–297. [https://doi.org/10.1016/S0010-4655\(02\)00280-1](https://doi.org/10.1016/S0010-4655(02)00280-1)
- Sanz, E., Voss, C.I., 2006. Inverse modeling for seawater intrusion in coastal aquifers: Insights about parameter sensitivities, variances, correlations and estimation procedures derived from the Henry problem. *Advances in Water Resources* 29, 439–457. <https://doi.org/10.1016/j.advwatres.2005.05.014>
- Sarkar, S., Witteveen, J.A., 2016. *Uncertainty Quantification In Computational Science: Theory And Application In Fluids And Structural Mechanics*. World Scientific.

- Saylor, C., Cardiff, M., Fort, M.D., 2018. Understanding the Geometry of Connected Fracture Flow with Multiperiod Oscillatory Hydraulic Tests. *Groundwater* 56, 276–287. <https://doi.org/10.1111/gwat.12580>
- Scudeler, C., Putti, M., Paniconi, C., 2016. Mass-conservative reconstruction of Galerkin velocity fields for transport simulations. *Advances in Water Resources* 94, 470–485. <https://doi.org/10.1016/j.advwatres.2016.06.011>
- Sebben, M.L., Werner, A.D., Graf, T., 2015. Seawater intrusion in fractured coastal aquifers: A preliminary numerical investigation using a fractured Henry problem. *Advances in Water Resources* 85, 93–108. <https://doi.org/10.1016/j.advwatres.2015.09.013>
- Ségol, G., 1994. *Classic groundwater simulations: proving and improving numerical models*. PTR Prentice Hall, Englewood Cliffs, N.J.
- Servan-Camas, B., Tsai, F.T.-C., 2009. Saltwater intrusion modeling in heterogeneous confined aquifers using two-relaxation-time lattice Boltzmann method. *Advances in Water Resources* 32, 620–631. <https://doi.org/10.1016/j.advwatres.2009.02.001>
- Servan-Camas, B., Tsai, F.T.-C., 2010. Two-relaxation-time lattice Boltzmann method for the anisotropic dispersive Henry problem: ANISOTROPIC LATTICE BOLTZMANN METHOD. *Water Resour. Res.* 46. <https://doi.org/10.1029/2009WR007837>
- Shahkarami, P., Liu, L., Moreno, L., Neretnieks, I., 2015. Radionuclide migration through fractured rock for arbitrary-length decay chain: Analytical solution and global sensitivity analysis. *Journal of Hydrology* 520, 448–460. <https://doi.org/10.1016/j.jhydrol.2014.10.060>
- Shao, Q., Fahs, M., Younes, A., Makradi, A., Mara, T., 2016. A new benchmark reference solution for double-diffusive convection in a heterogeneous porous medium. *Numerical Heat Transfer, Part B: Fundamentals* 70, 373–392. <https://doi.org/10.1080/10407790.2016.1215718>
- Shao, Q., Younes, A., Fahs, M., Mara, T.A., 2017. Bayesian sparse polynomial chaos expansion for global sensitivity analysis. *Computer Methods in Applied Mechanics and Engineering* 318, 474–496. <https://doi.org/10.1016/j.cma.2017.01.033>
- Shi, W., Lu, C., Ye, Y., Wu, J., Li, L., Luo, J., 2018. Assessment of the impact of sea-level rise on steady-state seawater intrusion in a layered coastal aquifer. *Journal of Hydrology* 563, 851–862. <https://doi.org/10.1016/j.jhydrol.2018.06.046>
- Simmons, C.T., Fenstemaker, T.R., Sharp, J.M., 2001. Variable-density groundwater flow and solute transport in heterogeneous porous media: approaches, resolutions and future challenges. *Journal of Contaminant Hydrology* 52, 245–275. [https://doi.org/10.1016/S0169-7722\(01\)00160-7](https://doi.org/10.1016/S0169-7722(01)00160-7)
- Simpson, M.J., Clement, T.P., 2003. Theoretical analysis of the worthiness of Henry and Elder problems as benchmarks of density-dependent groundwater flow models. *Advances in Water Resources* 26, 17–31. [https://doi.org/10.1016/S0309-1708\(02\)00085-4](https://doi.org/10.1016/S0309-1708(02)00085-4)
- Simpson, M.J., Clement, T.P., 2004. Improving the worthiness of the Henry problem as a benchmark for density-dependent groundwater flow models: IMPROVING THE HENRY PROBLEM. *Water Resour. Res.* 40. <https://doi.org/10.1029/2003WR002199>
- Singh, A., 2014. Groundwater resources management through the applications of simulation modeling: A review. *Science of The Total Environment* 499, 414–423. <https://doi.org/10.1016/j.scitotenv.2014.05.048>

- Small, C., Nicholls, R.J., 2003. A Global Analysis of Human Settlement in Coastal Zones. *Journal of Coastal Research* 19, 584–599. <https://doi.org/10.2307/4299200>
- Sobol', I.M., 2001. Global sensitivity indices for nonlinear mathematical models and their Monte Carlo estimates. *Mathematics and Computers in Simulation, The Second IMACS Seminar on Monte Carlo Methods* 55, 271–280. [https://doi.org/10.1016/S0378-4754\(00\)00270-6](https://doi.org/10.1016/S0378-4754(00)00270-6)
- Soto Meca, A., Alhama, F., González Fernández, C.F., 2007. An efficient model for solving density driven groundwater flow problems based on the network simulation method. *Journal of Hydrology* 339, 39–53. <https://doi.org/10.1016/j.jhydrol.2007.03.003>
- Stoeckl, L., Houben, G.J., Dose, E.J., 2015. Experiments and modeling of flow processes in freshwater lenses in layered island aquifers: Analysis of age stratification, travel times and interface propagation. *Journal of Hydrology* 529, 159–168. <https://doi.org/10.1016/j.jhydrol.2015.07.019>
- Sudret, B., 2008. Global sensitivity analysis using polynomial chaos expansions. *Reliability Engineering & System Safety* 93, 964–979. <https://doi.org/10.1016/j.ress.2007.04.002>
- Suk, H., 2016. Generalized semi-analytical solutions to multispecies transport equation coupled with sequential first-order reaction network with spatially or temporally variable transport and decay coefficients. *Advances in Water Resources* 94, 412–423. <https://doi.org/10.1016/j.advwatres.2016.06.004>
- Suk, H., 2017. Semi-analytical solution of land-derived solute transport under tidal fluctuation in a confined aquifer. *Journal of Hydrology* 554, 517–531. <https://doi.org/10.1016/j.jhydrol.2017.09.033>
- Suk, H., Park, E., 2019. Numerical solution of the Kirchhoff-transformed Richards equation for simulating variably saturated flow in heterogeneous layered porous media. *Journal of Hydrology* 579, 124213. <https://doi.org/10.1016/j.jhydrol.2019.124213>
- Sun, D., Niu, S., Zang, Y., 2017. Impacts of inland boundary conditions on modeling seawater intrusion in coastal aquifers due to sea-level rise. *Nat Hazards* 88, 145–163. <https://doi.org/10.1007/s11069-017-2860-0>
- Szymkiewicz, A., 2013. *Modelling Water Flow in Unsaturated Porous Media*, GeoPlanet: Earth and Planetary Sciences. Springer Berlin Heidelberg, Berlin, Heidelberg. <https://doi.org/10.1007/978-3-642-23559-7>
- Szymkiewicz, A., Gumuła-Kawęcka, A., Šimůnek, J., Leterme, B., Beegum, S., Jaworska-Szulc, B., Pruszkowska-Caceres, M., Gorczewska-Langner, W., Angulo-Jaramillo, R., Jacques, D., 2018. Simulations of freshwater lens recharge and salt/freshwater interfaces using the HYDRUS and SWI2 packages for MODFLOW. *Journal of Hydrology and Hydromechanics* 66, 246–256. <https://doi.org/10.2478/johh-2018-0005>
- Tartakovsky, D.M., 2000. An analytical solution for two-dimensional contaminant transport during groundwater extraction. *Journal of Contaminant Hydrology* 42, 273–283. [https://doi.org/10.1016/S0169-7722\(99\)00086-8](https://doi.org/10.1016/S0169-7722(99)00086-8)
- Tartakovsky, D.M., Di Federico, V., 1997. An Analytical Solution for Contaminant Transport in nonuniform Flow. *Transport in Porous Media* 27, 85–97. <https://doi.org/10.1023/A:1006579817668>

- Therrien, R., Sudicky, E.A., 1996. Three-dimensional analysis of variably-saturated flow and solute transport in discretely-fractured porous media. *Journal of Contaminant Hydrology* 23, 1–44. [https://doi.org/10.1016/0169-7722\(95\)00088-7](https://doi.org/10.1016/0169-7722(95)00088-7)
- Tokunaga, T.K., Wan, J., 2001. Surface-zone flow along unsaturated rock fractures. *Water Resour. Res.* 37, 287–296. <https://doi.org/10.1029/2000WR900242>
- Van der Hoven, S.J., Solomon, D.K., Moline, G.R., 2003. Modeling unsaturated flow and transport in the saprolite of fractured sedimentary rocks: Effects of periodic wetting and drying: MODELING UNSATURATED FLOW AND TRANSPORT. *Water Resour. Res.* 39. <https://doi.org/10.1029/2002WR001926>
- van Genuchten, M.Th., 1980. A Closed-form Equation for Predicting the Hydraulic Conductivity of Unsaturated Soils. *Soil Science Society of America Journal* 44, 892–898. <https://doi.org/10.2136/sssaj1980.03615995004400050002x>
- van Reeuwijk, M., Mathias, S.A., Simmons, C.T., Ward, J.D., 2009. Insights from a pseudospectral approach to the Elder problem: PSEUDOSPECTRAL APPROACH TO THE ELDER PROBLEM. *Water Resour. Res.* 45. <https://doi.org/10.1029/2008WR007421>
- Vauclin, M., Khanji, D., Vachaud, G., 1979. Experimental and numerical study of a transient, two-dimensional unsaturated-saturated water table recharge problem. *Water Resour. Res.* 15, 1089–1101. <https://doi.org/10.1029/WR015i005p01089>
- Vilarrasa, V., Carrera, J., 2015. Geologic carbon storage is unlikely to trigger large earthquakes and reactivate faults through which CO₂ could leak. *Proc Natl Acad Sci USA* 112, 5938–5943. <https://doi.org/10.1073/pnas.1413284112>
- Volker, R.E., Zhang, Q., Lockington, D.A., 2002. Numerical modelling of contaminant transport in coastal aquifers. *Mathematics and Computers in Simulation* 59, 35–44. [https://doi.org/10.1016/S0378-4754\(01\)00391-3](https://doi.org/10.1016/S0378-4754(01)00391-3)
- Voss, C.I., Simmons, C.T., Robinson, N.I., 2010. Three-dimensional benchmark for variable-density flow and transport simulation: matching semi-analytic stability modes for steady unstable convection in an inclined porous box. *Hydrogeol J* 18, 5–23. <https://doi.org/10.1007/s10040-009-0556-6>
- Walther, M., Graf, T., Kolditz, O., Liedl, R., Post, V., 2017. How significant is the slope of the sea-side boundary for modelling seawater intrusion in coastal aquifers? *Journal of Hydrology* 551, 648–659. <https://doi.org/10.1016/j.jhydrol.2017.02.031>
- Wang, J.S.Y., Narasimhan, T.N., 1985. Hydrologic Mechanisms Governing Fluid Flow in a Partially Saturated, Fractured, Porous Medium. *Water Resour. Res.* 21, 1861–1874. <https://doi.org/10.1029/WR021i012p01861>
- Wang, L., Hu, W., Sun, D., Li, L., 2019. 3D stability of unsaturated soil slopes with tension cracks under steady infiltrations. *Int J Numer Anal Methods Geomech* 43, 1184–1206. <https://doi.org/10.1002/nag.2889>
- Wang, X.-S., Jiang, X.-W., Wan, L., Ge, S., Li, H., 2011. A new analytical solution of topography-driven flow in a drainage basin with depth-dependent anisotropy of permeability: TECHNICAL NOTE. *Water Resour. Res.* 47. <https://doi.org/10.1029/2011WR010507>

- Wang, Y., Wu, C., Zhou, Y., 2017. Effect Study of Aperture Distribution on the Capillary Pressure-Saturation Relation for the Single Fracture. *Geofluids* 2017, 1–13. <https://doi.org/10.1155/2017/9656393>
- Waxman, M.H., Smits, L.J.M., 1968. Electrical Conductivities in Oil-Bearing Shaly Sands. *Society of Petroleum Engineers Journal* 8, 107–122. <https://doi.org/10.2118/1863-A>
- Weatherill, D., Simmons, C.T., Voss, C.I., Robinson, N.I., 2004. Testing density-dependent groundwater models: two-dimensional steady state unstable convection in infinite, finite and inclined porous layers. *Advances in Water Resources* 27, 547–562. <https://doi.org/10.1016/j.advwatres.2004.01.003>
- Werner, A.D., Bakker, M., Post, V.E.A., Vandenbohede, A., Lu, C., Ataie-Ashtiani, B., Simmons, C.T., Barry, D.A., 2013. Seawater intrusion processes, investigation and management: Recent advances and future challenges. *Advances in Water Resources* 51, 3–26. <https://doi.org/10.1016/j.advwatres.2012.03.004>
- Woumeni, R.S., Vauclin, M., 2006. A field study of the coupled effects of aquifer stratification, fluid density, and groundwater fluctuations on dispersivity assessments. *Advances in Water Resources* 29, 1037–1055. <https://doi.org/10.1016/j.advwatres.2005.09.002>
- Xie, Y., Simmons, C.T., Werner, A.D., Diersch, H.-J.G., 2012. Prediction and uncertainty of free convection phenomena in porous media. *Water Resources Research* 48, n/a-n/a. <https://doi.org/10.1029/2011WR011346>
- Xu, Z., Hu, B.X., Ye, M., 2018. Numerical modeling and sensitivity analysis of seawater intrusion in a dual-permeability coastal karst aquifer with conduit networks. *Hydrology and Earth System Sciences* 22, 221–239. <https://doi.org/10.5194/hess-22-221-2018>
- Yang, J., Graf, T., Herold, M., Ptak, T., 2013. Modelling the effects of tides and storm surges on coastal aquifers using a coupled surface–subsurface approach. *Journal of Contaminant Hydrology* 149, 61–75. <https://doi.org/10.1016/j.jconhyd.2013.03.002>
- Yang, L., Liu, E., 2020. Numerical Analysis of the Effects of Crack Characteristics on the Stress and Deformation of Unsaturated Soil Slopes. *Water* 12, 194. <https://doi.org/10.3390/w12010194>
- Yang, Z., Xue, S., Zheng, X., Chen, Y., 2019. Partitioning Dynamics of Gravity-Driven Unsaturated Flow Through Simple T-Shaped Fracture Intersections. *Water Resour. Res.* 55, 7130–7142. <https://doi.org/10.1029/2018WR024349>
- Ye, M., Pan, F., Wu, Y.-S., Hu, B.X., Shirley, C., Yu, Z., 2007. Assessment of radionuclide transport uncertainty in the unsaturated zone of Yucca Mountain. *Advances in Water Resources* 30, 118–134. <https://doi.org/10.1016/j.advwatres.2006.03.005>
- Yeh, H.D., Huang, C.S., Chang, Y.C., Jeng, D.S., 2010. An analytical solution for tidal fluctuations in unconfined aquifers with a vertical beach. *Water Resources Research* 46, n/a-n/a. <https://doi.org/10.1029/2009WR008746>
- Yoon, S., Williams, J.R., Juanes, R., Kang, P.K., 2017. Maximizing the value of pressure data in saline aquifer characterization. *Advances in Water Resources* 109, 14–28. <https://doi.org/10.1016/j.advwatres.2017.08.019>
- Younes, A., Ackerer, P., 2008. Solving the advection-dispersion equation with discontinuous Galerkin and multipoint flux approximation methods on unstructured meshes. *International Journal for Numerical Methods in Fluids* 58, 687–708. <https://doi.org/10.1002/fld.1783>

- Younes, A., Ackerer, P., Delay, F., 2010. Mixed finite elements for solving 2-D diffusion-type equations. *Rev. Geophys.* 48, RG1004. <https://doi.org/10.1029/2008RG000277>
- Younes, A., Ackerer, P., Lehmann, F., 2006. A new mass lumping scheme for the mixed hybrid finite element method. *Int. J. Numer. Meth. Engng* 67, 89–107. <https://doi.org/10.1002/nme.1628>
- Younes, A., Delay, F., Fajraoui, N., Fahs, M., Mara, T.A., 2016. Global sensitivity analysis and Bayesian parameter inference for solute transport in porous media colonized by biofilms. *Journal of Contaminant Hydrology* 191, 1–18. <https://doi.org/10.1016/j.jconhyd.2016.04.007>
- Younes, A., Fahs, M., 2014. A semi-analytical solution for saltwater intrusion with a very narrow transition zone. *Hydrogeol J* 22, 501–506. <https://doi.org/10.1007/s10040-014-1102-8>
- Younes, A., Fahs, M., 2015. Extension of the Henry semi-analytical solution for saltwater intrusion in stratified domains. *Comput Geosci* 19, 1207–1217. <https://doi.org/10.1007/s10596-015-9534-3>
- Younes, A., Fahs, M., Ahmed, S., 2009. Solving density driven flow problems with efficient spatial discretizations and higher-order time integration methods. *Advances in Water Resources* 32, 340–352. <https://doi.org/10.1016/j.advwatres.2008.11.003>
- Younes, A., Fahs, M., Belfort, B., 2013. Monotonicity of the cell-centred triangular MPFA method for saturated and unsaturated flow in heterogeneous porous media. *Journal of Hydrology* 504, 132–141. <https://doi.org/10.1016/j.jhydrol.2013.09.041>
- Younes, A., Mara, T.A., Fajraoui, N., Lehmann, F., Belfort, B., Beydoun, H., 2013. Use of Global Sensitivity Analysis to Help Assess Unsaturated Soil Hydraulic Parameters. *Vadose Zone Journal* 12, 0. <https://doi.org/10.2136/vzj2011.0150>
- Younes, A., Mose, R., Ackerer, P., Chavent, G., 1999. A New Formulation of the Mixed Finite Element Method for Solving Elliptic and Parabolic PDE with Triangular Elements. *Journal of Computational Physics* 149, 148–167. <https://doi.org/10.1006/jcph.1998.6150>
- Younes, A., Zaouali, J., Lehmann, F., Fahs, M., 2018. Sensitivity and identifiability of hydraulic and geophysical parameters from streaming potential signals in unsaturated porous media. *Hydrology and Earth System Sciences* 22, 3561–3574. <https://doi.org/10.5194/hess-22-3561-2018>
- Zha, Y., Yang, J., Yin, L., Zhang, Y., Zeng, W., Shi, L., 2017. A modified Picard iteration scheme for overcoming numerical difficulties of simulating infiltration into dry soil. *Journal of Hydrology* 551, 56–69. <https://doi.org/10.1016/j.jhydrol.2017.05.053>
- Zha, Y., Yang, J., Zeng, J., Tso, C.M., Zeng, W., Shi, L., 2019. Review of numerical solution of Richardson–Richards equation for variably saturated flow in soils. *WIREs Water* 6. <https://doi.org/10.1002/wat2.1364>
- Zhang, H., Schwartz, F.W., 1995. Multispecies Contaminant Plumes in Variable Density Flow Systems. *Water Resour. Res.* 31, 837–847. <https://doi.org/10.1029/94WR02567>
- Zhang, Q., Volker, R.E., Lockington, D.A., 2002. Experimental investigation of contaminant transport in coastal groundwater. *Advances in Environmental Research* 6, 229–237. [https://doi.org/10.1016/S1093-0191\(01\)00054-5](https://doi.org/10.1016/S1093-0191(01)00054-5)

- Zhao, C., 2016. Computational Methods for Simulating Some Typical Problems in Computational Geosciences. *Int. J. Comput. Methods* 13, 1640016. <https://doi.org/10.1142/S0219876216400168>
- Zhao, C., Hobbs, B.E., Ord, A., 2009. Fundamentals of computational geoscience: numerical methods and algorithms, Lecture notes in earth sciences. Springer, Berlin ; [New York].
- Zhao, Y., Wu, Y., Han, S., Xue, S., Fan, G., Chen, Z., El Abd, A., 2019. Water sorptivity of unsaturated fractured sandstone: Fractal modeling and neutron radiography experiment. *Advances in Water Resources* 130, 172–183. <https://doi.org/10.1016/j.advwatres.2019.06.006>
- Zhou, Q., Salve, R., Liu, H.-H., Wang, J.S.Y., Hudson, D., 2006. Analysis of a mesoscale infiltration and water seepage test in unsaturated fractured rock: Spatial variabilities and discrete fracture patterns. *Journal of Contaminant Hydrology* 87, 96–122. <https://doi.org/10.1016/j.jconhyd.2006.05.001>
- Zidane, A., Firoozabadi, A., 2014a. An efficient numerical model for multicomponent compressible flow in fractured porous media. *Advances in Water Resources* 74, 127–147. <https://doi.org/10.1016/j.advwatres.2014.08.010>
- Zidane, A., Firoozabadi, A., 2018. Reservoir simulation of fractured media in compressible single-phase flow in 2D, 2.5D and 3D unstructured gridding. *Advances in Water Resources* 121, 68–96. <https://doi.org/10.1016/j.advwatres.2018.08.005>
- Zidane, A., Younes, A., Huggenberger, P., Zechner, E., 2012. The Henry semianalytical solution for saltwater intrusion with reduced dispersion: HENRY SEMIANALYTICAL SOLUTION WITH REDUCED DISPERSION. *Water Resour. Res.* 48. <https://doi.org/10.1029/2011WR011157>
- Zlotnik, V.A., Cardenas, M.B., Tondykov, D., 2011. Effects of Multiscale Anisotropy on Basin and Hyporheic Groundwater Flow. *Ground Water* 49, 576–583. <https://doi.org/10.1111/j.1745-6584.2010.00775.x>

Appendices

Appendix A.

Coefficients and matrices for R^F and R^T

$$\varpi_h^1 = \begin{cases} 2, & \text{if } h = 0 \\ 1, & \text{if } h \neq 0 \end{cases} \quad (\text{A.1})$$

$$\tilde{B}_{r,h} = \begin{cases} B_{r,h} & \text{if } h \leq Ns \\ 0 & \text{else} \end{cases} \quad (\text{A.2})$$

$$\Gamma_{g,r} = (g+r) \frac{1 - (-1)^{g+r} e^{\Upsilon}}{\Upsilon^2 + \pi^2 (g+r)^2} + (g-r) \frac{1 - (-1)^{g-r} e^{\Upsilon}}{\Upsilon^2 + \pi^2 (g-r)^2} \quad (\text{A.3})$$

$$\Pi_{g,m} = \begin{cases} \left(\frac{1 - (-1)^{g+m}}{g+m} + \frac{1 - (-1)^{g-m}}{g-m} \right) & \text{if } g \neq m \\ 0 & \text{if } g = m \end{cases} \quad (\text{A.4})$$

F^{Disp} is a function representing the dispersion terms. It is given by:

$$\begin{aligned} F^{Disp} = & \Delta_{1,1} \frac{\partial^2 C}{\partial X^2} + 2\Delta_{1,2} \frac{\partial^2 C}{\partial X \partial Z} + \Delta_{2,2} \frac{\partial^2 C}{\partial Z^2} + \left(\frac{\partial C}{\partial X} + \frac{1}{\xi} \right) \left(\frac{\partial \Delta_{1,1}}{\partial X} + \frac{\partial \Delta_{1,2}}{\partial Z} \right) \\ & + \frac{\partial C}{\partial Z} \left(\frac{\partial \Delta_{1,2}}{\partial X} + \frac{\partial \Delta_{2,2}}{\partial Z} \right) \end{aligned} \quad (\text{A.5})$$

$$\varpi_g^2 = \begin{cases} 2 & \text{if } g = 0 \\ 1 & \text{if } g \neq 0 \end{cases} \quad (\text{A.6})$$

$$\eta_{g,m,r} = \delta_{m+r,g} + \delta_{r-m,g} + \delta_{m-r,g} \quad (\text{A.7})$$

$$\kappa_{g,m,r} = -\delta_{m+r,g} + \delta_{r-m,g} + \delta_{m-r,g} \quad (\text{A.8})$$

$$\theta_{h,n,s} = \frac{(-1)^{h+n+s} - 1}{h+n+s} + \frac{(-1)^{h+n-s} - 1}{h+n-s} + \frac{(-1)^{h-n+s} - 1}{h-n+s} + \frac{(-1)^{h-n-s} - 1}{h-n-s} \quad (\text{A.9})$$

$$\lambda_{h,n,s} = \frac{(-1)^{h+n-s} - 1}{h+n-s} + \frac{(-1)^{h-n+s} - 1}{h-n+s} - \frac{(-1)^{h+n+s} - 1}{h+n+s} - \frac{(-1)^{h-n-s} - 1}{h-n-s} \quad (\text{A.10})$$

$$\tilde{A}_{g,n} = \begin{cases} A_{g,n} & 0 \leq g \leq Nm \\ 0 & g > Nm \end{cases} \quad (\text{A.11})$$

$$\Lambda_{g,r} = \begin{cases} \frac{(-1)^{g+r} - 1}{g+r} + \frac{(-1)^{g-r} - 1}{g-r} & \text{if } g \neq r \\ 0 & \text{if } g = r \end{cases} \quad (\text{A.12})$$

Appendix B.

Coefficients of the final systems:

$$\varpi_i = \begin{cases} 2 & \text{if } i = 0 \\ 1 & \text{if } i \neq 0 \end{cases} \quad (\text{B.1})$$

$$\tilde{A}_{i,j} = \begin{cases} A_{i,j} & 0 \leq i \leq Nm \\ 0 & i > Nm \end{cases} \quad (\text{B.2})$$

$$\tilde{B}_{i,j} = \begin{cases} B_{i,j} & 0 \leq j \leq Ns \\ 0 & j > Ns \end{cases} \quad (\text{B.3})$$

$$\Lambda_{i,j} = \begin{cases} \frac{(-1)^{i+j} - 1}{i+j} + \frac{(-1)^{i-j} - 1}{i-j} & \text{if } i \neq j \\ 0 & \text{if } i = j \end{cases} \quad (\text{B.4})$$

$\delta_{i,j}$ is the kronecker symbol

$$\eta_{i,j,k} = \delta_{j+k,i} + \delta_{k-j,i} + \delta_{j-k,i} \quad (\text{B.5})$$

$$\hat{\eta}_{i,j,k} = \delta_{i,j+k} + \delta_{i,k-j} - \delta_{i,j-k} \quad (\text{B.6})$$

$$\bar{\eta}_{i,j,k} = \delta_{i,j-k} + \delta_{i,k-j} + \delta_{i,j+k} \quad (\text{B.7})$$

$$\kappa_{i,j,k} = -\delta_{j+k,i} + \delta_{k-j,i} + \delta_{j-k,i} \quad (\text{B.8})$$

$$\hat{\kappa}_{g,m,k} = \delta_{g,m+k} + \delta_{g,m-k} - \delta_{g,k-m} \quad (\text{B.9})$$

$$\bar{\kappa}_{g,m,k} = \delta_{g,m-k} + \delta_{g,k-m} - \delta_{g,k+m} \quad (\text{B.10})$$

$$\theta_{i,j,k} = \frac{(-1)^{i+j+k} - 1}{i+j+k} + \frac{(-1)^{i+j-k} - 1}{i+j-k} + \frac{(-1)^{i-j+k} - 1}{i-j+k} + \frac{(-1)^{i-j-k} - 1}{i-j-k} \quad (\text{B.11})$$

$$\hat{\theta}_{i,j,k} = \frac{(-1)^{i+j+k} - 1}{i+j+k} - \frac{(-1)^{i-j-k} - 1}{i-j-k} + \frac{(-1)^{i-j+k} - 1}{i-j+k} - \frac{(-1)^{i+j-k} - 1}{i+j-k} \quad (\text{B.12})$$

$$\bar{\theta}_{i,j,k} = - \left(\frac{(-1)^{k+i-j} - 1}{k+i-j} + \frac{(-1)^{k-i+j} - 1}{k-i+j} + \frac{(-1)^{k+i+j} - 1}{k+i+j} + \frac{(-1)^{k-i-j} - 1}{k-i-j} \right) \quad (\text{B.13})$$

$$\lambda_{i,j,k} = \frac{(-1)^{i+j-k} - 1}{i+j-k} + \frac{(-1)^{i-j+k} - 1}{i-j+k} - \frac{(-1)^{i+j+k} - 1}{i+j+k} - \frac{(-1)^{i-j-k} - 1}{i-j-k} \quad (\text{B.14})$$

$$\hat{\lambda}_{i,j,k} = \frac{(-1)^{i+j+k} - 1}{i+j+k} - \frac{(-1)^{i-j-k} - 1}{i-j-k} + \frac{(-1)^{i-k+j} - 1}{i-k+j} - \frac{(-1)^{i+k-j} - 1}{i+k-j} \quad (\text{B.15})$$

$$\bar{\lambda}_{i,j,k} = \left(\frac{(-1)^{k+i-j} - 1}{k+i-j} + \frac{(-1)^{k-i+j} - 1}{k-i+j} - \frac{(-1)^{k+i+j} - 1}{k+i+j} - \frac{(-1)^{k-i-j} - 1}{k-i-j} \right) \quad (\text{B.16})$$

$$\Upsilon_{i,j} = \begin{cases} 2 \left(\frac{(-1)^{j+i}}{j+i} + \frac{(-1)^{i-j}}{i-j} \right) & \text{if } j \neq i \\ \frac{1}{i} & \text{if } j = i \end{cases} \quad (\text{B.17})$$

$$\Sigma_{i,j} = \frac{1}{\pi} \left(\frac{(-1)^{i+j} - 1}{(i+j)^2} - \frac{(-1)^{i-j} - 1}{(i-j)^2} \right) \quad (\text{B.18})$$

$$I_1^{BC} = \int_0^{\xi} f_{Top}(X) \sin \left(n\pi \frac{X}{\xi} \right) \cos \left(\frac{h\pi X}{\xi} \right) dX \quad (\text{B.19})$$

$$I_2^{BC} = \int_0^{\xi} f'_{Top}(X) \cos \left(\frac{h\pi X}{\xi} \right) \cos \left(n\pi \frac{X}{\xi} \right) dX \quad (\text{B.20})$$

$$I_3^{BC} = \int_0^{\xi} \left(Pe^c f''_{Top}(X) - f'_{Top}(X) \right) \cos \left(\frac{h\pi X}{\xi} \right) dX \quad (\text{B.21})$$

$$J_1^{BC} = \int_0^1 f_{Land}(Z) \cos(m\pi Z) \cos(g\pi Z) dZ \quad (\text{B.22})$$

$$J_2^{BC} = \int_0^1 f'_{Land}(Z) \sin(m\pi Z) \cos(g\pi Z) dZ \quad (\text{B.23})$$

$$J_3^{BC} = \int_0^1 f_{Land}(Z) \cos(g\pi Z) dZ \quad (\text{B.24})$$

$$J_4^{BC} = \int_0^1 f''_{Land}(Z) \cos(g\pi Z) dZ \quad (\text{B.25})$$

The integrals I_1^{BC} , I_2^{BC} , I_3^{BC} , J_1^{BC} , J_2^{BC} , J_3^{BC} and J_4^{BC} are evaluated numerically using QDAWO integration routine from the IMSL libraries.

Appendix C.

Table C.1. Coefficients for the bi-exponential model used for the regression of A_c and M_c (surface contamination scenario).

| Pe | Y_0 | A_1 | t_1 | A_2 | t_2 |
|------|-------------|------------|---------|-----------|--------------------|
| | A_c | | | | |
| 10 | -6273.80334 | 0.32654 | 2.31438 | 6274.1983 | 1.10×10^6 |
| 50 | 0.09419 | 0.12038 | 1.72974 | 0.08971 | 11.84595 |
| 200 | 0.03512 | 0.06188 | 1.90672 | 0.04985 | 22.71617 |
| | M_c | | | | |
| | | | | | |
| 10 | -3678.1559 | 3678.28691 | 3.08962 | 0.08493 | 2.33×10^6 |
| 50 | -111.85293 | 111.90627 | 2.67844 | 0.04164 | 151094.592 |
| 200 | 0.01589 | 0.01521 | 2.15698 | 0.01559 | 13.78005 |

Table C.2. Coefficients for the second degree polynomial model used for the regression of F_c and \overline{Sh} (surface contamination scenario).

| Pe | B_0 | B_1 | B_2 |
|------|-----------------|----------|------------------------|
| | \overline{Sh} | | |
| 10 | 3.824225 | 0.307125 | -0.006025 |
| 50 | 7.75745 | 0.7242 | -0.01385 |
| 200 | 16.2514 | 1.435125 | -0.02315 |
| | F_c | | |
| | | | |
| 10 | 0.07882 | 0.00475 | -6.87×10^{-5} |
| 50 | 0.03324 | 0.00285 | -5.22×10^{-5} |
| 200 | 0.01699 | 0.00143 | -2.53×10^{-5} |

Table C.3. Coefficients for the second degree polynomial model used for the regression of A_c and M_c (Landward contamination scenario).

| Pe | B_0 | B_1 | B_2 |
|------|---------|-----------|----------|
| | A_c | | |
| 10 | 2.43973 | -0.0613 | 0.00115 |
| 50 | 2.33241 | -0.16018 | 0.00469 |
| 200 | 1.63068 | -0.11858 | 0.00359 |
| | M_c | | |
| | | | |
| 10 | 0.75099 | -0.02858 | 6.76E-04 |
| 50 | 0.78682 | -0.04927 | 0.00133 |
| 200 | 0.78478 | -0.05704 | 0.00159 |
| | F_c | | |
| | | | |
| 10 | 0.31201 | -0.00366 | 3.60E-04 |
| 50 | 0.30187 | -9.06E-04 | 1.98E-04 |
| 200 | 0.30528 | -0.00107 | 1.22E-04 |

Modeling water flow and mass transport in fractured porous media: application to seawater intrusion and unsaturated zone

Résumé

Ce mémoire de thèse traite de la modélisation des écoulements et du transport dans les milieux poreux fracturés, avec deux applications : l'intrusion saline dans les aquifères côtiers et l'écoulement dans la zone non saturée fracturée. Les principaux objectifs sont d'améliorer l'efficacité et la précision des modèles numériques afin de renforcer leur capacité à traiter des situations réelles de terrain. Une partie importante est consacrée au développement de solutions semi-analytiques pour l'intrusion d'eau de mer avec le modèle d'écoulement densitaire. Ces solutions sont utiles à des fins d'analyse comparative et de compréhension des processus physiques. Une technique robuste d'analyse de sensibilité avec un modèle de substitution est également développée pour étudier les incertitudes liées aux fractures sur l'intrusion saline. Une autre partie du mémoire décrit un schéma numérique efficace élaboré pour la simulation des écoulements variablement saturés dans les domaines fracturés. Ce nouveau schéma est utilisé pour étudier l'effet du changement climatique sur les ressources en eau souterraine dans un système fracturé au Liban.

Mots-clés : modélisation numérique ; intrusion saline ; milieux poreux fracturés ; solution semi-analytique ; modèle de substitution ; écoulement variablement saturé

Abstract

This work addresses the numerical modeling of flow and mass transport in fractured porous media with a focus on two applications: seawater intrusion in coastal aquifers and flow in the fractured vadose zone. The main objectives of this work are to improve the efficiency and accuracy of numerical models to enhance their capacity in dealing with real-world studies. A significant part is dedicated to the development of semi-analytical solutions for seawater intrusion with the variable density flow model. These solutions are useful for benchmarking purposes and understanding the physical processes. An appropriate and robust technique based on surrogate modeling is also developed to investigate the uncertainties related to fractures on seawater intrusion. An efficient numerical scheme is developed for the simulation of variably saturated flow in fractured domains. The new developed scheme is used to investigate the effect of climate change on groundwater resources in a karst aquifer/spring system in Lebanon.

Keywords: numerical modeling; seawater intrusion; fractured porous media; semi-analytical solution; surrogate modeling; variably saturated flow